

MECHANISTIC INVESTIGATIONS OF CATALYTIC
ORGANIC REACTIONS

BY

JOSEPH A. IZZO

BS, Mansfield University, 2014

DISSERTATION

Submitted in partial fulfillment of the requirements for
the degree of Doctor of Philosophy in Chemistry
in the Graduate School of
Binghamton University
State University of New York
2018

© Copyright by Joseph Anthony Izzo 2018

All Rights Reserved

Accepted in partial fulfillment of the requirements for
the degree of Doctor of Philosophy in Chemistry
in the Graduate School of
Binghamton University
State University of New York
2018

November 16, 2018

Eriks Rozners, Chair
Department of Chemistry, Binghamton University

Mathew J. Vetticatt, Faculty Advisor
Department of Chemistry, Binghamton University

Susan L. Bane, Member
Department of Chemistry, Binghamton University

Julien A. Panetier, Member
Department of Chemistry, Binghamton University

John D. Chisholm, Outside Examiner
Department of Chemistry, Syracuse University

ABSTRACT

MECHANISTIC INVESTIGATIONS OF CATALYTIC ORGANIC REACTIONS

In-depth mechanistic investigations were carried out on nine catalytic organic reactions reported in the literature. The L-proline-catalyzed α -amination of aldehydes; prolinol derivative-catalyzed Michael and epoxidation reactions; bifunctional (thio)urea/amine-catalyzed α -fluorination, α -hydroxylation, and Michael addition; borate-catalyzed aziridination; copper(II) bromide-catalyzed α -amination; and the Suzuki-Miyaura reaction were studied. A high-resolution picture of the turnover-limiting step for each reaction was obtained through the use of carbon-13 kinetic isotope effects measured at natural abundance and/or high-level density functional theory calculations.

The study of the L-proline-catalyzed α -amination of aldehydes, prolinol derivative-catalyzed epoxidation, and copper(II) bromide-catalyzed α -amination led to the discovery that previously suggested mechanisms were incongruent with our newly obtained data and thus required revision. New key transition states are proposed and supported for each reaction.

Interrogation of the prolinol derivative- and the bifunctional thiourea/tertiary amine-catalyzed Michael additions, and the Suzuki-Miyaura reaction generated a clearer understanding of the mechanistic discrepancies and studies reported in the literature. Mechanistic controversies were resolved, and evidence was supplied to differentiate between proposed mechanisms.

Finally, in the investigation of the bifunctional urea/quaternary ammonium-catalyzed α -fluorination and α -hydroxylation, and borate-catalyzed aziridination, our studies were conducted to lend a better understanding of the reactions developed in the labs of our synthetic collaborators. In some cases, the increased understanding led to improved methods.

All of these examples display the power of these physical organic chemistry tools to better understand mechanisms in organic catalysis.

Dedicated to the things that got me through: faith, family, friends, fun, and food.

ACKNOWLEDGEMENTS

I would like to first and foremost thank my advisor, Dr. Mathew J. Veticatt. We had our disagreements and our laughs, we had our failures and our successes. I learned so much from you beyond just the chemistry. Thank you.

I would like to thank Professors Rozners, Bane, Panetier, and Chisholm. I know how busy professors can get, and taking the time to read and edit this thesis is an honor. I appreciate the help you lent recently, and the guidance, support, and friendship you offered throughout my graduate career.

I also thank all the members of the Veticatt Group, past and present, for their support and, in some cases, collaboration. Having a group of colleagues who are knowledgeable and willing to help, certainly made work easier and more enjoyable. I am especially grateful for my co-authors: Melissa, Jen, Jeremy, Yars, Juliet, Sierra, Veronica, and Jin.

I thank Binghamton University for giving me a place to grow as a chemist and a person for the past four and a half years.

I thank my collaborators beyond Binghamton: Johanna Novacek from Mario Waser's lab at Johannes Kepler University; Gang Hu, Anil Gupta, Li Huang, Wenjun Zhao, Xiaopeng Yin, Wynter Osminski, and Rui Huang from William Wulff's lab at Michigan State University; and Pernille Poulsen from Karl Anker Jørgensen's lab at Aarhus University. Without working together we wouldn't have been able to make the advances we did.

My heartfelt appreciation goes out to my friends for their support. From lunch dates to brunch dates, from adventures out on the town to quiet time at home, from Friday nights to Sunday mornings, a local support system is crucial, and I can't thank you enough for being the ones on whom I leaned in my times of stress.

Finally, my family: Mom, Dad, Katie, Grandma and Grandpa. Your love and support through the past twenty-six years (and especially these past four and a half) have made me into the person I am today and are the reason I am here now. Thank you.

TABLE OF CONTENTS

List of Figures	xi
List of Tables	xvii
Chapter I: Introduction.....	1
1.1 Catalysis in Organic Chemistry	1
1.2 Overview of Kinetic Isotope Effects.....	9
1.3 Computational Methods	15
Chapter II: Secondary Amine Catalysis.....	18
2.1 Enamine Catalysis	18
2.1.1 Isotope Effects Reveal the Mechanism of Enamine Formation in L-Proline-Catalyzed α -Amination of Aldehydes	20
2.1.2 Isotope Effects Reveal Discrepancies in Current Mechanistic Understanding of Diphenylprolinol Silyl Ether-Catalyzed Michael Reaction of Aldehydes and Nitroolefins	30
2.2 “Iminium-ion” Catalysis	46
2.2.1 Kinetic Isotope Effects Reveal an Alternative Mechanism for “Iminium- Ion” Catalysis.....	47
Chapter III: Non-covalent Organocatalysis	60
3.1 Bifunctional Quaternary Amine-Urea.....	60
3.1.1 Bifunctional Ammonium Salt Catalyzed Asymmetric α -fluorination of β -Ketoesters	61
3.1.2 Bifunctional Ammonium Salt Catalyzed Asymmetric α -Hydroxylation of β -Ketoesters by Simultaneous Resolution of Oxaziridines	68
3.2 Isotope Effects Reveal Transition State of Bifunctional Thiourea-tertiary Amine-catalyzed Michael Addition	73
3.3 A DFT investigation of borox catalyzed aziridination.....	83
Chapter IV: Transition Metal Catalyzed Reactions	90
4.1 Isotope Effects Reveal Presence of Cu ^{III} Intermediate in α -Amination Reaction.....	90
4.2 Isotope Effects Reveal Nature of Transmetalation Transition State in the Catalytic Suzuki-Miyaura Reaction	100

Chapter V. Experimental and Computational Details.....	107
5.1 General notes.....	107
5.1.1 Experimental procedures	107
5.1.2 Computational methods	107
5.2 Secondary Amine Catalysis	109
5.2.1 Enamine catalysis.....	109
5.2.2 “Iminium-ion” catalysis.....	118
5.3 Non-covalent Organocatalysis	134
5.3.1 Quaternary ammonium salt catalysis	134
5.3.2 Isotope Effects Reveal Transition State of Bifunctional Thiourea- tertiary Amine-catalyzed Michael Addition	141
5.3.3 A DFT investigation of borox catalyzed aziridination	148
5.4 Transition Metal Catalyzed Reactions	148
5.4.1 Isotope Effects Reveal Presence of Cu ^{III} Intermediate In α -Amination Reaction	148
5.4.2 Isotope Effects Reveal Nature of Transmetalation Transition State in the Catalytic Suzuki-Miyaura Reaction.....	152
Bibliography	161

LIST OF FIGURES

Figures appearing in CHAPTER I: INTRODUCTION

Figure 1. 1. Two conceptions of catalysis.....	2
Figure 1. 2. Timeline of notable transition-metal catalyzed reactions from 1959-2000.....	4
Figure 1. 3. Three basic classes of secondary amine catalysts	7
Figure 1. 4. Basic catalysts employed in organocatalysis.....	8
Figure 1. 5. Graphical representation of the difference in energy wells of material in the ground-state versus the transition state	10
Figure 1. 6. Graphical representation of the difference in energy wells of starting material in the ground-state versus the transition state for (a) a normal isotope effect; (b) inverse isotope effect.....	12
Figure 1. 7. Singleton's original small KIE determination reaction.....	15

Figures appearing in CHAPTER II: SECONDARY AMINE CATALYSIS

Figure 2. 1. First steps of enamine catalysis	19
Figure 2. 2. Addition of an electrophile to an enamine	20
Figure 2. 3. The Houk-List model of L-proline catalysis.....	21
Figure 2. 4. Enantiodetermining step in the H-L model of proline catalysis (TS10)	21
Figure 2. 5. Seebach-Eschenmoser model of L-proline catalysis.....	22
Figure 2. 6. Gschwind's 2010 model of L-proline catalysis.....	23
Figure 2. 7. Distinguishing features of the three proposed mechanisms for L-proline catalysis.....	24

Figure 2. 8. Experimental KIEs measured for the L-proline-catalyzed reaction of 1a with 2a. The two sets of ^{13}C KIEs and two sets of ^2H KIEs represent independent experiments. The number in parentheses shows the uncertainty in the last digit.	25
Figure 2. 9. More O'Ferrall-Jencks plot for the possible pathways for conversion of 11 to 12	26
Figure 2. 10. Newly proposed TS14'	27
Figure 2. 11. Calculated geometry and predicted KIEs of TS14'a	27
Figure 2. 12. Stacked NMR spectra showing percent conversion monitoring of $\alpha\text{-D}_2\text{-1a}$ using $\text{DMSO-}d_6$ as an internal standard.....	29
Figure 2. 13. KIEs for (blue Arial) measured with $\alpha\text{-D}_2\text{-1a}$, (red bold) measured with $\alpha\text{-}h_2\text{-1a}$, (green italic) predicted for TS3	29
Figure 2. 14. Seebach and co-workers' proposed catalytic cycle.....	32
Figure 2. 15. Blackmond and co-workers' proposed catalytic cycle	34
Figure 2. 16. Studies conducted by Blackmond and co-workers; (a) EXSY NMR interpretations for mono- and di-substituted aldehyde; (b) deuterium KIE measurement	35
Figure 2. 17. Pihko and co-workers' proposed catalytic cycle.....	37
Figure 2. 18. Observed phenomenon by Pihko and co-workers	37
Figure 2. 19. Conditions used to first study of the title reaction and KIEs; Lavender Arial numbers were measured in the absence of acid co-catalyst, peach <i>Italic</i> numbers were measured in the presence of <i>p</i> -nitrophenol as a co-catalyst.....	38
Figure 2. 20. Conditions used in the second study of the title reaction and KIEs	39
Figure 2. 21. Conditions used in the third and fourth studies of the title reaction and KIEs	40
Figure 2. 22. DFT optimized transition state for carbon-carbon bond formation and predicted KIEs with acetic acid	41
Figure 2. 23. Acetic acid protonation of the nitronate carbon of (a) oxazine intermediate; (b) cyclobutane intermediate	42
Figure 2. 24. DFT optimized transition state for carbon-carbon bond formation and predicted KIEs with acetic acid	43

Figure 2. 25. Conditions used in the fifth study of the title reaction and KIEs	45
Figure 2. 26. LUMO-lowering strategies.....	46
Figure 2. 27. General mechanism for iminium-ion formation.....	47
Figure 2. 28. Jørgensen group's proposed catalytic cycle.....	49
Figure 2. 29. Santos group's proposed catalytic cycle	50
Figure 2. 30. Measured KIEs from four independent experiments.....	51
Figure 2. 31. Three possible mechanisms leading to a qualitative agreement of observed KIEs. Pink bubbles indicate location of expected normal KIE	53
Figure 2. 32. Parameters varied in systematic conformational search. (a) Orientation of chiral moiety of the catalyst; (b) pucker of the pyrrolidine ring; (c) orientation of the peroxide.....	54
Figure 2. 33. Lowest energy geometry for (a) TS-iminium; (b) TS- A_N ; (c) predicted and experimental KIEs. Experimental KIEs are the weighted average of all measurements.....	55
Figure 2. 34. Lowest energy geometry and predicted KIEs for TS- S_N2' . Experimental KIEs are the weighted average of all measurements.	56
Figure 2. 35. Lowest energy geometry for TS- S_N2' -ent	57
Figure 2. 36. Lowest energy geometry and predicted KIEs for TS-shift. Experimental KIEs are the weighted average of all measurements.	58
Figure 2. 37. General application of novel S_N2' mechanism	59
Figure 2. 38. Systems under study for continued evidence of the novel S_N2' mechanism	59

Figures appearing in CHAPTER III: NON-COVALENT ORGANOCATALYSIS

Figure 3. 1. DFT optimized transition state for Waser's fluorination using BM1	62
Figure 3. 2. DFT optimized transition state for Waser's fluorination using BM2	63
Figure 3. 3. DFT optimized transition state for Waser's fluorination using (a) BM3; (b) BM4	64

Figure 3. 4. Three relevant angle conformations around rotatable σ -bonds explored computationally.....	65
Figure 3. 5. DFT optimized transition state for Waser's fluorination using BM2, giving rise to the (a) minor enantiomer of product; (b) major enantiomer of product; critical CH-F interactions highlighted in pink	66
Figure 3. 6. Electrostatic potential map generated for Waser fluorination.....	67
Figure 3. 7. Lowest energy transition states leading to (a) major; (b) minor enantiomer of product.....	69
Figure 3. 8. Explanation of match/mis-match relationship.....	70
Figure 3. 9. Linear effects study using enantiopure (<i>S,S</i>)-oxaziridine.....	71
Figure 3. 10. Mis-matched oxaziridine/catalyst combination for the Waser hydroxylation	71
Figure 3. 11. Highlighted pi-stacking in the match case of oxaziridine and product	72
Figure 3. 12. Takemoto's proposed catalytic cycle.....	74
Figure 3. 13. Proposed binding modes A and B	75
Figure 3. 14. Experimental reaction conditions and measured KIEs.....	77
Figure 3. 15. Two methods of deprotonation investigated; (a) C-deprotonation; (b) O-deprotonation	78
Figure 3. 16. Predicted KIEs for TS17 (blue <i>italic</i> numbers represent predicted KIEs for TS17 _{O-deprot} ; red bold numbers represent predicted KIEs for TS17 _{C-deprot} ; black Arial numbers represent measured KIEs)	78
Figure 3. 17. Calculated transition states leading to the major enantiomer of product via BMC.....	79
Figure 3. 18. Calculated transition states leading to the minor enantiomer of product via BMD	80
Figure 3. 19. Predicted KIEs for TS2 (green <i>italic</i> numbers represent predicted KIEs for TS2; black Arial numbers represent measured KIEs).....	81
Figure 3. 20. Lowest energy geometries for TS19 via (a) O-protonation; (b) C-protonation	82

Figure 3. 21. Predicted KIEs for TS19 (blue <i>italic</i> numbers represent predicted KIEs for TS1 _{O-prot} ; red bold numbers represent predicted KIEs for TS1 _{C-prot} ; black Arial numbers represent measured KIEs)	82
Figure 3. 22. BINOL and vaulted ligands	84
Figure 3. 23. Reaction mechanism for the Brønsted Acid catalyzed aziridination of imines with diazo compounds	85
Figure 3. 24. Lowest energy TSs for <i>Si</i> -TS1 employing (a) <i>spiro</i> -borate 9; (b) boroxinate 8b as catalyst	86
Figure 3. 25. Energy diagrams regarding the title system catalyzed by (a) 55; (b) 54b ...	87
Figure 3. 26. Lowest energy TS for <i>Re</i> -TS2 employing boroxinate 8b as catalyst; critical CH-O interaction highlighted in pink	88

Figures appearing in CHAPTER IV: TRANSITION METAL CATALYSIS

Figure 4. 1. Proposed key transition states of the two mechanisms proposed by MacMillan and co-workers	91
Figure 4. 2. Experimentally measured ¹³ C KIEs and reaction	92
Figure 4. 3. DFT optimized TS-S _N 2 and predicted KIEs	93
Figure 4. 4. DFT optimized TS-deprot and predicted KIEs	94
Figure 4. 5. (a) proposed catalytic cycle for MacMillan's amination reaction via copper(III) reductive elimination; (b) mechanism for radical recombination	95
Figure 4. 6. DFT optimized TS-RE and predicted KIEs	96
Figure 4. 7. Predicted and measured KIEs for the title reaction	97
Figure 4. 8. Proposed asymmetric amination reaction	98
Figure 4. 9. DFT calculated transition states leading to the (a) major and (b) minor enantiomer of product; steric interactions highlighted in yellow	99
Figure 4. 10. Suzuki-Myaura reaction and proposed catalytic cycle	101
Figure 4. 11. Two possible pathways to form the pre-transmetalation species using (a) the boronate as the nucleophile or (b) the oxopalladium as the nucleophile	102

Figure 4. 12. Denmark proposed pre-transmetalation intermediates	103
Figure 4. 13. Experimental conditions and determined KIEs	104
Figure 4. 14. Average DFT optimized geometry and predicted KIEs for the transmetalation event occurring from 71a or 71c	105

Figures appearing in CHAPTER V: EXPERIMENTAL AND THEORETICAL
DETAILS

Figure 5. 1 ¹ H NMR of purified and fully deuterated α -D ₂ -3-phenylpropanal.....	110
Figure 5. 2. Stacked NMR spectra showing the monitoring of percent conversion	112
Figure 5. 3. Current reaction profile for Hayashi's Michael reaction	118
Figure 5. 4. Energy profile for the Jørgensen epoxidation	133
Figure 5. 5. Example stacked NMR spectra normalized to the α -protons of starting material	149

LIST OF TABLES

Tables appearing in CHAPTER V: EXPERIMENTAL AND THEORETICAL DETAILS

Table 5. 1. Comparative analysis of relative energies of the two steps in the iminium-ion mechanism for previously published (Santos) and the current study	128
Table 5. 2. Extrapolated Free energy barriers for the three key transition structures presented in Chapter 2.2.1 expressed versus separated starting materials, and versus the carbinol amine intermediate - using ten different high-level DFT single-point energy calculations and the PCM solvent model for water	128
Table 5. 3. Extrapolated Free energy barriers for the three key transition structures presented in Chapter 2.2.1 expressed versus separated starting materials, and versus the carbinol amine intermediate - using ten different high-level DFT single-point energy calculations and the SMD solvent model for water	129
Table 5. 4. Relative energies for conformational search of TS-S _N 2'	132
Table 5. 5. Relative energies and configurations of the conformational search	134
Table 5. 6. Summary of Natural Populations Analysis.....	135
Table 5. 7. Relative energies and configurations of the conformational search	139
Table 5. 8. Relative energies for lowest energy transition states representing all major binding modes investigated.....	147
Table 5. 9. Relative energies comparing C- and O- deprotonation/protonation.....	147
Table 5. 10. Activation energy of transition states in aziridination reaction	148
Table 5. 11. Predicted bond distances.....	158
Table 5. 12. Predicted KIEs for Suzuki-Miyaura reaction.....	159

CHAPTER I: INTRODUCTION

1.1 Catalysis in Organic Chemistry

Organic reactions pervade every facet of life. Whether it's the combustion reaction in the automobile we take to get to work, the chemical synthesis reactions that create the medicine we use when we're sick, or the biological reactions that trigger hormone production when we're hungry, chemical reactions exist in every piece of our existence. Understanding those reactions, however, can sometimes be incredibly complicated.

In order for a reaction to occur, the molecules must have the correct orientation and the requisite energy.¹ In some cases, however, the energy required is not obtainable under standard reaction conditions. For these reactions, chemists have developed catalysts. In high school chemistry, students are taught that “catalysts lower energy barriers.” Most commonly, a figure of the type shown in Figure 1.1a is used to explain this. It takes a certain amount of energy to surmount the barrier and turn starting materials (**SM**) into product (**Prod**). A catalyst lowers this barrier and can augment the transition state (**TS**) making it more readily obtainable (**TS'**). This is a simplistic view of catalysis and fairly illustrative in some cases. Not all catalysts act this way. A deeper understanding of transition state theory and mechanistic details leads to the development of the diagram in Figure 1.1b. In this case, a catalyst still lowers the overall energy barrier, but it now does so through a series of steps. In this case, various transition states are added between starting materials and product (**TS₁'**, **TS₂'**, and **TS₃'**). Between these new transition states are

intermediates (**Int₁** and **Int₂**) which may or may not be observable throughout the course of the reaction. Gaining a better understanding of any individual catalytic reaction can lead to improved methods of synthesis resulting in more economical, greener, and more efficient syntheses.

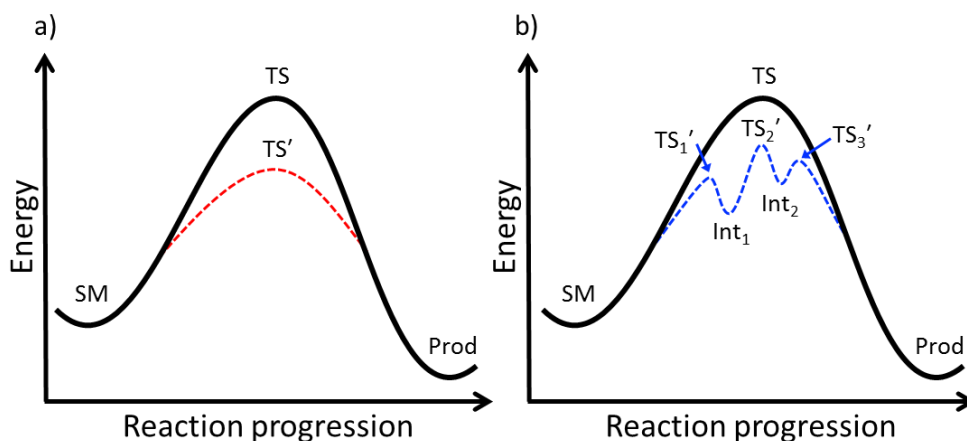


Figure 1. 1. Two conceptions of catalysis

The term “catalysis” comes from the Greek “*kata-*” meaning “down,” and “*lyein*” meaning “loosen.”² The term was first used in 1835 by Jöns Jacob Berzelius in description of the work done two decades previous by Gottlieb Sigismund Constantin Kirchoff in his discovery of the acid catalyzed conversion of starch to glucose.^{3,4} Over the next two hundred years, countless new catalytic systems have been discovered and studied expanding the fields of chemical, pharmaceutical, agrochemical, and material synthesis.^{5–8} It is estimated that 90% of all chemicals produced commercially owe their manufacturing to at least one step that is catalyzed.⁹ A full review of all these methods and all these areas is far beyond the scope of this thesis, but, for a better understanding of the results contained within, it is pertinent to establish a basic knowledge of catalysts used in organic synthesis.

The use of transition metals, as catalysts, can date its history back to the turn of the twentieth century with work by Glaser^{10,11} and Ullmann¹², but the methods didn't see wide utility until becoming popularized in 1959 with the advent of the Wacker Process¹³⁻¹⁵. The field then saw great expansion through the 1960s to the early 2000s with additions from Tsuji and Trost^{16,17}; Heck and Mizoroki¹⁸⁻²⁰; Kumada and Corriu^{21,22}; Sonogashira²³; Negishi^{24,25}; Grubbs, Schrock, and Chauvin²⁶⁻³⁰; Stille, Walton, Kosugi, and Migita³¹⁻³⁵; Suzuki and Miyaura³⁶⁻³⁸; Sharpless^{39,40}; Hiyama and Denmark⁴¹⁻⁴³; and Buchwald and Hartwig^{44,45} to name a few. These advancements were the topics of the 2001, 2005, and 2010 Nobel Prizes in Chemistry. This branch of chemistry has spurred hundreds of reactions and numerous reviews and is, without a doubt, one of the pillars of organic synthesis.⁴⁶⁻⁵⁵

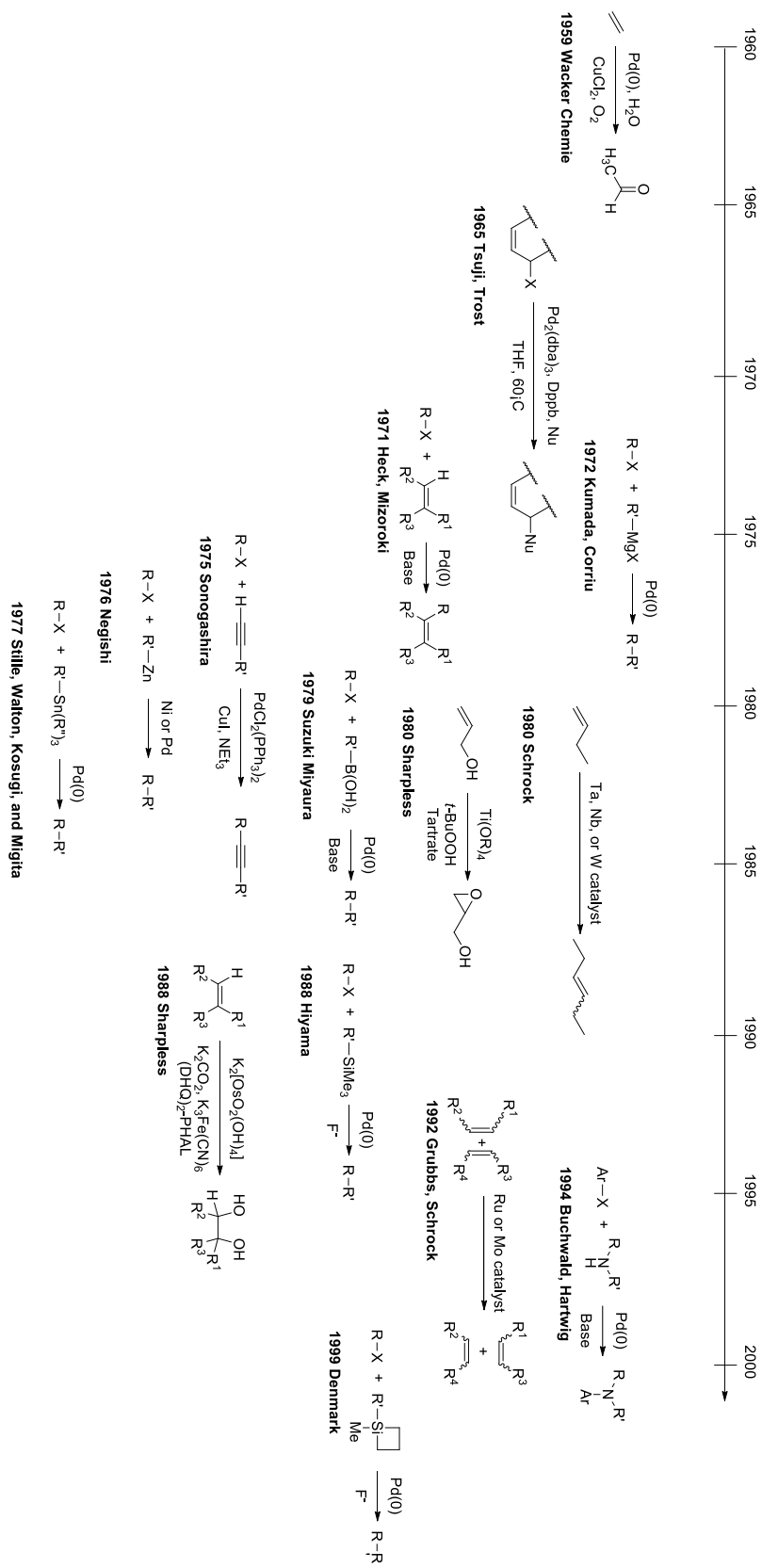


Figure 1. 2. Timeline of notable transition-metal catalyzed reactions from 1959-2000

Even with its broad utility, transition metal catalysis presents a fair number of drawbacks. Most notably, the use of heavy metals and generation of toxic byproducts can lead to environmental destruction. Over the past few decades, transition-metal-free syntheses have increased in appreciation.^{56,57} In the late 1990s and early 2000s, fueled by the desire to break transition-metal-dependence, a renaissance began focusing on the use of small organic molecules as catalysts. This mode of catalysis was coined “organocatalysis.”⁵⁸ One of the most complete chronicles of the advancements made in organocatalysis is the two book series by Professors Benjamin List and Keiji Maruoka called *Asymmetric Organocatalysis* and published by Thieme in their *Science of Synthesis* series.^{59,60} In their account, List and Maruoka separate the field based on one simple principal: organocatalysts donate or accept electrons or protons. Those that donate or accept electrons are Lewis bases or Lewis acids, respectively; those that donate or accept protons are Brønsted acids or Brønsted bases, respectively. These categories can be divided even broader into covalent catalysts and non-covalent catalysts. The former effect their transformations by covalently binding to one of the reactants to activate it for reaction. The systems belonging to the latter classification activate their substrate through the use of hydrogen bonds or electrostatic interactions without ever forming a covalent bond to the reactant. Herein, at least one example of all four members of the classifications put forth by List and Maruoka will be discussed, but they will be more broadly separated by this second classification. Lewis acids and bases will be discussed through the lens of covalent catalysis in CHAPTER II. Brønsted acids and bases will be discussed through the lens of non-covalent catalysis in CHAPTER III.

Primary and secondary amines are the most common catalysts used in covalent organocatalysis. It has been long understood that these compounds have the ability to condense with carbonyl-containing compounds to yield enamines and iminium-ions. Enamines are strong nucleophiles that can readily attack various electrophilic centers to yield new bonds between carbon and other heavy atoms. These reactions have been catalyzed by enzymes since the beginning of life.⁶¹ In the mid-1890s, Knoevenagel applied this idea to organic synthesis in the form of the aldol reaction.⁶² This reaction would go on to inspire works over the next century particularly by Langenbeck, Miescher, and Woodward, but wouldn't gain broad use until much later.⁶³⁻⁶⁵ The first stride toward more common use of this mode of catalysis came in the early-1970s with the birth of the Hajos-Parrish-Eder-Sauer-Wiechert reaction.^{66,67} This proline-catalyzed, intermolecular, aldol reaction paved the way for modern-day organocatalysis. The wider applicability of the reaction wasn't fully realized and deemed particular for the studied system. Later, in the mid- to late-1990s, the groups of Yian Shi, Dan Yang, and Scott Denmark each independently investigated the area of using small organic molecules to perform asymmetric epoxidations.⁶⁸⁻⁷⁰ In the early 2000s, List and co-workers showed that the amino acid L-proline could be used to catalyze a range of reactions through enamine catalysis.⁷¹⁻⁷³ Over the years, proline and proline-derivatives have been shown to productively catalyze Mannich reactions,^{74,75} α -aminoxylation reactions,⁷⁶⁻⁷⁸ α -fluorinations,⁷⁹⁻⁸¹ α - and γ -aminations,^{82,83} α -alkylations,⁸⁴ Michael additions,⁸⁵ aldol reactions,⁷² cascade reactions,⁸⁶⁻⁸⁸ and Mortia-Baylis-Hillman reactions,⁸⁹ to name a few.

At the same time that List's chemistry was leading to the birth of enamine chemistry, David MacMillan's group was developing iminium-ion catalysis.⁵⁸ Again,

proline-derivatives were employed to effect these transformations. This mode of catalysis has also seen significant growth being used to catalyze Diels-Alder reactions^{90,91}, cyclopropanations^{92,93}, Aza-Michael reactions,^{94,95} sulfa-Michael additions,⁹⁶ indole alkylations,⁹⁷ hydride reductions,⁹⁸ amine conjugate additions,⁹⁹ 1,3-dipolar cycloadditions,¹⁰⁰ Michael additions¹⁰¹, monofluorovinylation,¹⁰² Friedel-Crafts Alkylations,¹⁰³ aldol reactions,¹⁰⁴ Nazarov Cyclizations,¹⁰⁵ epoxidations,¹⁰⁶ and the synthesis of pyrimidines,¹⁰⁷ spirooxindoles,¹⁰⁸ and cyclopentenones,¹⁰⁹ along with a plethora of other examples.¹¹⁰

The majority of the secondary amine catalysts used in both enamine and iminium-ion catalysis tend to fall into three general classes: (A) L-proline and its derivatives; (B) Hayashi-Jørgensen type; (C) MacMillan type. The first class gained popularity from List's publications and from the simplicity and availability of the substrate. Yujiro Hayashi and Karl Anker Jørgensen added substantially to these two fields with the independent development of catalysts of Class B.¹¹¹⁻¹¹⁴ The final class saw the most expansion in the MacMillan lab.^{58,80}

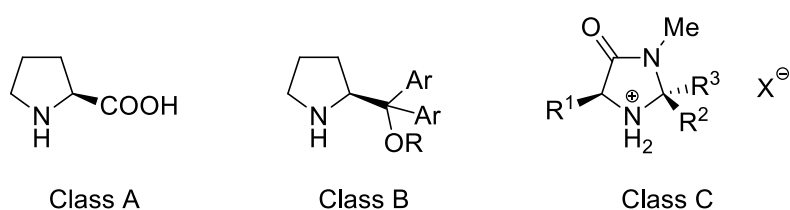


Figure 1. 3. Three basic classes of secondary amine catalysts

As the field of secondary amine catalysis expanded, other subsections of organocatalysis began to develop as well. The groups of Glorius¹¹⁵, Rovis¹¹⁶, Enders^{117,118}, and Bode¹¹⁹⁻¹²¹ worked on the use of *N*-heterocyclic carbenes for umplong

chemistry. Fuchibe¹²² and List^{123,124} developed phosphoric acids as competent catalysts, and Takemoto¹²⁵ and Jacobsen¹²⁶ introduced the power of thiourea catalysts. Representatives of these catalysts are shown in Figure 1.4.

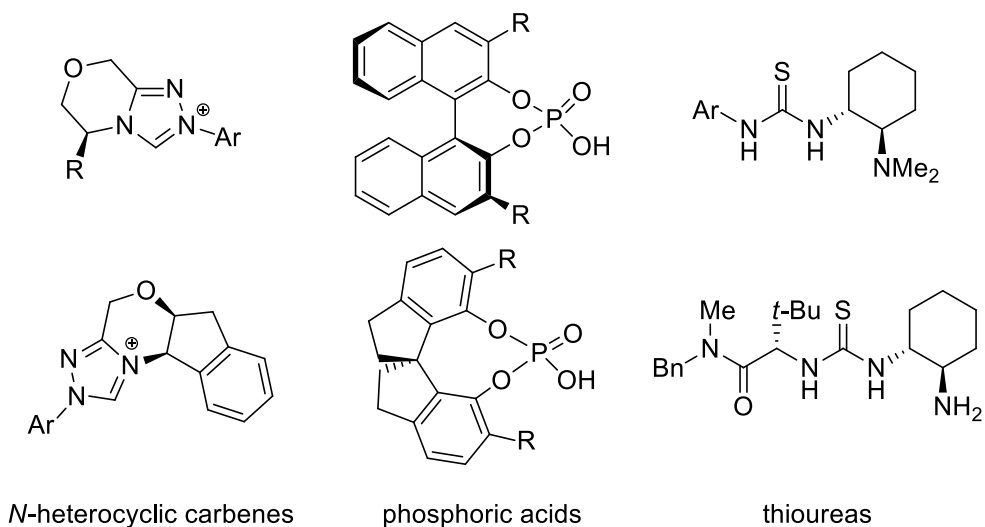


Figure 1. 4. Basic catalysts employed in organocatalysis

The field of organocatalysis saw exponential growth through the first decade of the twenty-first century, and continues to be the focus of hundreds of publications each year. Organocatalysis owes this explosion of use to the various advantages it presents over transition-metal catalysis: (1) Organocatalysts are typically insensitive to moisture and air, making them easier to handle; (2) they are frequently derived from simple, affordable molecules; (3) they do not tend to produce toxic waste. Unfortunately, this mode of catalysis does present drawbacks: (1) catalyst loadings are typically an order of magnitude higher than their transition-metal counterparts; (2) the catalysts can be promiscuous and lead to side-reactions; (3) as of yet, the reaction scope is limited and does not include many of the transformations accessible *via* organometallic methods. For these reasons, a synergistic approach to catalysis is most beneficial. A better understanding of transition-

metal catalysis and organocatalysis can help chemists develop new procedures that overcome the shortcomings of one mode with the other. It is for this reason that we put emphasis on a universal understanding of all branches of catalysis in organic synthesis. This thesis comprises a discussion of nine investigations that delve into various fields of catalysis in organic synthesis with the anticipation that a deeper mechanistic understanding will lead to a more prolific development of reactions and methodologies.

1.2 Overview of Kinetic Isotope Effects

The study of organic reaction mechanisms is pivotal to understanding reactivity and selectivity in reactions. Kinetic isotope effects (KIEs) allow an individual to observe how specific atoms are reacting during the first irreversible step of the reaction. This step is commonly referred to as the rate-determining step (RDS) of a reaction. The substituting of one isotope for another at or near a position which is undergoing a bond change (making, breaking, or rehybridizing) typically leads to a change in rate of the reaction.¹²⁷ The KIE is then the quotient of the rate constant for the reaction with the natural abundance isotope, and the rate constant for the reaction with an altered isotope (Equation 1). In many of the common cases, the natural isotope is lighter than that of the altered isotope (¹H vs ²H or ³H, ¹²C vs ¹³C or ¹⁴C, ¹⁴N vs ¹⁵N, ¹⁶O vs ¹⁷O or ¹⁸O).

$$KIE = \frac{k_{natural}}{k_{altered}}$$

Equation 1. Simplest means of calculating an isotope effect given the rates of a reaction with natural ($k_{natural}$) and heavy ($k_{altered}$) isotope substitutions

Frequently, measuring the KIE requires two experiments to be set up, both essentially identical with the difference of what isotopomer is used. From these two

reactions, two rates can be measured and the KIE can be deduced. Alternatively, the two isotopomers can be added to the same reaction and a competition experiment can be designed if the experimentalist is able to differentiate the reactivity of the two species. If the rate does not differ with substitution, k_{natural} is equal to k_{altered} , and the KIE equals 1. This is considered a “unity isotope effect” and, in most classes, it suggests that the atom being interrogated does not undergo a bond change at the RDS. Qualitatively, it represents that the vibrational energy well of the atom in the ground-state is equal to that in the transition state as shown in Figure 1.6. In Figure 1.6, the lower line in the starting material well (red) represents the energy of the relevant vibrational mode of the heavier isotopomer, the higher line (green) represents the same vibrational mode for the lighter isotopomer. The difference in heights corresponds to the difference in zero-point energy (ZPE) of the bond being analyzed whether the light or the heavy isotopomer is used. This calculation makes use of Equation 2. With the reduced mass (m_r) as the denominator, the energy will decrease as the mass of the atoms involved in the bond increases. Therefore, the heavy isotopomer will have a lower ZPE than the light isotopomer.

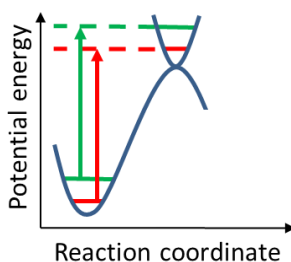


Figure 1. 5. Graphical representation of the difference in energy wells of material in the ground-state versus the transition state

$$ZPE = \frac{h}{4\pi} \sqrt{\frac{k}{m_r}}$$

Equation 2. Equation for determination of the zero-point energy of a bond. h=Planck's constant; k=force constant; m_r=reduced mass

These lines denoting the ZPE in the ground state are mimicked in the transition state which is represented by the orthogonal surface to the reaction coordinate. As can be seen by this figure, the energy the heavier isotopomer (red) has to overcome ($\Delta G^\ddagger_{\text{heavy}}$) is equal to that which the lighter isotopomer (green) has to overcome ($\Delta G^\ddagger_{\text{light}}$). With the knowledge of the activation energy required for these transition states, the Eyring equation (Equation 3) can be used to determine the rates of reactions. Due to the fact that all non-energy terms in the Eyring equation are constants, for a given reaction, at a given temperature, it becomes obvious that the rate of the reaction is proportional to the ΔG^\ddagger of the reaction ($k \propto \Delta G^\ddagger$), and when the ΔG^\ddagger of the reaction is identical for two reactions—as is the case in Figure 1.6—it can be deduced that the rates are the same. If the rates are the same, then Equation 1 tells us that the KIE equals 1.

$$k = \frac{\kappa k_B T}{h} e^{-\frac{\Delta G^\ddagger}{RT}}$$

Equation 3. The Eyring equation. k=reaction rate; κ =transmission coefficient; k_B =Boltzmann's constant; T=temperature; h=Planck's constant; ΔG^\ddagger =energy; R=universal gas constant

Variations from this unity give rise to normal and inverse isotope effects. If the energy well at the transition state is looser than at the ground state, $\Delta G^\ddagger_{\text{light}}$ is smaller than $\Delta G^\ddagger_{\text{heavy}}$ as shown in Figure 1.7a. In this case, using the same proportionality and equation described above, it can be deduced the rate constant for the lighter isotopomer (k_{light}) is

greater than the rate constant for the heavier isotopomer (k_{heavy}) therefore the KIE would be greater than 1 (in cases when the natural isotope is the lighter isotope). This is called a “normal isotope effect” as a heavier isotope slows the reaction. In the alternative case, if the energy well at the transition state is tighter than at the ground state, $\Delta G^{\ddagger}_{\text{light}}$ is larger than the $\Delta G^{\ddagger}_{\text{heavy}}$ as shown in Figure 1.7b. Following the previous logic k_{light} would be less than k_{heavy} and the KIE would be less than 1 (in cases when the natural isotope is the lighter isotope). This is considered an “inverse isotope effect” as the heavier isotope hastens the reaction.

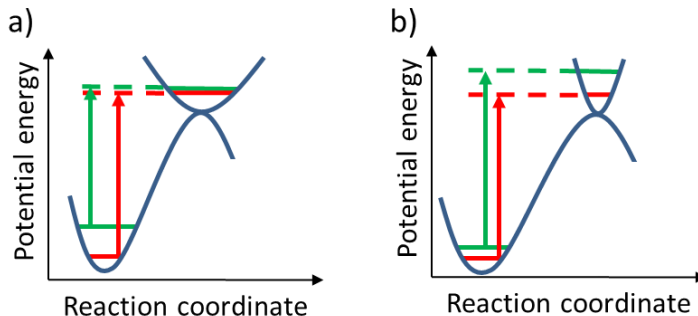


Figure 1. 6. Graphical representation of the difference in energy wells of starting material in the ground-state versus the transition state for (a) a normal isotope effect; (b) inverse isotope effect

The use of deuterium isotope effects (i.e. $k_{\text{hydrogen}} / k_{\text{deuterium}}$) has been used to probe reactions for decades due to the relative simplicity of substituting hydrogen by deuterium and the fact that deuterium is so much larger than hydrogen. This second fact results in an easily measurable, large difference of rates.^{128,129} Although installation of deuterium atoms at many locations on an organic molecule is trivial, the need to label substrates still presents some difficulties: (1) not all locations in a molecule can be easily converted; (2) deuterium-rich substrates are significantly more costly; (3) many times equilibria are established in deuteration experiments which result in the loss of material and the potential loss of the label. In 1986, Robert Pascal devised the first means to measure isotope effects at natural

abundance.¹³⁰ Using ^2H NMR, Pascal and co-workers were able to quantify how frequently a deuterium atom reacted as opposed to a chemically equivalent proton. This was certainly an impressive advancement in KIEs, but it lacked wider applicability. The method could only be used in the case where there was intramolecular competition between chemically equivalent hydrogen atoms, something not guaranteed in all cases. Furthermore, despite the ubiquity of hydrogen atoms in organic chemistry, many reactions do not involve a bond change at a hydrogen atom at the RDS. These points begot a requirement for other atom KIEs.

The major downside to KIEs measured on atoms other than deuterium (heavy-atom KIEs) is that, as the difference in masses of the isotopes decreases, so too does the magnitude of the isotope effect. Deuterium is 100% heavier than hydrogen, therefore the difference in the reduced masses for Equation 2 is much larger making the difference in energies, and, by extrapolation, the rates larger and easier to quantify. In the case of the naturally occurring isotopes of carbon, carbon-13 is only 8.3% heavier than carbon-12. In the case of the naturally occurring isotopes of oxygen, oxygen-16 is only 6.3% heavier than oxygen-17. These smaller differences result in much smaller isotope effects. Nevertheless, the information that could be gleaned from these KIEs is potentially invaluable to understanding a reaction's mechanism. Work throughout the 1980s and 1990s, using labeled substrates in conjunction with spectrometry^{131,132}, gas chromatography¹³³, and scintillation counting¹³⁴⁻¹³⁹, allowed for the determination of $k_{\text{C-12}}/k_{\text{C-13}}$, $k_{\text{C-12}}/k_{\text{C-14}}$, $k_{\text{N-14}}/k_{\text{N-15}}$, and $k_{\text{O-16}}/k_{\text{O-18}}$ isotope effects, but not until 1995 were the ideas of Pascal's measurement at natural abundance combined with heavy-atom isotope effects. The group of Daniel Singleton at Texas A&M University first reported a method of precisely measuring carbon

isotope effects at natural abundance using ^{13}C NMR.¹⁴⁰ “The Singleton method” did not require labeled substrates, and allowed for simultaneous determination of KIEs for every carbon in the molecule. The method would later be expanded to involve $k_{\text{H-1}}/k_{\text{H-2}}$ and $k_{\text{O-16}}/k_{\text{O-17}}$.^{141,142}

The Singleton method (and several of the other mentioned methods) takes advantage of the fact that, as the reaction progresses, the unreacted starting material becomes enriched in the slower reacting isotopomer. If a reaction is taken to a high fractional percent conversion (F%) and the unreacted material is re-isolated, the isotopic composition could be compared to material not subjected to the reaction condition and the change in relative isotopic composition would yield a KIE. In 1995, Singleton and Thomas used the Diels-Alder reaction between isoprene and maleic anhydride to test this method on carbon-13 (Figure 1.8). After the majority of the isoprene had reacted (high fractional percent conversion) the reaction was quenched and the unreacted isoprene was isolated. A sample of isoprene from the same batch, which had not been subjected to the reaction conditions, was then compared to the re-isolated material using ^{13}C NMR. One atom (the methyl group carbon)—an atom that was unmistakably not involved in the reaction—was designated as a “standard” and the relative integrations of all other carbon atoms were compared. This ratio (R/R_0) could then be submitted to equation 3 (along with the fractional percent conversion, F%) to determine the KIE.¹⁴³

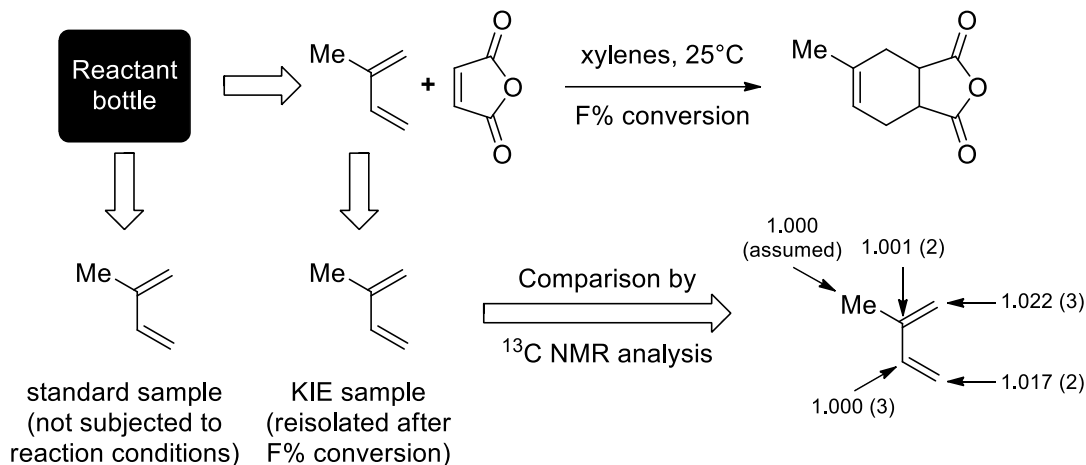


Figure 1. 7. Singleton's original small KIE determination reaction

$$KIE = \frac{\ln(1 - F\%)}{\ln((1 - F\%) \times (R/R_0))}$$

Equation 4. Saunders's equation used to calculate starting material KIEs when given the fractional conversion of lighter isotopomer (F%) and the proportion of minor isotopic component in recovered material to that of starting material (R/R₀)

Since 1995, the Singleton method has been cited almost 300 times to give a deeper understanding of reaction mechanisms.¹⁴⁴⁻¹⁴⁸ This approach is used extensively in almost every project discussed herein. A detailed description of the method of procurement and the raw data for each experiment are included in CHAPTER V: EXPERIMENTAL AND COMPUTATIONAL DETAILS.

1.3 Computational Methods

Computational chemistry has been expanding at an exponential rate with the increase of both computer power and interest in the theoretical prediction of reactivity.¹⁴⁹⁻

¹⁵¹ In many cases, computational models allow researchers to better understand selectivity in reactions¹⁵², predict reactivity¹⁵³, and even develop new methodologies¹⁵⁴. In the

interpretation of KIEs, the presence, absence, or location of a normal or inverse KIE can frequently be enough to draw helpful qualitative information about a reaction. There are times, however, when more quantitative means are necessary to fully understanding the transition state that gives rise to the observed changes in rate. In the case of the Diels-Alder reaction mentioned earlier, computations gave insight on the asynchronicity of the reaction.¹⁵⁵ This account was the first marriage of isotope effects experimentally measured using the Singleton Method and computational predictions. The predicted values were in triple digit agreement with the measured values in almost all cases standing as a testament to this synergy and leading to the pairing of calculations with experimental measurements becoming common place.

Calculations within this thesis consist of high-level density functional theory (DFT) predictions of transition states and ground states. Although computational chemistry brings with it errors in approximations, the utmost care is taken to minimize these errors in our projects. Appropriate functionals and basis sets are chosen for each individual project based on computational cost and benchmarks which suggest the best match for experimental data. Solvent effects and dispersion corrections are taken into consideration to aid in a full description of the reaction conditions. In many cases multiple methods are chosen to describe a single system and trends in the predictions are utilized instead of relying on the accuracy of a single calculation. From these calculations, KIEs are predicted using the method developed by Bigeleisen and Mayer for all proposed mechanistic pathways for a complete understanding of the potential energy surface (PES) of the reaction.^{156,157}

The Bigeleisen-Mayer method assumes that quantum mechanical tunneling is absent. Although tunneling is frequently minimal in the case of heavy atoms, hydrogen

movement has been proven to frequently induce tunneling and require corrections for standard calculations.¹⁵⁸ To minimize errors due to tunneling, the one-dimensional infinite parabola or Wigner tunneling correction is applied to all predicted KIEs in this thesis.^{159,160}

KIEs are incredibly sensitive to geometry.¹²⁷ For this reason, we find it pertinent to model the same transition state several times using different functionals and methods each leading to an individual KIE prediction. Again, trends are observed and the average of these methods is taken as the prediction for the system.

CHAPTER II: SECONDARY AMINE CATALYSIS

2.1 Enamine Catalysis

The idea of secondary amines as catalysts has already been discussed in Section 1.1, but here, we will take a deeper look into this class of reactions. First, the basic steps of the reaction mechanism should be understood. The initial steps of a standard enamine reaction are outlined in Figure 2.1. The secondary amine attacks the carbonyl-carbon of the reactant and creates zwitterionic intermediate I. A proton transfer occurs (TS2) to yield carbinolamine II. A generic acid, either from solution, or from a moiety on the catalyst, then protonates the hydroxyl group of the carbinolamine facilitating the loss of water (TS4) and the formation of the iminium-ion intermediate IV. A generic base, again either from solution or from a moiety on the catalyst deprotonates the α -carbon and yields the enamine intermediate V.

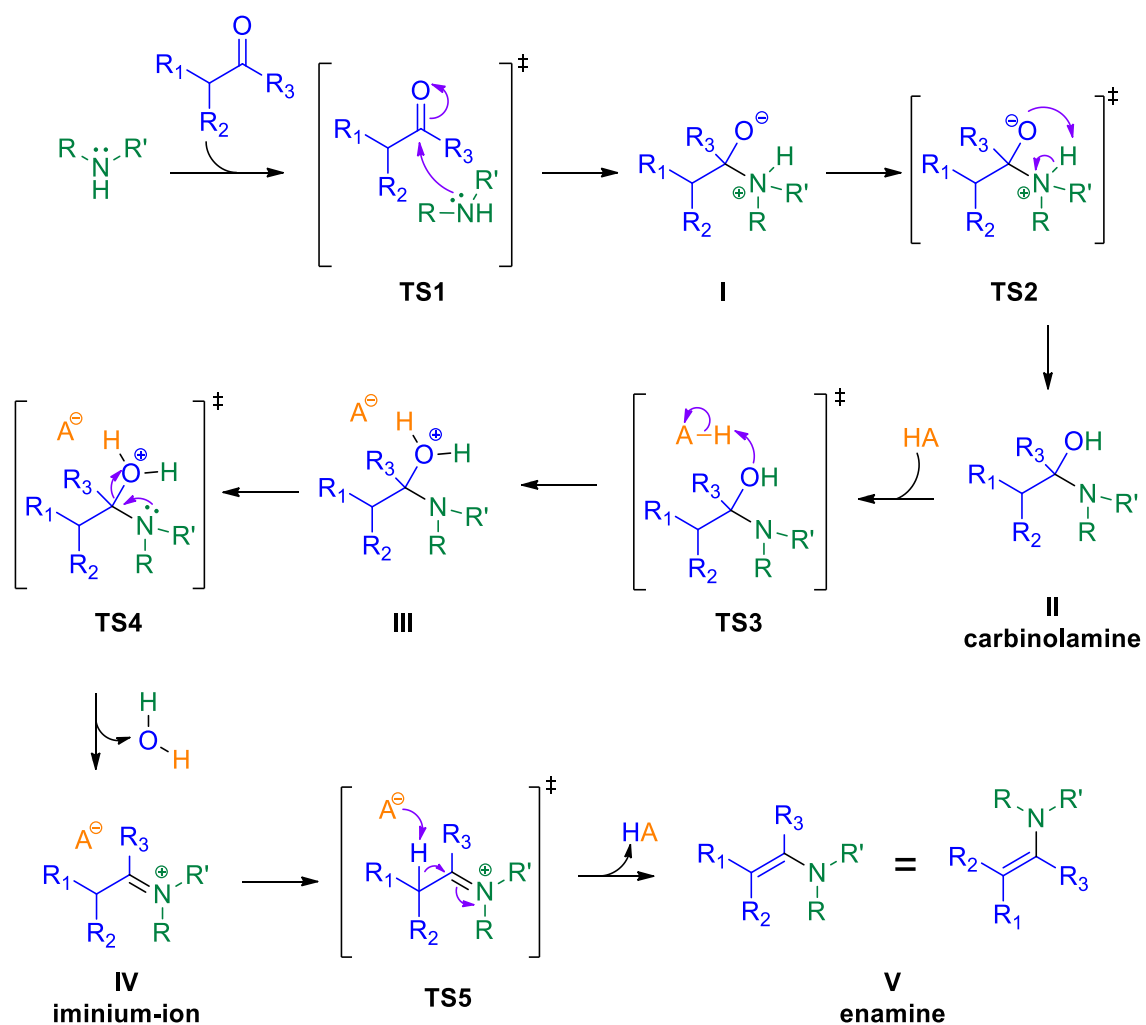


Figure 2. 1. First steps of enamine catalysis

After formation of the enamine, the molecule is now a nucleophile which can add to electrophiles to effect the transformations noted earlier. The generic transition state of this step is shown as TS6 in Figure 2.2. This step results in the formation of the product iminium-ion VI, which undergoes hydrolysis to yield the final α -functionalized product.

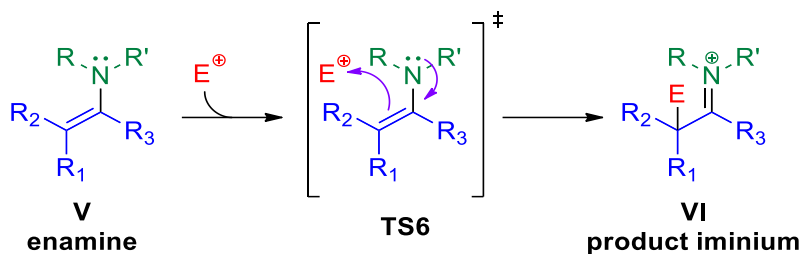


Figure 2. 2. Addition of an electrophile to an enamine

2.1.1 Isotope Effects Reveal the Mechanism of Enamine Formation in L-Proline-Catalyzed α -Amination of Aldehydes

As mentioned earlier, List and co-workers' advancements to the field of organocatalysis came from showing how versatile the natural amino acid L-proline (**3**) could be in catalyzing reactions. The groups of Houk and List developed a general model for these reactions shown in Figure 2.3.¹⁶¹ This model follows the steps represented in the above section, but several key elements are specific due to the use of proline as the catalyst. The carboxylic acid group on proline serves four major functions that allow it to facilitate the reaction and give stereochemical control. First, the group causes species **8**, the *anti*-enamine, to be preferred over the alternative *syn*-enamine. This is due to the steric interaction between the carboxy-group and the hydrogen atoms on the α -carbon making the *syn*-enamine higher in energy. Second, the carboxylic acid moiety acts as a directing group for the incoming electrophile controlling the facial selectivity. Third, as the electrophile adds, the carboxylic acid group protonates the species leading to a more stable intermediate (TS10). The combination of disfavoring the *syn*-enamine and directing the electrophile to add to the same face as the carboxylic acid was the basis to explain the enantioselectivity of the reaction as illustrated in Figure 2.4.

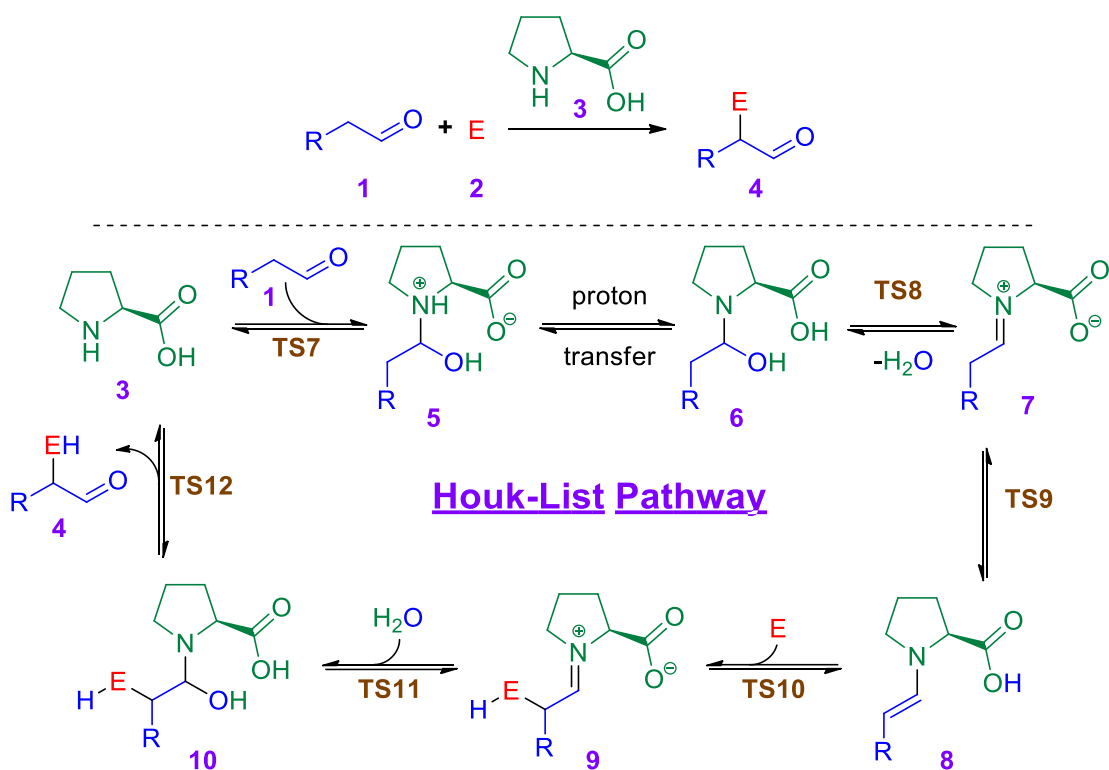


Figure 2. 3. The Houk-List model of L-proline catalysis

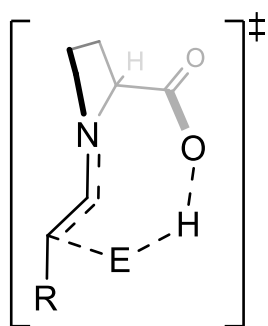


Figure 2. 4. Enantiodetermining step in the H-L model of proline catalysis (TS10)

In 2007, the groups of Seebach and Eschenmoser identified two oxazolidinone species, **11** and **13**, via ^1H NMR spectroscopy and proposed an alternative model of catalysis (Figure 2.5).¹⁶² This cycle is markedly different in that intermediate **8** is *not* the key intermediate. Instead, in the Seebach-Eschenmoser pathway (S-E pathway), the key intermediate is *syn*-enamine carboxylate **12**. The groups proposed that an E2 elimination

of **11** yielded **12** (TS14_{Seebach}) and the intramolecular lactonization occurred concomitantly with electrophile-addition in the enantiodetermining step (TS15).

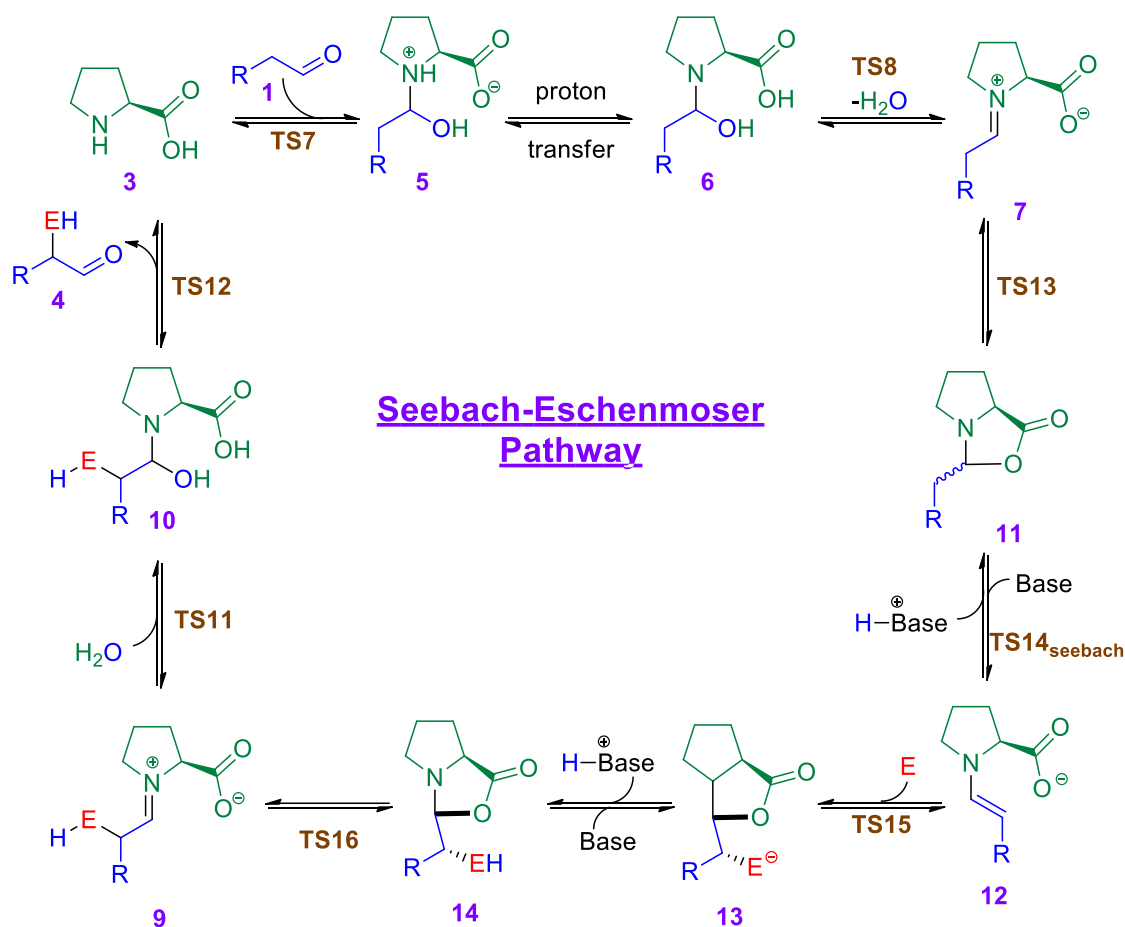


Figure 2. 5. Seebach-Eschenmoser model of L-proline catalysis

In 2010, Gschwind and co-workers proposed a third mechanism combining elements from both previous reports.¹⁶³ In the Gschwind Pathway, oxazolidinone intermediate **11**, proposed in the S-E pathway, leads to formation of *anti*-enamine intermediate **8**, proposed in the H-L pathway. In 2015, Gschwind and co-workers recanted their assessment and instead agreed with the H-L pathway as it was suggested.¹⁶⁴

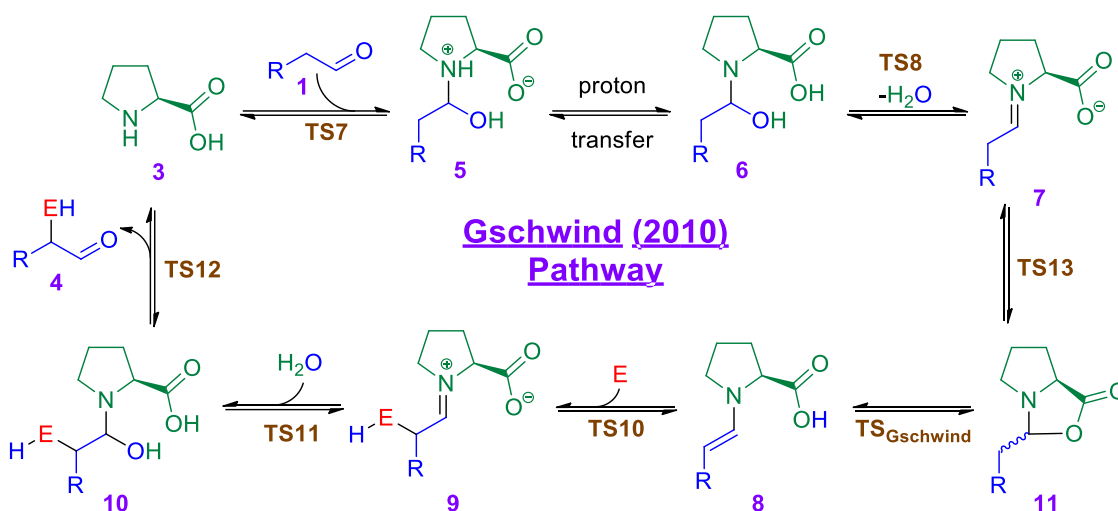


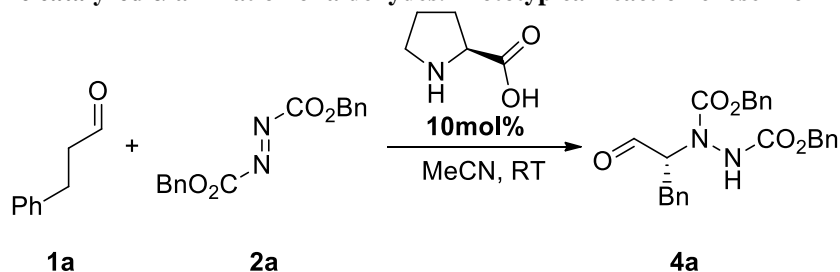
Figure 2. 6. Gschwind's 2010 model of L-proline catalysis

These three proposed mechanisms differ in four distinct ways: (1) The key intermediate; (2) The mechanism of enamine formation; (3) The role of oxazolidinone intermediate **11**; and (4) The nature of the enantiodetermining step. These differences are summarized in Figure 2.7. The points of greatest interest to us were (2) The mechanism of enamine formation, and (3) the role of oxazolidinone intermediate **11**. Prior work in the Veticatt Group decided to undertake a combined experimental and theoretical ^2H and ^{13}C KIE study to probe this reaction and obtain the first vivid insight into the transition-state geometry for enamine formation.¹⁴⁴ For this study, the α -amination of 3-phenylpropanal (**1a**) by dibenzylazodicarboxylate (**2a**) was chosen as an archetypical reaction.¹⁶⁵ This reaction had been studied experimentally^{166–168} and computationally¹⁶⁹, in the past. Studies by Blackmond and co-workers suggested that enamine formation, for this particular reaction, was the rate-determining step.¹⁶⁸ Thus it stood to be the perfect reaction to study using kinetic isotope effects (KIEs).

	<u>Houk-List Pathway</u>	<u>Seebach- Eschenmoser Pathway</u>	<u>Gschwind 2010 Pathway</u>
Key enamine intermediate	8	12	8
Mechanism of enamine formation	TS9	TS14 _{Seebach}	TS _{Gschwind}
Role of oxazolidinone	Parasitic	Non-Parasitic	Non-Parasitic
Enantio- determining TS	TS10	TS15	TS10

Figure 2. 7. Distinguishing features of the three proposed mechanisms for L-proline catalysis

Scheme 2. 1. Proline catalyzed α -amination of aldehydes. Prototypical reaction chosen for KIE study



Carbon-13 KIEs were measured using the earlier discussed methodology pioneered by Singleton and co-workers for **1a**. The ^2H KIEs were also measured for the α -hydrogens of **1a**. All KIEs are shown in Figure 2.8. Qualitatively, the large, normal, isotope effect on C1 and the α -hydrogens were determined to suggest that both of these atoms are involved in the rate-determining step of the reaction. This is consistent with an E2-type elimination.

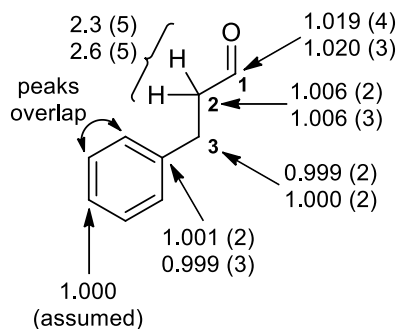


Figure 2. 8. Experimental KIEs measured for the L-proline-catalyzed reaction of 1a with 2a. The two sets of ^{13}C KIEs and two sets of ^2H KIEs represent independent experiments. The number in parentheses shows the uncertainty in the last digit.

Calculations were performed by other members of the Veticatt group which ruled out all steps not involving enamine formation as well as **TS9**. The conversion of oxazolidinone **11** to either *syn*-enamine carboxylate **12** or *anti*-enamine **8** (**TS14-Seebach** or **TS-Gschwind**, respectively), however, could qualitatively account for the observed C1 and α -H KIEs. The involvement of deprotonation of the α -hydrogen, with concomitant C–O bond breakage, would give rise to normal isotope effects being observed at each location. This concerted mechanism is represented by the diagonal of the More O’Ferrall-Jencks plot in Figure 2.9.

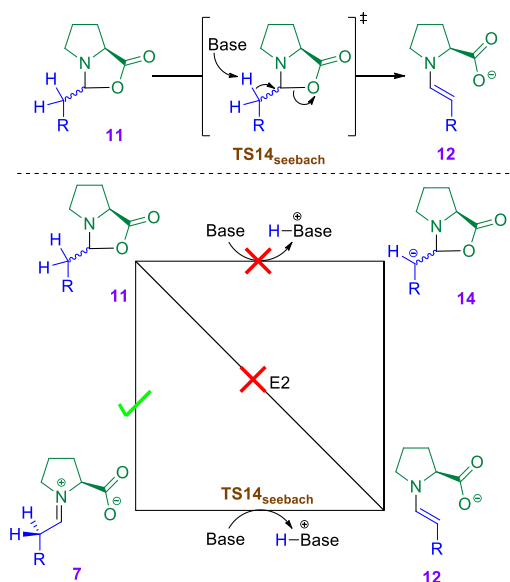


Figure 2. 9. More O'Ferrall-Jencks plot for the possible pathways for conversion of 11 to 12

Attempts to find such a transition state all ended in failure. In its stead, transition states wherein the C–O bond had already been completely broken were located. This represents the second step in an E1-type reaction starting from iminium carboxylate **7** (bottom horizontal of the More O'Ferrall-Jencks plot). In order to temper the acidity of the α -hydrogen atoms, in an attempt to find a transition state more in following with the proposed concerted pathway, a novel mechanism was proposed wherein a bifunctional acid-base protonates the pyrrolidine nitrogen of the catalyst with concomitant deprotonation of the α -hydrogen. This transition state is shown in Figure 2.10. This new transition state **TS14'** results in an *N*-protonated *syn*- or *anti*-enamine carboxylate **12•H⁺**. This intermediate can then re-enter the H-L pathway through intramolecular proton transfer to yield enamine carboxylic acid **8**.

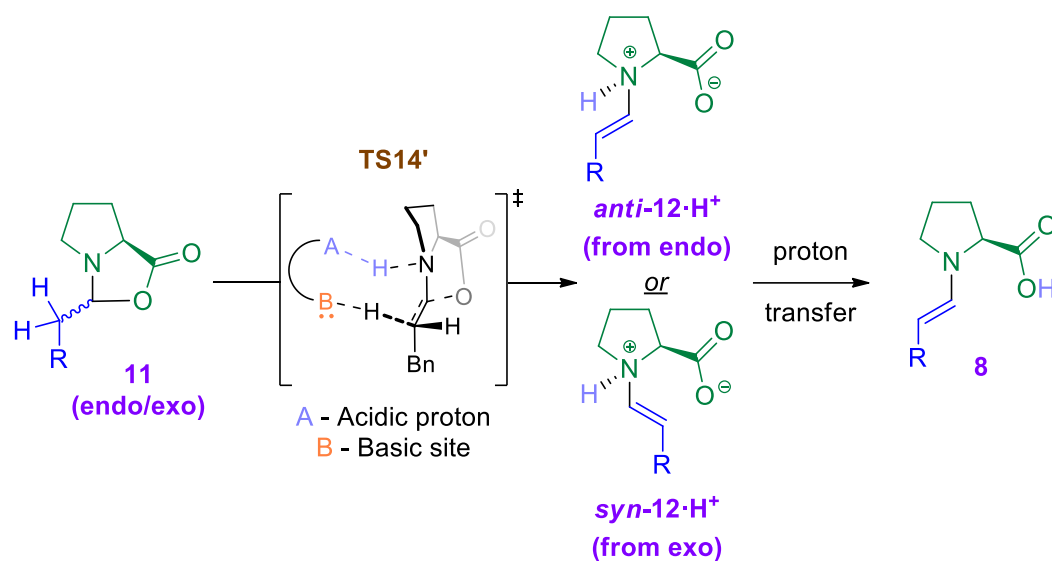


Figure 2. 10. Newly proposed TS14'

Many bifunctional bases were tested, but the best fit for experiment was the prediction given when a product-proline complex effected the transformation of *exo*-**11** to *syn*-**12·H⁺**. This transition state and predicted KIEs are shown in Figure 2.11. Considering the lack of agreement in all other proposed transition states, it was decided that the predicted values for this transition state, **TS14'a**, were closest to all the conclusions made from the experimental measurements (*i.e.* the large normal KIEs on C1 and the α -hydrogens, and the small normal KIE on C2).

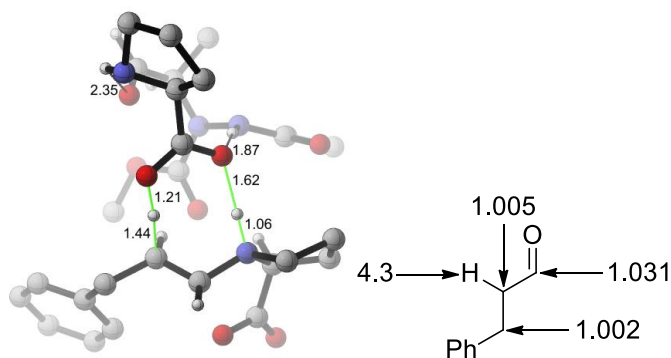


Figure 2. 11. Calculated geometry and predicted KIEs of TS14'a

This proposal is consistent with two key points made regarding the autocatalysis of the reaction. First, it follows Seebach's proposal that the origin of autocatalysis is related to base catalysis.¹⁶² The use of the bifunctional base is needed to effect the concerted E2 elimination proposed as **TS14'a**. Second, this proposal supports Blackmond's observation that reaction benefits from "a catalytic cycle involving only soluble proline complexes or soluble proline adducts".¹⁶⁶ The complex formed between the product and the proline solubilizes the proline in the acetonitrile reaction solvent.

The conclusions made by this prior work most closely fits with the catalytic cycle presented by Gschwind and co-workers in 2010 (Figure 2.6).¹⁶³ As mentioned earlier, however, work in 2015 led Gschwind and co-workers to recant their findings and side instead with the proposal put forth by the H-L pathway (Figure 2.4).¹⁶⁴ This new finding gave cause to pause. Invoking the Houk-List Pathway, one could suggest that **TS8** and **TS9** are co-rate-determining. If this was true, the observed KIEs would be reflective of both steps and could explain both the results garnered by the Gschwind group and the Veticatt group.

In order to test this hypothesis, it was rationalized that one could artificially make one step higher in energy than the other. This shift would then affect the KIEs measured. We therefore measured the carbon-13 KIEs for the reaction using α -D₂-**1a** as the aldehyde. If **TS9**, deprotonation of the α -carbon of iminium **7**, was co-rate-determining, replacing the protons by deuterium would increase the barrier of the step causing it to become "more rate-determining." The measured KIEs would then better reflect the predictions for **TS9**.

To probe this idea, α -D₂-1a was synthesized and the KIE for C1 was determined using the Singleton Method.¹⁴⁰ Two separate reactions were taken to 71.6 ± 2% and 71.0 ± 2% conversion in the aldehyde substrate. The reaction was monitored via ²H NMR using DMSO-*d*₆ as an internal standard. The stacked spectra obtained from this method are shown in Figure 2.12.

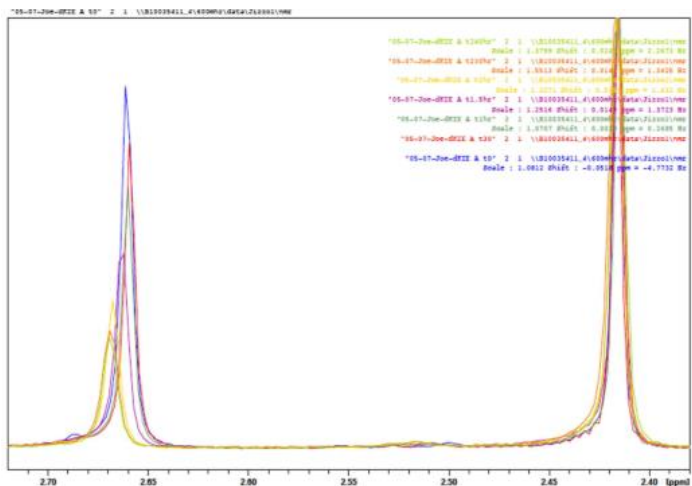


Figure 2. 12. Stacked NMR spectra showing percent conversion monitoring of α -D₂-1a using DMSO-*d*₆ as an internal standard

Upon re-isolation of the unreacted starting material, the KIEs for C1 were measured. The other carbon atoms were not measured as the α -carbon was split due to deuterium coupling and all other values were expected to be unity. The measured KIEs, along with the KIEs measured using α -H₂-1a, and the predicted values for TS3 are shown in Figure 2.13.



Figure 2. 13. KIEs for (blue Arial) measured with α -D₂-1a, (red bold) measured with α -H₂-1a, (green italic) predicted for TS3

If **TS8** and **TS9** were co-rate-determining, the use of α - D_2 -**1a** should cause the measured KIEs to resemble the value predicted for **TS9** more closely than the KIEs measured with α - H_2 -**1a**. This is not the case. The newly measured values are in agreement with the KIEs measured using non-labeled substrate therefore disqualifying the idea of co-rate-determining steps. The discrepancy between our study and that of Gschwind and co-workers from 2015 is likely attributed to the electrophile employed in the reaction. Gschwind and co-workers' study examines the self-aldol reaction of 3-methylbutanal. 3-methylbutanal has numerous differences from the electrophile used herein, **2a**, and could likely lead to a difference in rate-determining steps.

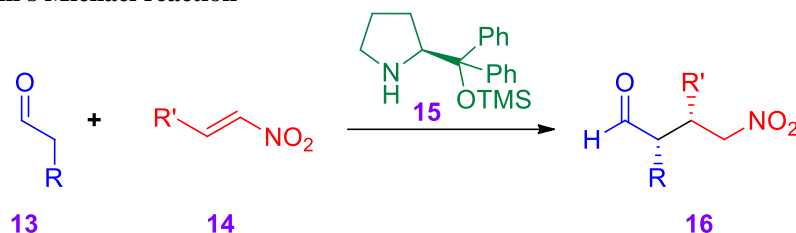
CONCLUSION The combined experimental and theoretical KIE study reported here provides a detailed picture of the transition state of the rate-determining step for the proline-catalyzed α -amination of aldehydes. A mechanism involving a novel E2 elimination directly converting oxazolidinone intermediate **11** to the *N*-protonated enamine **12•H⁺** is proposed. This provides the first experimental evidence that intermediate **11** is not parasitic, but actually a key reacting partner in the mechanism of enamine formation in proline catalysis.

2.1.2 Isotope Effects Reveal Discrepancies in Current Mechanistic Understanding of Diphenylprolinol Silyl Ether-Catalyzed Michael Reaction of Aldehydes and Nitroolefins

INTRODUCTION The Michael addition of aldehydes **13** to nitroolefins **14** is a powerful reaction that creates two, adjacent, stereogenic centers. In 2005, Hayashi and co-workers showed that this reaction could be catalyzed by diphenylprolinol silyl ether **15** to

obtain the desired product in 99% ee, 9:1 dr, and >70% yield in most cases.¹¹² It was discovered, later on, that the addition of catalytic amounts of acid (usually *p*-nitrophenol or acetic acid) increases the rate of the reaction without decreasing yield or selectivity.¹⁷⁰

Scheme 2. 2. Hayashi's Michael reaction



In the little more than a decade since this reaction was first introduced, it has accrued almost 800 citations. The reaction has also generated a fair amount of controversy with regards to its mechanism. Very few groups, however, have actually examined the role of the acid additive in accelerating the reaction.¹⁷¹

Three mechanisms are proposed for this reaction. The first was proposed by Seebach and co-workers between 2011-2013.^{170,172,173} This catalytic cycle (herein, “the Seebach Cycle”) involves condensation of the starting aldehyde with the catalyst to form the enamine **17** by the same means described in the introduction of this chapter. Then nucleophilic attack of the enamine establishes the carbon-carbon bond and yields the iminium-nitronate intermediate **18**. From this intermediate, the group suggested that two, off-cycle, species could form. Either 5,6-dihydro-1,2-oxazine *N*-oxide species **19** or cyclobutane species **20**. Both of these species have been isolated and fully characterized in the aforementioned studies. Seebach and co-workers suggest that these are parasitic species and deter from the catalytic cycle wherein **18** becomes protonated at the nitronate carbon to form the product-iminium **21** which is finally hydrolyzed to yield product and promote

catalyst turnover. The group supports their claim by (1) the Huisgen test for (2+2) cycloadditions *via* zwitterionic intermediates; and (2) “catching” the zwitterion with a nitroolefin bearing a nucleophilic substituent.^{173–175}

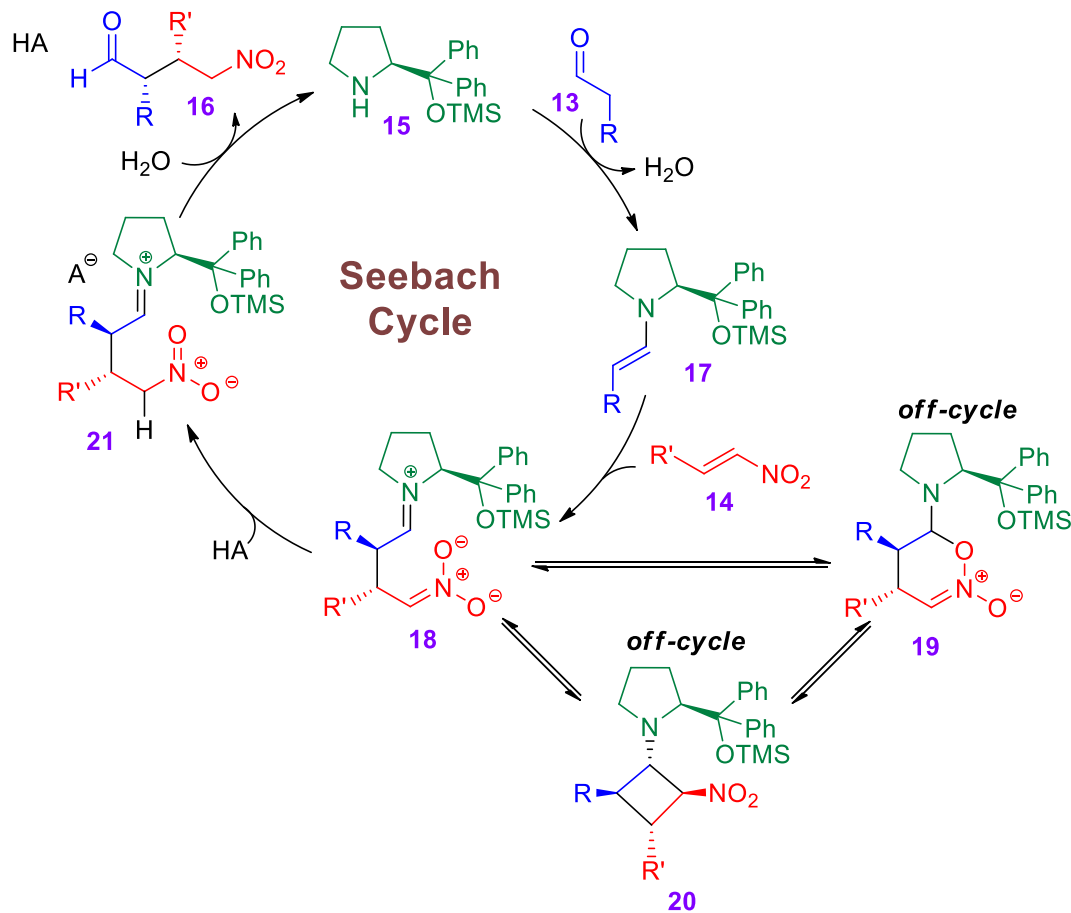


Figure 2. 14. Seebach and co-workers' proposed catalytic cycle

The second mechanism comes from Blackmond and co-workers who have performed numerous kinetic studies on this system and isolated several cyclobutanes and oxazines.^{176–179} The catalytic cycle the group proposes is in contrast with Seebach's conclusion about the off-cycle species. After iminium-nitronate **18** forms, Blackmond and co-workers believe that ring-closure leads to the cyclobutane and consider it not a parasitic intermediate, but a crucial “catalyst resting state” in the mechanism. The authors then

propose that the ring can open to either the oxazine **19**, or, after deprotonation, enamino-nitronate **22**. These “fleeting species” then lead to the formation of **23**, a product-enamine. The product-enamine is then protonated, and the catalytic cycle returns to Seebach’s proposal with hydrolysis of product-iminium **21**. The support for the cyclobutane being on-cycle comes from the observation that α,α -disubstituted aldehydes are almost completely inactive. This is rationalized by suggesting that the loss of the α -proton is crucial in the reaction, and, in March of 2012, the group presented EXSY NMR spectra which led them to the conclusion that there existed an equilibrium between cyclobutane **20a** and enamino-nitronate **22a** (Figure 2.16a).¹⁷⁷ These peaks were not observed in the case of α,α -disubstituted aldehydes thus leading the group to conclude that the cyclobutane must be on-cycle, and the next step must involve loss of the α -proton of the aldehyde. Furthermore, an α -deuterium KIE of 3.25 was measured using non-competitive kinetics with α -D₂-propanal and acetic acid-d₄ (Figure 2.16b). The simple qualitative interpretation of this result was that the α -proton is involved in the rate-determining step.

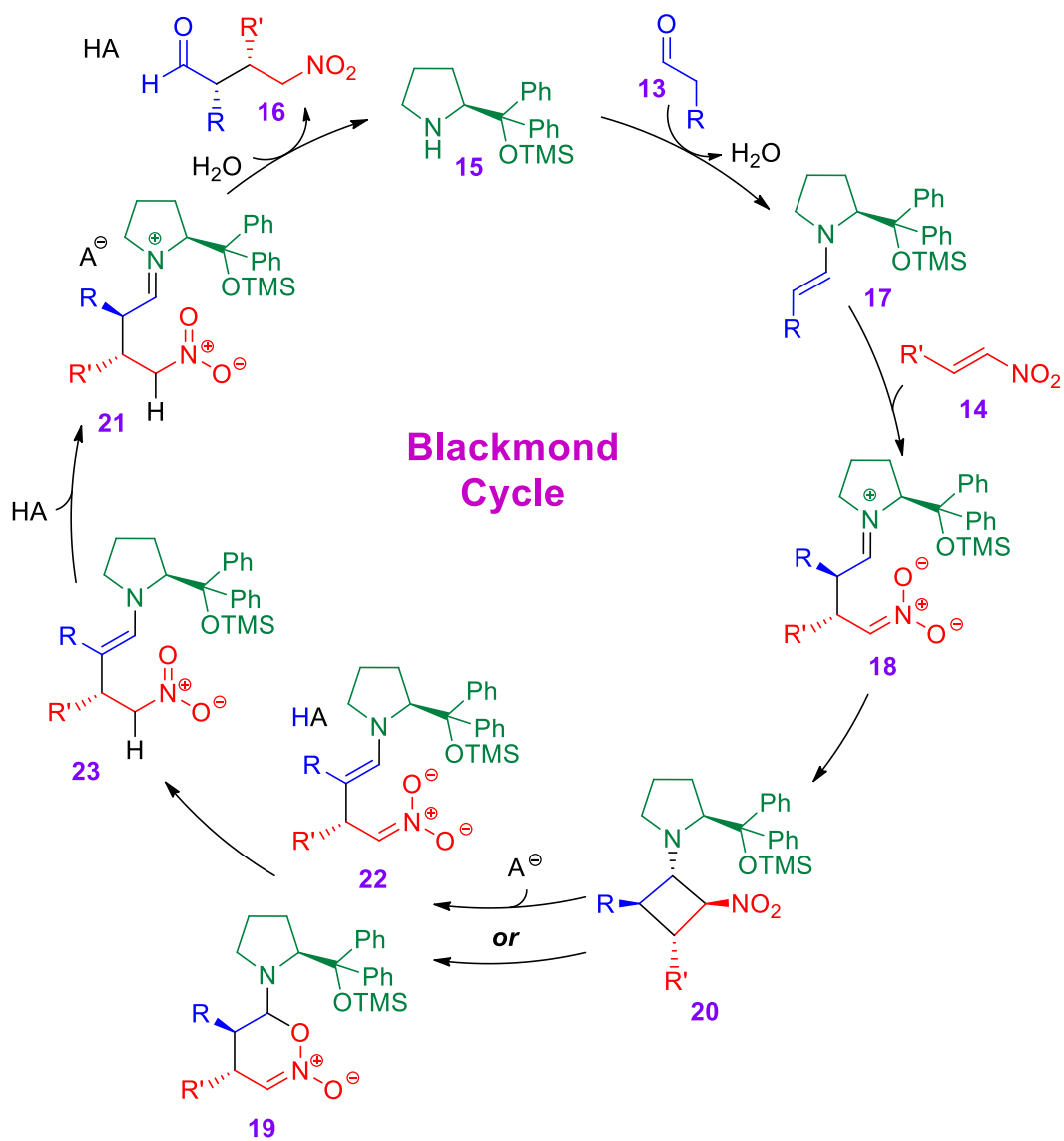


Figure 2. 15. Blackmond and co-workers' proposed catalytic cycle

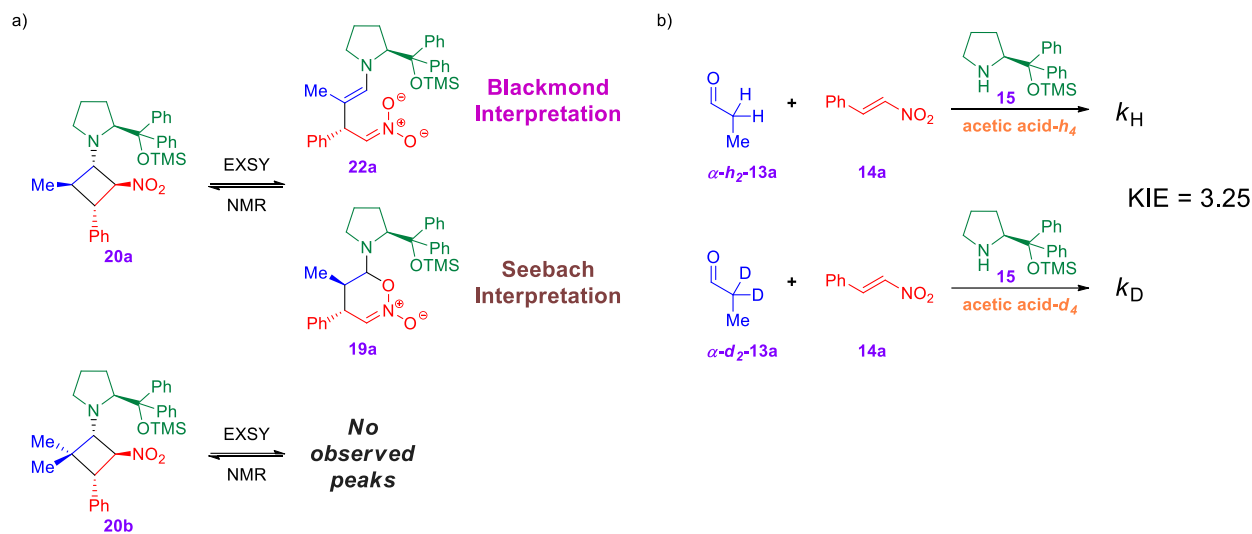


Figure 2. 16. Studies conducted by Blackmond and co-workers; (a) EXSY NMR interpretations for mono- and di-substituted aldehyde; (b) deuterium KIE measurement

In May of 2012, Seebach and co-workers performed the same EXSY NMR experiment as Blackmond and co-workers, obtained the same data, but drew the final conclusion that the species in equilibrium with cyclobutane **20a** was oxazine **19a**.¹⁷² The group also contested Blackmond's conclusion based on an intuitive assumption that enamino-nitronate **22a** would not be stable. In August of the same year, Blackmond and co-workers issued a correction to their earlier conclusions based on Seebach's assessment and asserted that their data *did* imply a cyclobutane/oxazine equilibrium.¹⁷⁸ In February 2013, Seebach and co-workers retracted their earlier contention and, through truncated ground-state calculations, concluded that enamino-nitronate **22a** was sufficiently stable to be a proposed intermediate.¹⁷³ Nevertheless, the group's assessment of the EXSY NMR results remained in favor of the cyclobutane/oxazine equilibrium. Finally, in 2016, Blackmond and co-workers again published, reasserting their conclusion that cyclobutane

20 was a “resting state” of the catalyst, and admitting that they were unsure of the exact path by which it was converted to product-enamine **23**.

In November 2012, a third mechanism was proposed by the groups of Imre Pápai and Petri Pihko (herein, “the Pihko cycle”).¹⁸⁰ The authors refute Seebach’s assessment that the iminium-nitronate is ever formed on the basis of computational analysis which determines that the species is prohibitively high in energy. This is in contrast to two other computational studies performed in 2008 and 2009.^{181,182} Pihko and co-workers suggest that the enamine undergoes a (2+4) cycloaddition with the nitroolefin to yield oxazine **19** directly and on-cycle. The group then suggests that this species can undergo ring-contraction to form the cyclobutane as an off-cycle, parasitic intermediate, supporting Seebach’s conclusion, but refuting Blackmond’s. The cycle continues, as the “Seebach Cycle” did, with protonation at the nitronate-carbon, but with the added concomitant C–O bond cleavage to yield product-iminium **21**. Spectroscopic studies led the authors to observe an equilibrium between product-iminium **21** and product-enamine **23** in support of Blackmond’s findings. The group made an additional finding that α -alkyl nitroolefins were also capable of undergoing the reaction, and did *not* create their cyclobutane counterparts (Figure 2.18). This observation is used to support the conclusion that the cyclobutane is not required for reactivity and therefore an “off-cycle” intermediate. In 2017, the group performed a much more in-depth computational study continuing to support that iminium-nitronate **18** is created only during the asynchronous concerted formation of oxazine **19**, since ring closure “lags behind” carbon-carbon bond formation as observed through internal reaction coordinate calculations (IRCs).¹⁸³

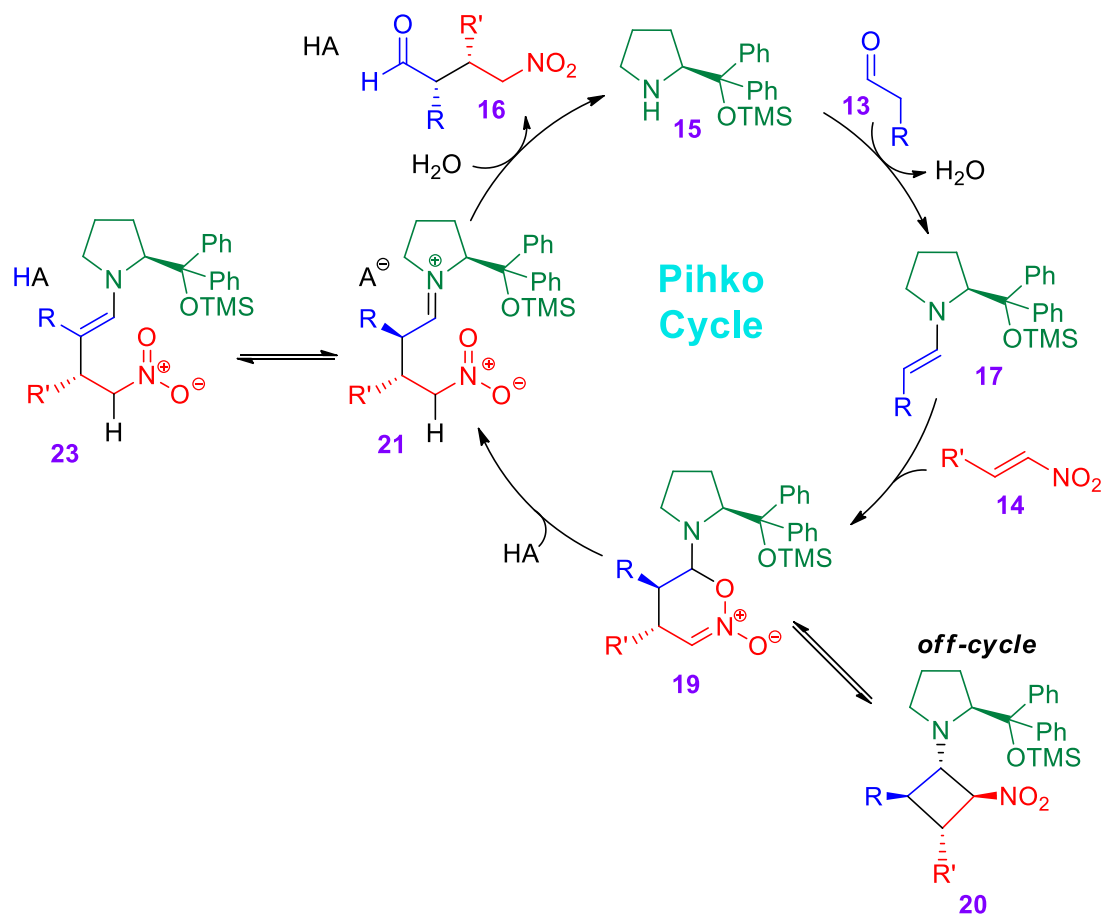


Figure 2.17. Pihko and co-workers' proposed catalytic cycle

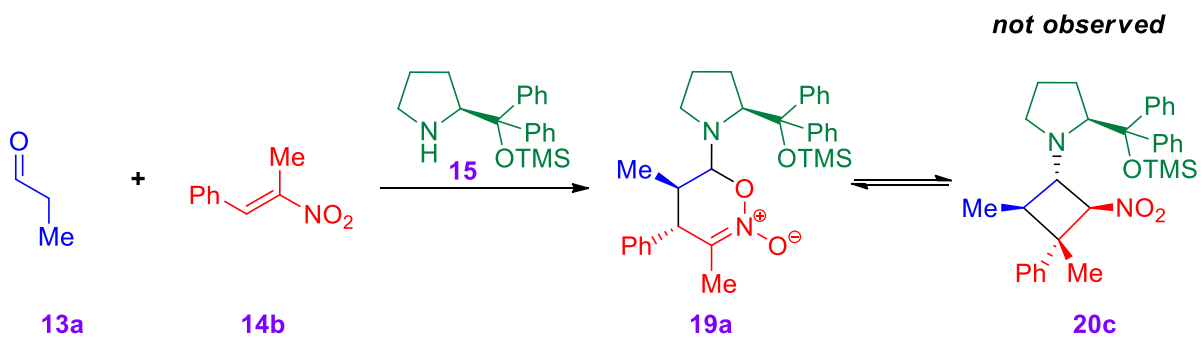


Figure 2.18. Observed phenomenon by Pihko and co-workers

The steadfast points on which all three mechanisms agree are: (1) The reaction takes place *via* an enamine pathway; (2) cyclobutane and oxazine species are formed in many

cases; (3) formation of the carbon-carbon bond is reversible. This final point was made abundantly evident by both Seebach and co-workers as well as Blackmond and co-workers, and the energies calculated by Pihko and co-workers agrees with the rate-determining step happening after carbon-carbon bond formation. In an attempt to understand the mechanism and rate-determining step of this reaction, we undertook a comprehensive mechanistic study using our synergistic experimental and computational KIE approach.

RESULTS AND DISCUSSION Study of this reaction began with prior work done in the Veticatt group utilizing the reaction in Figure 2.19. 3-phenylpropanal (**13b**) was used as the aldehyde with the intent of being able to reisolate both reacting partners for KIE analysis. The reaction was run both with and without *p*-nitrophenol as a co-catalyst additive. Reisolation of the aldehyde proved difficult, but two sets of measurements were performed on the nitrostyrene (**14a**) for both conditions as shown in Figure 2.19. The observed 1-1.5% KIE on the β -carbon of the nitrostyrene agrees, qualitatively, with rate-determining protonation.

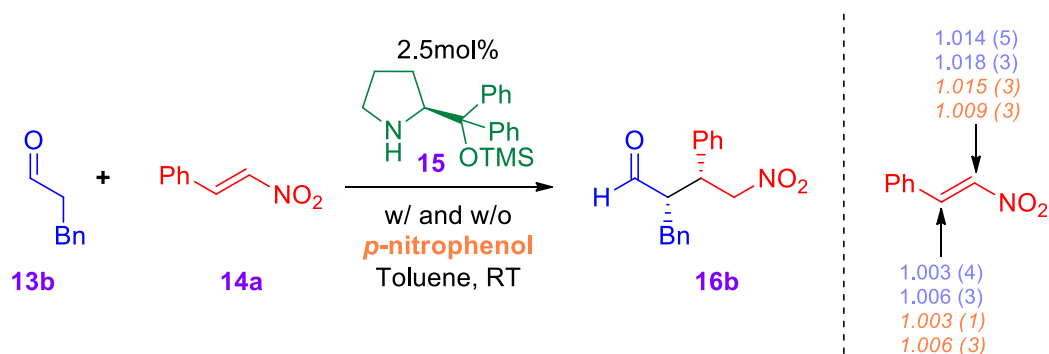


Figure 2. 19. Conditions used to first study of the title reaction and KIEs; Lavender Arial numbers were measured in the absence of acid co-catalyst, peach *Italic* numbers were measured in the presence of *p*-nitrophenol as a co-catalyst

The decision was then made to measure the isotope effects in the presence of acetic acid as a co-catalyst. Due to the issues of purification it was decided that propanal (**13a**)

would be used. KIE measurement using the system shown in Figure 2.20, revealed a discovery contradictory to the early conclusion. The 3% KIE observed on the α -carbon of the nitrostyrene suggested C–C bond formation to be the rate-determining step of the reaction. This measurement was repeated four times to ensure accuracy, and each time the same qualitative conclusion was drawn: the rate-determining step (RDS) has changed. To ensure that these measurements were accurate, two of the four experiments were performed by another graduate student.

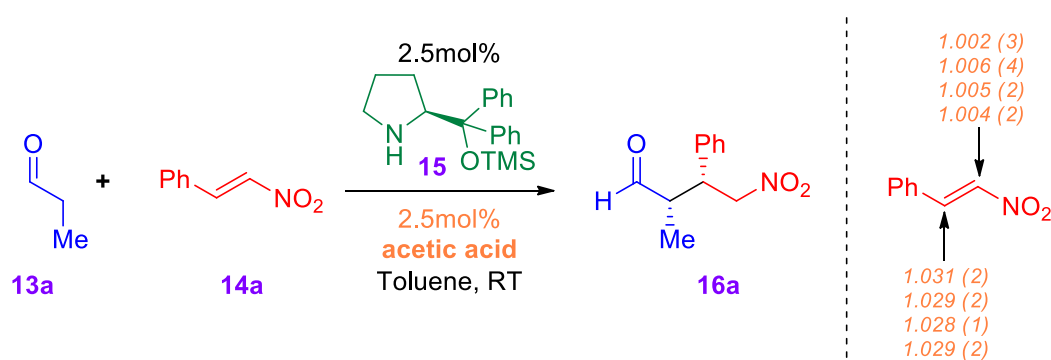


Figure 2. 20. Conditions used in the second study of the title reaction and KIEs

In order to assess whether the change in RDS was brought on by the change in aldehyde (propanal **13a** instead of 3-phenylpropanal **13b**) or co-catalyst (acetic acid instead of *p*-nitrophenol), the KIEs were measured for the reaction of **13b** and acetic acid and **13a** with no acid. The results from this line of inquiry continued to contradict earlier conclusions. The 2% KIE on the β -carbon when **13b** and acetic acid are used (Figure 2.21a) again suggest protonation is the RDS and reveals that changing the aldehyde changes the nature of the RDS (Figure 2.21a compared to Figure 2.20). The reaction with **13a** and no co-catalyst (Figure 2.21b) resulted in a normal KIE on the α -carbon, retaining the earlier conclusion that C–C bond formation is the RDS, but the magnitude is now considerably lower (Figure 2.21b compared to Figure 2.20).

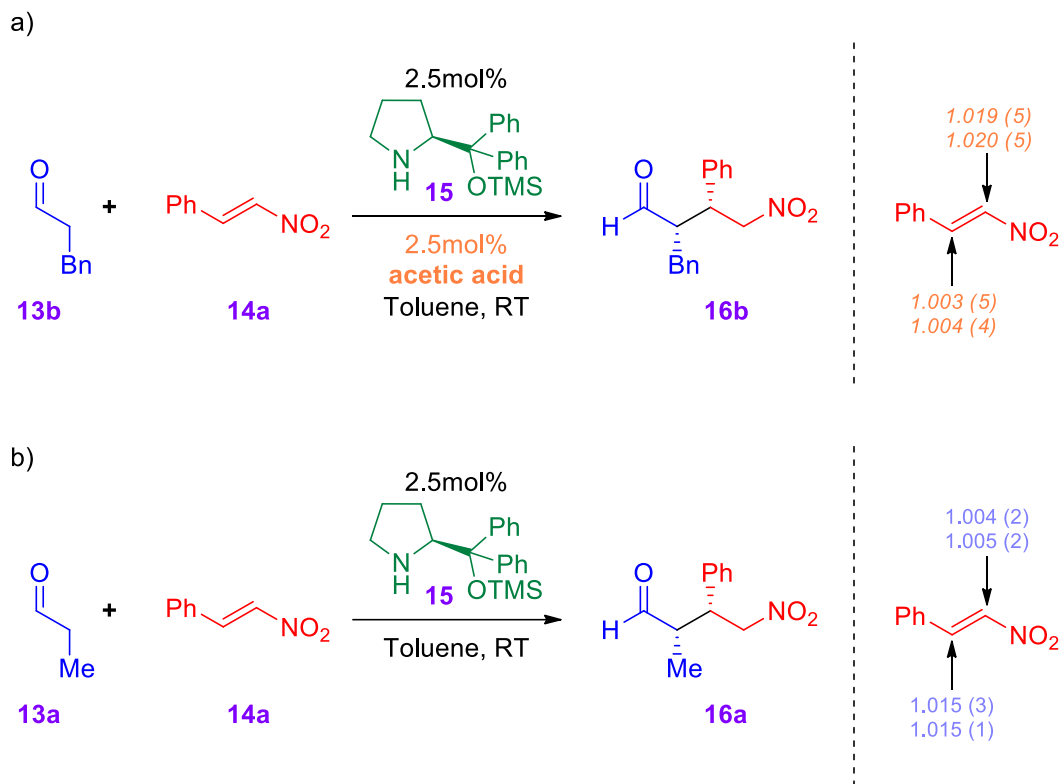


Figure 2. 21. Conditions used in the third and fourth studies of the title reaction and KIEs

The decrease in observed KIE in the absence of acid led to the hypothesis that C–C bond formation and protonation could be co-rate-determining. When two transition states are similar in energy, the observed KIE is a weighted value of the individual transition states with respect to their relative energies.^{148,184} This appears to be the case in the reaction performed with **13a** in the absence of acid (Figure 2.21b) where the KIE observed on the α -carbon of **14a** is significantly reduced in magnitude. The unity KIE expected at this position for the protonation step would decrease the observed normal KIE expected from the C–C bond formation step. When acetic acid is added, the energy of the protonation step is, in theory, decreased due to acetic acid's relative low pKa. With the energy barrier of protonation lower, C–C bond formation becomes more rate determining.

This line of reasoning is supported by DFT calculations. The C–C bond forming event was modeled with acetic acid at the B3LYP/6-31G* level of theory.^{185–188} IRCs confirmed the conclusions drawn by Pihko and co-workers that, after C–C bond formation, the system spontaneously cyclizes to oxazine **19a**. The isotope effects for **14a** were predicted from scaled vibrational frequencies using *ISOEFF98*.^{189,190} The acetic acid was strategically placed to coordinate to the nitro group of **14a** as this is where the negative charge is building up during the transition state. The acid is stabilized by a weak hydrogen-bond from one of the phenyl groups on the catalyst. From this calculation, we see a predicted KIE of 1.032 on the α -carbon of **14a**. This value is marginally higher than the measured KIEs, but that can be attributed to protonation still being partially rate-determining.

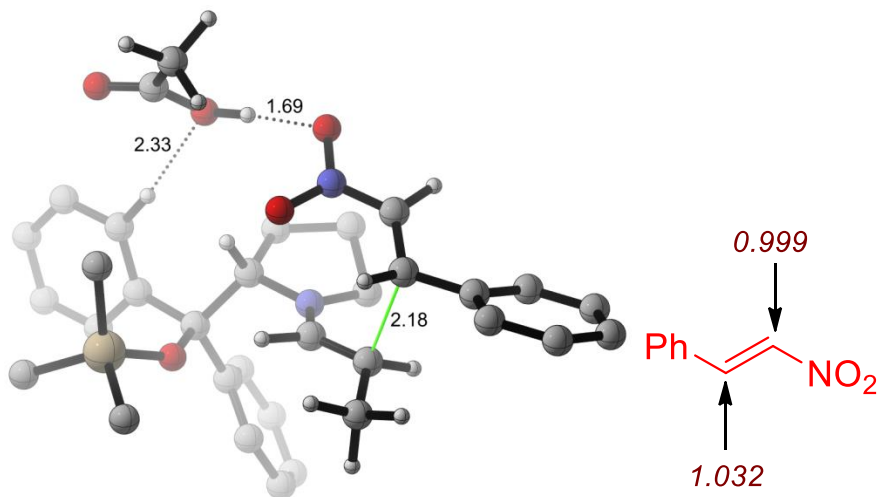


Figure 2. 22. DFT optimized transition state for carbon-carbon bond formation and predicted KIEs with acetic acid

To support that claim, the protonation of the nitronate carbon was modeled using both the oxazine **19a** and the cyclobutane **20a** in following with the Pihko and Blackmond cycles, respectively. In both cases, ring-opening is observed as concomitant with proton

transfer. For the transition from oxazine **19a**, Figure 2.23a, the C–O bond of the ring breaks at 2.31 Å with an early proton transfer. The nature of the proton transfer is likely explained by the three CH···O hydrogen-bonds established to the acid's carbonyl-oxygen. These stabilizing interactions make the proton more acidic and therefore promote an early transfer. In the case of the transition from the cyclobutane **20a**, Figure 2.23b, the geometry of the cyclobutane does not allow for these interactions and the proton transfer is therefore later, as is the ring-opening with the C–C bond breaking at 2.74 Å. Both of these transition states predict a β -carbon KIE of 1-1.5% and an α -carbon KIE of near unity. Energetically speaking, the transition from the oxazine (Figure 2.23a) is favored by ~ 10 kcal mol⁻¹ (B3LYP-D3(BJ)/6-311++G**/SMD(toluene) // B3LYP/6-31G*).^{191–193}

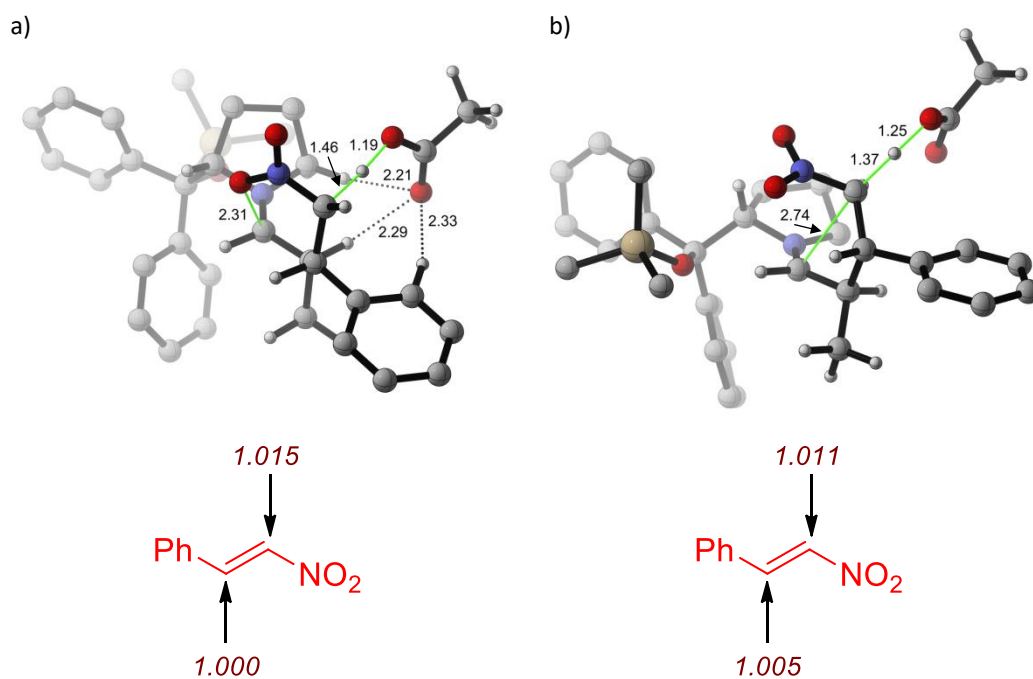


Figure 2. 23. Acetic acid protonation of the nitronate carbon of (a) oxazine intermediate; (b) cyclobutane intermediate

If the transition state in Figure 2.23a is ~ 1.2 kcal mol⁻¹ lower in energy than the C–C bond formation step in Figure 2.22, the weighted α -carbon KIE would be a match for the

1.029 observed experimentally. In addition, such a small gap would account for the delicacy of the potential energy surface. Current predictions have a much greater difference in these energies ($-3.3 \text{ kcal mol}^{-1}$), but these DFT methods are known to fail when predicting energies for proton transfers and a more comprehensive computational analysis is underway.¹⁴⁸

To investigate the potential energy surface in the absence of the co-catalyst, C–C bond formation was modeled without the acetic acid. Without the acidic proton to balance the build-up of negative charge on the nitro-group, the transition state becomes later with the C–C bond distance decreasing by 0.2 \AA . This results in a larger KIE prediction of 1.036 as shown in Figure 2.24.

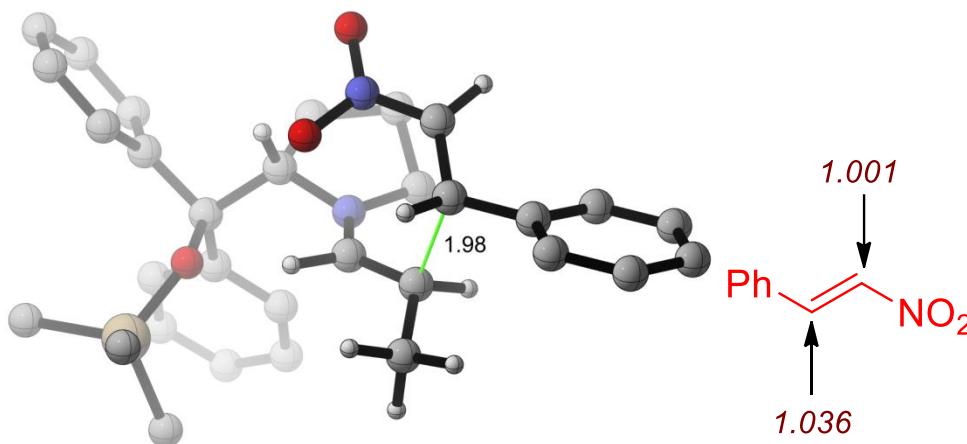


Figure 2. 24. DFT optimized transition state for carbon-carbon bond formation and predicted KIEs with acetic acid

Although the species responsible for effecting the protonation is not known when the co-catalyst is absent, one can assume that the prediction for the α -carbon for protonation by acetic acid (Figure 2.23) stands as a decent example. In that case, considering the predicted KIEs in Figure 2.23a and Figure 2.24, if the protonation step is $\sim 0.4 \text{ kcal mol}^{-1}$

higher in energy than the C–C bond formation, the α -carbon KIE would match the 1.015 observed value.

The conclusion that, in the presence of acetic acid, C–C bond formation is almost completely rate-determining (for **13a**) is inconsistent with the 3.25 α -methylene k_H/k_D measured by Blackmond and co-workers for this same reaction (Figure 2.16b).¹⁷⁷ Since no hydrogen is forming or breaking bonds at the transition state modeled in Figure 2.22, a unity k_H/k_D would be expected. That is, of course, if this transition state was consistently rate-determining. As we have already shown, the energy difference between C–C bond formation and protonation is incredibly delicate. In Blackmond and co-workers' experiment, they measure the rate of the reaction with α -H₂-**13a** and acetic acid, and then again with α -D₂-**13a** and acetic acid-*d*₄. Since deuterium is larger, it would likely raise the energy barrier for protonation. If the two barriers are initially close, this change would cause a shift in the contribution of the two co-RDSs. An analogous experiment was used in the earlier section to disprove the possibility of co-RDSs.¹⁴⁴ To provide support for this line of reasoning, ¹³C KIEs were measured employing the substrates used in Blackmond and coworkers' k_D experiment. These conditions and measured KIEs are shown in Figure 2.25. The presence of normal KIEs on both carbon atoms suggests that, in the presence of deuterated substrates, C–C bond formation stops being completely rate-determining and protonation becomes comparable in energy again (as is the case in the system without co-catalyst).

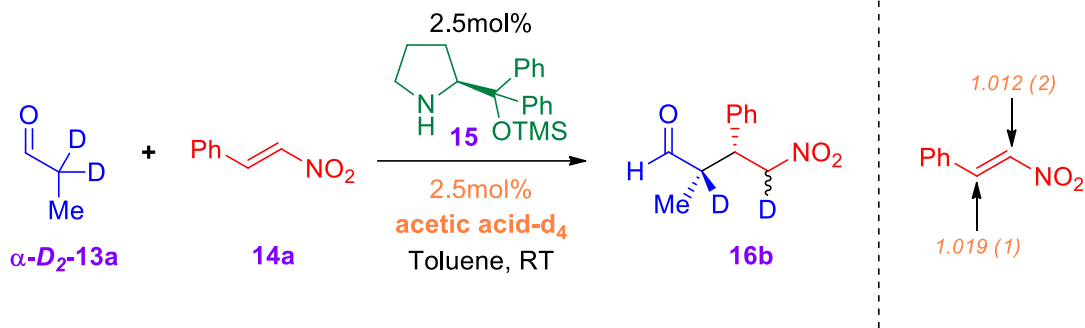


Figure 2. 25. Conditions used in the fifth study of the title reaction and KIEs

CONCLUSIONS From the experiments and calculations discussed above, it can be seen that there is a very small difference between the energies of the C–C bond formation and the protonation step. Three observations are made: (1) changing the substrate from 3-phenylpropanal **13b** to propanal **13a**, caused a change in the relative energies substantial enough to cause a shift in the observed KIEs; (2) when **13a** is used, adding acetic acid as a co-catalyst also causes a shift in the relative energies as seen in the changing magnitude of the KIEs; (3) labeling **13a** and acetic acid with deuterium causes a change in the relative energy of the protonation event which leads to the C–C bond formation no longer being completely rate-determining. In the light of these data, many of the conclusions drawn in the literature are no longer at odds as the energy surface experimentally appears to be flat enough that minor changes in substrates and conditions cause notable changes in the energy barriers and therefore do not allow for experiments with different conditions to be safely compared.

2.2 “Iminium-ion” Catalysis

As discussed in the introduction, primary and secondary amines have evolved a second branch of organocatalysis: Iminium-ion catalysis. This work was primarily pioneered by David MacMillan’s group.⁵⁸ It was known that Lewis acids would coordinate to the carbonyl-oxygen of α,β -unsaturated aldehydes and lower the energy of the lowest unoccupied molecular orbital (LUMO) of the substrate. This would then activate the β -carbon for nucleophilic attack due to the contributing resonance structure shown in Figure 2.26. MacMillan and co-workers proposed that an amine could condense with the same substrate and generate an iminium-ion. This intermediate would act similar to the Lewis acid complex by generating an analogous resonance structure in Figure 2.26.

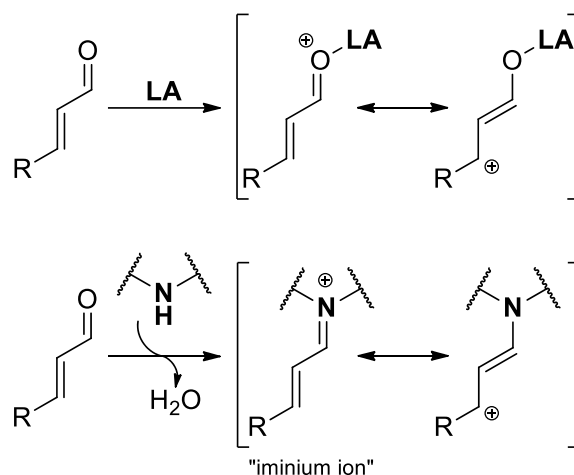


Figure 2. 26. LUMO-lowering strategies

The mechanism for iminium-ion formation is almost identical to that of enamine formation with the exception that the α -proton is not extracted. These steps are illustrated in Figure 2.27. The iminium-ion has been characterized in several cases by use of amine salts as catalysts and stoichiometric conditions.^{194–200} Under neutral amine conditions, however, there has been very little evidence of this intermediate with one exception from

Gschwind and co-workers who characterized an iminium-ion intermediate in an enamine-type reaction with L-proline.²⁰¹ Nevertheless, the copious examples in the literature of this mode of activation prove it to be a valuable catalytic archetype.

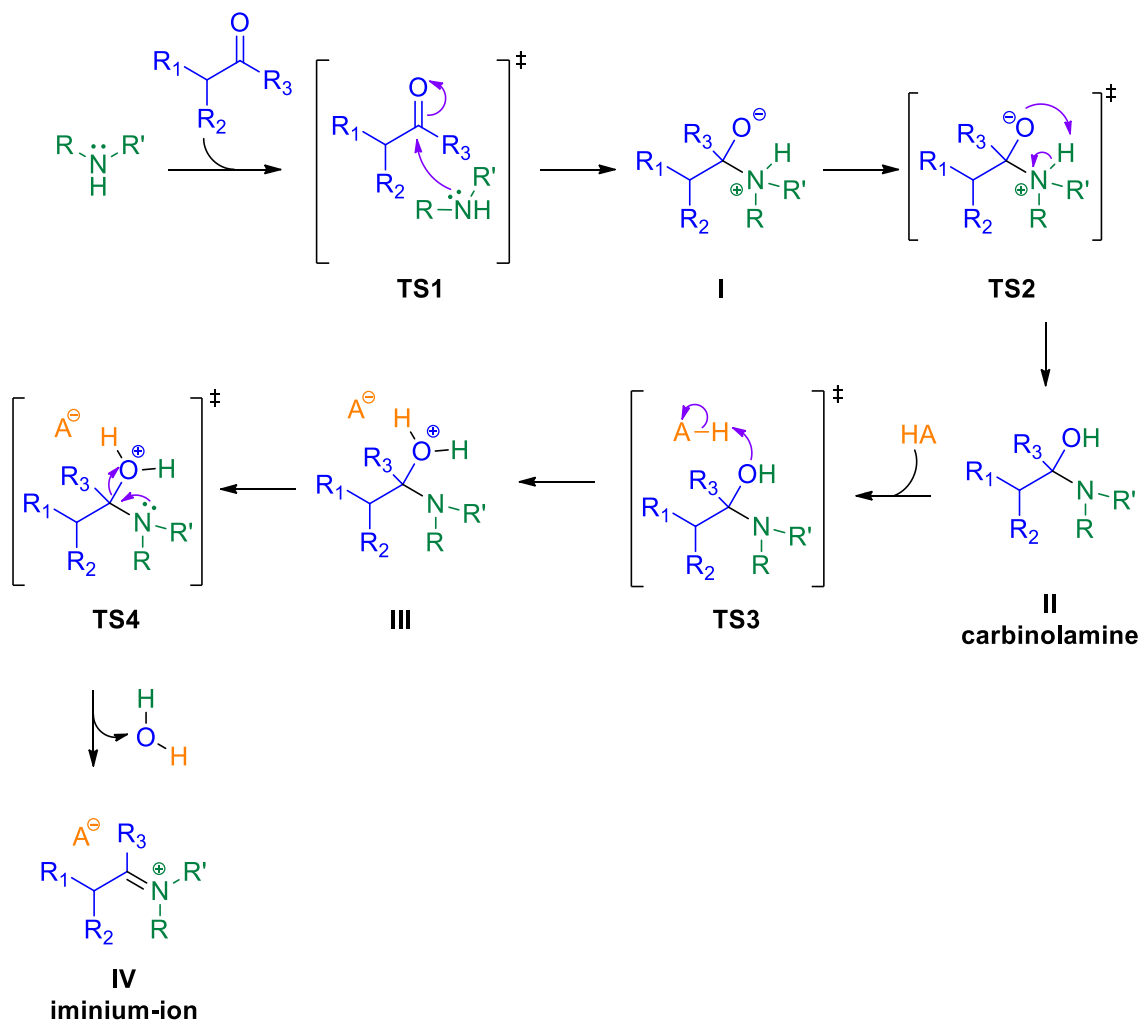


Figure 2. 27. General mechanism for iminium-ion formation

2.2.1 Kinetic Isotope Effects Reveal an Alternative Mechanism for “Iminium-Ion” Catalysis

INTRODUCTION In 2005, the group of Karl Anker Jørgensen reported the secondary amine-catalyzed asymmetric epoxidation of α,β -unsaturated aldehydes, or enals (**24**) with

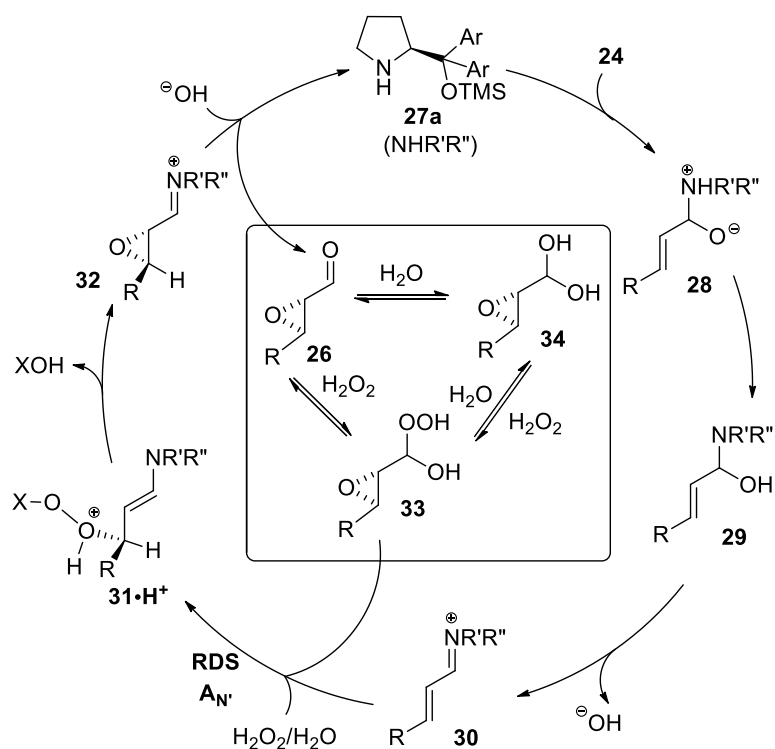


Figure 2. 28. Jørgensen group's proposed catalytic cycle

In 2013, Duarte and Santos published a computational investigation of the reaction and suggested several alterations to the Jørgensen group's proposal.²⁰³ First, the Santos group modified the formation of the iminium-ion by the inclusion of an explicit hydrogen peroxide molecule in their calculations. This molecule then was suggested to coordinate to the lost hydroxide-ion therefore activating the nucleophilic oxygen of the hydrogen peroxide for β -carbon attack. Most notably, in addition to the reworking of this part of the catalytic cycle, the Santos group suggested that the proton transfer from the initially formed zwitterion (**28**) to the neutral carbinolamine (**29**) was the RDS of the reaction (Figure 2.29). To gain a better understanding of this reaction, our group, along with the Jørgensen group, set out to perform a synergistic ^{13}C KIE and DFT analysis.²⁰⁴

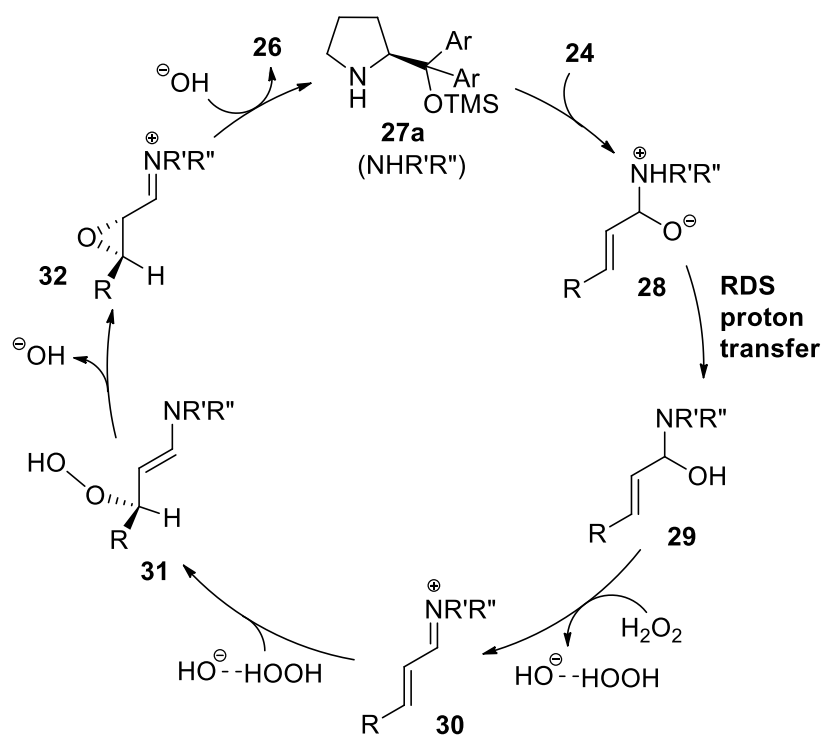


Figure 2. 29. Santos group's proposed catalytic cycle

EXPERIMENTAL KIES The reaction with *p*-chlorocinnamaldehyde (**24a**) was chosen for this study. Four reactions were taken to $72 \pm 2\%$, $77 \pm 2\%$, $68 \pm 2\%$, and $61 \pm 2\%$ conversion as determined by ^1H NMR analysis of the crude reaction mixture after reduction with sodium borohydride. Starting material was then recovered *via* column chromatography and the isotopic composition was compared to material from the same batch of chemical that had not been subjected to the reaction conditions. Three samples were reduced to the corresponding alcohol for comparison. This was done to decrease the amount of time required for sample analysis on the NMR. One sample was analyzed as the aldehyde to ensure the derivatization method was complete and did not influence the isotopic composition of the material. From the ratio of the isotopic composition of the standard and the re-isolated sample, KIEs were determined in the standard way.¹⁴³ The KIEs for these four separate reactions are shown in Figure 2.30.

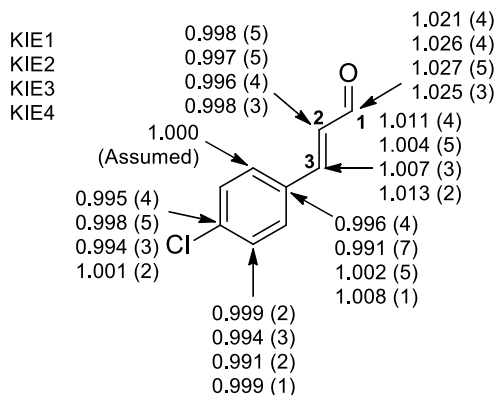


Figure 2. 30. Measured KIEs from four independent experiments

QUALITATIVE INTERPRETATION OF EXPERIMENTAL KIEs Qualitatively, the large primary KIE (2-2.5%) on the carbonyl carbon (C1) suggests that this carbon is involved in either a bond-formation or bond-cleavage at the rate-determining step. In addition, the smaller, yet non-unity KIE (0.5-1%) on the β -carbon (C3) suggests that this carbon too is involved in a bond change at the RDS. All other carbon atoms display a near-unity isotope effect. The assessment that these two atoms are *both* involved in bond changes at the RDS is inconsistent with the proposal made by Santos in which *neither* of these atoms is undergoing a change in bonding.²⁰³ These data also call into question the “classical” iminium-ion mechanism set forth by the Jørgensen group.²⁰² No single step can account for bond changes at both locations. Therefore, a different proposal was needed to explain the findings.

Three possible scenarios emerged as the most likely explanations of these observations and were investigated (Figure 2.31). The first possible explanation is the iminium-ion formation and conjugate addition (A_N) are co-RDSs. In this case, the energy of the formation of the iminium-ion (i.e. **29** \rightarrow **30**) and the energy of the nucleophilic attack of hydrogen peroxide on the β -carbon (i.e. **30** + **25⁻** \rightarrow **31**) are close enough in energy that

the observed KIE would be a weighted average of the two individual steps. In this case, the first TS (iminium-ion formation) would account for the KIE observed on **C1** and the second TS (A_N) would account for the KIE observed on **C3**.

The second explanation invokes a nucleophilic substitution from the carbinolamine intermediate (**29**) to directly form the peroxyenamine (**31**). This concerted transition state (S_N2') would account for both observed KIEs as a bond is being broken between **C1** and the hydroxyl group, and a bond is concomitantly being formed between **C3** and the incoming peroxy group.

The third possibility involves a 1,3-sigmatropic rearrangement. In this scenario, the peroxide anion **25**⁻ first attacks **C1** to yield peroxyamine **35**, then rearranges to intermediate **31**. This second step (**TS-shift**) accounts for both of the observed isotope effects as **C1** is breaking a bond with the peroxy group while **C3** is forming a bond with the same group. All three of these possibilities are illustrated in Figure 2.31. Due to the fact that all three can *qualitatively* be used to explain the observed KIEs, a *quantitatively* analysis could be performed through the use of density functional theory (DFT) analysis to refute/support certain scenarios.

I) Iminium-ion formation and conjugate addition (A_N) are co-RDS

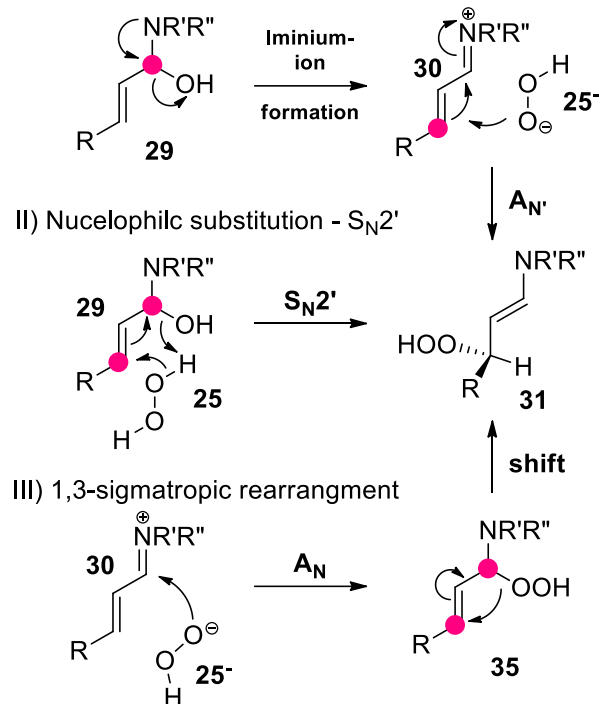


Figure 2. 31. Three possible mechanisms leading to a qualitative agreement of observed KIEs. Pink bubbles indicate location of expected normal KIE

COMPUTATIONAL METHODS The entire system of **26a**-catalyzed epoxidation of **24a** with **25** was modeled (84 atoms) using the B3LYP functional^{185–187}, and 6-31G* basis set¹⁸⁸, as implemented by the *Gaussian09* software package²⁰⁵. Transition states and intermediates were calculated for each step of the catalytic cycle to generate a free energy profile. For all transition structures explored, a systematic conformational search was carried out by varying three key criteria of the reaction: (1) orientation of the chiral moiety; (2) pucker of the pyrrolidine ring; (3) orientation of the peroxide. These variations are shown in Figure 2.32. From this search, the lowest energy geometries were used to calculate theoretical isotope effects. The KIEs were predicted from the vibrational frequencies of the transition structures using *ISOEFF98*¹⁹⁰ (with 0.9614 scaling factor¹⁸⁹). An infinite parabola¹⁵⁹ or Wigner¹⁶⁰ tunneling correction was applied to include the effects

of tunneling on the reaction. To assess the feasibility of the suggested transition states, extrapolated free energies were obtained by applying the free energy correction from the aforementioned level of theory to single point energies conducted at the B3LYP-D3(BJ)/6-311++G**/SMD(water) level of theory.^{191–193,206} The energies discussed herein are the energies obtained by this method. For a thorough understanding, ΔG^\ddagger values were also calculated using ten other DFT methods with two different solvent continuum models (these data are presented in SECTION V: EXPERIMENTAL AND COMPUTATIONAL DETAILS to avoid redundancy here).

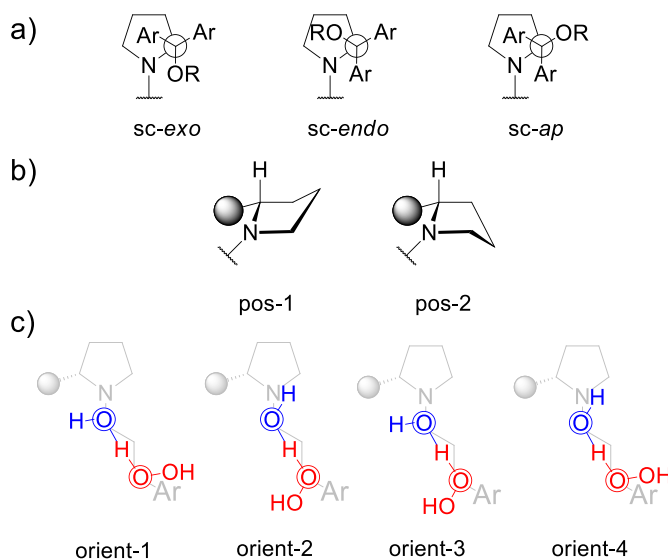


Figure 2. 32. Parameters varied in systematic conformational search. (a) Orientation of chiral moiety of the catalyst; (b) pucker of the pyrrolidine ring; (c) orientation of the peroxide

SCENARIO I: IMINIUM-ION FORMATION AND $A_{N'}$ ARE CO-RDS The transition states representing the formation of the iminium-ion and $A_{N'}$ were modeled with the explicit inclusion of hydrogen peroxide and hydroxide ion in following with the suggestion from Santos and co-workers (Figure 2.33).²⁰³ Examination of the formation of the iminium ion (TS-iminium) shows that the hydrogen peroxide acts as a Brønsted acid assisting in the expulsion of the hydroxyl group. Weak, albeit present, $CH\cdots O$ interactions from the

catalyst stabilize the formation of this negatively charged complex. The calculated ΔG^\ddagger for this step is 7.8 kcal mol⁻¹. Observation of the conjugate addition (TS-A_N) shows that this transition state is “early” with the carbon-oxygen bond forming at 2.49Å. The calculated ΔG^\ddagger for this step is 19.3 kcal mol⁻¹. A $\Delta\Delta G^\ddagger$ of 11.5 kcal mol⁻¹ would correspond to sole-rate-determining conjugate addition. That fact, coupled with the inappropriately low KIEs predicted for **C1** and **C3**, effectively rules out this mechanistic scenario as a possible explanation of the experimental KIEs.

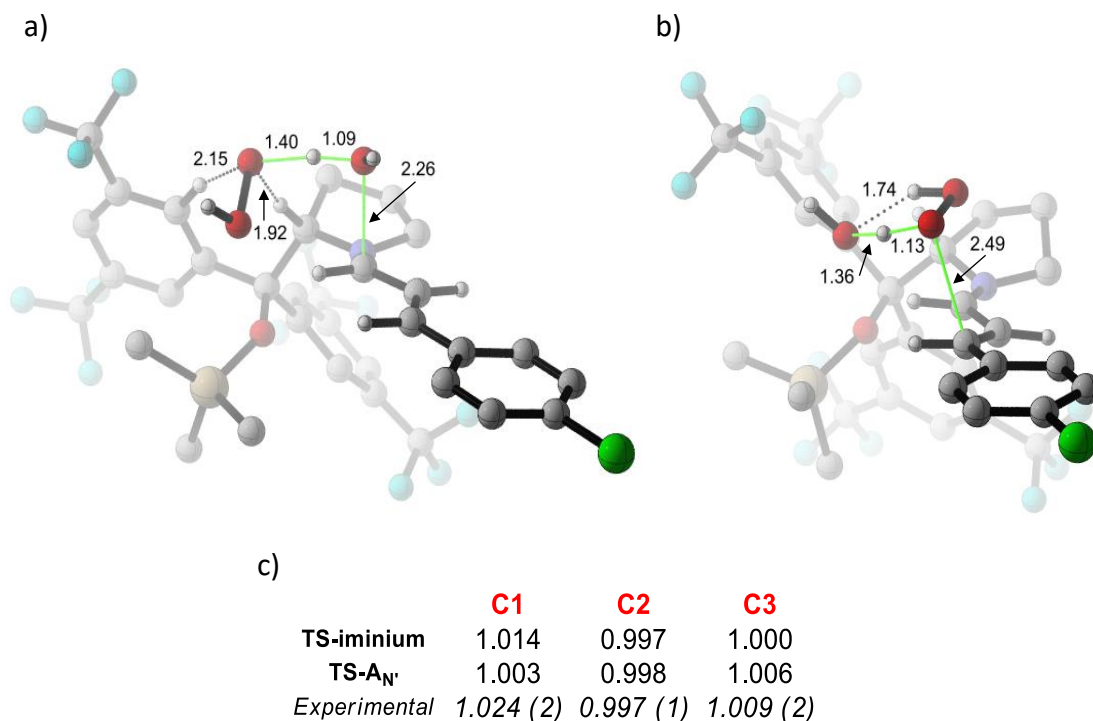


Figure 2. 33. Lowest energy geometry for (a) TS-iminium; (b) TS-A_N; (c) predicted and experimental KIEs. Experimental KIEs are the weighted average of all measurements.

SCENARIO II: NUCLEOPHILIC ADDITION – S_N2' The S_N2' transition state is characterized by the *syn*-orientation of the leaving group (water) and the incoming nucleophile (hydrogen peroxide). This stereochemical course has been extensively studied by Stork and others.^{207–212} The C1–O bond breaks at 2.24Å and the O–C3 bond forms at

2.43Å leading to a 2% KIE on **C1** and a 0.8% KIE on **C3**. The magnitude of these predictions is directly related to the distance of the forming or breaking bond. The O–**C3** is more broken thus the KIE is lower, whereas the **C1**–O is more formed resulting in a larger isotope effect. Further credence is lent to this explanation by the predicted energy. TS-S_N2' is not only energetically feasible at the reaction temperature (15.3 kcal mol⁻¹), but it is also 4.0 kcal mol⁻¹ lower in energy than TS-A_N' making it the energetically favored pathway for the reaction.

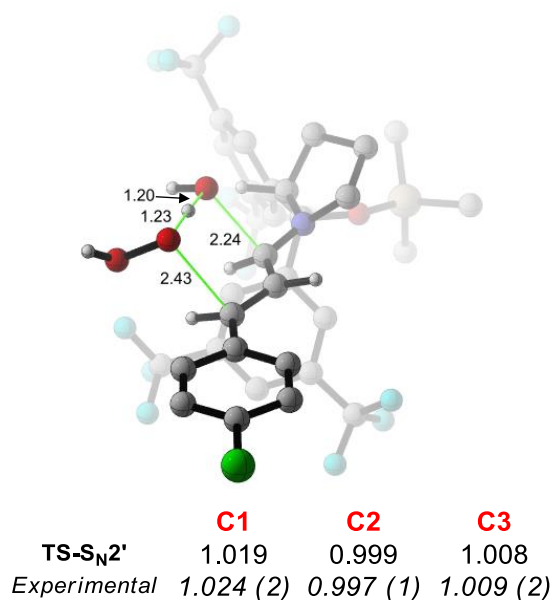


Figure 2. 34. Lowest energy geometry and predicted KIEs for TS-S_N2'. Experimental KIEs are the weighted average of all measurements.

To continue to support the likelihood of this transition state, the transition state leading to the enantiomer of product, TS-S_N2'-ent, was modeled (Figure 2.35). This TS was found to be 1.7 kcal mol⁻¹ higher than TS-S_N2' corresponding to a predicted enantiomeric excess of 89%, in good qualitative following with the observed 98%.

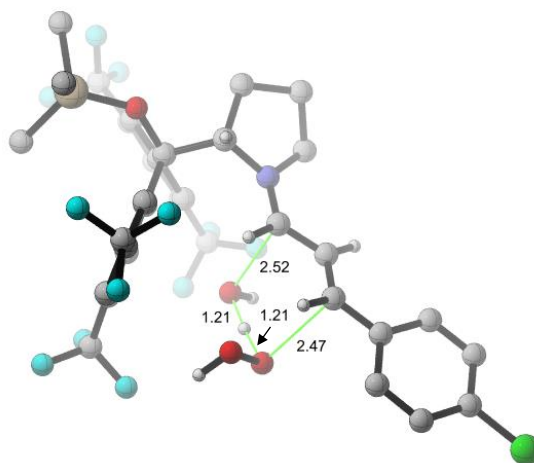


Figure 2. 35. Lowest energy geometry for TS-S_N2'-ent

SCENARIO III: 1,3-SIGMATROPIC REARRANGEMENT An explicit water molecule was included in the investigation of the TS-shift to make it isoelectric with the key transition states from the other two scenarios for accurate comparison. In this TS, the peroxy group undergoes a 1,3-shift from **C1**, breaking at 2.47Å, to **C3**, forming at 2.25Å (Figure 2.36). Again, we see the effect of the extent of bond scission/formation on the KIE. Only a 0.6% KIE is predicted for **C1** as the peroxy group is more removed from this center, and almost double that is observed on **C3** where the peroxy group is much closer. The nature of this observation shows the mis-match that this prediction provides for the KIEs. In this case, the KIE on **C3** is larger than **C1**, in conflict with the experimental KIEs. Further evidence to refute this transition state comes from the calculated ΔG^\ddagger being 21.2 kcal mol⁻¹, 5.9 kcal mol⁻¹ higher than TS-S_N2'.

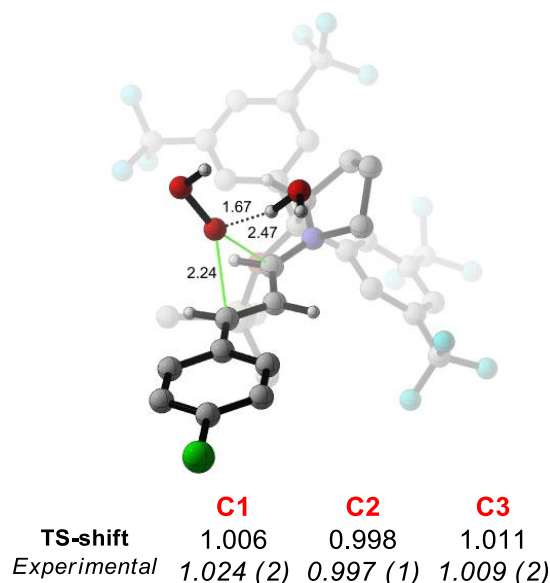


Figure 2. 36. Lowest energy geometry and predicted KIEs for TS-shift. Experimental KIEs are the weighted average of all measurements.

CONCLUSION It is clear that the typical understanding of “iminium-ion catalysis” cannot be rationalized with the data gathered. We therefore submit the alternative mechanism, herein referred to as TS-S_N2', as a means of explaining our observations and shedding a new light on this famous mode of catalysis. It should be noted that iminium formation is still facile, in this case—7.5 kcal mol⁻¹ lower in energy than the proposed RDS—and therefore likely forms. Experimental and predicted KIEs, along with extrapolated energies suggest that this species is an off-cycle, parasitic intermediate and the productive pathway conducts itself via the carbinolamine intermediate **29**.

AVENUES FOR FUTURE RESEARCH It is expected that this basic mode of catalysis could be applied to any system containing a “Nuc-H” type nucleophile, provided there is no acid additive in the reaction (Figure 2.37). Numerous reactions have been explained using the “iminium-ion” pathway which could instead progress *via* the newly proposed S_N2'-type mechanism. A short list of some of the reactions currently under study in the

Veticatt lab is shown in Figure 2.38 and include conjugate additions of Nuc-H over the double bond, as well as more intricate domino reactions.^{213–219}

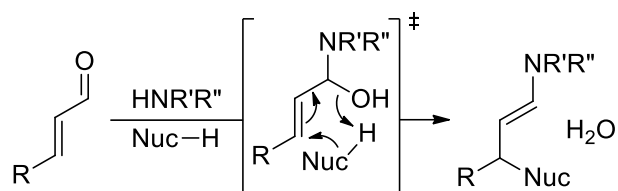


Figure 2. 37. General application of novel S_N2' mechanism

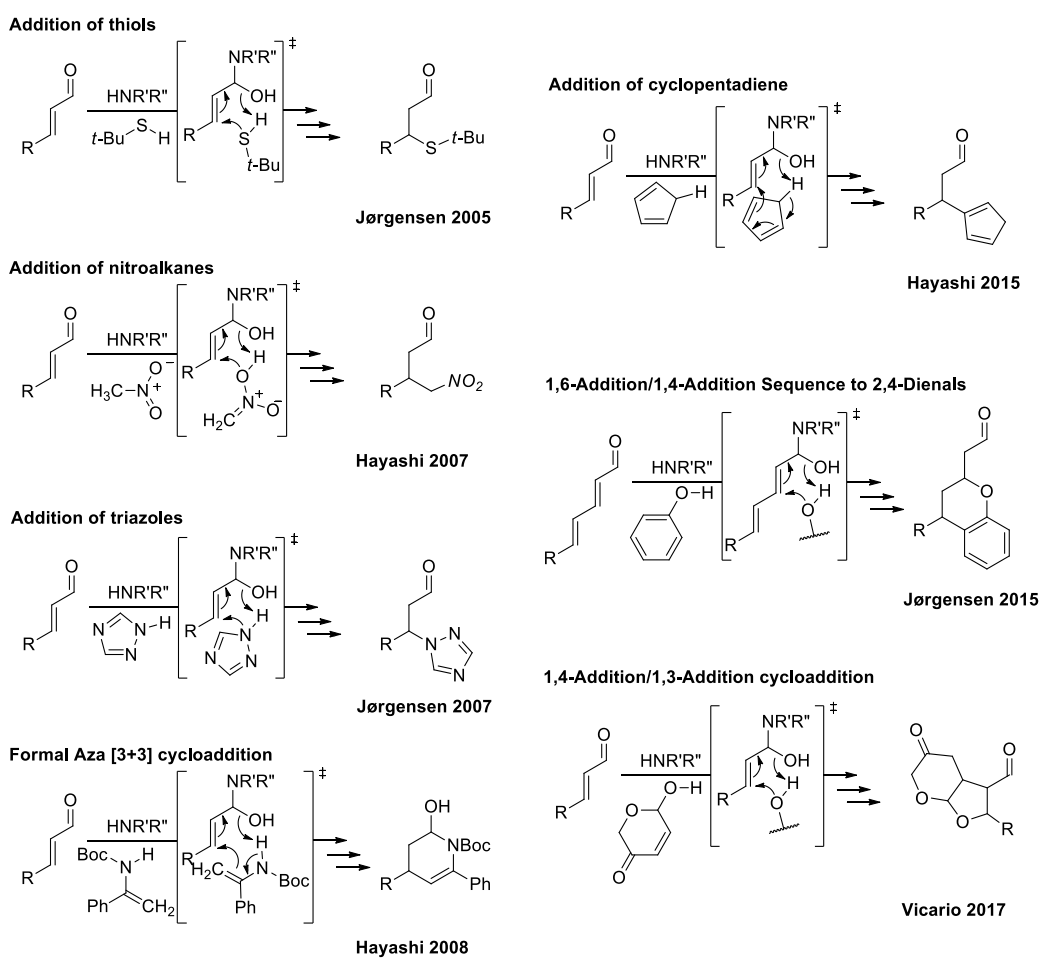


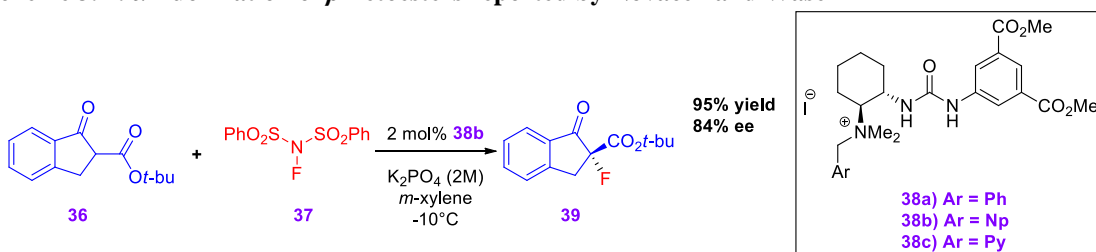
Figure 2. 38. Systems under study for continued evidence of the novel S_N2' mechanism

(thio)urea-quaternary ammonium salts to catalyze α -chlorinations,²⁴⁵ α -fluorinations,²⁴⁶ and α -hydroxylations²⁴⁷ of β -ketoesters, Michael additions,²⁴⁸ and cascade reactions²⁴⁹. This section will focus on two particular collaborations with the Waser group wherein computational chemistry was used to better understand the reactivity of these catalysts.

3.1.1 Bifunctional Ammonium Salt Catalyzed Asymmetric α -fluorination of β -Ketoesters

INTRODUCTION In 2014, Novacek and Waser published the (thio)urea-quaternary ammonium salt-catalyzed α -fluorination reaction of β -ketoesters.²⁴⁶ More than 60 catalysts were synthesized, but the final optimized catalyst was catalyst **38b** which, when combined with β -ketoester **36**, *N*-fluorobenzenesulfonimide (NFSI) **37**, and potassium phosphate (K_3PO_4) yielded α -fluorinated product **39** in 95% yield and 86% ee.

Scheme 3. 1. α -fluorination of β -ketoesters reported by Novacek and Waser



In the initial manuscript, the authors suggest that the reaction likely proceeds by dual activation of the substrates. After the base deprotonates the β -ketoester to form the enolate intermediate, ion-pairing between the enolate and the quaternary ammonium moiety are used to stabilize the two species and form a chiral complex. The NFSI then coordinates to the urea moiety and fluorine (as an F^+) is transferred preferentially to one face of the β -ketoester enolate. After this publication, a collaboration began between the

Veticatt group and the Waser group to develop a better understanding of the mechanism and origin of enantioselectivity of this reaction.

BINDING MODE STUDY Computational investigations began in order to test the hypothesis of activation presented by Novacek and Waser in 2014. The proposed method of activation was found (Figure 3.1) at the B3LYP/6-31G* level of theory.^{185–188} As predicted, the oxygen atoms on of the NFSI coordinated to the hydrogen atoms of the urea moiety on the catalyst at distances of 1.94Å and 2.20Å. The carbonyl oxygens of the enolate, coordinated to the α -protons of the quaternary ammonium moiety at between 2.05-2.44Å.

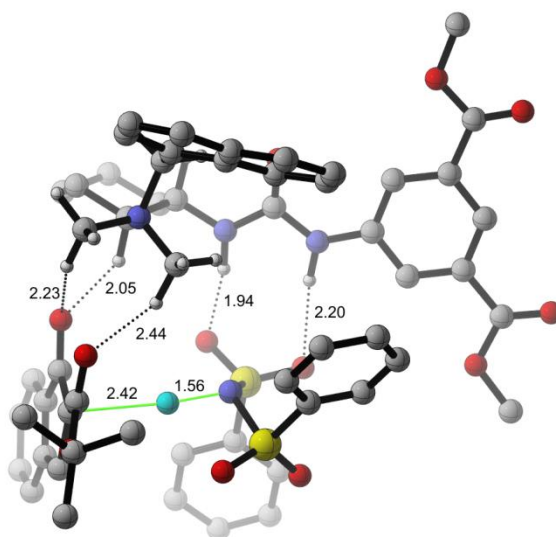


Figure 3. 1. DFT optimized transition state for Waser's fluorination using BM1

In order to fully understand the potential energy surface of this reaction, it was then proposed that the two substrates, enolate and NFSI, could switch their coordination partners. This led to the development of a second “binding mode.” The aforementioned transition state was labeled “Binding Mode 1” (**BM1**), and this new proposal was called “Binding Mode 2” (**BM2**). The transition state for **BM2** was found in the same way as

earlier mentioned and provided the structure shown in Figure 3.2. In **BM2**, the hydrogen atoms of the urea moiety coordinate to the oxygen of the keto moiety of the enolate at 1.84Å and 1.90Å, and the carbonyl of the ester group coordinates most strongly to one of the α -hydrogens of the quaternary ammonium moiety. The NFSI only forms one coordination and that is to a hydrogen on one of the methyl groups of the quaternary ammonium.

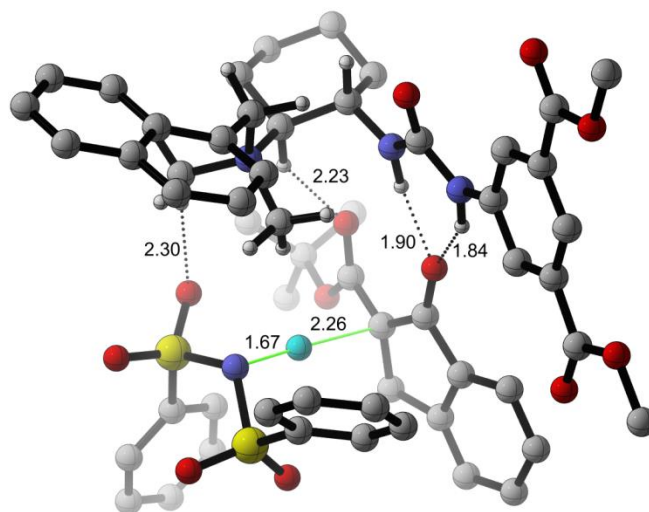


Figure 3. 2. DFT optimized transition state for Waser's fluorination using BM2

These two diastereomeric transition states were compared and the $\Delta\Delta G^\ddagger$ was found to be 6.9 kcal mol⁻¹ in favor of **BM2**. This was an exciting discovery as **BM2** was not the commonly relied upon mode of activation when dealing with ion pairs. Emboldened by this discovery, and still interested in fully understanding the potential energy surface for the reaction, two more binding modes were proposed and investigated. “Binding Mode 3” (**BM3**) was oriented such that the enolate was coordinated to the urea hydrogens and the NFSI approached from the reverse side of the quaternary ammonium. The reasoning behind this proposal was that the aryl group on the quaternary ammonium could act as a steric hindrance and drive reaction from this “backside” attack giving rise to the observed

enantioselectivity. “Binding Mode 4” (**BM4**) was oriented such that one proton of the urea moiety activated the NFSI and the other activated the enolate. The reasoning for this orientation was to allow the bulk of the *tert*-butyl group on the enolate to stick out and away from any other portion of the other molecule so as to minimize steric clashing. The lowest energy transition states found for **BM3** and **BM4** are shown in Figure 3.3. Both **BM3** and **BM4** were found to be less favorable than **BM2** by 7.8 and 2.9 kcal mol⁻¹, respectively.

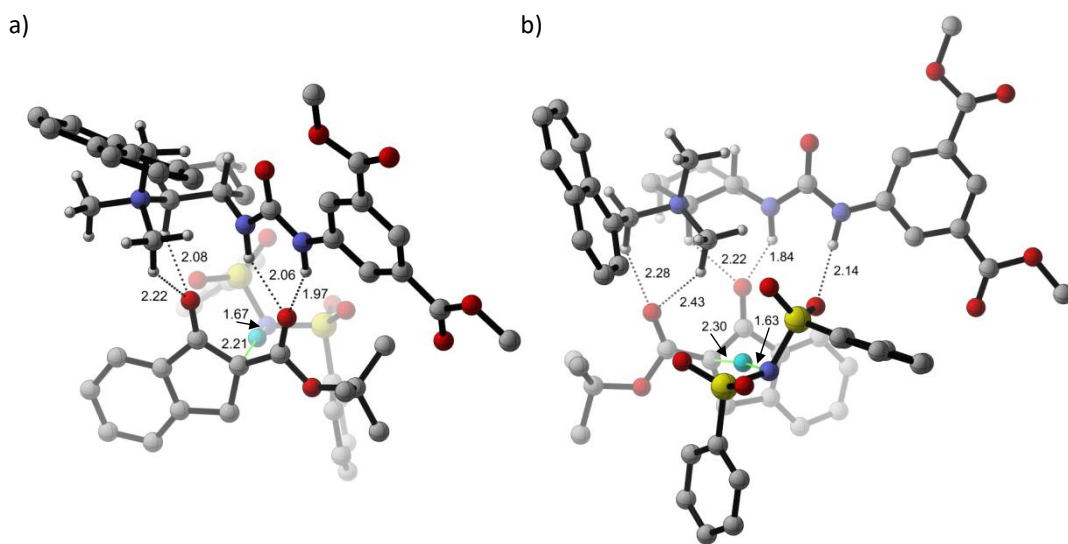


Figure 3. 3. DFT optimized transition state for Waser's fluorination using (a) BM3; (b) BM4

SYSTEMATIC CONFORMATIONAL ANALYSIS It should be noted that this transition state search was carried out in a thorough fashion. The catalysts employed in these calculations have layer of complexity due to the presence of three crucial σ -bonds which can rotate to give rise to different conformations. The quaternary ammonium group can assume three different staggered conformations depending on the rotation about the bond that connects it to the chiral scaffold. These conformations, designated “ α ” and numbered 1-3, are shown in Figure 3.4. The catalyst also has a benzylic methylene attached to the

quaternary ammonia. This also has three possible staggered conformations, designated “ β ”, as shown in Figure 3.4. Finally, the catalyst contains a naphthyl group which can assume four different positions: away from the reactive pocket, sticking down into the reactive pocket, laying across the reactive pocket, or sticking straight out of the reactive pocket. These conformations are designated “ γ ” and are also shown in Figure 3.4. A representative array of all possible 36 conformations, for all four binding modes and both enantiomers was tested. The majority of the located transition states have been omitted to avoid repetition and only the most illustrative conformations are discussed.

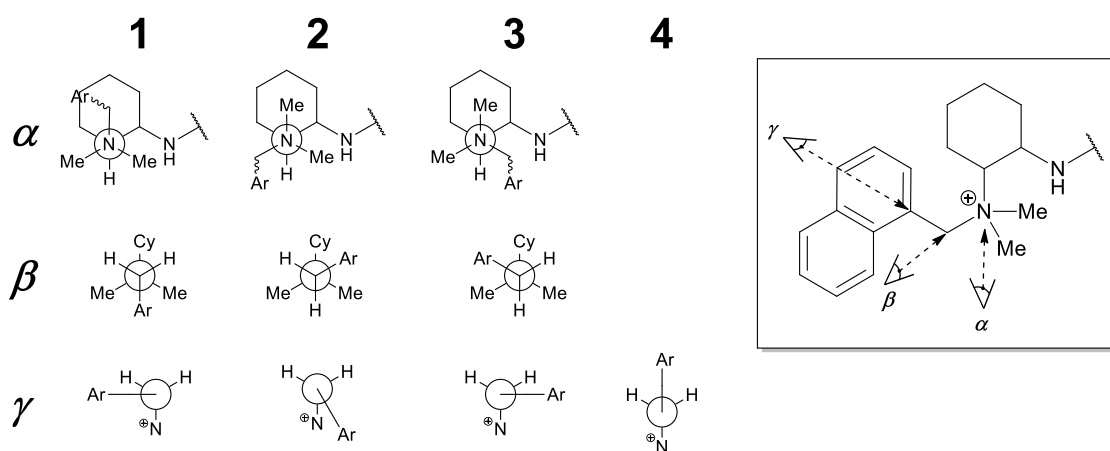


Figure 3. 4. Three relevant angle conformations around rotatable σ -bonds explored computationally

PREDICTION AND ORIGIN OF ENANTIOSELECTIVITY Upon settling on the mode of activation for the major enantiomer of product—**BM2** being the most likely—the endeavor was set forth to model the enantiomeric transition state and discover the origin of the observed selectivity. Again, a battery of transition states were found varying the α , β , and γ -angles, and investigating the different binding modes. In the end, the transition state shown in Figure 3.5a was determined to be the lowest in energy. Like its major enantiomer counterpart, this TS assumes a **BM2** configuration. Due to the steric interaction of the *tert*-

butyl group on the enolate, the nucleophile is shifted slightly causing the urea moiety to split its hydrogen atoms, one to the ketone-oxygen and the other to the ester at 1.80Å and 1.97Å, respectively. The NFSI retained its single hydrogen bond to the α -methyl group of the quaternary ammonium. The $\Delta\Delta G^\ddagger$ of these two enantiomeric transition states was found to be 1.4 kcal mol⁻¹ leading to a predicted ee of 86% which is in excellent agreement with the observed 84%. On the basis of these calculations, a rational design of catalyst was undertaken. The Waser group had already synthesized and tested catalyst **38a** where the aryl group off the quaternary ammonium is a phenyl. The observed ee was 77%. A computational treatment of this new catalyst returned a predicted ee of 75%. It was then predicted that if the aryl group was extended to a pyrenyl group, the selectivity would increase to 91%. Experimentally, this was vindicated and a 90% ee was measured.

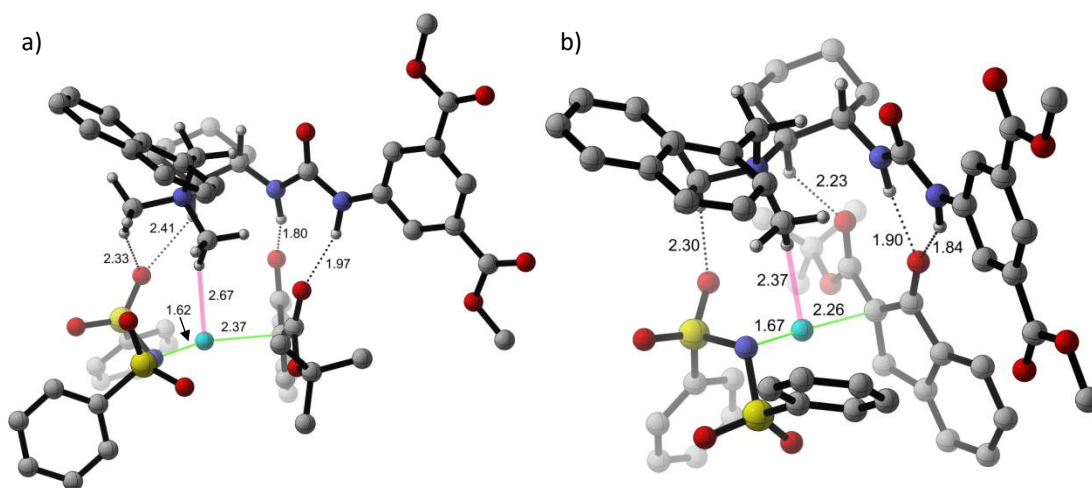


Figure 3. 5. DFT optimized transition state for Waser's fluorination using BM2, giving rise to the (a) minor enantiomer of product; (b) major enantiomer of product; critical CH-F interactions highlighted in pink

With these transition states identified, the question became: what is the cause of this selectivity? The lowest energy transition state for the major enantiomer, as catalyzed

by **38b**, is re-printed in Figure 3.6b with a specific bond shown in pink. The corresponding bond for the minor enantiomer is shown in Figure 3.6a. This non-conventional hydrogen-bond is 0.3Å closer in the major enantiomer TS than the minor. It is from this difference, that we propose, comes the observed selectivity. Most practitioners of nucleophilic fluorination will disregard this interaction since NFSI is delivering an electrophilic fluorine (formally an “F⁺”). It defies common intuition that an electron-deficient fluorine should coordinate to an acidic hydrogen. To provide a deeper insight into this observation, a natural bond order (NBO) analysis was conducted at the B3LYP/6-311+G** level of theory.^{191,250} The electrostatic potential map generated from this calculation is shown in Figure 3.6. As can be seen from this calculation, at the transition state, the fluorine still has quite a bit of electron density around it, making it a reasonable hydrogen-bond acceptor.

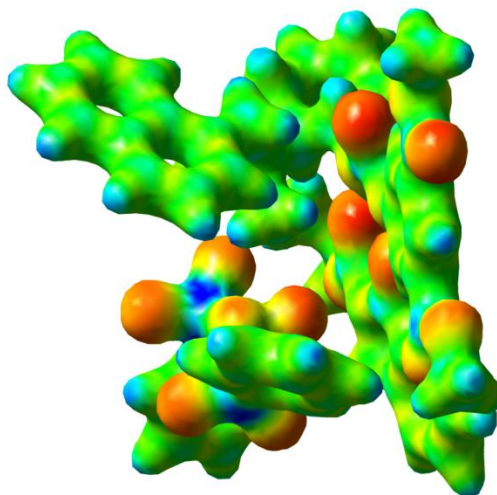


Figure 3. 6. Electrostatic potential map generated for Waser fluorination

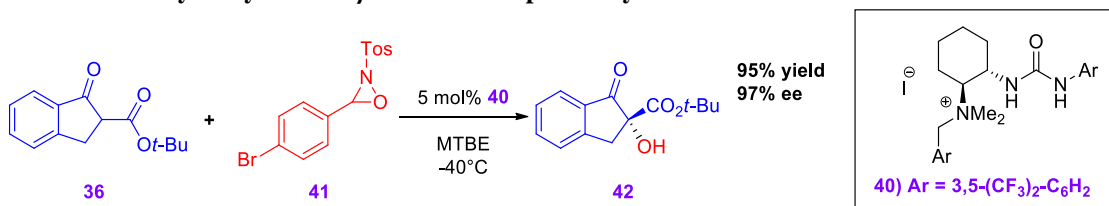
CONCLUSION This project displays the great importance of non-classical hydrogen bonds. Whereas the catalyst still makes use of the classical N-H···O⁻ bonding motif with the urea moiety’s coordination to the enolate, the key interaction discovered in this

transition state analysis is in a C-H...F⁺ hydrogen bond. It is from these non-classical hydrogen bonds that this catalyst derives its versatility and substrate promiscuity.

3.1.2 Bifunctional Ammonium Salt Catalyzed Asymmetric α -Hydroxylation of β -Ketoesters by Simultaneous Resolution of Oxaziridines

INTRODUCTION The collaboration between the Waser group and the Veticatt group continued to grow. In 2016, again we were asked to help the group understand a new reaction they had developed.²⁴⁷ This reaction is very similar to the abovementioned fluorination. A slightly different catalyst is employed (**40**), but the structure remains similar to that of **38**. It was found that the same β -ketoester, **36**, is capable of undergoing α -hydroxylation with the use of an oxaziridine, **41**, giving 95% yield and 97% ee (Scheme 3.2). Our assistance was solicited by the Waser group to better understand the reaction using DFT calculations.

Scheme 3. 2. α -hydroxylation of β -ketoesters reported by Waser and co-workers



BINDING MODE, CONFORMATIONAL, AND ENANTIOSELECTIVITY STUDY All binding modes were tested as earlier mentioned. For the major enantiomer of product, **BM2** again proved to be the lowest energy. In the case of the minor enantiomer, however, **BM4** now proved to be most favorable. These two transition states also showed that an α -angle of 3 was preferable to that of 1 displayed in the fluorination TSs (Figure 3.4). In the case of the major enantiomer (Figure 3.7a), the enolate was again activated by the N-H hydrogen bonds of the urea moiety, but also one of the particularly acidic protons adjacent to the

quaternary ammonium, establishing a 2.19Å bond. A second α -proton coordinated to the oxygen of the sulfonyl group on the oxaziridine at 2.21Å. For the minor enantiomer (Figure 3.7b), one proton from the urea moiety coordinated to the ester carbonyl of the enolate at 1.93Å, the other to the sulfonyl oxygen of the oxaziridine at 2.36Å. The difference in energies of these two transition states leads to a predicted ee of 97.2% which is in excellent agreement with the observed 97.0%.

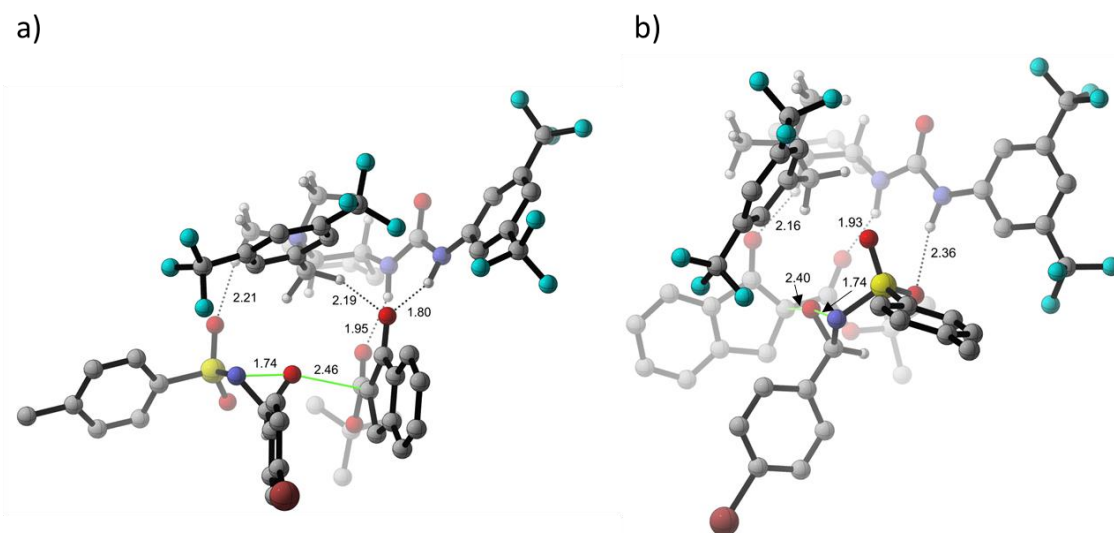


Figure 3. 7. Lowest energy transition states leading to (a) major; (b) minor enantiomer of product

SIMULTANEOUS KINETIC RESOLUTION During the optimization of this reaction, a curious phenomenon was observed. When an excess of racemic oxaziridine **41** was used, the recovered material was almost completely enantiomerically pure (Scheme 3.3). This is similar to the kinetic resolution reported by Liu and co-workers.²⁵¹ This finding sparked interest in obtaining a better understanding of the reaction. When **36** and (*S,S*)-**41** combine to make the enolate-catalyst complex, it can react with either oxaziridine (*S,S*)-**41** or (*R,R*)-**41** to yield either product (*R*)-**42** or (*S*)-**42** (Figure 3.8). Based on the observation by the Waser lab that (*R,R*)-**41** is leftover, it can be deduced that the enolate-catalyst complex

preferentially reacts with (*S,S*)-**41** leaving the unconsumed starting material enriched in the slower reacting enantiomer.

Scheme 3. 3. Observation of kinetic resolution in α -hydroxylation of β -ketoesters

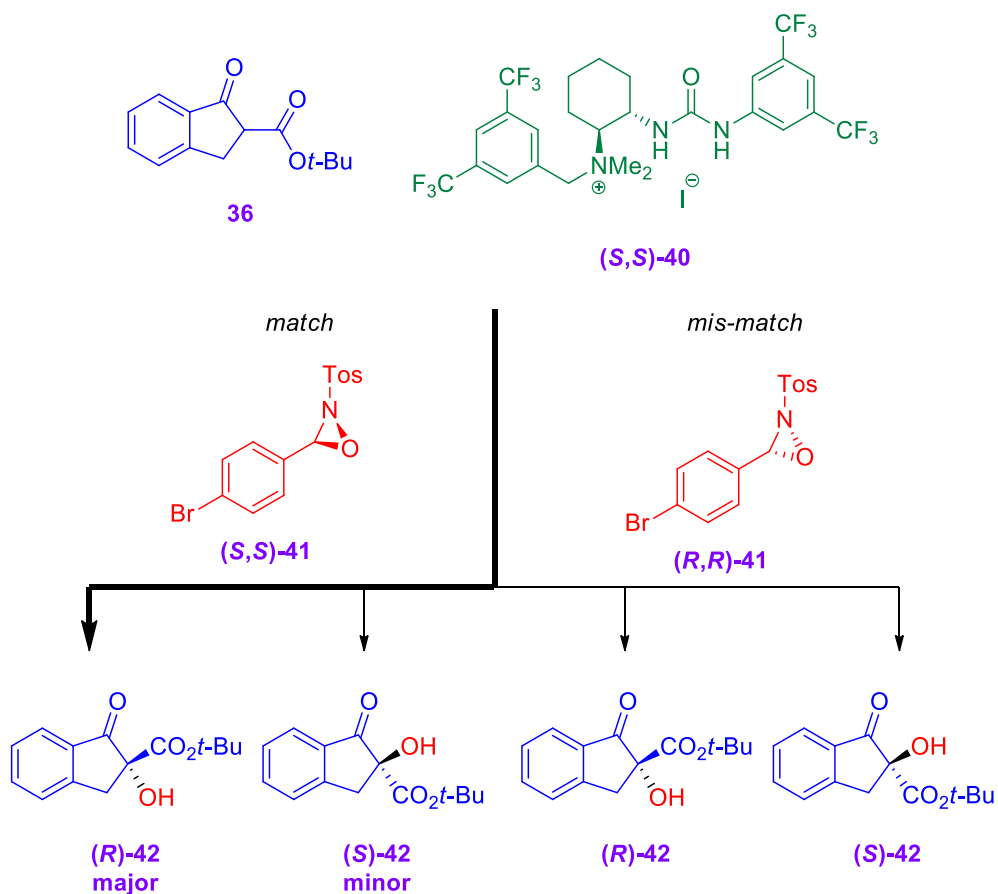
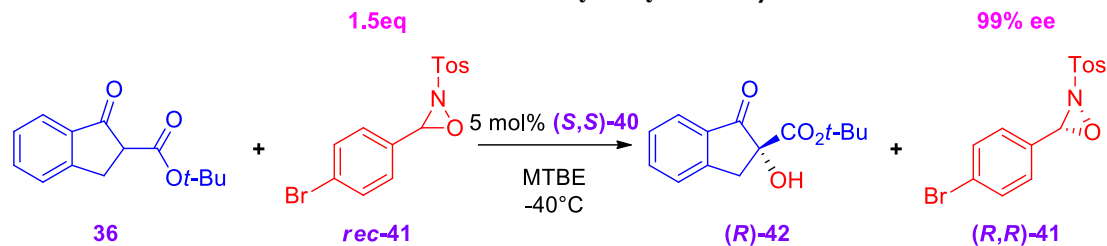


Figure 3. 8. Explanation of match/mis-match relationship

When enantiopure (*S,S*)-**41** was added to a reaction containing racemic catalyst, a >90% ee was still observed in the product (Figure 3.9).²⁴⁷ This confirms that oxaziridine (*S,S*)-**41** preferentially yields product (*R*)-**42** regardless of the catalyst used. To understand

this relationship, the mis-matched catalyst/oxaziridine pair (*S,S*)-**40**/*(R,R)*-**41** was calculated using the same thorough systematic approach discussed earlier. The lowest energy transition state assumed **BM2**, with the urea coordinated to the enoalte at 1.93 and 1.80Å and the α -protons of the quaternary ammonium coordinated to the oxaziridine through non-classical hydrogen bonds of 2.39 and 2.40Å (Figure 3.10).

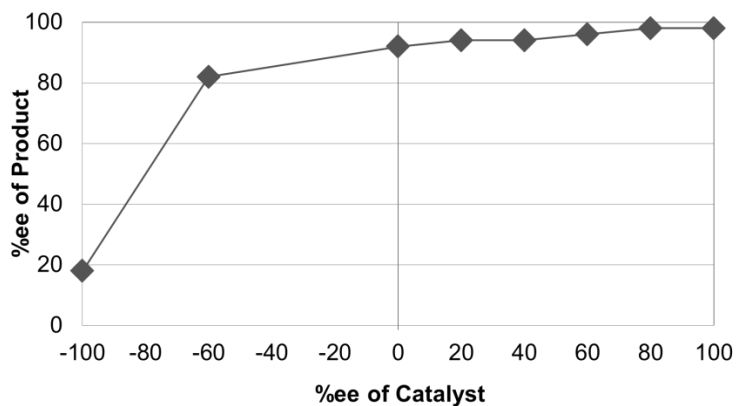


Figure 3. 9. Linear effects study using enantiopure (*S,S*)-oxaziridine

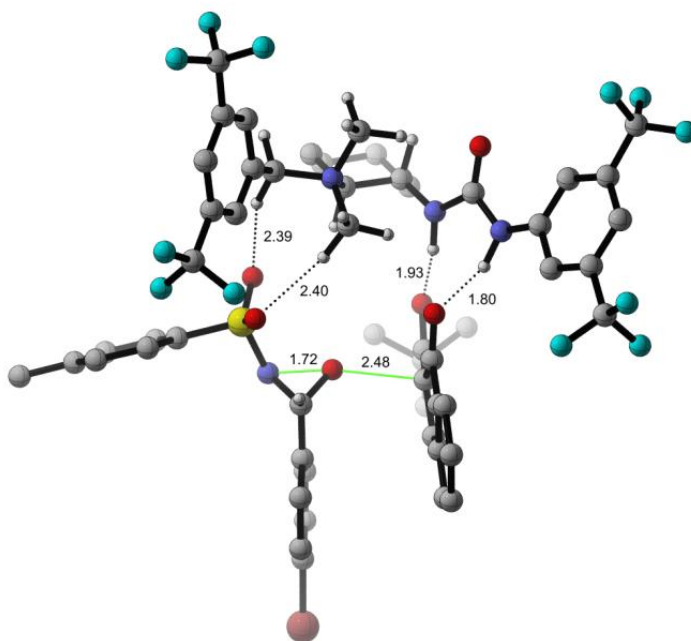


Figure 3. 10. Mis-matched oxaziridine/catalyst combination for the Waser hydroxylation

Upon comparison of the matched TS (Figure 3.7a) and the mis-matched TS (Figure 3.10), it can be seen that the matched TS contains a beneficial pi-stacking interaction between the enolate and the oxaziridine. This interaction is highlighted in Figure 3.11. When (*R,R*)-**41** is employed, the oxygen and nitrogen of the oxaziridine ring are still oriented in the same manner to deliver the oxygen to the enolate and coordinate the *tosyl*-group to the quaternary ammonium moiety, as shown in figure 3.11. The relative locations of the aryl-group and the proton of the oxaziridine, however, are reversed. This change results in a loss of the energetically favorable pi-stacking. The $\Delta\Delta G^\ddagger$ of these two transition states is $0.8 \text{ kcal mol}^{-1}$ in favor of the matched TS which would account for the observed preferential reactivity.

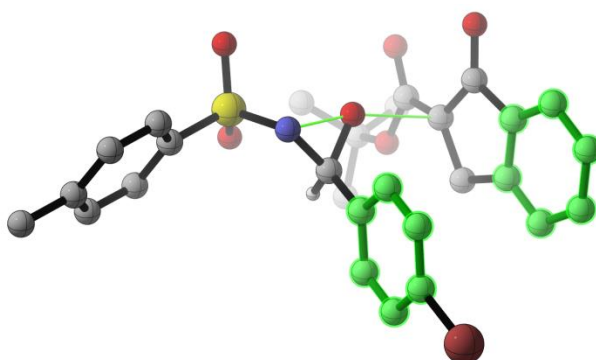


Figure 3. 11. Highlighted pi-stacking in the match case of oxaziridine and product

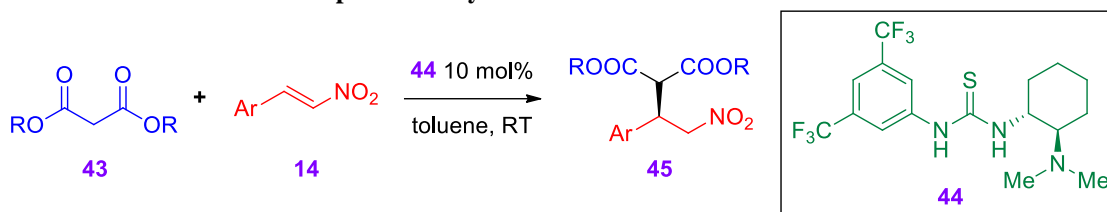
CONCLUSIONS Kinetic studies in the form of a linear effects study, coupled with a systematic DFT investigation led to the understanding of this new reaction and the observed kinetic resolution. As with the fluorination example, this different catalyst and different electrophile prefer the same binding mode for the lowest energy confirmation: coordinating the hydrogen atoms of the urea moiety to the enolate while the α -hydrogens of the quaternary ammonium coordinate to the electrophile. The different shapes of the

electrophiles lead to some subtle differences in the overall geometry, but the general understanding remains the same and can likely be extrapolated to similar systems.

3.2 Isotope Effects Reveal Transition State of Bifunctional Thiourea-tertiary Amine-catalyzed Michael Addition

INTRODUCTION In CHAPTER 3.1, the acidic hydrogen atoms in the α -position of a quaternary ammonium group were used in dual coordination with the urea moiety of the catalyst. Here, we look at a tertiary amine-thiourea catalyst. In this case, the tertiary amine moiety can act as a Brønsted base. This activates one of the substrates, and creates a polar N^+-H bond that can serve as a potent hydrogen-bond donor. This particular class of catalysts was introduced by Takemoto and co-workers in 2003 and was demonstrated to catalyze the Michael addition of malonates (**43**) to nitro-olefins (**14**).¹²⁵ The final, most promising, iteration of catalyst was **44** with a 3,5-bis(trifluoromethyl)phenyl group attached to one side of the thiourea core and a chiral scaffold barring the tertiary amine on the other. The reaction, at room temperature in toluene, boasted yields and enantiomeric excesses >90% for most substrates. Since its inception, Takemoto's catalyst has gone on to prove successful at catalyzing a myriad of reactions including the aza-Henry reaction²⁵², dynamic kinetic resolution of azlactones²⁵³, Michael addition to α,β -unsaturated imides²⁵⁴, aldol reactions²⁵⁵, sp^2 -alkylations²⁵⁶, and *spiro*-ketal formation²⁵⁷, as well as many others.

Scheme 3. 4. Michael reaction published by Takemoto and co-workers



Almost 1,000 citations have followed Takemoto's original report. Despite this extensive scrutiny, the mechanism and exact understanding of this bi-functional activation still remains a point of argument.^{258–260} Takemoto's proposed mechanism is shown in Figure 3.13. Deprotonation of **43** by the tertiary amine moiety of **44** leads to an enolate-protonated catalyst ion-pair intermediate. The now protonated catalyst has been activated for coordination. The next step in the mechanism is the Michael addition to the α -carbon of the nitro-olefin **14** forming the C–C bond. Finally, the Michael adduct **46** deprotonates the tertiary amine to yield product **45** and effect catalyst turnover.

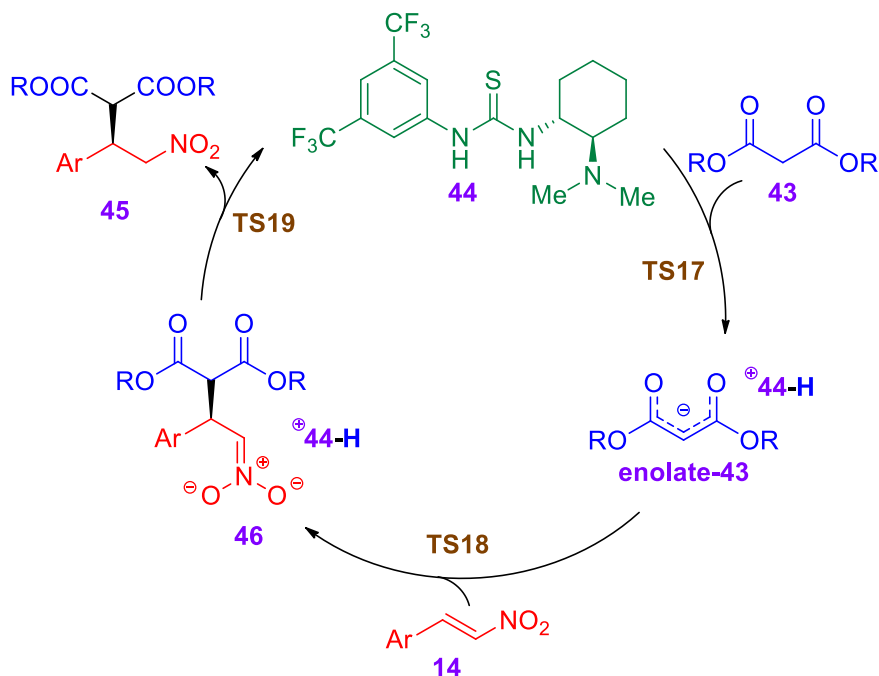


Figure 3. 12. Takemoto's proposed catalytic cycle

Two major “binding modes” have been suggested in the literature regarding the method of activation of these substrates for the Michael addition. Bind Mode A (**BMA**) involves the thiourea hydrogens coordinating to the nitroolefin, and the protonated tertiary amine coordinating to the malonate. Binding Mode B (**BMB**) reverses the locations of the two substrates activating the malonate with the thiourea moiety and the nitroolefin with the amine.

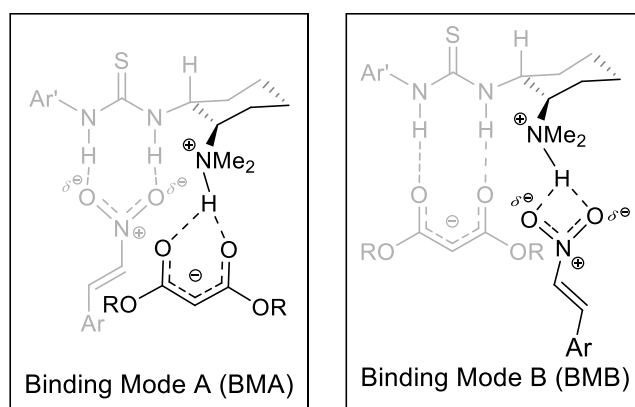


Figure 3.13. Proposed binding modes A and B

In order to support his proposed mechanism, Takemoto and co-workers performed kinetic studies in 2005.²⁵⁸ The authors observed that the reaction is first order in **43**, **14**, and **44**, suggesting that the rate-determining step involves all three species. This study was followed by two computational studies. The first, in 2006, by Liu and co-workers utilized truncations of both the nitro-olefin and the catalyst to build an energy profile of the reaction.²⁶¹ The authors concluded that the proton transfer to the nitronate-carbon is the rate-determining step. It is assessed that protonation at the oxygen is lower in energy, but the tautomerization event to yield the final product is too high in energy to consider the pathway. Unfortunately, the geometry for the tautomerization event is not supplied by the authors, and no mention of the step is given to confirm the findings.²⁶¹ Later that year,

Pápai and co-workers published a conflicting account.²⁵⁹ The authors contest Takemoto and Liu's proposal that **BMA** is preferred by computationally showing that **BMB** is lower in energy by 2.7 kcal mol⁻¹. Furthermore, the group's calculations support the assessment that carbon-carbon bond formation is the rate-determining step.

The interest that Takemoto's original paper has elicited, combined with the widespread use of bifunctional thiourea catalysts, gives sufficient cause for greater understanding of this reaction mechanism. In an attempt to settle the aforementioned debates, we again turned to the combination of experimental and theoretical carbon-13 kinetic isotope effects (KIEs). Herein are the results garnered from our study which led to a high-resolution picture of the transition state at the rate-determining step of the reaction.

¹³C KIEs: MEASUREMENT AND QUALITATIVE INTERPRETATION To study this mechanism, the reaction of **43a**, **14a**, and **44** was chosen as a prototypical reaction. Using the same methodology discussed earlier, the KIEs were measured. As shown in Figure 3.15, a 3% normal isotope effect was observed on the α -carbon of **43a**. This suggests that the first irreversible step for this substrate must involve a bond change at this carbon. Based on the mechanism proposed in Figure 3.13, this suggests that the first irreversible step for **43a** is either deprotonation from a ketone species to form the enolate (**TS17**), or C–C bond formation (**TS18**). Also observed was a 3% normal isotope effect on the α -carbon of **14a** the only step in which this carbon is involved is C–C bond formation. With these data in hand, the scenario proposed by Liu and co-workers involving rate-determining protonation of the nitronate carbon can be ruled out. If this was the case, a normal isotope effect would be expected on the β -carbon of **14a**.

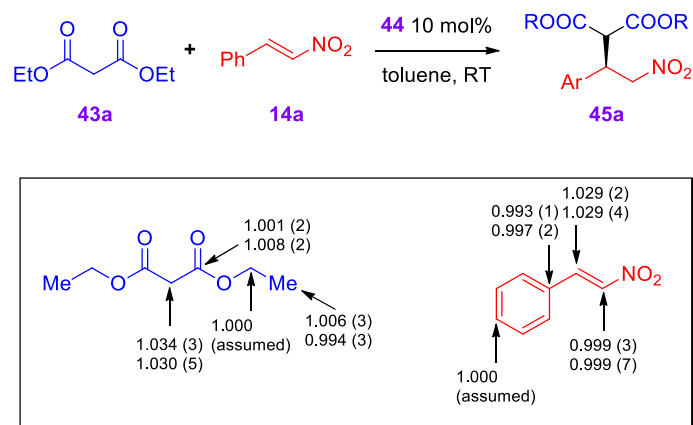


Figure 3. 14. Experimental reaction conditions and measured KIEs

THEORETICAL INVESTIGATION In order to lend further understanding to this reaction, theoretical calculations were carried out and KIEs were predicted for all major steps in the reaction. The entire system was modeled and optimized, without any truncations, at the B3LYP/6-31+G** level of theory employing a polarizable continuum solvent model for toluene (the reaction solvent) as implemented by *Gaussian09*, and KIEs were obtained from the scaled vibrational frequencies using the *ISOEFF98* software package.^{185–190,205,262}

It stands to reason that **TS17**, the deprotonation of **43a** can occur from two separate species: (i) the ketone form; (ii) the enol form. In either case, the secondary amine on the catalyst is employed as the base, and the urea moiety is used to coordinate to the uninvolved oxygen atom(s). Using the DFT method from above, these two transition states were located. Deprotonation from the enol form of the malonate (**TS17_{O-deprot}**) proved to be 1.9 kcal mol⁻¹ lower in energy than from the ketone form (**TS17_{C-deprot}**). On the basis of energetics at room temperature (reaction temperature), this suggests that the enol form is approximately 25 times more likely to be deprotonated.

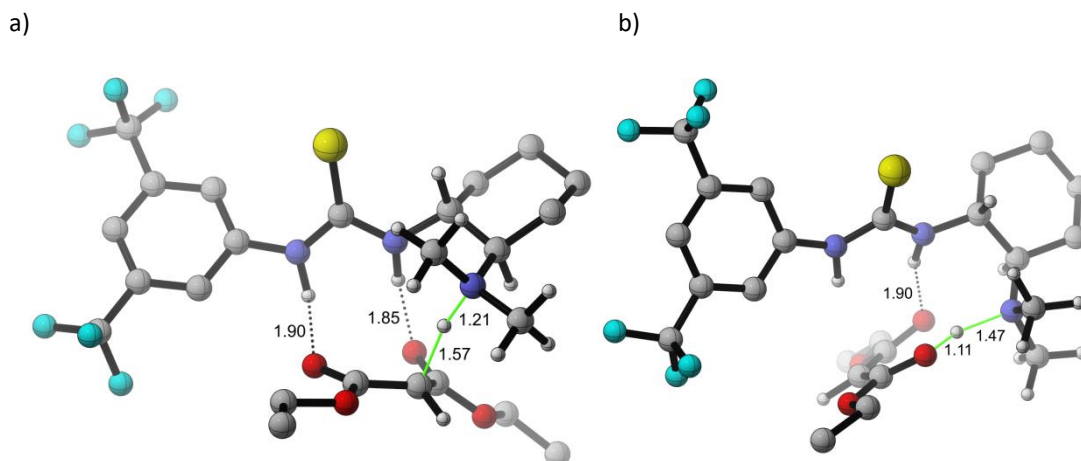


Figure 3. 15. Two methods of deprotonation investigated; (a) C-deprotonation; (b) O-deprotonation

The KIEs were calculated for both transition states and led to the typical observance of a small, albeit non-unity, isotope effect on the α -carbon for **TS17_{C-deprot}** and a similar isotope effect on the β -carbon for **TS17_{O-deprot}**. Both of these predictions are incongruent with the measured isotope effect and allow us to consequently discredit **TS17** as the rate-determining step.

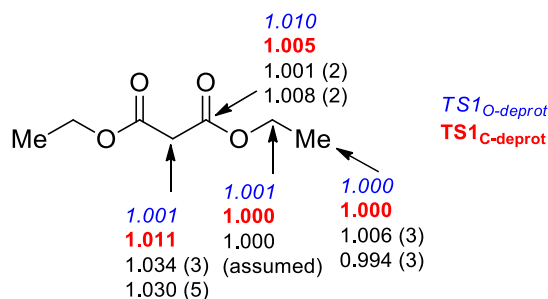


Figure 3. 16. Predicted KIEs for TS17 (blue *italic* numbers represent predicted KIEs for **TS17_{O-deprot}; red **bold** numbers represent predicted KIEs for **TS17_{C-deprot}**; black Arial numbers represent measured KIEs)**

With regards to **TS18**, both **BMA** and **BMB** were examined using the above method and both enantiomers of product were modeled. To ensure that a complete search of the potential energy surface was conducted, the quantum mechanical method DFTB with

the Slater-Koster parameters was employed to run simulations from several of the lowest energy transition structures for both the major and minor enantiomers.^{263–265} A third binding mode was located through this method reminiscent of **BMA** (**BMC**). Unlike **BMA**, in **BMC** the proton on the tertiary amine, as well as the protons of the thiourea moiety, coordinate to the nitroolefin. The protons on the methyl groups of tertiary amine are involved in a hydrogen bond network to activate the malonate. From our sampling, **BMC** proved to be the most favored by more than 1.3 kcal mol⁻¹ for the major enantiomer (Figure 3.18).

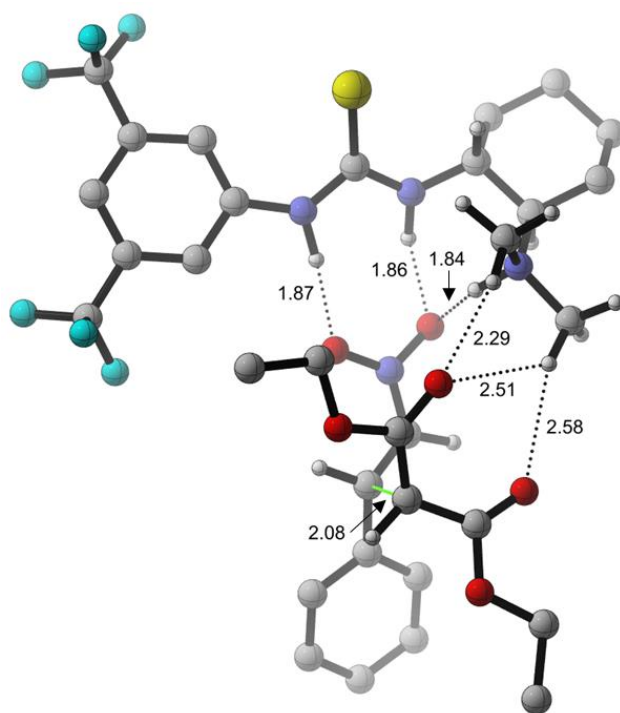


Figure 3. 17. Calculated transition states leading to the major enantiomer of product *via* BMC

This mode of activation was not as easily accessible to the minor enantiomer transition state owing to the fact that the malonate could not be appropriately aligned with the methyl-groups' hydrogen atoms. Throughout the simulations, a new binding mode was located and proved to be lower in energy than either of the three previously proposed

configurations for the minor enantiomer. In this new orientation (**BMD**), the thiourea moiety is split, one side activating one of the oxygens on the nitroolefin, and one activating the malonate. The proton on the tertiary amine is coordinated to the second oxygen of the nitroolefin, and two α -protons to the amine are coordinated to the second oxygen of the malonate (Figure 3.19). This binding mode presents a transition state that is 2.2 kcal mol⁻¹ higher in energy than the major enantiomer. At room temperature, this corresponds to an enantioexcess of 96% which is in excellent agreement with the observed enantioselectivity of 93%.

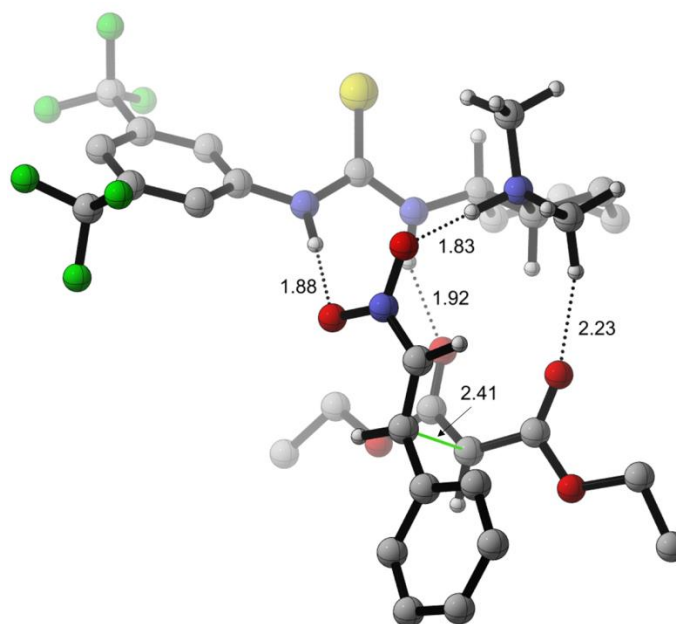


Figure 3. 18. Calculated transition states leading to the minor enantiomer of product via BMD

Normal isotope effects are predicted for the α -carbon of both substrates (Figure 3.19). The 3.5% isotope effect is a slight over estimation of the measured value. This is likely due to how late the transition state is in Figure 3.17 ($r_{C-C} = 2.08 \text{ \AA}$). It can be noted that the minor enantiomer TS (Figure 3.18) is much earlier ($r_{C-C} = 2.41 \text{ \AA}$). This would lead to a much smaller isotope effect. The experimentally observed isotope effect is a

composite of all transition states and would therefore be lower than that predicted for just the TS in Figure 3.17. Regardless, the prediction is in good qualitative agreement with the measured value.

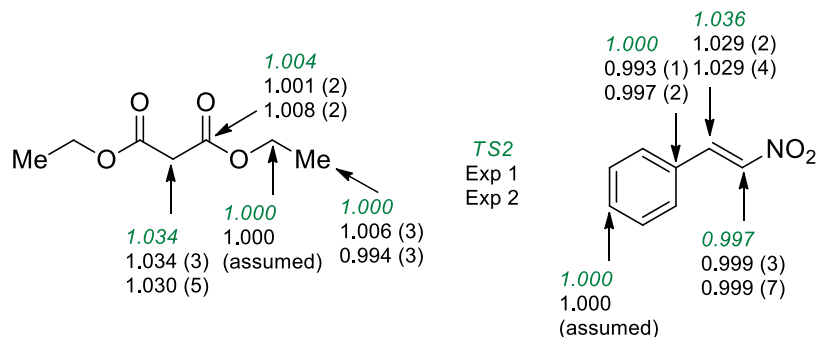


Figure 3. 19. Predicted KIEs for TS2 (green *italic* numbers represent predicted KIEs for TS2; black Arial numbers represent measured KIEs)

Next, our attention turned to TS19. As with TS17, TS19 could plausibly proceed through two separate transition states: (i) protonation of the nitronate carbon to form product; (ii) protonation of the nitronate oxygen and then subsequent tautomerization to form product (Figure 3.20). It is this first scenario (TS19_{C-prot}) which Liu and co-workers suggest is the rate-determining step. Whereas our calculated energies do follow the same trend as theirs, and we confirm that this scenario is higher in energy than the alternative (TS19_{O-prot}), we do not find it likely that any tautomerization event could make up for the energy gap between these two pathways. Regardless, we may rely on our predicted KIEs to support the nature of the rate-determining step. Theoretical KIEs were predicted for each of these transition states and the results again disagree with the measured values. Unity isotope effects are predicted for all carbon atoms on 43a, and only in the case of TS19_{C-prot} is a normal KIE predicted for any carbon on 14a. This prediction is a 2% KIE on the

β -carbon which does not agree with the observed unity measurement at this location (Figure 3.21).

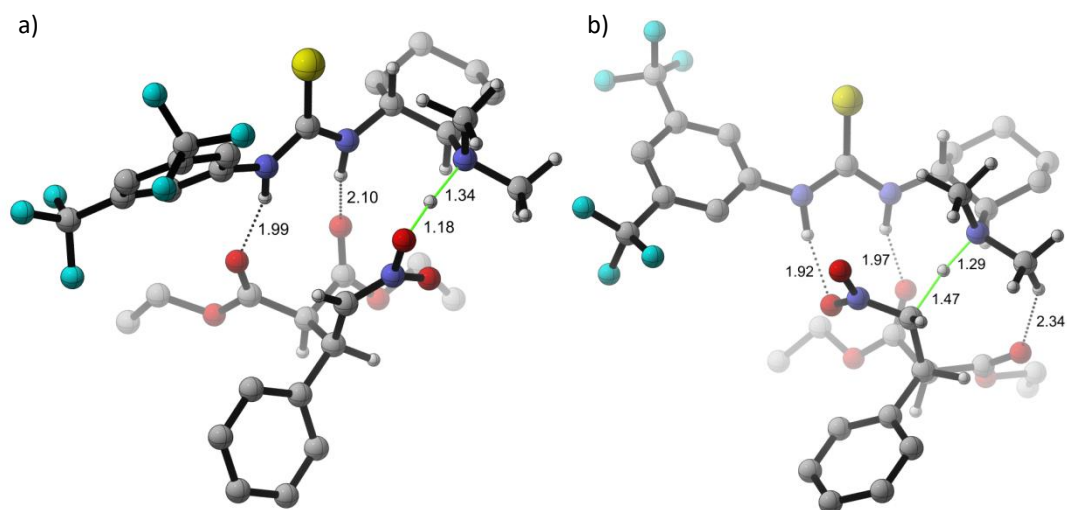


Figure 3. 20. Lowest energy geometries for TS19 via (a) O-protonation; (b) C-protonation

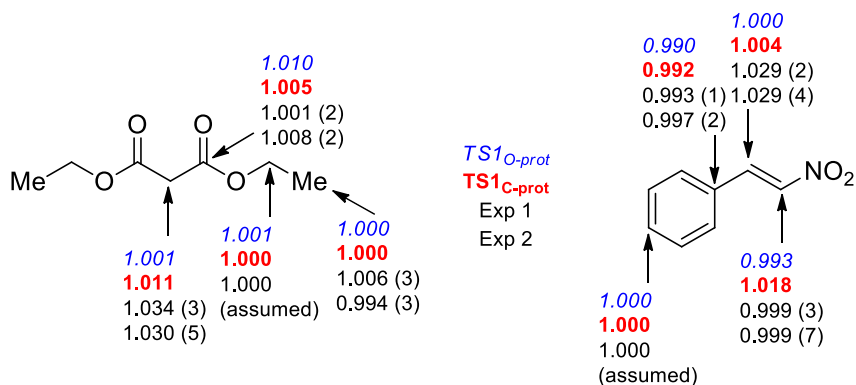


Figure 3. 21. Predicted KIEs for TS19 (blue *italic* numbers represent predicted KIEs for TS1_{O-prot}; red **bold** numbers represent predicted KIEs for TS1_{C-prot}; black Arial numbers represent measured KIEs)

CONCLUSION Here we have reported a new insight into a widely used reaction. The bifunctional tertiary amine/thiourea catalyzed Michael addition of malonates to nitroolefins helped pave the way for a new method of catalysis. Since then, many groups have studied the reaction, but conclusions conflicted. With our combined KIE and DFT

study, we have been able to disprove the claims that the final protonation is rate-determining, and discover a new binding mode that accounts for the observed enantioselectivity in the reaction.

3.3 A DFT investigation of borox catalyzed aziridination

INTRODUCTION Thus far, we have only discussed bifunctional non-covalent catalysis. Our group has also done work in the field of Brønsted Acid catalysis.²⁶⁶ The heart of this work came from a collaboration with the Wulff group from Michigan State University. BINOL has been proven to be a very effective ligand in both transition metal catalysis and organocatalysis.^{267,268} The use of BINOL (**47a**), as a ligand, however, is notorious for giving low enantioselectivity. The reasoning behind this is that the “chiral pocket,” that is the space where the chiral information of the molecule is conveyed, is displaced from the reactive center. This hurdle is frequently overcome by the ornamentation of the 3- and 3'-positions of the molecule.²⁶⁹

In 1993, the Wulff group introduced a new family of ligands for boron-catalysis.²⁷⁰ These “vaulted” ligands (Figure 3.22) present a similar reactivity to the classic BINOL scaffold, but the chiral pocket was now focused around the center of reactivity. Amongst the numerous reactions that these ligands have proven to effect (see citations in ref [²⁶⁶]), the aziridination of imines (**50**) with diazo compounds (**51**) is possibly the most notable.²⁷¹ As expected, VANOL (**48**) and VAPOL (**49**) provide highly improved enantio- and diastereoselectivity over BINOL and 3,3'-substituted BINOL. Previous work by the Wulff group established a thorough understanding of the mechanism with the vaulted ligands, but not nearly as much research had been conducted to understand how BINOL derivatives catalyze this reaction.^{272,273} A collaborative effort was undertaken between the Veticatt

Group and the Wulff group to shed more light on the use of BINOL to catalyze this reaction.

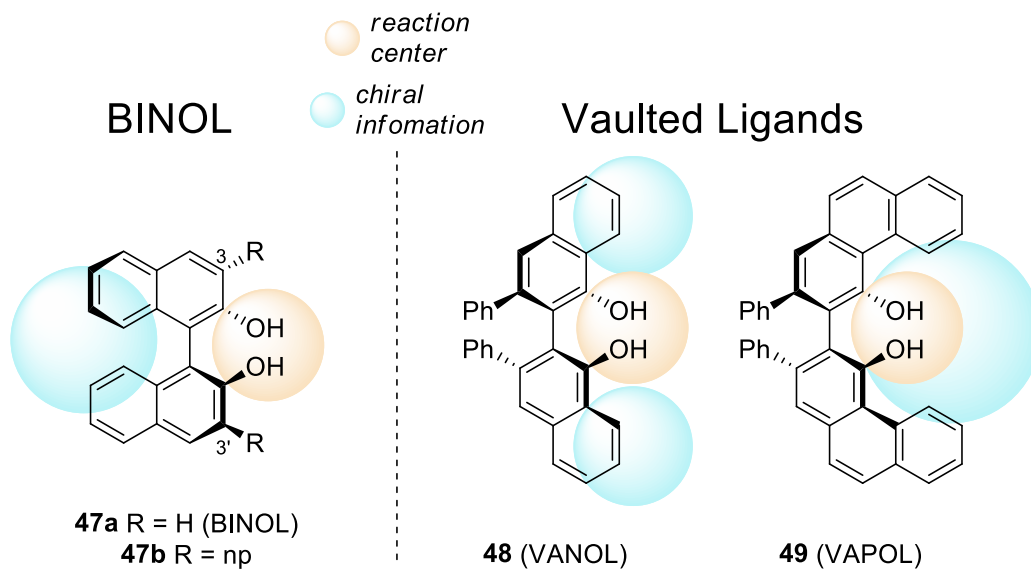
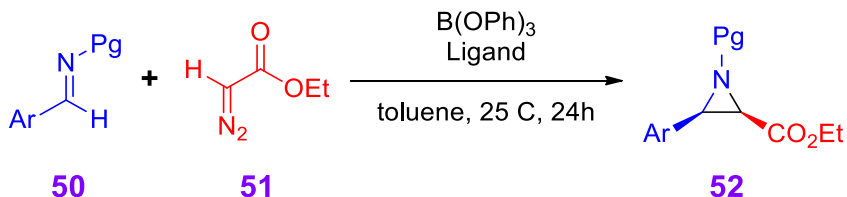


Figure 3. 22. BINOL and vaulted ligands

Scheme 3. 5. Wulff aziridination



The assumption was made that the reaction would progress the same way for the BINOL system as it does for the VAPOL system. This is depicted in Figure 3.23. The group found that the best way to effect this transformation was to heat B(OPh)_3 with the ligand for one hour, then remove all volatiles under vacuum. This process yielded what was considered the “pre-catalyst” (H-X^* in Figure 3.23). In catalysis, the pre-catalyst acts as a Brønsted acid and delivers a proton to the imine substrate, **50**. The X^{*-} and $\text{50}\cdot\text{H}^+$ then form a hydrogen-bonded ion-pair complex. This complex activates the imine for nucleophilic attack by the diazoacetate, **51** (**TS20**) resulting in the formation of **53**, the

diazonium ion. Rotation about the newly formed σ -bond orients the molecule for S_N2 displacement of diatomic nitrogen by the nitrogen originally of the imine (**TS21**). After this ring-closure, the proton on the nitrogen is lost to yield the product aziridine **7** and regenerate the pre-catalyst.

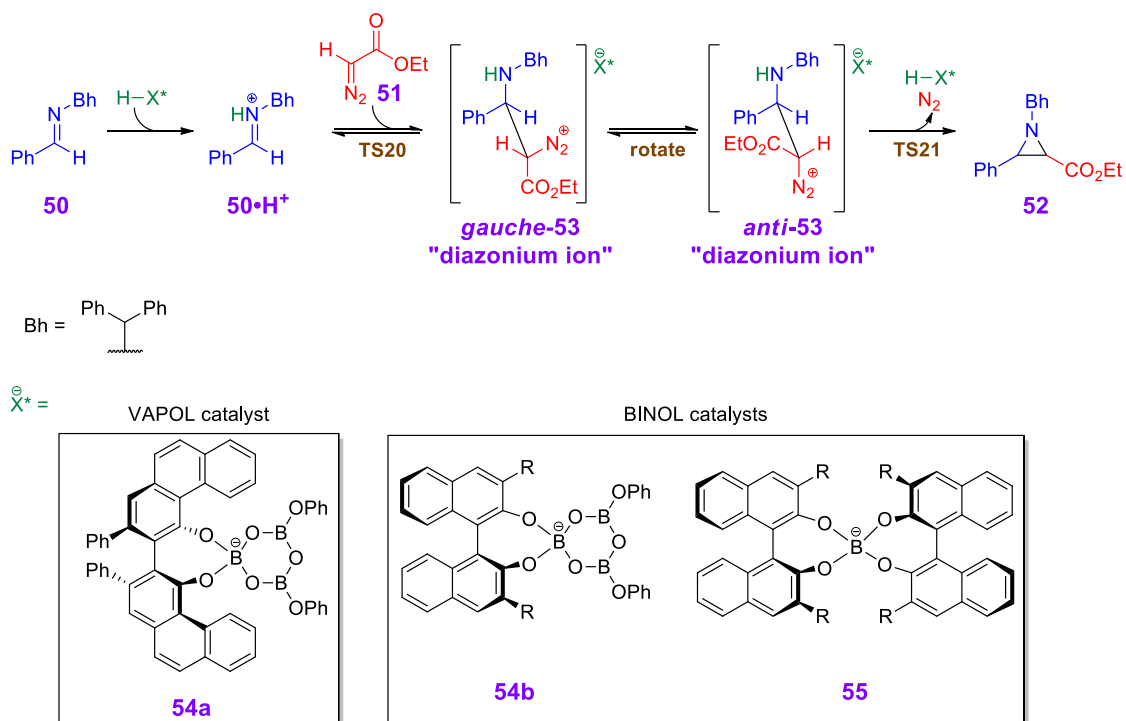


Figure 3. 23. Reaction mechanism for the Brønsted Acid catalyzed aziridination of imines with diazo compounds

When the vaulted ligands are used in this process, the sole catalytic species is boroxinate **54a**.²⁷² The supposition was made that BINOL would react similarly. Crystallographic and spectroscopic studies, conducted by the Wulff group, revealed that this is an erroneous conclusion. Instead, two catalytic species were observed: boroxinate **54b** (akin to the vaulted catalyst) and *spiro*-borate **55**. We then undertook a computational study of the reaction with the goal of understanding the duality of catalysis to gain a deeper understanding of the reaction.

COMPUTATIONAL INVESTIGATION Both facial attacks of **TS20** (*Re*-**TS20** and *Si*-**TS20**) and both possible ring-closure events (*Re*-**TS21** and *Si*-**TS21**) leading to **52** were modeled for both catalysts at the B3LYP/6-31G* level of theory as implemented by the *Gaussian09* software package.^{185–188,205} In the case of the system employing **54b** as well as that employing **55** as catalyst, *Si*-**TS20** proved to be lower in energy than *Re*-**TS20**. The optimized geometries of these TSs are shown in Figure 3.24.

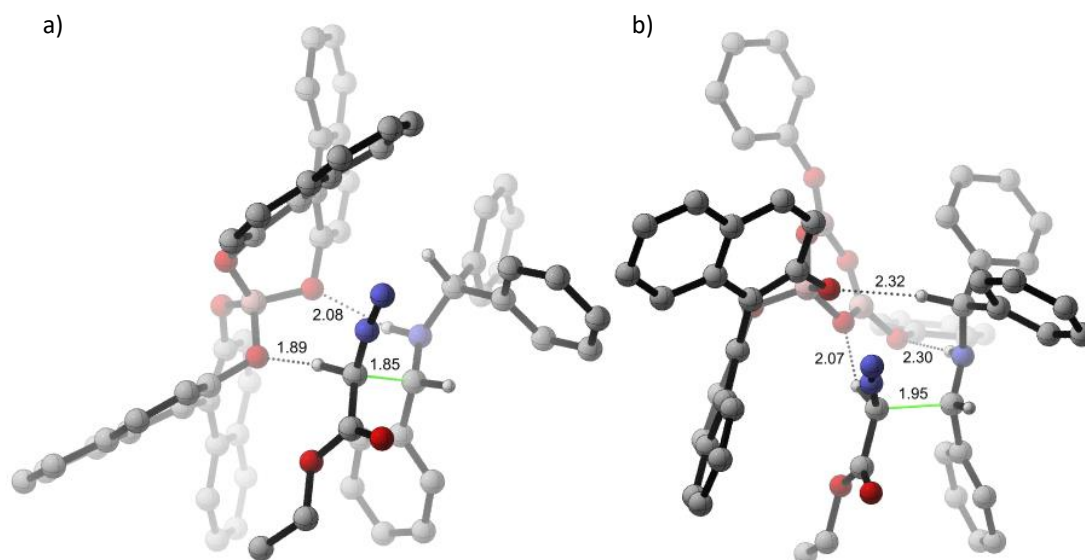


Figure 3. 24. Lowest energy TSs for *Si*-**TS1** employing (a) *spiro*-borate **9**; (b) boroxinate **8b** as catalyst

In the case of the system employing *spiro*-catalyst **55**, the ring closure from the intermediated generated after *si*-face attack was determined to be lower than that from *re*-face attack. This suggests that, when **55** acts as the catalyst, product (*S,S*)-**52** would be preferred. The enantioselectivity would be derived from the $\Delta\Delta G^\ddagger$ of *Si*-**TS21** and *Re*-**TS21**. (Figure 3.25a). When boroxinate **54b** is utilized as the catalyst, *Si*-**TS21** was higher than all other predicted transition states. (Figure 3.25b). This suggests that *si*-face attack is faster, but reversible, causing the major product to be (*R,R*)-**52** and the enantioselectivity

derived from the $\Delta\Delta G^\ddagger$ of *Re*-**TS20** and *Si*-**TS21**. This finding suggests that the observed poor selectivity of BINOL, for this reaction, is *not* due to the chiral information being removed from the reactive pocket, but from the two competing catalysts leading to opposite enantiomers of product.

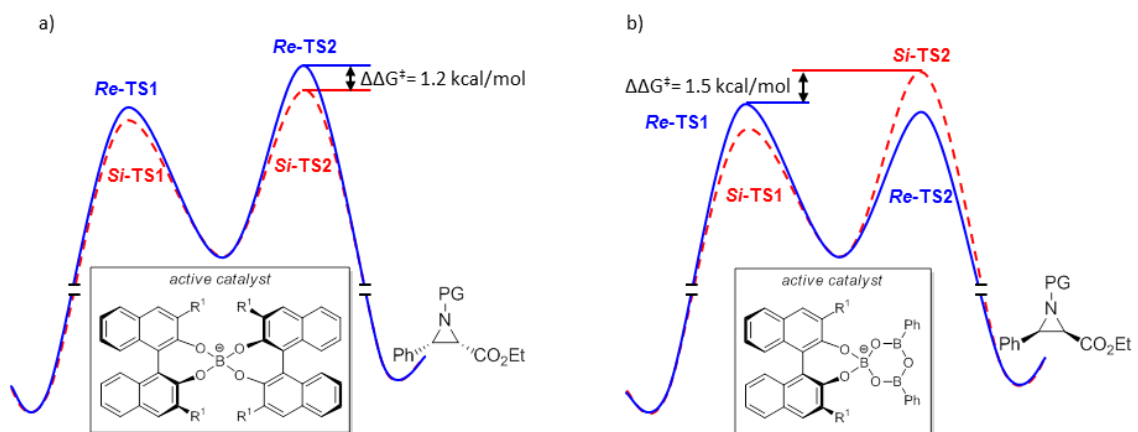


Figure 3. 25. Energy diagrams regarding the title system catalyzed by (a) 55; (b) 54b

Our analysis then turned to better understand the origin of this reversal in enantioselectivity. A non-classical hydrogen-bond between the benzhydryl CH and one of the oxygen atoms of BINOL in the **54b**-catalyzed *Re*-**TS21** of 2.41Å was identified (Figure 3.26). This hydrogen atom is acidic due to its proximity to two aromatic rings, and can easily form a non-classical hydrogen-bond with the negative oxygen atom of the catalyst. This interaction is missing in the analogous TS for the **55**-catalyzed system likely causing the observed change in the energy profile.

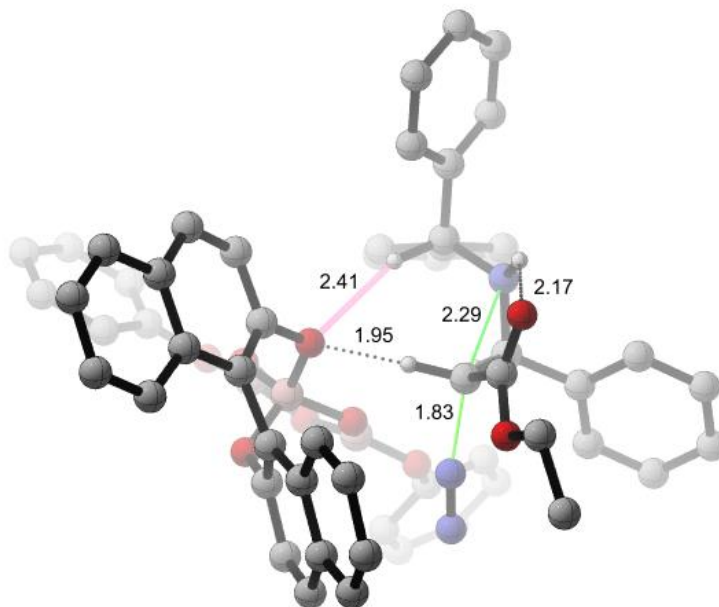


Figure 3. 26. Lowest energy TS for *Re*-TS2 employing boroxinate **8b** as catalyst; critical CH-O interaction highlighted in pink

It should be noted that the $\Delta\Delta G^\ddagger$ of *Re*-TS20 and *Si*-TS21 is 1.5 kcal mol⁻¹ which corresponds to a predicted selectivity of 89% ee at room temperature. If boroxinate catalyst **55** could be exclusively formed, it stands to be a very selective catalyst, rivaling those derived from the vaulted ligands. Furthermore, it can be suggested that a protecting group analogous to the benzhydryl group but substituted with electron withdrawing substituents could make the methine proton more acidic and increase the strength of the hydrogen bond leading to an even greater selectivity.

CONCLUSION Our computational study of this system lent a great deal of understanding to the work done by our collaborators. The identification of the presence of two different catalysts led us to model all relevant transition states for *both* catalytic systems and derive that the origin of poor selectivity, for the boron-catalyzed aziridination of imines with diazo compounds with BINOL, is *not* due to the lack of chiral information

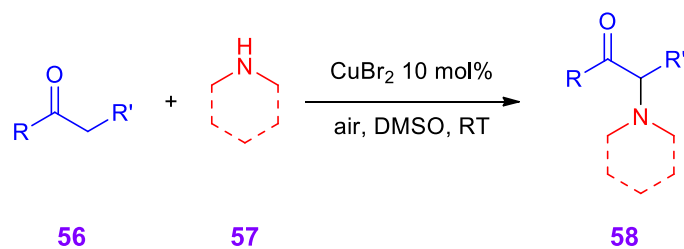
at the reaction center, but the fact that the two different catalysts generate conflicting enantiomers. A non-classical hydrogen-bond was located to rationalize this change and may be exploited in further work to improve this reaction.

CHAPTER IV: TRANSITION METAL CATALYZED REACTIONS

4.1 Isotope Effects Reveal Presence of Cu^{III} Intermediate in α -Amination Reaction

INTRODUCTION The synthesis of α -amino carbonyls is an important process in the pharmaceutical industry.^{274–276} Traditional methods for the preparation of these substrates come from reacting the nucleophilic α -carbon with an electrophilic amine. These methods frequently result in requiring further steps to obtain the actually desired α -amino carbonyl compound.^{82,277–281} Recently, work has been done to use nitrogen nucleophiles to yield the desired product directly.²⁸² In 2013, MacMillan and co-workers presented an elegant methodology to access these synthons using copper(II) bromide to catalyze the addition of nucleophilic nitrogen containing cyclic and acyclic amines to the α -position of esters, ketones, and aldehydes.²⁸³

Scheme 4. 1. MacMillan's α -amination reaction



The authors propose two possible mechanisms for their reaction (Figure 4.1). The first explains the use of the copper catalyst to promote bromination at the α -position of carbonyl compound **56** to yield an α -bromocarbonyl species. This species then undergoes a substitution reaction, **TS-S_N2**, with an amine **57** to yield product **58**. The authors' second

proposal involves the reductive elimination from a copper(III) species, **TS-RE**. This latter proposal was discredited in the manuscript based on the observed poor catalytic activity of copper(II) salts lacking bromine.²⁸³ Herein, we present an argument for the reductive elimination TS using experimentally measured and theoretically predicted kinetic isotope effects (KIEs) along with synthetic organic probes as a part of a collaboration with Professor Sherry Chemler's lab at The State University of New York at Buffalo.

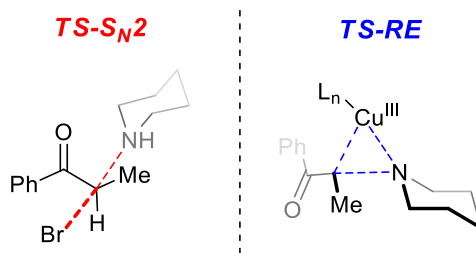
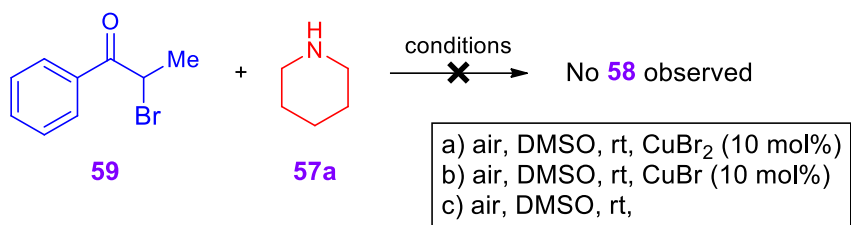


Figure 4. 1. Proposed key transition states of the two mechanisms proposed by MacMillan and co-workers

RESULTS AND DISCUSSION We performed control reactions using α -bromopropiophenone, **59**, and piperidine, **57a**, under three different conditions in order to test the competency an α -bromocarbonyl species in the title reaction (Scheme 4.2). After 24hrs, no product was observed. If **TS-S_N2** was the active pathway, then the pre-formed intermediate should be able to yield product. This leads us to question the validity of the presence of such a species in the catalytic cycle. The reaction between **59** and secondary amines has been shown to be successful under different conditions.²⁸⁴ However, in our hands, and, more importantly, under MacMillan's conditions, we see no reactivity. Sharley *et al.* showed these conditions to be ineffective in producing an isolable α -bromocarbonyl which casts further doubt about the legitimacy of this intermediate in the catalytic cycle.²⁸⁵

Scheme 4. 2. Control reactions used to test TS-S_N2



To obtain a clearer picture of the reaction, KIEs were measured, for the reaction of **56a** and **57a**, using ¹³C NMR methodology at natural abundance (Figure 4.2).¹⁴⁰ The ~1.5% carbon-13 KIE on the α-carbon is qualitatively consistent with a bond change occurring at that position at the first irreversible step for **56a**. Qualitatively, this is consistent with both **TS-S_N2** and **TS-RE** being the RDS, therefore a computational investigation was required.

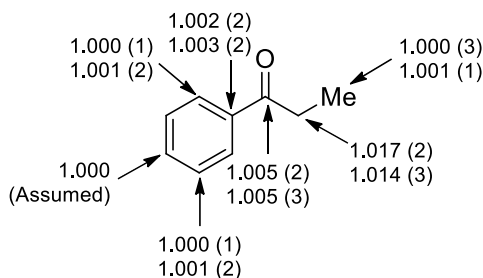
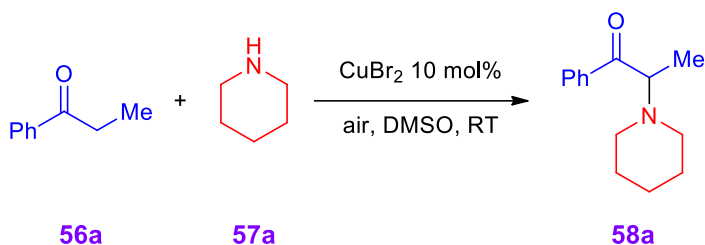


Figure 4. 2. Experimentally measured ¹³C KIEs and reaction

QUANTITATIVE INTERPRETATION OF KIEs Predicted KIEs for fully rate-limiting S_N2 displacement were based on transition structures located using the M06-2X functional²⁸⁶ with a Grimme D3 dispersion correction²⁰⁶, and the polarizable continuum model²⁶² for dimethylsulfoxide (DMSO). The SDD basis set²⁸⁷ was used for bromine and

the 6-31+G** basis set¹⁸⁸ was used for all other atoms. As before, transition state calculations were carried out using *Gaussian '09*, the isotope effects were calculated from scaled frequencies using *ISOEFF98*, and an infinite parabola tunneling correction was applied to the predicted KIEs.^{159,189,190,205} The geometry and predicted KIEs are shown in Figure 4.3. The predicted KIEs are in disagreement with the measured values. Although, qualitatively, a normal isotope effect is observed on the α -carbon, the prediction suggests that, if **TS-S_N2** was the operational mechanism, the observed value should be ~7% instead of the ~1.5% seen experimentally.

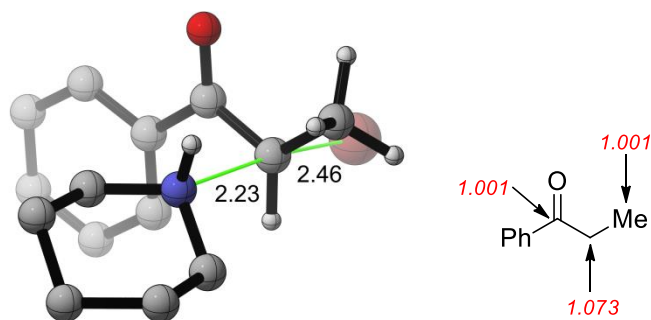


Figure 4. 3. DFT optimized TS-S_N2 and predicted KIEs

This piece of evidence disproves the notion that **TS-S_N2** is the rate-determining step, but it does *not* rule out the entire pathway as suggested by MacMillan and co-workers. In MacMillan's proposed mechanism, the ketone is first converted to an enolate. The deprotonation event *would* involve the α -carbon and could, therefore, rationalize the measured KIEs. Using the same level of theory described above (SDD basis set on copper), this transition state (**TS-deprot**) was located and the KIEs were predicted as shown in Figure 4.4.²⁸⁷ For this transition state, the catalyst (CuBr₂) is coordinated to the carbonyl-oxygen of the ketone in order to make the α -proton more acidic, and the reaction partner, piperidine **57a**, is used as the base. These predictions suggest that deprotonation would

provide a KIE much smaller than that experimentally observed. This refutes deprotonation as the RDS and, consequentially, allows for the rejection of the mechanism favored by MacMillan and co-workers.

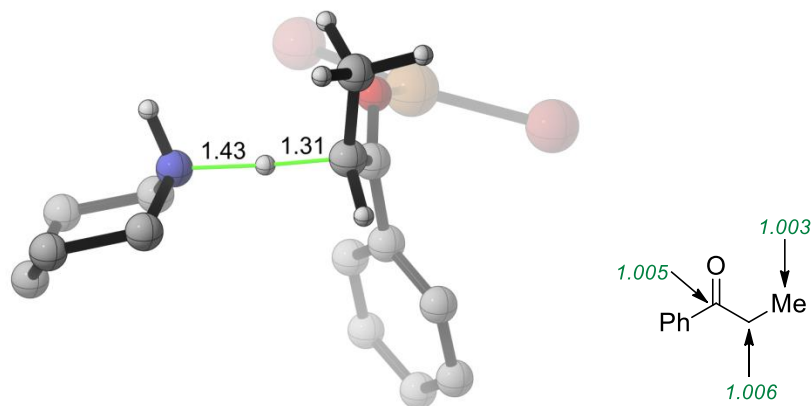


Figure 4. 4. DFT optimized TS-deprot and predicted KIEs

With the **TS-S_N2** mechanism disproven, our focus shifted to the second proposed mechanism: reductive elimination from Cu(III) (Figure 3.27a). The Cu(III) mechanism would likely begin similarly to the S_N2 mechanism with coordination of the ketone and subsequent deprotonation to yield the copper catalyst bound to an enolate via the oxygen atom **61_{O-enolate}**. Homolysis and consequential radical recombination would give the C-bound enolate as the ligand **61_{C-enolate}** (Figure 3.27b). This type of rearrangement has precedent in similar reactions.²⁸⁸ Coordination and deprotonation of the amine would give a copper(II) species with both substrates as ligands **62**. A second molecule of the copper catalyst could then perform a disproportionation with the substrate-bound copper to yield a copper(I) and the activated copper(III). Complex **63** can then undergo reductive elimination to provide the product and copper(I). Disproportionations and reductive eliminations from copper(III) complexes have been investigated and supported both

experimentally^{289–291} and theoretically^{292,293} in other cases. Oxidation from the acid generated during the process of the reaction and the ambient oxygen then effects catalyst turnover.

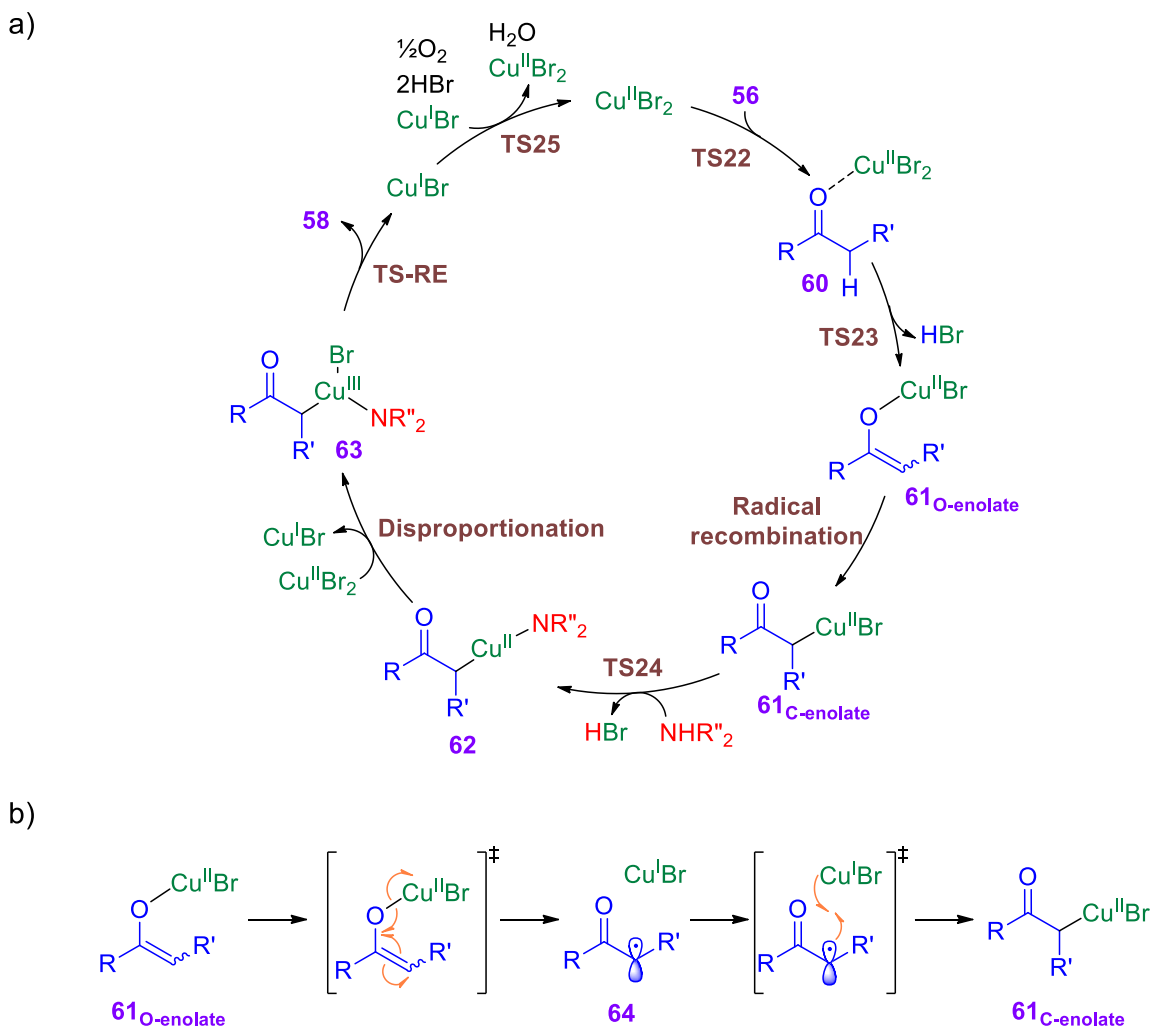


Figure 4. 5. (a) proposed catalytic cycle for MacMillan's amination reaction via copper(III) reductive elimination; (b) mechanism for radical recombination

With this proposal, the next requirement was to see if the predicted KIEs would match our experimental values. The reductive elimination **TS-RE** was therefore modeled. The geometry and predicted KIEs are shown in Figure 4.5. Due to the inherent instability

of a Cu(III) intermediate, a molecule of DMSO (the reaction solvent) was employed to coordinate to the copper. The 1.016 KIE predicted for the α -carbon is in excellent agreement with the ~1.5% KIE measured experimentally and is in following with literature KIEs for reductive eliminations from Cu(III) intermediates.²⁹⁴

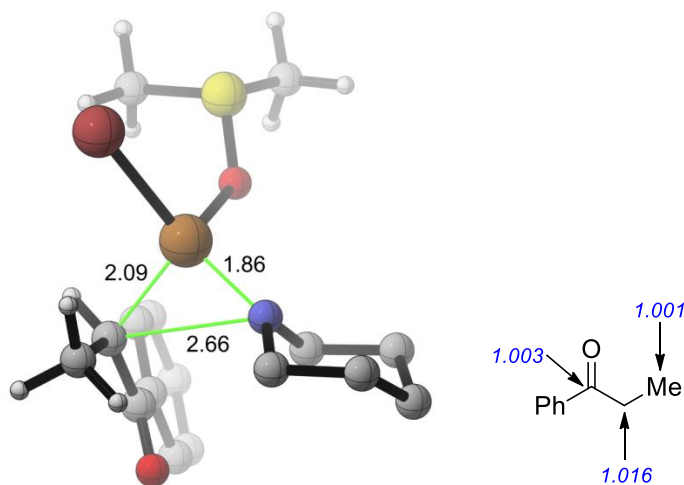
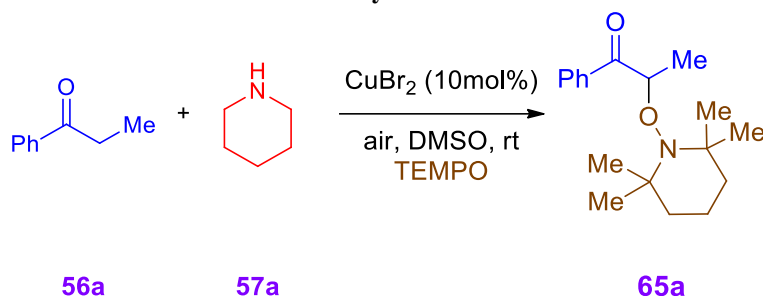


Figure 4. 6. DFT optimized TS-RE and predicted KIEs

Further support for this pathway was provided by the collaborators in the Chemler lab. The radical scavenger (2,2,6,6-Tetramethylpiperidin-1-yl)oxidanyl (TEMPO) was added to a reaction of **56a** and **57a**. The TEMPO adduct, **65a**, was isolated and characterized (Scheme 4.3). This is interpreted to be evidence of the radical intermediate and likely comes from reaction between TEMPO and **64**.

Scheme 4. 3. Evidence of radical recombination by observation of TEMPO adduct



CONCLUSION The KIEs for all proposed rate-determining steps are shown in Figure 4.7. **TS-deprot**, provided an isotope effect too low to be considered as an explanation for the observed measurements, **TS-S_N2** was too high, but the KIE predictions based on fully turnover-limiting reductive elimination, **TS-RE**, are in excellent agreement.

<u>TS</u>	<u>Carbon-1</u>	<u>Carbon-2</u>	<u>Carbon-3</u>
<i>S_N2</i>	1.001	1.073	1.001
<i>deprot</i>	1.009	1.006	1.001
<i>RE</i>	1.003	1.016	1.001
Exp1	1.005 (2)	1.017 (2)	1.000 (3)
Exp2	1.005 (3)	1.014 (3)	1.001 (1)

Figure 4. 7. Predicted and measured KIEs for the title reaction

The use of KIEs and DFT predictions have shed light on the fact that the initially proposed mechanism for copper(II) bromide-catalyzed α -amination of carbonyl-containing compounds is likely incorrect and a mechanism involving turnover-limiting reductive elimination from a copper(III) intermediate is far more likely. This is an exciting proof-of-principle for the field of copper catalysis as it stands as the first occasion evidence for a

copper(III) intermediate in a *catalytic* reaction is delivered without changing the reaction conditions.²⁹⁵

AVENUES FOR FUTURE RESEARCH Ideally, it would be proposed that, with a better understanding of the reaction, one could use the turnover-limiting step to devise an asymmetric variant of this reaction. With that idea in mind, an *in silico* study was briefly performed, in our lab. Of the chiral ligands investigated, a bidentate pyridine-oxazolidine ligand (**Ligand***) was predicted to give the highest enantioselectivity. The DFT predicted lowest energy transition states leading to the major and minor enantiomers are shown in figure 4.7a and 4.7b respectively. The calculated $\Delta\Delta G^\ddagger$ is 1.47 kcal mol⁻¹ corresponding to a predicted enantiomeric excess of 84%. The origin of this selectivity is credited to the steric interactions between the *tert*-butyl group on the catalyst and the methyl group of **56a** in the minor enantiomer transition state (highlighted in Figure 4.8). The next step in this project would be to obtain **Ligand*** and optimize reaction conditions to yield the chiral product.

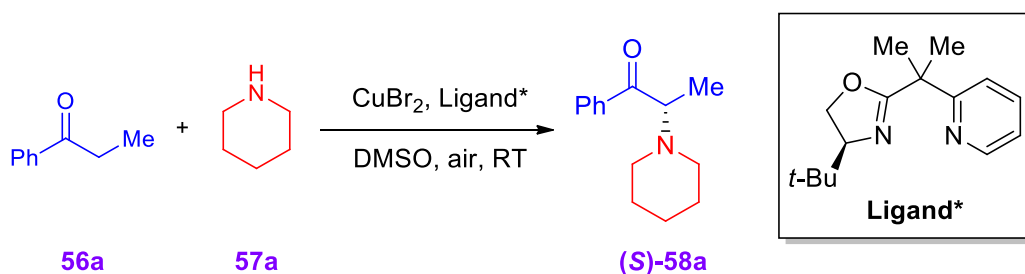
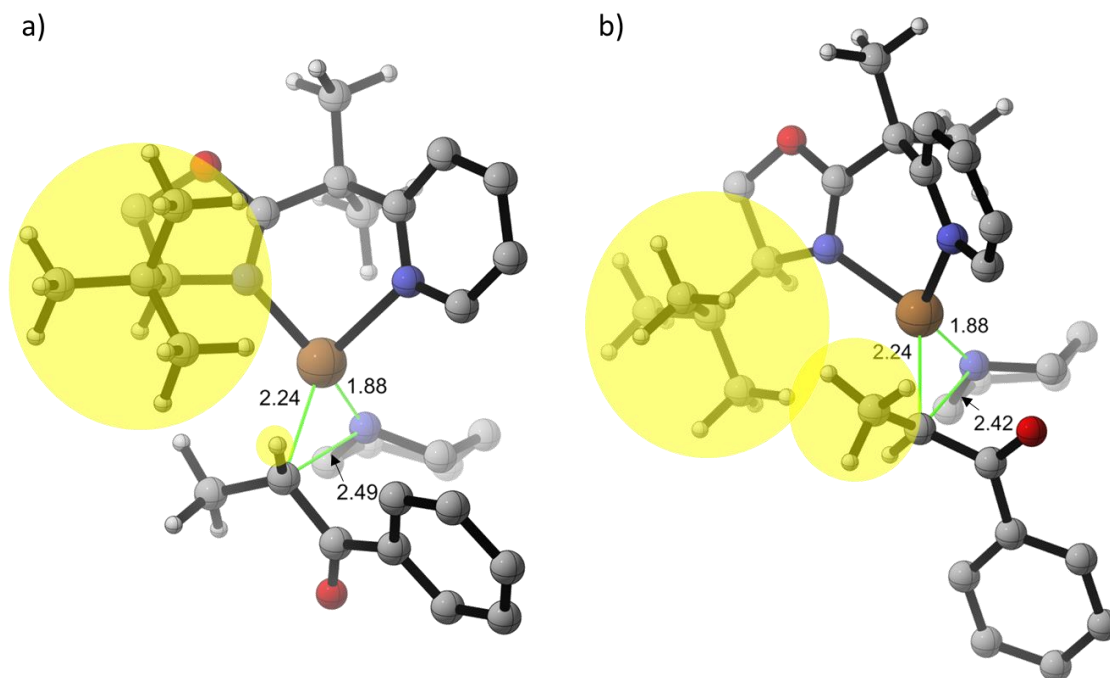


Figure 4. 8. Proposed asymmetric amination reaction



4.2 Isotope Effects Reveal Nature of Transmetalation Transition State in the Catalytic Suzuki-Miyaura Reaction

INTRODUCTION Palladium catalyzed cross-coupling reactions are among the most utilized reaction in the organic chemist's toolbox.²⁹⁶ In particular, the coupling of arylhalides, **66**, with aryl boronic acids, **67**, the "Suzuki-Miyaura reaction" stands out as the premier cross-coupling method. Its wide substrate tolerance, mild conditions, and consistent reliability have led to extensive uses in medicinal, agricultural, and synthetic chemistry.^{7,297} Numerous studies have been conducted to better understand this reaction both experimentally^{36,298-301} and theoretically³⁰²⁻³⁰⁶. Nevertheless, even over the course of forty years, a thorough understanding of the mechanism of this reaction has evaded chemists. Herein, we present a combined experimental and computational approach which allows for the elucidation a high-resolution glimpse into the nature of the species involved in the transmetalation step.

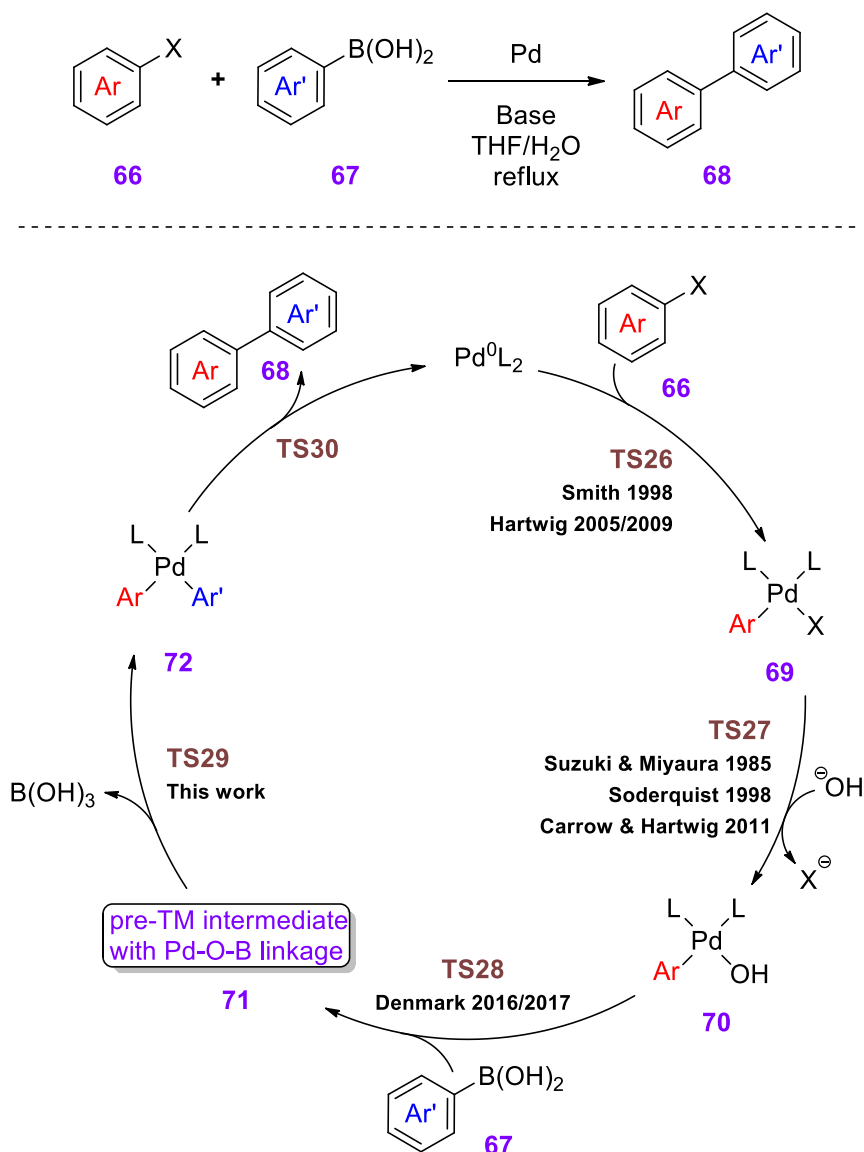


Figure 4. 10. Suzuki-Miyaura reaction and proposed catalytic cycle

Work by Smith and co-workers gave the first insight into the oxidative addition step (**TS26**) of the reaction.²⁹⁹ HPLC studies revealed that this step was the rate-determining step (RDS) when aryl bromides were the coupling partner (**67** when X=Br), but not when aryl iodides were used (**67** when X=I). These conclusions were later supported by kinetic studies with bulky ligands carried out by Hartwig and co-workers.^{307,308} The next steps in the catalytic cycle (**TS27** and **TS28**) have been a source

of the greatest amount of scrutiny. Starting in 1979 with Suzuki and Miyaura's studies, it was postulated that the added base attacked the boron to give a more nucleophilic aryl center (Figure 4.10a). This was supported by studies that showed boronate salts to be competent reaction partners.^{36,38} In 1985, the assessment was altered to suggest the possibility that the base forms an oxopalladium which acts as the nucleophile (Figure 4.10b).²⁹⁸ In 1998, Soderquist and co-workers showed that different boron reagents and different conditions affected which path was most active.³⁰⁹ Over the past twenty years, studies have continued to probe this step.^{53,310}

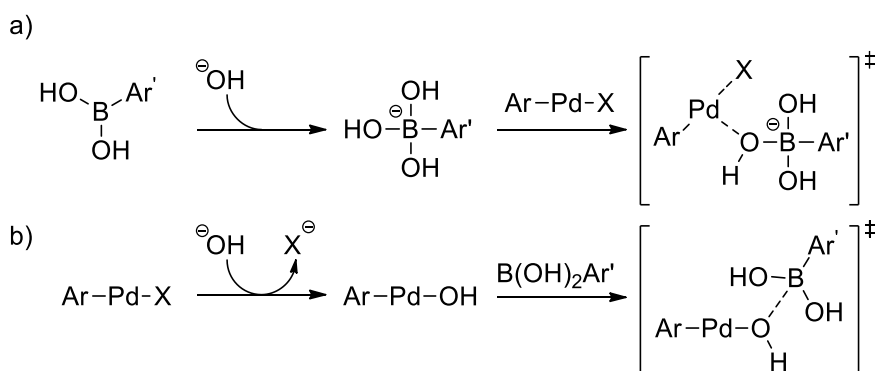


Figure 4. 11. Two possible pathways to form the pre-transmetalation species using (a) the boronate as the nucleophile or (b) the oxopalladium as the nucleophile

Whereas work has been done extensively to identify the process by which the pre-transmetalation species is formed, the transient nature of this putative intermediate left it unable to be observed by most standard methods. In 2016, Thomas and Denmark utilized rapid-injection NMR and stoichiometric conditions to form three possible intermediates.³¹¹ Preformed oxopalladium was added to boronic acid at -78° to yield intermediate **71a**, a tricoordinate 6-B-3 species. Combining a dimeric monoligated arylpalladium hydroxy complex with boronic acid at -78°C followed by warming to -60°C and then cooling to -100°C led to the formation of **71b**, a dinuclear complex. Finally, addition of more boronic

acid and methanol to **71b** gave species **71c**, a tetracoordinate 8-B-4 species. All three of these species proved to be reactive.³¹¹ It was finally asserted that the identity of the pre-transmetalation species could not be unambiguously determined *via* the methods at hand. Later, in 2017, Denmark and co-workers resolved that **71b** likely first converted to **71c** before reaction, but the authors admitted that they could not confirm this spectroscopically.³¹² Here we report the results of a combined experimental and theoretical ¹³C kinetic isotope effect (KIE) study that provide the first experimental insights into the transition-state geometry for the transmetalation event and clarifies the identity of the pre-transmetalation species under catalytic conditions.

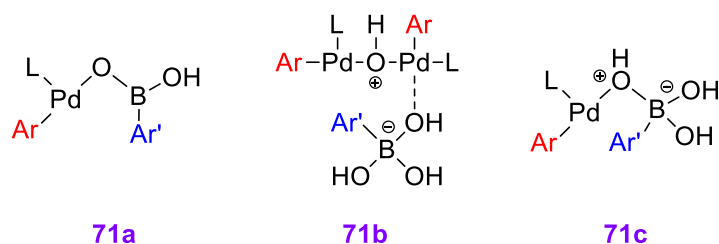


Figure 4. 12. Denmark proposed pre-transmetalation intermediates

EXPERIMENTAL KIES The reaction of *p*-*tert*-butyliodobenzene (**66a**) and *p*-toluylboronic acid (**67a**), catalyzed by palladiumtetrakis(triphenylphosphine) (Pd(PPh₃)₄) was chosen for the determination of experimental ¹³C KIEs at natural abundance. In 2011, Carrow and Hartwig showed that, for these conditions, the oxopalladium pathway is favored by more than four orders of magnitude over the boronate pathway.³⁰¹ The ¹³C KIEs were measured for both **66a** and **67a** in the standard way by Juliet M. Macharia and Sungjin Kim.¹⁴⁰ The results from their experimental measurements are summarized in Figure 4.12.

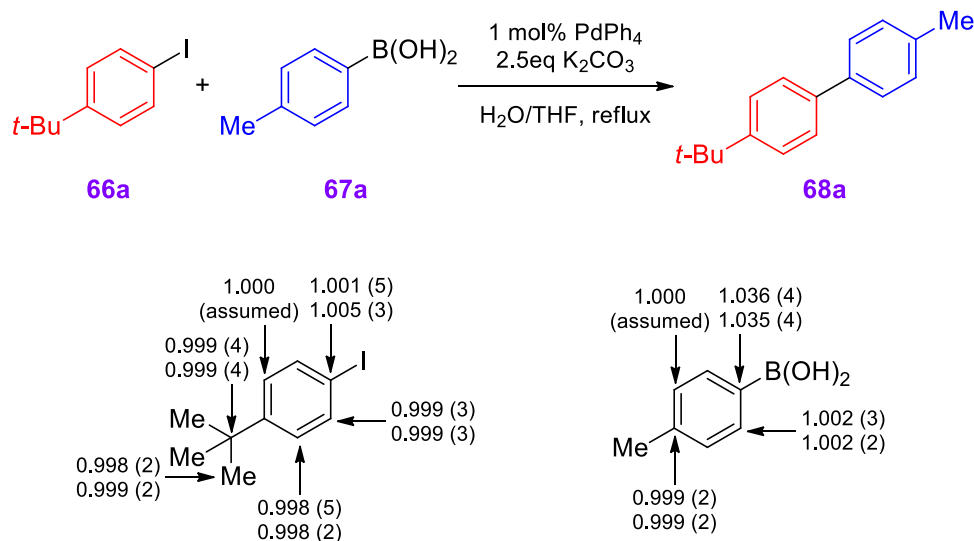


Figure 4. 13. Experimental conditions and determined KIEs

QUALITATIVE INTERPRETATION OF EXPERIMENTAL KIEs The unity KIE on the carbon bearing the iodine of **66a** is qualitatively consistent with no difference in k_{C-12} or k_{C-13} leading to the conclusion that there is no bond change at this carbon at the rate-determining step. This suggests **TS27**, **TS28**, and **TS29** are the only steps that could be rate-determining as they do not involve a bond change at this carbon. This agrees with Smith's findings as it was suggested that aryl iodides did not undergo a rate-limiting oxidative addition.²⁹⁹ The presence of a significant (3.5%) normal KIE on the carbon bearing the boron of **67a** reveals that this carbon *is* undergoing a bond change at the RDS. Consequently, **TS27** and **TS28** can be excluded as possible RDSs. The combination of these two isotope effects provides support that transmetalation (**TS29**) is the rate-determining step for the reaction studied. A quantitative interpretation of the geometry of this transition state and the exact species involved is deferred until both are predicted.

THEORETICAL STUDIES To aid in this quantitative interpretation of the experimental KIEs, transition structures for transmetalation from **71a** and **71c** were

computed using 10 different methods. The *tert*-butyl group of the aryl halide was omitted in the interest of computational cost. For a full comprehensive catalogue of all transition states located, see CHAPTER V: EXPERIMENTAL AND COMPUTATIONAL DETAILS. As before, the ^{13}C KIEs were computed from the scaled vibrational frequencies of the respective transition structures using the program *ISOEFF98* and the infinite parabola tunneling correction was applied.^{159,189,190} The average geometry and predicted KIEs for the boronic acid for both mechanisms are shown in Figure 4.13.

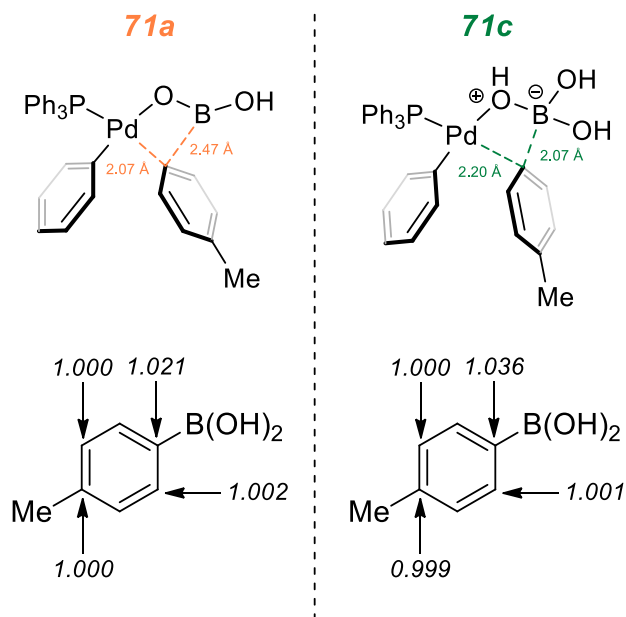


Figure 4. 14. Average DFT optimized geometry and predicted KIEs for the transmetalation event occurring from **71a** or **71c**

The difference between the KIEs predicted for the transmetalation from **71a** and the transmetalation from **71c** should be noted. As most data obtained *via* this method are capable of measuring ^{13}C KIEs to within 0.5%, a 1.5% difference is a notable one. The change originates from the difference in nucleophilicity of the migrating aryl group. In the case of **71a**, the aryl group is leaving a neutral, tricoordinate boron and the resulting product will be a B^+ . This loss in stability manifests itself as a “late” TS with the boron–carbon

bond being almost completely broken ($r_{\text{B-C}} = 2.47\text{\AA}$) and the carbon–palladium bond being almost completely formed ($r_{\text{C-Pd}} = 2.07\text{\AA}$). The vibrational frequency becomes muted with the carbon so close to the large palladium atom resulting in a smaller KIE: 1.021. For **71c**, the aryl group is being transferred from a tetracoordinate B^- resulting in a neutral boron in the product. In this case, the increased electron density causes the aryl group to be more nucleophilic and consequently the TS is “earlier.” A short boron–carbon bond ($r_{\text{B-C}} = 2.07\text{\AA}$) and long carbon–palladium ($r_{\text{C-Pd}} = 2.20\text{\AA}$) results in the carbon being farther away from the dampening effect of the palladium. On the basis of this structure, a larger KIE would be expected for the carbon bearing the boron. Indeed, this is seen: 1.036.

The KIEs predicted for transmetalation occurring from **71c** are in excellent agreement with those experimentally observed for the carbon bearing the boron. For forty years, the pre-transmetalation intermediate has been surmised, but not until now has there been evidence for the exact identity under catalytic conditions.

AVENUES FOR FUTURE RESEARCH We are aware of the fact that changes in aryl halide²⁹⁹, base^{313,314}, boronic acid³⁰⁹, and ligand concentration³¹² as well as other aspects of the reaction conditions can alter these results and change conclusions as they have been proven to cause variations in other aspects of the reaction. Current work is underway, in our lab, to develop a means of high-throughput screening of these conditions to better determine what affects the mechanism with the hope of being able to apply this information to developing better protocols in the future.

CHAPTER V. EXPERIMENTAL AND COMPUTATIONAL DETAILS

5.1 General notes

5.1.1 Experimental procedures

All reagents were measured open to the atmosphere, and reactions were run in sealed flasks. Methylene chloride, acetonitrile, toluene, chloroform, and tetrahydrofuran were dried using a J.C. Meyer solvent purification system. All other solvents and commercial reagents were used as provided, unless otherwise noted. Flash column chromatography was performed employing 40-63 μm silica gel (SiliaFlash P60 from Silicycle). Thin-layer chromatography (TLC) was performed on silica gel 60 F₂₅₄ plates (EMD). Organic solutions were concentrated using a Büchi or Heidolph rotary evaporator.

¹H and ¹³C NMR spectra were recorded in CDCl₃ (except where noted) on a Bruker Avance III 600, a Bruker Avance III 400, or a Bruker AC 300 instrument. Data for ¹H NMR are reported as follows: chemical shift (δ ppm), multiplicity (s = singlet, br s = broad singlet, d = doublet, t = triplet, dd = doublet of doublets, m = multiplet), coupling constant (Hz), integration, and assignment. Data for ¹³C are reported in terms of chemical shift. Spectra were processed in TopSpin™.

5.1.2 Computational methods

All calculations were carried out on the entire system being studied experimentally except where noted truncations were made in the interest of conserving computational resources. Lower level calculations were performed using a smaller basis set (typically double- ζ) with no diffuse functions and polarization only on heavy atoms. After sufficient exploration of the potential energy surface was made, most promising calculations were

“scaled up” by employing polarization functions on both heavy atoms and hydrogen, as well as adding diffuse functions to heavy atoms in an implicit solvent model. Single-point calculations were performed typically using the geometries obtained from the “scaled up” calculations while employing a triple- ζ basis set and polarization and diffuse functions on all atoms in a solvent model. The primarily used functional chosen in each section of this thesis is based on a case study conducted of the benchmark reactions and measurements carried out throughout the literature. Additional functionals typically used for similar systems is also employed as a means to observing computational trends when interpreting data.

All calculations were carried out by use of the *Gaussian09* software package.²⁰⁵ The default convergence criteria (Maximum force threshold – 4.5×10^{-4} ; RMS force threshold – 3×10^{-4} ; Maximum displacement threshold – 1.8×10^{-3} ; RMS displacement threshold – 1.2×10^{-3}) were used for transition state and ground state optimizations. A pruned grid having 75 radial shells and 302 angular points per shell was utilized.

All transition structures were characterized by a single imaginary frequency and all ground states were confirmed to be minima (no imaginary frequency). Transition states were further characterized through the use of internal reaction coordinate (IRC) calculations and subsequent geometry optimizations.

All geometry figures were generated using CYLview (CYLview, 1.0b; Legault, C. Y., Université de Sherbrooke, 2009 (<http://www.cylview.org>)).

Geometries and raw energies for individual calculations are not included herein but available upon request from Dr. Mathew J. Veticatt (veticatt@binghamton.edu).

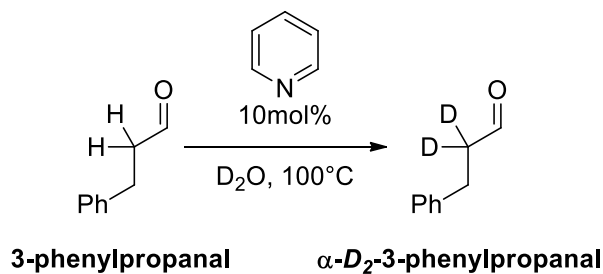
5.2 Secondary Amine Catalysis

5.2.1 Enamine catalysis

5.2.1.1 Isotope Effects Reveal the Mechanism of Enamine Formation in l-Proline-

Catalyzed α -Amination of Aldehydes

α -deuteration of 3-phenylpropanal



In a pressurized 100mL round bottom flask, 13.414g (100mmol) of 3-phenylpropanal, 0.7902g (10mmol) of pyridine, and 16mL of deuterium oxide were added. The flask was stoppered and submerged in an oil bath set to 100°C. Stirring progressed for 4hrs after which time the flask was allowed to cool. The contents were extracted three times with methylene chloride, the organic layers were combined, dried, and concentrated. The percent deuterium incorporation was determined via NMR and the procedure was repeated until full incorporation was observed adding fresh pyridine and deuterium oxide each time.

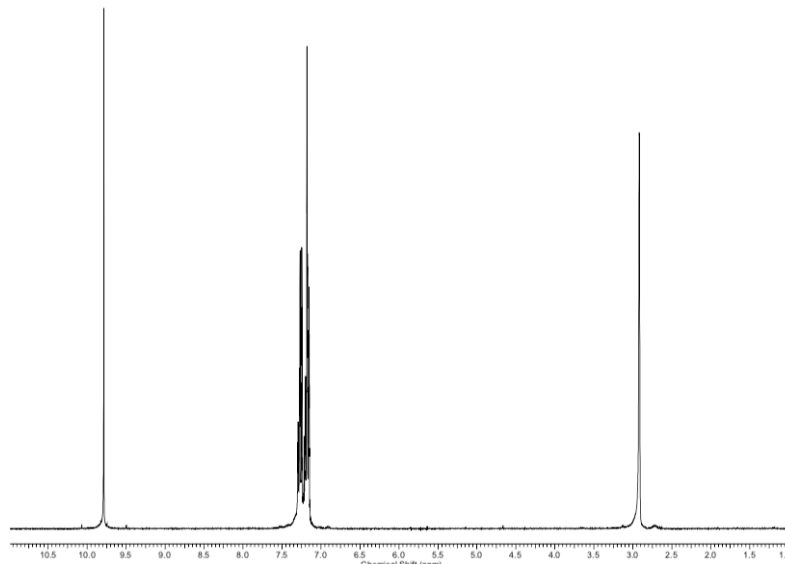


Figure 5. 1 ^1H NMR of purified and fully deuterated $\alpha\text{-D}_2\text{-3-phenylpropanal}$

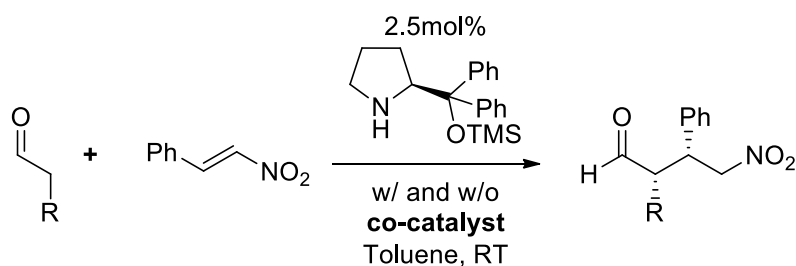
KIE Reaction with $\alpha\text{-D}_2\text{-3-phenyl propanal}$

Each KIE experiment was run at room temperature using 15 mmol of $\alpha\text{-D}_2\text{-3-phenyl propanal}$, 13 mmol of diazodibenzylidene dicarboxylate, 1.5 mmol of L-proline, and 5 mmol of DMSO- d_6 in ~80 mL of dry acetonitrile. Aliquots were extracted from the reaction pot and subjected to ^2H NMR analysis at regular time intervals. The decrease in signal produced by the starting material was monitored using the DMSO- d_6 as an internal standard. The reactions were quenched at 71.6% and 71.0% by the addition of half-saturated ammonium chloride after a final NMR spectrum was acquired. The mixture was then extracted into ethyl acetate and concentrated *in vacuo*. The crude mixture was loaded on a column and the unreacted aldehyde of $\alpha\text{-D}_2\text{-3-phenyl propanal}$ was isolated by elution with a 9:1 hexane:ethyl acetate mixture. The isolated aldehyde was quantitatively reduced to the corresponding alcohol (of $\alpha\text{-D}_2\text{-3-phenyl propanol}$) by reduction with 1.5 eq NaBH_4 in ethanol. The alcohol was then isolated by column chromatography using a 6:1 mixture of hexane:ethyl acetate. The ^{13}C isotopic composition of these samples was compared to a

‘Standard’ sample of the alcohol obtained by reduction of the aldehyde not subject to reaction conditions.

5.2.1.2 Isotope Effects Reveal Discrepancies in Current Mechanistic Understanding of Diphenylprolinol Silyl Ether-Catalyzed Michael Reaction of Aldehydes and Nitroolefins

Basic KIE reaction



To a round-bottom flask was added 25mmol of the aldehyde, 2.983g (20mmol) of nitrostyrene, 0.841g (5mmol) of dinitrobenzene (internal standard), and 20mL of dry toluene. The solution was allowed to stir for ~60min to ensure full solvation of the internal standard. <0.01mL was extracted (without exposing the solution to air), placed in an NMR tube, and diluted with CDCl₃. This sample was used to confirm that no reaction had taken place in the time since the starting materials were added together. Next, if a co-catalyst was used, 0.029mL (0.5mmol; 2.5mol%) of acetic acid or 0.0696g (0.5mmol; 2.5mol%) of *p*-nitrophenol was added. Then 0.5mL of a 1M stock solution of (*S*)-(-)- α,α -diphenyl-2-pyrrolidinemethanol trimethylsilyl ether in toluene (0.5mmol; 2.5mol%) was added. Periodically, <0.01mL aliquots were removed from the reaction mixture, without subjecting the reaction to air. The aliquot was diluted with chloroform-d and an NMR spectrum was acquired. 1,4-dinitrobenzene was used as an internal standard and integrated to 1.0000. The relative integration of the nitrostyrene doublet was compared to the relative

integration of the nitrostyrene doublet from the spectrum obtained prior to the addition of catalyst (i.e. $t = 0$ min). Figure 5.2 shows the composite of this procedure in the case of propanal. All spectra are normalized to the same height using DNB as the standard; the peak at 9.86ppm corresponds to the aldehyde hydrogen on the starting material (Propanal), the peak at 9.77ppm corresponds to the aldehyde hydrogen of the major diastereomer of the Michael adduct (Product_{maj}), the peak at 8.44ppm corresponds to the four hydrogen atoms of the 1,4-dinitrobenzene standard, the peak at 8.07ppm corresponds to the hydrogen on the β -carbon of the nitrostyrene.

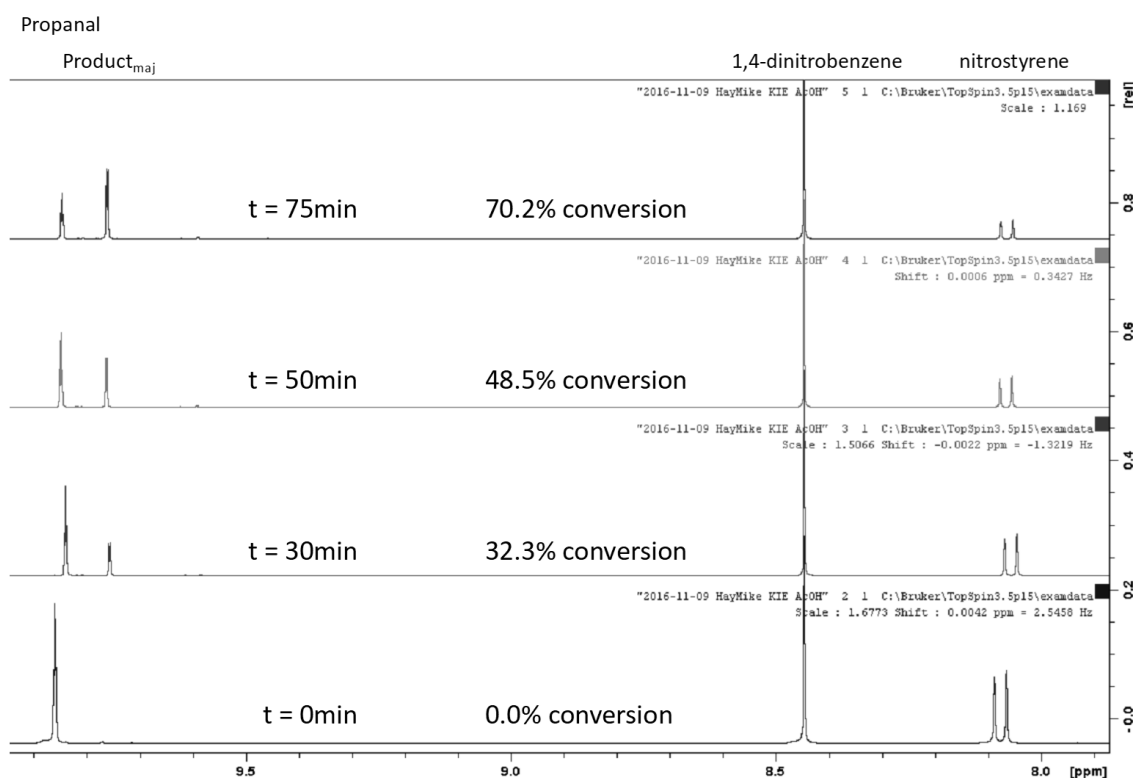


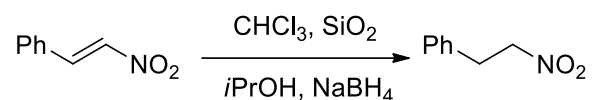
Figure 5. 2. Stacked NMR spectra showing the monitoring of percent conversion

When the reaction was deemed to have reached a high enough conversion, 20mL of 1M HCl_(aq) was added to the flask and stirred in. The organic layer was then extracted with several volumes of methylene chloride. The combined organic layers were dried over

sodium sulfate and concentrated *in vacuo*. The nitrostyrene, aldehyde, and internal standard was separated from the product via column chromatography eluting 9:1 hexanes to ethyl acetate.

KIE sample derivatization

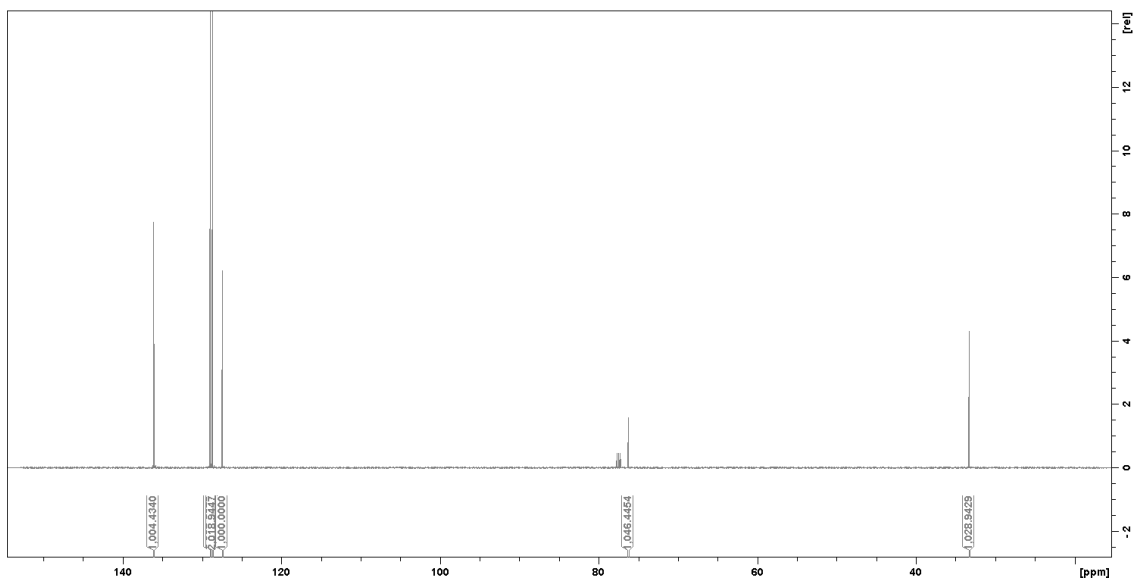
Owing to the wideness of the β -carbon's ^{13}C NMR signal, it was decided that a reduction of the double bond was ideal to give clean integrations. The recovered material was therefore derivatized in the following manner according to literature procedure.³¹⁵



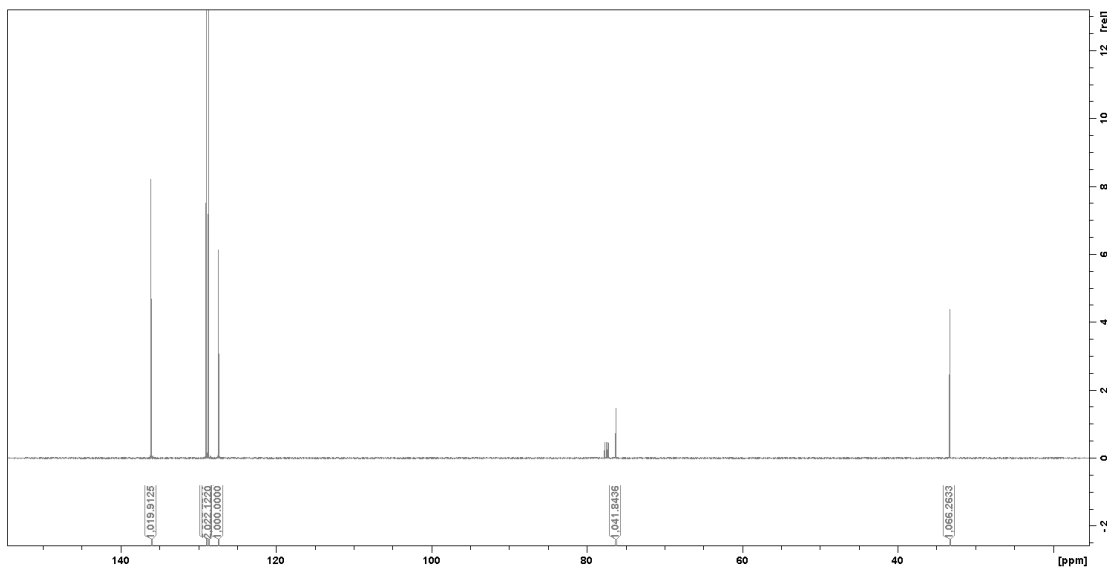
NMR analysis was used to determine the amount of nitrostyrene in the recovered mixture. 2.0g of silica gel and 3.0mL of isopropyl alcohol were added for every 1mmol of observed nitrostyrene. The slurry was stirred as 8.0 mL of chloroform was added for every 1 mmol of nitrostyrene observed. At room temperature, 4.1mmol of sodium borohydride was slowly added for every 1mmol of nitrostyrene observed. Another 8.0 mL of chloroform every 1mmol of nitrostyrene was then added and used to wash the walls of the flask. The solution was allowed to stir, at room temperature overnight in a sealed flask with a nitrogen balloon attached. The next day, 0.1M aqueous hydrochloric acid was slowly added to decompose the unreacted sodium borohydride. The resulting mixture was extracted with dichloromethane, dried over sodium sulfate and concentrated *in vacuo*. Quantitative conversion was confirmed by ^1H NMR. The crude mixture was purified by column chromatography eluting 7:3 hexanes to dichloromethane.

Sample spectra for the determination of isotopic enrichment

Standard:



Experimental:



Integrations of Standard and Experimental NMR spectra (propanal with AcOH)

First Set								
Standard								
peak	fid1	fid2	fid3	fid4	fid5	fid6	average	stddev
para	1000.0000	1000.0000	1000.0000	1000.0000	1000.0000	1000.0000	1000.0000	0.0000
beta	1037.8733	1046.4454	1041.1258	1040.8440	1038.9415	1037.9866	1040.5361	3.2092
alpha	1025.6915	1028.9429	1029.1979	1028.7787	1030.5043	1028.1878	1028.5505	1.5967
ipso	1016.3908		1015.0488	1017.9747	1020.9249	1019.8365	1018.0351	2.4094

ortho	2006.7278	2008.3089	2006.6659	2007.7011	2007.1093	2008.1029	2007.4360	0.7040
meta	2016.0691	2018.9447	2019.3486	2022.4804	2022.2015	2021.3851	2020.0716	2.4445
Experimental								
peak	fid1	fid2	fid3	fid4	fid5	fid6	average	stddev
para	1000.0000	1000.0000	1000.0000	1000.0000	1000.0000	1000.0000	1000.0000	0.0000
beta	1045.2232	1041.4836	1043.2641	1043.8002	1043.5602	1041.9204	1043.2086	1.3543
alpha	1066.5111	1066.2633	1065.5766	1066.2473	1063.2520	1068.9118	1066.1270	1.8168
ipso	1013.7376	1019.9125	1017.9880	1020.1866	1020.1778	1025.6396	1019.6070	3.8527
ortho	2006.1379	2002.8944	2002.1765	2007.7173	2003.6284	2006.1649	2004.7866	2.1931
meta	2021.6401	2022.1220	2020.1784	2022.0288	2022.2058	2024.0732	2022.0414	1.2485
	Conver:	70.0%						
peak	KIE	stdev						
para	1.000	0.000						
beta	1.002	0.003						
alpha	1.031	0.002						
ipso	1.001	0.004						
ortho	0.999	0.001						
meta	1.001	0.001						

Second Set								
Standard								
peak	fid1	fid2	fid3	fid4	fid5	fid6	average	stddev
para	1000.0000	1000.0000	1000.0000	1000.0000	1000.0000	1000.0000	1000.0000	0.0000
beta	1029.3076	1031.1210	1031.9848	1028.6018	1033.3925	1028.5210	1030.4881	1.9949
alpha	1027.2842	1025.9476	1026.4507	1026.5690	1024.7922	1025.6271	1026.1118	0.8604
ipso	1022.8276	1021.1742	1025.1716	1025.4875	1021.5610	1020.6303	1022.8087	2.0849
ortho	2010.7491	2009.4514	2009.9200	2014.8460	2010.0588	2009.2457	2010.7118	2.0921
meta	2016.8588	2016.9053	2018.5753	2020.4595	2017.6199	2018.5989	2018.1696	1.3573
Experimental								
peak	fid1	fid2	fid3	fid4	fid5	fid6	average	stddev
para	1000.0000	1000.0000	1000.0000	1000.0000	1000.0000	1000.0000	1000.0000	0.0000
beta	1040.7695	1035.2770	1037.9617	1031.2803	1032.8995	1037.0539	1035.8737	3.4648
alpha	1053.2482	1051.4982	1051.5706	1047.9371	1049.1983	1051.2554	1050.7846	1.8996
ipso	1014.7546	1017.9251	1017.1935	1012.9483	1015.8937	1016.1891	1015.8174	1.7800
ortho	2009.6117	2013.7955	2010.1689	2007.7066	2010.2697	2009.7899	2010.2237	1.9830
meta	2021.4742	2024.1021	2020.4412	2017.6832	2019.6409	2019.7568	2020.5164	2.1518
	Conver:	57.0%						
peak	KIE	stdev						
para	1.000	0.000						
beta	1.006	0.004						
alpha	1.029	0.002						
ipso	0.992	0.003						
ortho	1.000	0.001						
meta	1.001	0.001						

Integrations of Standard and Experimental NMR spectra (propanal without AcOH)

First Set								
Standard								
peak	fid1	fid2	fid3	fid4	fid5	fid6	average	stddev
ipso	1022.7555	1022.5185	1026.0998	1023.8938	1024.0952	1022.9142	1023.7128	1.3310
ortho	1995.3003	1995.6896	2000.7250	1998.1852	1998.9388	1999.5831	1998.0703	2.1654
meta	2014.4230	2013.7002	2018.3061	2017.9103	2017.1921	2018.2952	2016.6378	2.0490
para	1000.0000	1000.0000	1000.0000	1000.0000	1000.0000	1000.0000	1000.0000	0.0000
beta	1013.1568	1013.9413	1017.0522	1016.6261	1014.8331	1013.7973	1014.9011	1.5994
alpha	1026.0835	1026.9657	1028.4207	1026.6536	1026.9231	1027.0653	1027.0187	0.7730
Experimental								
peak	fid1	fid2	fid3	fid4	fid5	fid6	average	stddev
ipso	1023.4485	1022.3218	1021.3055	1022.2237	1024.0592	1022.1835	1022.5904	0.9917
ortho	1996.8428	1997.0992	1994.5446	1998.2946	1997.3812	1998.3591	1997.0869	1.3919
meta	2015.9812	2016.0142	2012.5741	2017.5929	2018.4552	2018.4442	2016.5103	2.2233

para	1000.0000	1000.0000	1000.0000	1000.0000	1000.0000	1000.0000	1000.0000	0.0000
beta	1028.1144	1027.6075	1024.0004	1027.1103	1026.2590	1027.6665	1026.7930	1.5071
alpha	1061.5135	1060.8710	1060.5872	1062.2010	1062.4009	1060.4601	1061.3390	0.8316
	Conver:	89.0%						
peak	KIE	stdev						
ipso	1.000	0.002						
ortho	1.000	0.001						
meta	1.000	0.001						
para	1.000	0.000						
beta	1.005	0.002						
alpha	1.015	0.001						

Second Set								
Standard								
peak	fid1	fid2	fid3	fid4	fid5	fid6	average	stddev
ipso	1032.2015	1031.2764	1034.4567	1032.0866	1031.0818	1027.0000	1031.3505	2.4462
ortho	2006.9480	2006.5719	2010.1161	2007.6333	2009.1704	2008.6117	2008.1752	1.3652
meta	2030.2370	2028.9643	2032.7382	2031.6224	2031.3889	2032.3712	2031.2203	1.4054
para	1000.0000	1000.0000	1000.0000	1000.0000	1000.0000	1000.0000	1000.0000	0.0000
beta	1026.6569	1027.0106	1029.7267	1028.7464	1027.5677	1026.2287	1027.6562	1.3369
alpha	1031.9573	1032.6073	1033.2736	1032.1781	1031.9990	1031.4193	1032.2391	0.6354
Experimental								
peak	fid1	fid2	fid3	fid4	fid5	fid6	average	stddev
ipso	1031.4748	1030.6023	1030.5454	1030.9179	1031.5775	1026.5752	1030.2839	1.8678
ortho	2005.5128	2006.7431	2005.1626	2008.0735	2006.9063	2008.1842	2006.7638	2.0171
meta	2028.9216	2030.4236	2027.9465	2032.2543	2032.6608	2032.5190	2030.7876	2.0171
para	1000.0000	1000.0000	1000.0000	1000.0000	1000.0000	1000.0000	1000.0000	0.0000
beta	1040.3994	1040.4788	1037.2837	1039.9208	1038.8446	1040.0793	1039.5011	1.2346
alpha	1066.3753	1066.2465	1065.8393	1068.2500	1068.2500	1067.4539	1066.2374	0.9198
	Conver:	89.0%						
peak	KIE	stdev						
ipso	1.000	0.003						
ortho	1.000	0.001						
meta	1.000	0.001						
para	1.000	0.000						
beta	1.005	0.002						
alpha	1.015	0.001						

Integrations of Standard and Experimental NMR spectra (3-phenylpropanal with AcOH)

First Set								
Standard								
peak	fid1	fid2	fid3	fid4	fid5	fid6	average	stddev
para	1024.4845	1015.3518	1013.2158	1016.4173	1017.9200	1017.5923	1017.4970	3.8239
ortho	1991.7596	1991.5436	1994.0210	1995.7309	1991.6177	1998.9310	1993.9340	2.9669
meta	1996.7653	1995.7914	1993.1710	2002.2393	1994.2511	2001.1798	1997.2330	3.6967
ipso	1000.0000	1000.0000	1000.0000	1000.0000	1000.0000	1000.0000	1000.0000	0.0000
beta	1018.6777	1016.7578	1014.3905	1008.4547	1017.6131	1019.3620	1015.8760	4.0269
alpha	1018.6323	1014.3434	1017.5934	1020.8238	1016.0462	1021.0915	1018.0884	2.6547
Experimental								
peak	fid1	fid2	fid3	fid4	fid5	fid6	average	stddev
para	1014.8306	1012.9864	1009.5904	1017.6627	1016.0835	1017.4085	1014.7604	3.0681
ortho	1984.9158	1986.7830	1982.4934	1989.1456	1994.7012	1994.3837	1988.7371	5.0005
meta	1992.2583	1989.5720	1988.1132	1996.2213	2000.0955	1996.2437	1993.7507	4.5617
ipso	1000.0000	1000.0000	1000.0000	1000.0000	1000.0000	1000.0000	1000.0000	0.0000
beta	1041.2902	1043.5634	1039.4743	1043.0370	1042.3315	1048.5771	1043.0456	3.0728
alpha	1023.5502	1022.8101	1015.4688	1024.2466	1025.9706	1026.3276	1023.0623	3.9620
	Conver:	76.0%						

peak	KIE	stdev
para	0.998	0.005
ortho	0.998	0.003
meta	0.999	0.003
ipso	1.000	0.000
beta	1.019	0.005
alpha	1.003	0.005

Second Set								
Standard								
peak	fid1	fid2	fid3	fid4	fid5	fid6	average	stddev
para	1024.4845	1015.3518	1013.2158	1016.4173	1017.9200	1017.5923	1017.4970	3.8239
ortho	1991.7596	1991.5436	1994.0210	1995.7309	1991.6177	1998.9310	1993.9340	2.9669
meta	1996.7653	1995.7914	1993.1710	2002.2393	1994.2511	2001.1798	1997.2330	3.6967
ipso	1000.0000	1000.0000	1000.0000	1000.0000	1000.0000	1000.0000	1000.0000	0.0000
beta	1018.6777	1016.7578	1014.3905	1008.4547	1017.6131	1019.3620	1015.8760	4.0269
alpha	1018.6323	1014.3434	1017.5934	1020.8238	1016.0462	1021.0915	1018.0884	2.6547
Experimental								
peak	fid1	fid2	fid3	fid4	fid5	fid6	average	stddev
para	1014.6617	1017.7366	1016.4936	1012.5741			1015.3665	2.2496
ortho	1982.1350	1992.7292	1985.2034	1986.1085			1986.5440	4.4603
meta	1990.6432	1993.3272	1994.7065	1991.8443			1992.6303	1.7666
ipso	1000.0000	1000.0000	1000.0000	1000.0000			1000.0000	0.0000
beta	1046.9508	1046.4595	1041.7169	1045.9181			1045.2613	2.4003
alpha	1022.9746	1025.0561	1026.1083	1020.2741			1023.6033	2.5732
	Conver:	76.0%						
peak	KIE	stdev						
para	0.999	0.004						
ortho	0.997	0.003						
meta	0.998	0.002						
ipso	1.000	0.000						
beta	1.020	0.005						
alpha	1.004	0.004						

Energy profile

As stated in Chapter 2.1.2, the current prediction for $\Delta\Delta G^\ddagger$ of the C–C bond formation and the protonation is not yet in agreement with the conclusions drawn from the experimental KIE study. Work is underway to rectify that, but the current energy profile is shown below in Figure 5. With all transition states linked to intermediates by IRC calculations and all energies extrapolated at the B3LYP-D3(BJ)/6-311++G**/SMD(toluene) // B3LYP/6-31G* level of theory.

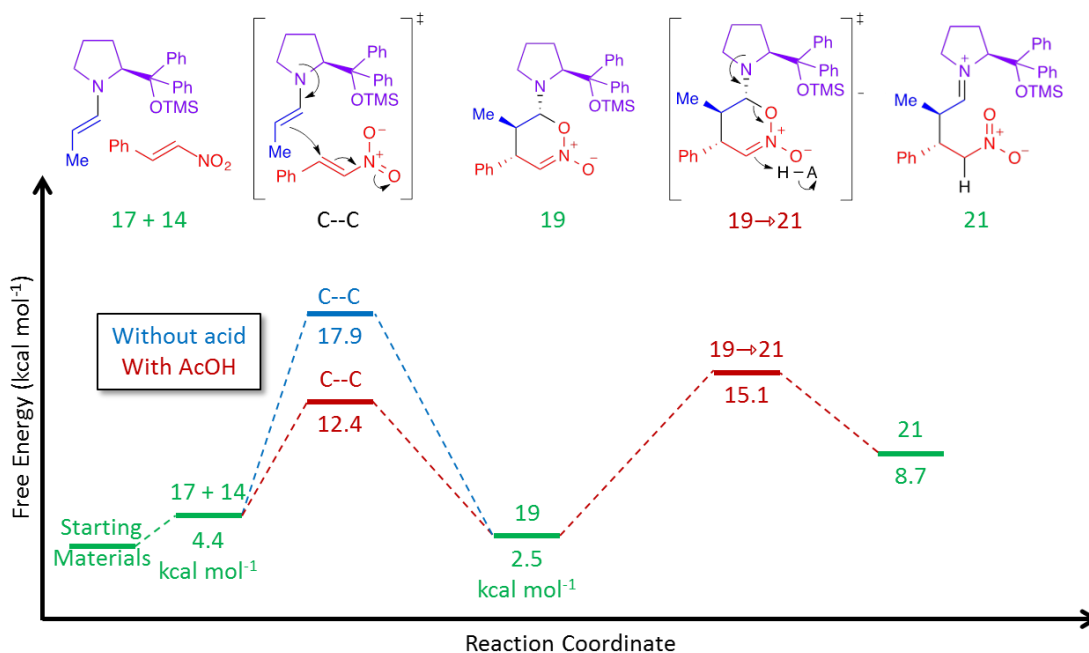
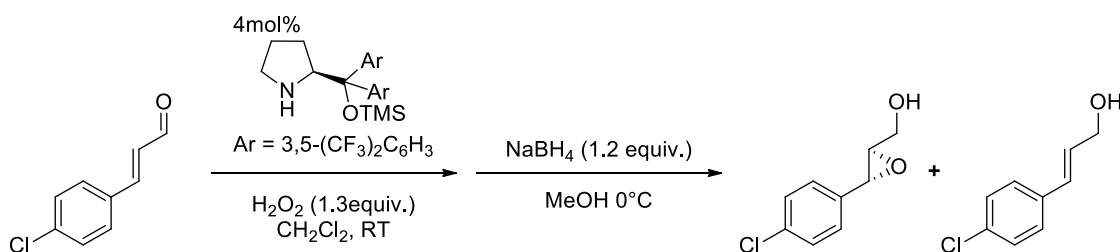


Figure 5. 3. Current reaction profile for Hayashi's Michael reaction

5.2.2 “Iminium-ion” catalysis

5.2.2.1 Isotope Effects Reveal an Alternative Mechanism for “Iminium-Ion” Catalysis

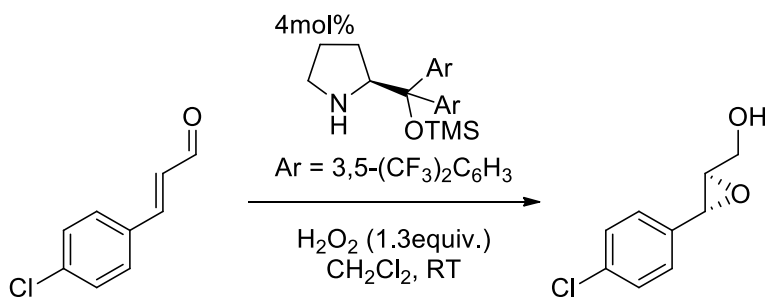
Procedure for ^{13}C KIE determination by analysis of *p*-chlorocinnamyl alcohol



293mg of (*S*)- α,α -Bis[3,5-bis(trifluoromethyl)phenyl]-2-pyrrolidinemethanol trimethylsilyl ether (0.4mmol, 0.04equiv) was added to a solution of *p*-chlorocinnamaldehyde (1.67g, 10mmol, 1.0equiv) in CH_2Cl_2 (20mL) at room temperature followed by dropwise addition of hydrogen peroxide solution (1.14mL, 13mmol, 1.3equiv, 35 wt.% in H_2O). The reaction mixture was stirred at room temperature for approximately

3h before it was cooled to 0 °C and quenched by addition of NaBH₄ (454mg, 12mmol, 1.2equiv) and cold MeOH (10mL). The exact conversion was determined by ¹H NMR analysis of the crude reaction mixture. The reaction mixture was stirred for 1 h before saturated aqueous ammonium chloride (20mL) was added. The phases were separated and the aqueous phase was extracted with CH₂Cl₂ (3 x 15 mL). The combined organic phase was dried over MgSO₄ and concentrated. *p*-Chlorocinnamyl alcohol was isolated by FC on silica (EtOAc/pentane 10:90 to 30:70) followed by a second purification by FC on silica (CH₂Cl₂) as a white solid

Procedure for ¹³C KIE determination by analysis of p-chlorocinnamaldehyde



The catalyst (*S*)- α,α -Bis[3,5-bis(trifluoromethyl)phenyl]-2-pyrrolidinemethanol trimethylsilyl ether (1.195 g, 2 mmol, 0.10 equiv) was added to a solution of *p*-chlorocinnamaldehyde **1a** (3.34 g, 20 mmol, 1.0 equiv) in CH₂Cl₂ (40 mL) at room temperature followed by addition of hydrogen peroxide solution (2.28 mL, 26 mmol, 1.3 equiv, 35 wt.% in H₂O). Aliquots were removed periodically and quenched by addition of NaBH₄ and MeOH to determine percent conversion. When the reaction had reached the desired conversion, as determined by ¹H NMR analysis, saturated aqueous ammonium chloride was added to halt the reaction. The phases were separated and the aqueous phase was extracted with CH₂Cl₂. The combined organic phase was dried over Na₂SO₄ and

concentrated. The unreacted starting material was re-isolated by FC on silica (EtOAc/hexanes 95:5).

The ^{13}C isotopic composition of the above 'KIE sample' of **1a** was compared to a 'Standard' sample of **1a** from the same batch (not subjected to reaction conditions). To ensure purity of this sample, 0.835 g (5 mmol) was purified by FC on silica (EtOAc/hexanes 95:5).

^{13}C Sample preparation for NMR analysis

The first three KIE measurements were performed by analysis of three samples of *p*-chlorocinnamylalcohol – Exp1, Exp2, and Exp3 – re-isolated after *in-situ* reduction of the reaction mixture taken to $72 \pm 2\%$, $77 \pm 2\%$, and $68 \pm 2\%$, respectively. These samples were compared to Std1, Std2, and Std3, respectively, which were reduced unreacted starting material **1a** from the same batch as the respective experimental samples (Exp1-3). These experiments were performed in the Jørgensen lab as described in Section B of this document. A fourth KIE measurement was performed by comparative analysis of two samples of **1a** (not derivatized) – Exp4 and Std4 – which were from the same batch of **1a**. The reaction from which sample Exp4 was conducted was taken to $61 \pm 2\%$ conversion. The experiments leading to these two samples were was performed in the Vetticatt lab following the procedure outlined in Section C of this document.

KIE1

A sample was prepared from 166 mg of re-isolated material from Exp1 was transferred to a new 5 mm NMR tube quantitatively using HPLC grade deuterated chloroform (CDCl_3). The sample was filled to a height of 5 cm. 163 mg of purified material from Std1 was transferred to a new 5 mm NMR tube quantitatively using HPLC grade

CDCl₃. The sample was filled to a height of 5 cm. The ¹³C NMR spectra were recorded at 150 MHz using inverse gated decoupling with an acquisition time of 10 sec, a delay time of 60 sec (5 times T1), and 128 transients were used to acquire six spectra for both samples. Integrations were numerically determined using a constant integration region (equal to 10 times the peak-widths at half-height for each peak). The meta carbon was set to an integration value of 2000.0000. All integrals are listed below represented by FID1, FID2, FID3, FID4, FID5, and FID6.

KIE2

A sample was prepared from 159 mg of re-isolated material from Exp2 was transferred to a new 5 mm NMR tube quantitatively using HPLC grade deuterated chloroform (CDCl₃). The sample was filled to a height of 5 cm. 156 mg of purified material from Std2 was transferred to a new 5 mm NMR tube quantitatively using HPLC grade CDCl₃. The sample was filled to a height of 5 cm. The ¹³C NMR spectra were recorded at 150 MHz using inverse gated decoupling with an acquisition time of 10 sec, a delay time of 60 sec (5 times T1), and 128 transients were used to acquire six spectra for both samples. Integrations were numerically determined using a constant integration region (equal to 10 times the peak-widths at half-height for each peak). The meta carbon was set to an integration value of 2000.0000. All integrals are listed below represented by FID7, FID8, FID9, FID10, FID11, and FID12.

KIE3

A sample was prepared from 168 mg of re-isolated material from Exp3 was transferred to a new 5 mm NMR tube quantitatively using HPLC grade deuterated chloroform (CDCl₃). The sample was filled to a height of 5 cm. 163 mg of purified material

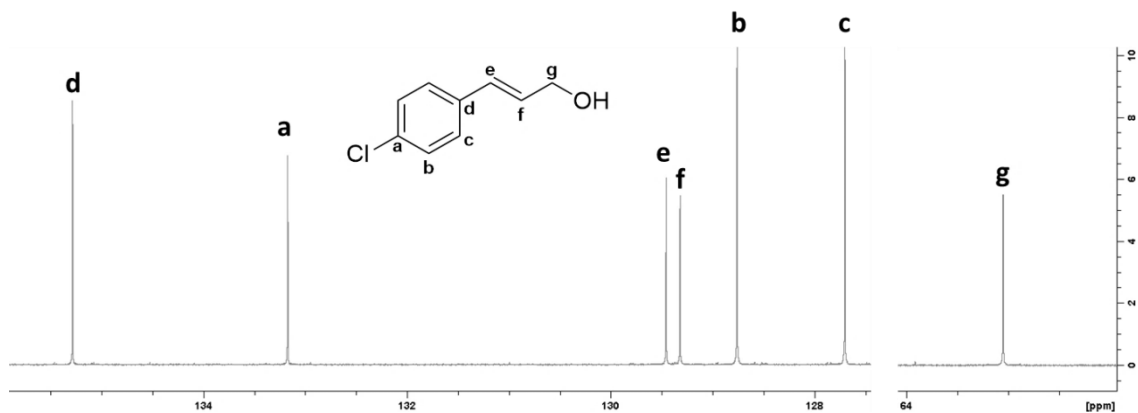
from Std3 was transferred to a new 5 mm NMR tube quantitatively using HPLC grade CDCl_3 . The sample was filled to a height of 5 cm. The ^{13}C NMR spectra were recorded at 150 MHz using inverse gated decoupling with an acquisition time of 10 sec, a delay time of 60 sec (5 times T_1), and 128 transients were used to acquire six spectra for both samples. Integrations were numerically determined using a constant integration region (equal to 10 times the peak-widths at half-height for each peak). The meta carbon was set to an integration value of 2000.0000. All integrals are listed below represented by FID13, FID14, FID15, FID16, FID17, and FID18.

KIE4

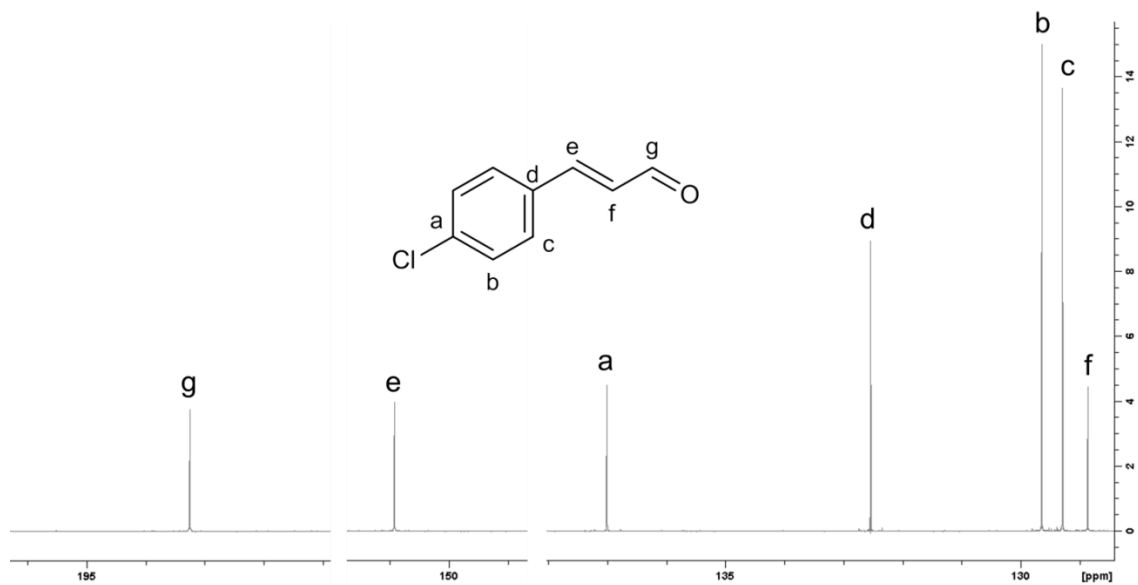
A sample was prepared from 307 mg of re-isolated material from Exp4 was transferred to a new 5 mm NMR tube quantitatively using HPLC grade deuterated chloroform (CDCl_3). The sample was filled to a height of 5 cm. 307 mg of purified material from Std4 was transferred to a new 5 mm NMR tube quantitatively using HPLC grade deuterated chloroform (CDCl_3). The sample was filled to a height of 5 cm. The ^{13}C NMR spectra were recorded at 150 MHz using inverse gated decoupling with an acquisition time of 5 sec, a delay time of 42 sec (5 times T_1), and 128 transients were used to acquire seven spectra for both samples. Integrations were numerically determined using a constant integration region (equal to 10 times the peak-widths at half-height for each peak). The meta carbon was set to an integration value of 2000.0000. All integrals are listed below represented by FID19, FID20, FID21, FID22, FID23, FID24 and FID25

Sample spectra for the determination of isotopic enrichment

For KIE 1, 2, and 3:

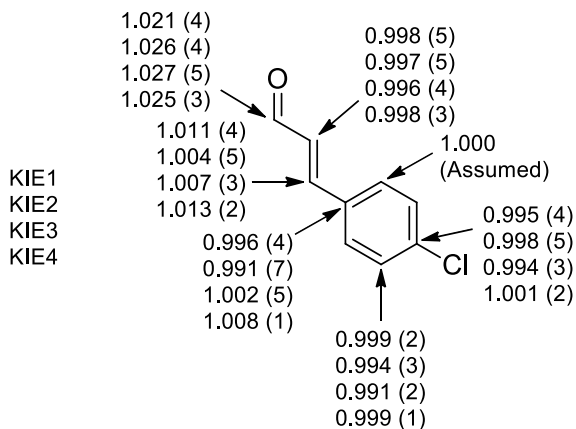


For KIE 4:



Integrations of Standard and Experimental NMR spectra

FID1-6 were obtained from KIE1. FID7-12 were obtained from KIE2. FID13-18 were obtained from KIE3. FID19-25 were obtained from KIE4. The calculated KIEs for each carbon atom from all 25 comparisons along with the average KIE and standard deviations at a 95% confidence interval are also shown.



Standard

	FID1	FID2	FID3	FID4	FID5	FID6	FID7
Carbonyl	999.9450	995.1678	998.7200	1000.8705	1000.1896	991.1734	999.3382
alpha	1009.9400	1008.5253	1009.6639	1006.8823	1009.0799	1011.2273	1016.7798
beta	1004.6400	1001.6036	1004.2749	1002.8434	1007.9150	1005.0845	1021.7365
ipso	1003.8200	1002.7052	1002.6492	1005.3689	1006.5251	1000.6444	1009.9590
ortho	2000.0000	2000.0000	2000.0000	2000.0000	2000.0000	2000.0000	2000.0000
meta	1997.9500	1992.7937	1999.8207	1999.8992	2001.5606	1998.0436	2001.3133
para	1005.0900	1002.6279	1001.7994	1003.2964	1003.1178	1002.4769	1017.3539
	FID8	FID9	FID10	FID11	FID12	FID13	FID14
Carbonyl	994.9161	1000.4009	996.3514	991.2866	999.0613	997.1477	987.8562
alpha	1006.9993	1003.5986	1008.2950	1009.2477	1008.6778	1012.3506	1007.4926
beta	1015.2787	1022.2499	1020.1071	1024.4772	1012.2755	1001.0561	1000.8182
ipso	1003.0734	1004.5855	999.6574	1002.7479	997.3259	1001.6707	1003.8573
ortho	2000.0000	2000.0000	2000.0000	2000.0000	2000.0000	2000.0000	2000.0000
meta	1993.1244	1996.0091	1994.8830	1995.6872	1993.6511	2015.2471	2013.4102
para	1012.1689	1016.3148	1013.5592	1015.4147	1018.1231	998.7126	995.8012
	FID15	FID16	FID17	FID18	FID19	FID20	FID21
Carbonyl	997.9377	996.2890	996.0902	990.8309	1022.3358	1021.2684	1026.0193
alpha	1006.0455	1010.6613	1012.1137	1013.5130	1009.0510	1005.6209	1009.6268
beta	1002.4195	1006.5244	1000.4638	1002.2177	1026.1832	1027.7100	1029.2155
ipso	1003.0011	1007.3926	1005.8330	1005.4780	1048.8826	1049.0559	1051.0140
ortho	2000.0000	2000.0000	2000.0000	2000.0000	2000.0000	2000.0000	2000.0000
meta	2010.2040	2015.9408	2022.3142	2017.0584	2045.8204	2047.3703	2052.1031
para	994.6799	999.2388	997.0173	996.4283	1015.5494	1014.2484	1016.2770
	FID22	FID23	FID24	FID25			
Carbonyl	1022.1287	1023.6108	1026.0809	1022.8834			
alpha	1002.6671	1007.1519	1009.8458	1009.7016			
beta	1027.6064	1029.2976	1026.2104	1030.5278			
ipso	1047.7568	1049.1057	1049.0315	1049.1660			
ortho	2000.0000	2000.0000	2000.0000	2000.0000			
meta	2046.7132	2046.4900	2048.7828	2048.3092			
para	1015.7240	1015.3491	1014.3319	1016.2536			

Experimental

	FID1	FID2	FID3	FID4	FID5	FID6	FID7
Carbonyl	1013.7721	1025.2879	1022.3254	1022.8439	1026.0520	1026.5845	1032.6940
alpha	1009.2268	1012.9708	1003.2035	1003.2739	1002.0300	1008.2993	1009.5825
beta	1023.3813	1020.6660	1013.5214	1014.5941	1017.7900	1020.1084	1026.5898
ipso	997.2870	1004.8453	997.5289	994.5248	997.4500	997.2334	995.2924
ortho	2000.0000	2000.0000	2000.0000	2000.0000	2000.0000	2000.0000	2000.0000
meta	1992.7126	1998.5969	1992.6885	1992.1197	1993.9600	1998.9512	1998.5203
para	1000.4732	1002.0450	995.3993	996.1033	996.3000	990.7455	1009.8149
	FID8	FID9	FID10	FID11	FID12	FID13	FID14
Carbonyl	1035.9363	1030.8820	1036.1909	1032.1311	1037.3907	1024.0971	1024.5210
alpha	1001.9303	1003.4730	1005.0266	1006.1728	1005.1303	1008.4293	1009.3552
beta	1024.3695	1026.3869	1025.0974	1022.1747	1025.7833	1011.2722	1011.4072
ipso	989.3285	986.8934	987.6185	981.5342	994.8743	996.3373	999.1540
ortho	2000.0000	2000.0000	2000.0000	2000.0000	2000.0000	2000.0000	2000.0000
meta	1999.3889	1990.4701	1998.3337	2000.7122	2000.6795	1990.0758	1997.9207
para	1005.6759	1005.9232	1003.2213	1006.2162	1003.8437	1000.1477	1000.1500
	FID15	FID16	FID17	FID18	FID19	FID20	FID21
Carbonyl	1027.9139	1019.7282	1025.1746	1026.1664	1049.7763	1046.5167	1050.0337
alpha	1006.0247	1005.8741	1004.4005	1000.2568	1004.5812	1006.6991	1008.0525
beta	1008.1225	1007.3498	1010.6878	1009.3508	1041.5413	1041.7738	1042.4451
ipso	996.6836	998.2529	999.3033	994.3016	1050.4127	1050.0789	1050.6744
ortho	2000.0000	2000.0000	2000.0000	2000.0000	2000.0000	2000.0000	2000.0000
meta	1992.7502	1992.8161	1996.7548	1995.4916	2045.6269	2049.0612	2047.0662
para	999.8950	993.2497	1006.2255	998.7183	1024.0756	1023.1033	1023.1998
	FID22	FID23	FID24	FID25			
Carbonyl	1048.1311	1045.8721	1045.1385	1043.7043			
alpha	1006.9813	1005.6812	1008.2614	1002.5222			
beta	1038.5036	1038.6504	1038.8879	1039.1591			
ipso	1050.8729	1050.4298	1048.1003	1047.4008			
ortho	2000.0000	2000.0000	2000.0000	2000.0000			
meta	2047.7224	2044.6926	2042.9038	2044.5818			
para	1023.7286	1021.8183	1021.6836	1022.3455			

Kinetic Isotope Effects

	KIE1	KIE2	KIE3	KIE4	KIE5	KIE6	KIE7
Carbonyl	1.011	1.024	1.019	1.017	1.020	1.028	1.023
alpha	0.999	1.003	0.995	0.997	0.995	0.998	0.995
beta	1.015	1.015	1.007	1.009	1.008	1.012	1.003
ipso	0.995	1.002	0.996	0.992	0.993	0.997	0.990
ortho	1.000	1.000	1.000	1.000	1.000	1.000	1.000
meta	0.998	1.002	0.997	0.997	0.997	1.000	0.999
para	0.996	1.000	0.995	0.994	0.995	0.991	0.995
	KIE8	KIE9	KIE10	KIE11	KIE12	KIE13	KIE14
Carbonyl	1.028	1.021	1.027	1.028	1.026	1.024	1.033
alpha	0.997	1.000	0.998	0.998	0.998	0.997	1.002
beta	1.006	1.003	1.003	0.998	1.009	1.009	1.009
ipso	0.991	0.988	0.992	0.986	0.998	0.995	0.996

ortho	1.000	1.000	1.000	1.000	1.000	1.000	1.000
meta	1.002	0.998	1.001	1.002	1.002	0.989	0.993
para	0.996	0.993	0.993	0.994	0.990	1.001	1.004
	KIE15	KIE16	KIE17	KIE18	KIE19	KIE20	KIE21
Carbonyl	1.027	1.021	1.026	1.032	1.029	1.027	1.025
alpha	1.000	0.996	0.993	0.989	0.995	1.001	0.998
beta	1.005	1.001	1.009	1.006	1.016	1.015	1.014
ipso	0.994	0.992	0.994	0.990	1.002	1.001	1.000
ortho	1.000	1.000	1.000	1.000	1.000	1.000	1.000
meta	0.992	0.990	0.989	0.991	1.000	1.001	0.997
para	1.005	0.995	1.008	1.002	1.009	1.009	1.007
	KIE22	KIE23	KIE24	KIE25	Avg. KIE	Stdv. KIE	95% conf
Carbonyl	1.027	1.023	1.020	1.022	1.024	0.005	0.002
alpha	1.005	0.998	0.998	0.992	0.997	0.003	0.001
beta	1.011	1.010	1.013	1.009	1.009	0.005	0.002
ipso	1.003	1.001	0.999	0.998	0.995	0.005	0.002
ortho	1.000	1.000	1.000	1.000	1.000	0.000	0.000
meta	1.001	0.999	0.997	0.998	0.997	0.004	0.003
para	1.008	1.007	1.008	1.006	1.000	0.007	0.004

Single point calculations

Single point calculations were performed on the optimized geometries using a series of functionals, each with a triple- ζ basis set 6-311++G** and a PCM or SMD solvent model for water^{191,192,262} Based on a recent review by Mardirossian and Head-Gordon, ten different methods were chosen.³¹⁶ The D3 empirical dispersion correction presented by Grimme²⁰⁶ and/or the Becke-Johnson dampening variant¹⁹³ were applied when deemed appropriate. The methods utilized are as follows:

- {1} B3LYP-D3(0)/6-311++G**¹⁸⁵⁻¹⁸⁷
- {2} B3LYP-D3(BJ)/6-311++G**
- {3} M05-2X-D3(0)/6-311++G**³¹⁷
- {4} M06-2X-D3(0)/6-311++G**²⁸⁶
- {5} M06L-D3(0)/6-311++G**³¹⁸

- {6} ω B97X-D/6-311++G**³¹⁹
- {7} PBE0-D3(BJ)/6-311++G**³²⁰
- {8} MPW1K/6-311++G**³²¹
- {9} ω B97X-D/def2-TZVPP³²²
- {10} MN15-L/6-311++G**³²³

It should be noted that the MN15-L functional is not available with *Gaussian09*, so the *Gaussian16* package was used to perform this calculation.³²⁴

Evaluation of previous computational studies

The calculations presented in Section 2.2.1 and herein differ from those performed by Duarte and Santos.²⁰³ There are three key differences between the calculations: (a) the DFT methods used for optimizations and single-point energy calculations; Duarte and Santos utilized mPW2PLYP/6-311+G**//M062X/6-31+G** calculations for the description of their system, (b) the diarylprolinol catalyst; we used the bis(trifluoromethyl) substituted catalyst, while Duarte and Santos utilized a simplified version (α,α -bis-phenyl-2-pyrrolidinemethanol trimethylsilyl ether), and (c) Duarte and Santos utilize 2-pentenal while we used *p*-chlorocinnamaldehyde for our study.

The computed difference between **TS-iminium** and **TS-A_{N'}**, as reported by Duarte and Santos, is 0.6 kcal mol⁻¹. This is inconsistent with the 11.5 kcal mol⁻¹ difference reported in our investigation. The geometries corresponding to **TS-iminium** and **TS-A_{N'}** presented in the supporting information of the Santos study were re-calculated using B3LYP/6-31G* and the relative energetics evaluated using a series of single point calculations (*vide supra*). The energy difference between these two TSs was found to be an average of 3.2 kcal mol⁻¹ (See Table 5.1). This difference is much lower than the 11.5

kcal mol⁻¹ difference observed for our system (see Chapter 2.2.1) but higher than the 0.6 kcal mol⁻¹ difference reported by Santos.²⁰³ We surmise that the origin of this difference comes from the fact that **TS-A_{N'}** is likely more energetically disfavored for *p*-chlorocinnamaldehyde compared to 2-pentenal (due to disruption in the π -conjugation with the aromatic ring of *p*-chlorocinnamaldehyde). Our evaluation of Santos's work and comparison to our results conclude that (a) **TS-iminium** and **TS-A_{N'}** are closer in energy for the 2-pentenal than *p*-chlorocinnamaldehyde, and (b) The large difference in energy (>10 kcal mol⁻¹) between **TS-iminium** and **TS-A_{N'}** for *p*-chlorocinnamaldehyde (Table 5.1) strongly suggests that these steps cannot be co-rate-determining.

Table 5. 1. Comparative analysis of relative energies of the two steps in the iminium-ion mechanism for previously published (Santos) and the current study

Solvent model = PCM(water)	Santos System (2-pentenal)		System analyzed in this study (<i>p</i> -chlorocinnamaldehyde)	
	TS-iminium ΔG_{rel} (kcal mol ⁻¹)	TS-A _{N'} ΔG_{rel} (kcal mol ⁻¹)	TS-iminium ΔG_{rel} (kcal mol ⁻¹)	TS-A _{N'} ΔG_{rel} (kcal mol ⁻¹)
From Ref. 10	0.00	0.61	---	---
B3LYP-D3(0)/6-311++G**	0.00	2.54	0.00	12.33
B3LYP-D3(BJ)/6-311++G**	0.00	2.92	0.00	12.50
M05-2X-D3(0)/6-311++G**	0.00	3.51	0.00	13.12
M06-2X-D3(0)/6-311++G**	0.00	5.57	0.00	13.45
M06L-D3(0)/6-311++G**	0.00	0.22	0.00	10.47
ω B97X-D/6-311++G**	0.00	3.06	0.00	13.58
PBE0-D3(BJ)/6-311++G**	0.00	3.38	0.00	11.74
MPW1K/6-311++G**	0.00	5.31	0.00	13.20
ω B97X-D/def2-TZVPP	0.00	3.13	0.00	12.19
MN15-L/6-311++G**	2.27	0.00	0.00	10.30

Table 5. 2. Extrapolated Free energy barriers for the three key transition structures presented in Chapter 2.2.1 expressed versus separated starting materials, and versus the carbinol amine intermediate - using ten different high-level DFT single-point energy calculations and the PCM solvent model for water

Solvent model = PCM(water)	TS-iminium	TS-A _{N'}	TS-S _N 2'
-------------------------------	------------	--------------------	----------------------

DFT method	ΔG versus separated starting materials (kcal mol ⁻¹)	ΔG versus carbinol amine (kcal mol ⁻¹)	ΔG versus separated starting materials (kcal mol ⁻¹)	ΔG versus carbinol amine (kcal mol ⁻¹)	ΔG versus separated starting materials (kcal mol ⁻¹)	ΔG versus carbinol amine (kcal mol ⁻¹)
B3LYP-D3(0)/6-311++G**	20.43	7.77	32.76	20.10	29.05	16.39
B3LYP-D3(BJ)/6-311++G**	19.80	8.08	32.30	20.59	28.65	16.94
M0-2X-D3(0)/6-311++G**	20.02	15.77	33.14	28.90	28.39	24.14
M06-2X-D3(0)/6-311++G**	21.75	16.99	35.20	30.45	30.57	25.81
M06L-D3(0)/6-311++G**	23.39	9.28	33.86	19.75	31.66	17.55
ω B97X-D(0)/6-311++G**	23.42	15.96	37.00	29.54	32.82	25.36
PBE0-D3(BJ)/6-311++G**	20.64	14.21	32.38	25.96	28.94	22.51
MPW1K/6-311++G**	36.72	24.45	49.92	37.65	43.43	31.16
ω B97X-D/def2-TZVPP	28.18	19.27	40.37	31.64	36.98	28.07
MN15-L/6-311++G**	29.01	17.12	39.31	27.41	37.18	25.28

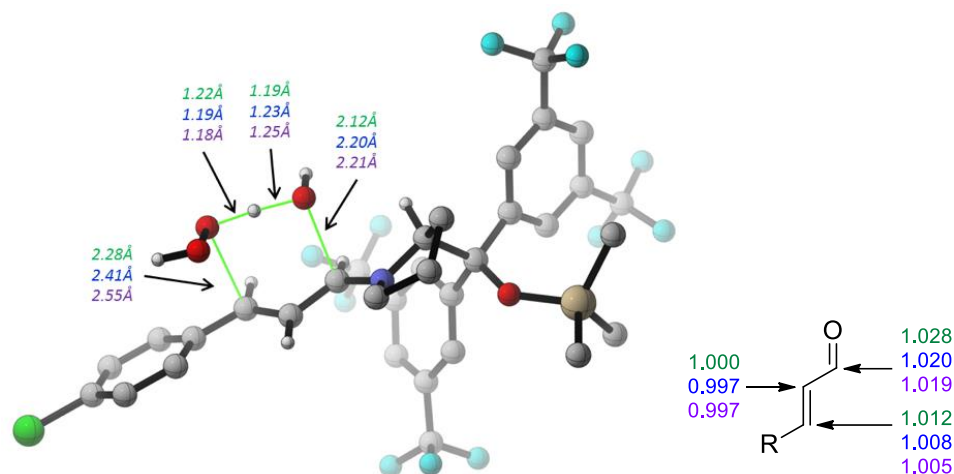
Table 5. 3. Extrapolated Free energy barriers for the three key transition structures presented in Chapter 2.2.1 expressed versus separated starting materials, and versus the carbinol amine intermediate - using ten different high-level DFT single-point energy calculations and the SMD solvent model for water

DFT method	TS-iminium		TS-A _N		TS-S _N 2'	
	ΔG versus separated starting materials (kcal mol ⁻¹)	ΔG versus carbinol amine (kcal mol ⁻¹)	ΔG versus separated starting materials (kcal mol ⁻¹)	ΔG versus carbinol amine (kcal mol ⁻¹)	ΔG versus separated starting materials (kcal mol ⁻¹)	ΔG versus carbinol amine (kcal mol ⁻¹)
B3LYP-D3(0)/6-311++G**	18.91	11.79	30.20	23.07	26.24	19.11
B3LYP-D3(BJ)/6-311++G**	18.28	7.79	29.74	19.25	25.84	15.35
M0-2X-D3(0)/6-311++G**	18.46	18.34	30.17	30.04	25.10	24.97
M06-2X-D3(0)/6-311++G**	19.78	19.96	31.77	31.96	27.01	27.20
M06L-D3(0)/6-311++G**	21.42	14.80	31.19	24.56	28.94	22.32
ω B97X-D(0)/6-311++G**	21.73	19.70	34.12	32.09	29.70	27.67
PBE0-D3(BJ)/6-311++G**	19.06	18.14	29.79	28.87	26.00	25.08
MPW1K/6-311++G**	34.08	27.58	46.90	39.41	40.16	32.66
ω B97X-D/def2-TZVPP	25.99	24.03	37.16	35.20	33.52	31.56

Detailed analysis of TS-S_N2': Modeling TS-S_N2' with additional functionals

To verify that the geometries and KIEs predicted for **TS-S_N2'** are not unique to B3LYP/6-31G*, **TS-S_N2'** was located and isotope effects were predicted using three

additional functionals commonly used in the literature: ω B97X-D (green numbers), B3LYP-D3 (blue numbers), M06L (purple numbers).

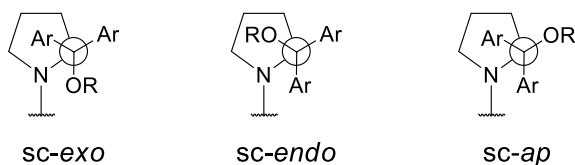


Detailed analysis of TS- S_N2' : Systematic conformational search

As the final step in identifying the lowest energy structure corresponding to **TS- S_N2'** , an in-depth search was performed analyzing a range of possible conformations available. Three major aspects of the TS geometry were modified to arrive at the lowest energy conformation of this TS: (1) the orientation of the diaryl group on the catalyst; (2) the puckering of the five-membered ring of the catalyst; (3) the orientation of the hydrogen peroxide and the carbonolamine hydroxide. The major orientations are discussed below.

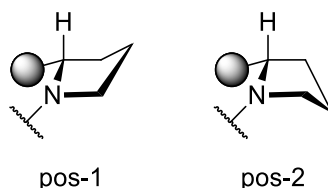
1. Orientation of the diaryl group of the catalyst

Diaryl prolinol catalysts like (*S*)- α,α -Bis[3,5-bis(trifluoromethyl)phenyl]-2-pyrrolidinemethanol trimethylsilyl ether are known to have three major orientations: *sc-exo*, *sc-endo*, and *sc-ap*. These orientations were explored in detail.



2. Puckering of the five-membered ring of the catalyst

The five-membered ring of the catalyst can assume two different puckering positions. The C-4 atom can either point upward in an anti-periplanar direction with respect to the catalyst arm (pos-1), or it can point down in a similar fashion to that of the catalyst's arm (pos-2). These orientations were explored for all transition structures identified in this conformational search.



3. Orientation of the hydrogen peroxide and the carbonolamine hydroxide

The final variable explored in the conformational search was the configuration of the hydrogen peroxide –OH group and the carbonolamine –H group. Both of these groups could either point to the same side as the catalyst arm or away. This gives rise to the four orientations: orient-1, orient-2, orient-3, and orient-4.

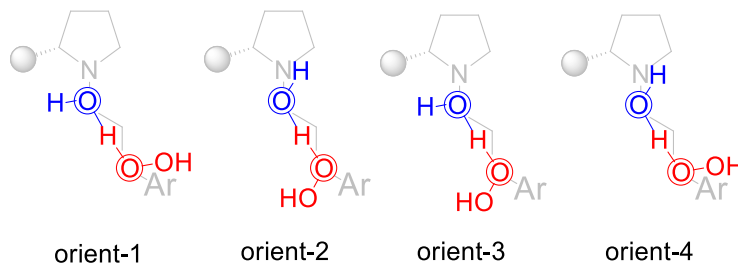


Table 5.4 contains the extrapolated ΔG^\ddagger for the 20 lowest energy transition state structures. Column 1 identifies the enantiomer being formed in the TS. Column 2 identifies the orientation of the catalyst arm. Column 3 identifies the puckering of the catalyst ring.

Column 4 identifies the orientation of the hydrogen peroxide and the carbinolamine hydroxide. Below are the coordinates and energies for the TSs from the conformational search, not appearing in Chapter 2.2.1 (Entry 2-20). The lowest five conformations resulting from this conformational search corresponded to the major enantiomer. Typically, we would predict the ^{13}C KIEs as a weighed average (based on relative energetics) of the predicted KIEs of these TSs. However, the predicted KIEs for all these TSs were near identical and so we presented the predicted KIE for the geometry corresponding to Entry 1 in Table 5.4.

TS-S_N2'-Ent, the lowest energy confirmation of the minor enantiomer (Entry 6 in Table 5.4), was subjected to a single point calculation using B3LYP-D3(BJ)/6-311++G**/SMD(water). The extrapolated free energy yielded an uncorrected ΔG^\ddagger value of 27.5 kcal mol⁻¹. This corresponds to a $\Delta\Delta G^\ddagger$ energy of 1.63 kcal mol⁻¹ between the two enantiomeric transition states meaning a predicted enantiomeric excess of 88.1%.

Table 5. 4. Relative energies for conformational search of TS-S_N2'

Entry	Enantiomer	Arm	Ring	-H / -OH	$\Delta\Delta G^\ddagger$ (kcal mol ⁻¹)
1	maj	endo	pos-2	orient-3	0.000
2	maj	endo	pos-2	orient-1	0.488
3	maj	endo	pos-1	orient-1	0.532
4	maj	endo	pos-1	orient-3	0.929
5	maj	endo	pos-2	orient-4	1.268
6	min	ap	pos-1	orient-1	1.400
7	maj	ap	pos-1	orient-3	1.595
8	maj	endo	pos-2	orient-1	1.658
9	maj	exo	pos-1	orient-1	1.787
10	maj	endo	pos-1	orient-2	1.876
11	maj	exo	pos-1	orient-3	2.011
12	maj	exo	pos-1	orient-1	2.524
13	min	exo	pos-2	orient-1	2.794
14	min	exo	pos-1	orient-1	3.312
15	maj	exo	pos-2	orient-3	3.496
16	maj	exo	pos-2	orient-4	3.544
17	min	exo	pos-1	orient-1	4.096

18	min	endo	pos-2	orient-3	10.254
19	min	endo	pos-2	orient-3	10.693
20	min	endo	pos-1	orient-3	12.144

Energy profile

From the B3LYP/6-31G* optimized structures and a B3LYP-D3/6-31+G**/PCM(water) single point calculation, a Free Energy Profile was assembled for all major steps in the catalytic cycle. Numbering and nomenclature remains the same from the Chapter 2.2.1. Figure S7 was generated using a [aldehyde-catalyst-hydrogen peroxide] non-covalent complex as the ‘Starting Material’. The coordinates of each of these TSs and intermediates are given below.

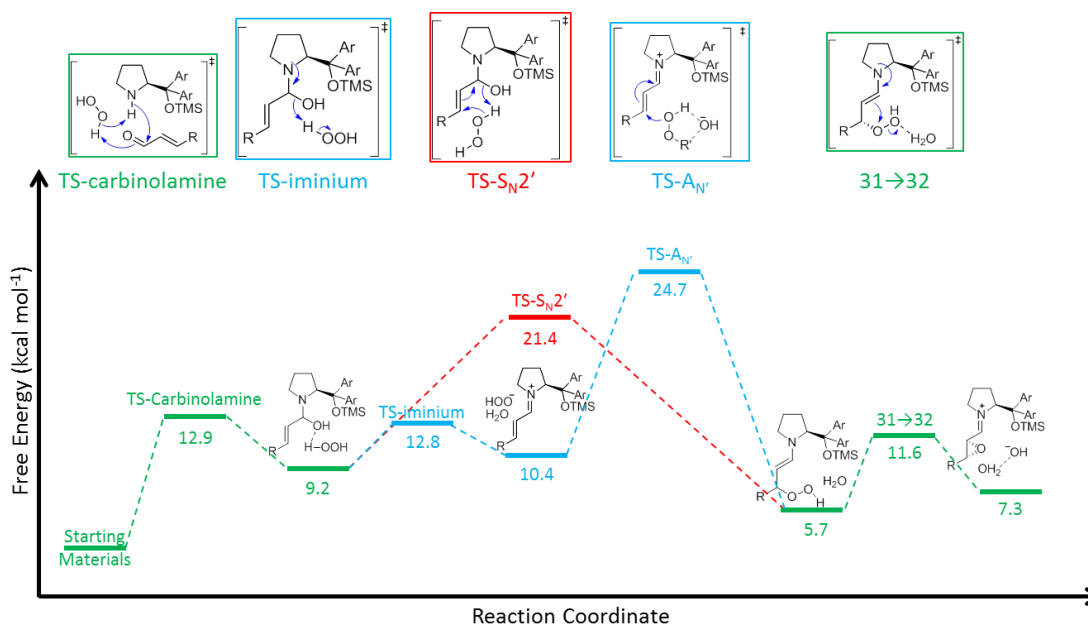


Figure 5. 4. Energy profile for the Jørgensen epoxidation

5.3 Non-covalent Organocatalysis

5.3.1 Quaternary ammonium salt catalysis

5.3.1.1 Bifunctional Ammonium Salt Catalyzed Asymmetric α -fluorination of β -Ketoesters

Computational investigation of binding modes

As discussed in Chapter 3.1.1, a systematic search was performed of the conformational variety of the catalyst and system. Table 5.5 tabulates the entry number, enantiomer of product being formed, binding mode, α -angle, β -angle, γ -angle, and relative free, zero-point, and potential energies in kcal mol⁻¹, respectively from left to right.

Table 5.5. Relative energies and configurations of the conformational search

Entry	Enant	BM	α	β	γ	Δ Free (kcal mol ⁻¹)	Δ ZPE (kcal mol ⁻¹)	Δ PE (kcal mol ⁻¹)
1	R	2	1	1	1	0.000	0.442	0.430
2	R	2	1	1	1	0.097	0.000	0.000
3	S	2	1	1	1	1.354	3.349	3.894
4	S	2	1	1	1	1.621	3.439	3.884
5	R	2	1	1	3	1.726	2.750	3.019
6	R	2	1	1	1	1.806	1.562	1.485
7	R	2	2	1	3	2.225	1.443	1.218
8	R	2	2	1	2	2.225	1.443	1.218
9	R	2	1	1	3	2.305	2.729	3.084
10	S	2	1	1	3	2.334	2.984	3.422
11	R	2	1	1	1	2.530	3.221	3.260
12	R	2	1	1	1	2.543	3.223	3.259
13	R	4	1	1	1	2.937	3.020	3.069
14	R	4	2	1	3	2.984	3.321	3.617
15	S	2	2	1	3	3.224	3.843	4.229
16	R	4	1	1	1	3.262	3.181	3.265
17	R	4	1	1	3	3.395	4.369	4.897
18	R	2	3	1	1	3.459	1.089	0.656
19	R	2	2	1	3	3.525	3.144	3.147
20	S	2	1	1	1	3.940	4.530	4.841

Figure 3.2

Figure 3.5a

Figure 3.3b

21	S	2	1	1	1	3.948	4.613	4.903	Figure 3.3a
22	S	3	1	1	1	5.125	7.887	8.283	
23	R	2	1	2	1	6.116	5.333	5.232	
24	R	2	3	1	1	6.903	5.609	5.498	Figure 3.1
25	R	1	1	1	3	6.938	7.031	7.639	
26	R	2	3	1	1	7.209	6.798	6.971	
27	R	2	2	1	3	7.775	9.206	9.322	
28	R	2	3	1	3	7.864	6.421	6.327	
29	R	3	1	1	3	7.946	8.926	9.106	
30	S	1	2	1	3	8.494	9.151	9.559	
31	R	1	2	1	3	8.763	8.658	8.948	
32	R	2	2	1	4	9.048	9.126	9.377	
33	R	1	2	1	3	10.082	8.973	9.402	

Electrostatic potential map

The electrostatic potential map in Figure 3.6 was generated from an NBO.²⁵⁰ Table 5.6 records these charges.

Table 5.6. Summary of Natural Populations Analysis

Atom	Number	Natural Charge	Natural Population			
			Core	Valence	Rydberg	Total
C	1	-0.38713	1.99921	4.37278	0.01514	6.38713
C	2	-0.04630	1.99909	4.01801	0.02919	6.04630
C	3	-0.00334	1.99905	3.97577	0.02852	6.00334
C	4	-0.40501	1.99920	4.39267	0.01313	6.40501
C	5	-0.37269	1.99926	4.36046	0.01297	6.37269
C	6	-0.38164	1.99926	4.36965	0.01273	6.38164
N	7	-0.69640	1.99929	5.67520	0.02190	7.69640
C	8	0.80977	1.99935	3.14796	0.04292	5.19023
N	9	-0.65072	1.99924	5.63354	0.01794	7.65072
C	10	0.12993	1.99907	3.84098	0.03003	5.87007
C	11	-0.07740	1.99904	4.06144	0.01693	6.07740
C	12	-0.17954	1.99881	4.15266	0.02807	6.17954
C	13	-0.15288	1.99890	4.13664	0.01735	6.15288
C	14	-0.15745	1.99896	4.13829	0.02019	6.15745
C	15	-0.15795	1.99889	4.14227	0.01679	6.15795
N	16	-0.35979	1.99950	5.34171	0.01858	7.35979
C	17	-0.19755	1.99908	4.17285	0.02562	6.19755
O	18	-0.70661	1.99976	6.69642	0.01043	8.70661
C	19	-0.36331	1.99925	4.34909	0.01497	6.36331
C	20	-0.35646	1.99922	4.33653	0.02070	6.35646

H	21	0.44582	0.00000	0.54917	0.00501	0.55418
H	22	0.21803	0.00000	0.77804	0.00393	0.78197
H	23	0.24564	0.00000	0.75213	0.00223	0.75436
H	24	0.27257	0.00000	0.72558	0.00186	0.72743
H	25	0.45902	0.00000	0.53667	0.00431	0.54098
H	26	0.22801	0.00000	0.76946	0.00253	0.77199
H	27	0.25764	0.00000	0.73761	0.00475	0.74236
H	28	0.21250	0.00000	0.78563	0.00187	0.78750
H	29	0.19505	0.00000	0.80273	0.00222	0.80495
H	30	0.20263	0.00000	0.79502	0.00235	0.79737
H	31	0.20479	0.00000	0.79340	0.00182	0.79521
H	32	0.20829	0.00000	0.78982	0.00189	0.79171
H	33	0.19024	0.00000	0.80757	0.00219	0.80976
H	34	0.22460	0.00000	0.77326	0.00214	0.77540
H	35	0.21572	0.00000	0.78248	0.00180	0.78428
H	36	0.26525	0.00000	0.73166	0.00309	0.73475
H	37	0.21049	0.00000	0.78749	0.00202	0.78951
H	38	0.21425	0.00000	0.78258	0.00317	0.78575
H	39	0.25358	0.00000	0.74197	0.00445	0.74642
H	40	0.21988	0.00000	0.77660	0.00352	0.78012
H	41	0.22470	0.00000	0.77329	0.00201	0.77530
H	42	0.20354	0.00000	0.79482	0.00163	0.79646
H	43	0.25226	0.00000	0.74601	0.00173	0.74774
O	44	-0.88302	1.99981	6.87369	0.00952	8.88302
S	45	2.16158	9.99824	3.63687	0.20332	13.83842
O	46	-0.88057	1.99981	6.86873	0.01203	8.88057
N	47	-0.70748	1.99969	5.67835	0.02944	7.70748
C	48	-0.17740	1.99873	4.15113	0.02754	6.17740
C	49	-0.21290	1.99911	4.17587	0.03793	6.21290
C	50	-0.20202	1.99913	4.17999	0.02290	6.20202
C	51	-0.17525	1.99915	4.15707	0.01902	6.17525
C	52	-0.20452	1.99914	4.18729	0.01808	6.20452
C	53	-0.22218	1.99913	4.18611	0.03695	6.22218
H	54	0.24699	0.00000	0.74878	0.00423	0.75301
H	55	0.23748	0.00000	0.75972	0.00281	0.76252
H	56	0.20908	0.00000	0.78895	0.00196	0.79092
H	57	0.20849	0.00000	0.78952	0.00199	0.79151
H	58	0.23393	0.00000	0.76274	0.00333	0.76607
S	59	2.17961	9.99821	3.61737	0.20482	13.82039
C	60	-0.29339	1.99874	4.26158	0.03307	6.29339
C	61	-0.18494	1.99899	4.16351	0.02243	6.18494

C	62	-0.19592	1.99914	4.18013	0.01665	6.19592
C	63	-0.17285	1.99916	4.15689	0.01680	6.17285
C	64	-0.19510	1.99914	4.17902	0.01693	6.19510
C	65	-0.16964	1.99902	4.15191	0.01871	6.16964
H	66	0.25134	0.00000	0.74488	0.00378	0.74866
H	67	0.21283	0.00000	0.78547	0.00169	0.78717
H	68	0.21178	0.00000	0.78706	0.00116	0.78822
H	69	0.21297	0.00000	0.78537	0.00166	0.78703
H	70	0.24621	0.00000	0.75204	0.00175	0.75379
O	71	-0.87561	1.99981	6.86537	0.01044	8.87561
O	72	-0.91581	1.99980	6.90296	0.01304	8.91581
O	73	-0.79214	1.99974	6.73417	0.05823	8.79214
C	74	0.62390	1.99899	3.33243	0.04468	5.37610
C	75	-0.22790	1.99896	4.17875	0.05019	6.22790
C	76	-0.04701	1.99902	4.01851	0.02949	6.04701
C	77	0.78370	1.99901	3.16495	0.05233	5.21630
O	78	-0.69580	1.99973	6.68313	0.01293	8.69580
O	79	-0.60903	1.99970	6.58655	0.02278	8.60903
C	80	-0.23471	1.99917	4.18449	0.05104	6.23471
C	81	-0.21433	1.99916	4.19534	0.01983	6.21433
C	82	-0.18754	1.99917	4.16859	0.01978	6.18754
C	83	-0.25500	1.99915	4.21499	0.04086	6.25500
C	84	0.12384	1.99908	3.85160	0.02548	5.87616
H	85	0.20885	0.00000	0.78592	0.00524	0.79115
H	86	0.20908	0.00000	0.78893	0.00199	0.79092
H	87	0.20283	0.00000	0.79533	0.00184	0.79717
H	88	0.20393	0.00000	0.79178	0.00428	0.79607
C	89	-0.44053	1.99922	4.41396	0.02735	6.44053
H	90	0.23748	0.00000	0.75844	0.00407	0.76252
H	91	0.22197	0.00000	0.77468	0.00335	0.77803
C	92	0.27109	1.99909	3.70537	0.02444	5.72891
F	93	-0.32018	1.99998	7.30094	0.01926	9.32018
C	94	-0.60020	1.99922	4.59035	0.01063	6.60020
H	95	0.20254	0.00000	0.79600	0.00146	0.79746
H	96	0.22322	0.00000	0.77498	0.00180	0.77678
H	97	0.20536	0.00000	0.79306	0.00157	0.79464
C	98	-0.60152	1.99920	4.59111	0.01121	6.60152
H	99	0.19727	0.00000	0.80128	0.00145	0.80273
H	100	0.22327	0.00000	0.77508	0.00165	0.77673
H	101	0.21389	0.00000	0.78392	0.00219	0.78611
C	102	-0.57700	1.99922	4.56621	0.01158	6.57700

H	103	0.20508	0.00000	0.79308	0.00183	0.79492
H	104	0.20255	0.00000	0.79615	0.00130	0.79745
H	105	0.20687	0.00000	0.79155	0.00158	0.79313
C	106	-0.10519	1.99904	4.07375	0.03240	6.10519
C	107	0.07959	1.99891	3.90024	0.02125	5.92041
C	108	-0.19284	1.99909	4.16774	0.02601	6.19284
C	109	-0.23345	1.99919	4.20501	0.02925	6.23345
C	110	-0.09776	1.99909	4.07154	0.02713	6.09776
C	111	-0.13069	1.99914	4.12240	0.00915	6.13069
H	112	0.21872	0.00000	0.77745	0.00383	0.78128
C	113	-0.18964	1.99915	4.17303	0.01746	6.18964
H	114	0.19509	0.00000	0.80187	0.00305	0.80491
C	115	-0.16523	1.99908	4.15008	0.01607	6.16523
C	116	-0.18111	1.99913	4.15633	0.02565	6.18111
H	117	0.20518	0.00000	0.79280	0.00203	0.79482
C	118	-0.19969	1.99914	4.18204	0.01851	6.19969
H	119	0.21061	0.00000	0.78812	0.00127	0.78939
H	120	0.20664	0.00000	0.79101	0.00235	0.79336
H	121	0.20444	0.00000	0.79125	0.00431	0.79556
H	122	0.21024	0.00000	0.78801	0.00174	0.78976
C	123	0.79753	1.99928	3.15548	0.04771	5.20247
C	124	0.80059	1.99927	3.15235	0.04779	5.19941
O	125	-0.59393	1.99975	6.58371	0.01047	8.59393
O	126	-0.55569	1.99973	6.53999	0.01598	8.55569
O	127	-0.62109	1.99975	6.60701	0.01433	8.62109
O	128	-0.54877	1.99972	6.53313	0.01592	8.54877
C	129	-0.21173	1.99921	4.19624	0.01628	6.21173
H	130	0.18682	0.00000	0.81174	0.00144	0.81318
H	131	0.18532	0.00000	0.81269	0.00199	0.81468
H	132	0.18753	0.00000	0.81055	0.00193	0.81247
C	133	-0.21193	1.99922	4.19599	0.01672	6.21193
H	134	0.18428	0.00000	0.81425	0.00147	0.81572
H	135	0.18672	0.00000	0.81123	0.00204	0.81328
H	136	0.18561	0.00000	0.81234	0.00206	0.81439
Total		0.02576	165.94109	393.75723	2.27591	561.97424

5.3.1.2 Bifunctional Ammonium Salt Catalyzed Asymmetric α -Hydroxylation of β -
Ketoesters by Simultaneous Resolution of Oxaziridines

Computational investigation of binding modes 5.3.2 Bifunctional thiourea-tertiary amine catalysis

As discussed in Chapter 3.1.2, a systematic search was performed of the conformational variety of the catalyst and system. Table 5.7 tabulates the entry number, enantiomer of product being formed, binding mode, enantiomer of oxaziridine being used, α -angle, β -angle, γ -angle, and relative free, zero-point, and potential energies in kcal mol⁻¹, respectively from left to right for the naphthyl catalyst.

Table 5.7. Relative energies and configurations of the conformational search

<u>Entry</u>	<u>Prod Enant</u>	<u>Oxaz</u>	<u>BM</u>	<u>α</u>	<u>β</u>	<u>ΔFree (kcal mol⁻¹)</u>	<u>ΔZPE (kcal mol⁻¹)</u>	<u>ΔPE (kcal mol⁻¹)</u>
1	R	SS	2	3	1	0.000	0.000	0.000
2	R	SS	2	3	1	0.006	0.004	0.001
3	R	SS	2	2	1	0.127	3.011	3.342
4	R	SS	2	3	1	0.129	0.318	0.249
5	R	SS	2	3	1	0.238	0.574	0.644
6	R	SS	2	3	1	0.244	0.611	0.614
7	R	RR	2	2	1	0.783	4.561	5.189
8	R	RR	2	3	1	1.054	2.742	2.814
9	R	SS	2	1	1	1.707	4.046	4.270
10	S	RR	4	3	1	1.966	2.868	3.100
11	R	RR	4	2	1	2.171	3.501	3.682
12	R	RR	2	3	1	2.191	3.138	3.124
13	R	SS	2	1	3	2.201	5.152	5.404
14	R	SS	2	2	1	2.263	3.043	3.094
15	S	RR	2	3	1	2.280	3.101	3.197
16	S	RR	4	2	1	2.281	3.392	3.630
17	S	SS	4	2	1	2.296	2.728	2.878
18	S	SS	2	3	1	2.441	2.741	2.504
19	R	SS	4	2	1	2.457	3.092	3.123
20	S	SS	2	3	1	2.830	2.764	2.471
21	S	SS	2	3	1	2.855	2.478	2.229

Figure 3.7a

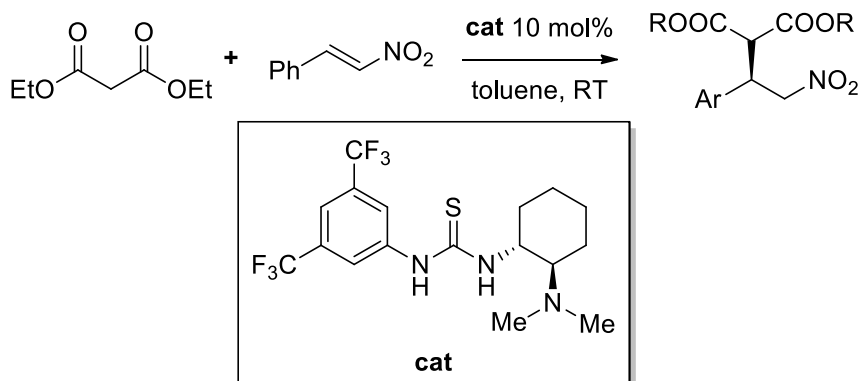
Figure 3.10

Figure 3.7b

22	S	SS	2	3	1	2.883	2.673	2.420
23	S	SS	2	2	1	3.077	6.924	7.523
24	R	RR	2	1	1	3.388	4.539	4.684
25	R	SS	2	1	1	3.423	4.244	4.135
26	R	SS	4	2	1	3.801	4.246	4.419
27	R	RR	1	3	1	4.019	4.925	5.302
28	R	RR	1	2	1	4.053	6.914	7.412
29	S	SS	2	1	1	4.062	5.962	6.269
30	R	SS	4	2	1	4.092	4.276	4.409
31	R	SS	2	2	1	4.204	4.335	4.019
32	R	SS	2	2	1	4.287	4.338	4.015
33	R	SS	4	1	1	4.309	6.247	6.438
34	R	SS	2	1	1	4.494	6.617	6.714
35	S	SS	4	3	1	4.617	5.393	5.548
36	R	RR	1	1	1	4.873	8.305	8.875
37	S	SS	2	2	1	5.082	6.795	7.071
38	R	SS	2	2	1	5.398	6.797	6.954
39	S	SS	2	1	1	5.643	5.836	5.862
40	R	RR	2	3	1	6.032	4.379	4.054
41	S	SS	4	2	1	6.074	5.622	5.540
42	S	RR	2	3	1	6.193	4.840	4.534
43	S	RR	1	1	1	6.281	8.744	9.069
44	R	SS	1	3	1	6.332	6.243	6.440
45	R	SS	2	2	2	6.379	9.372	9.659
46	S	SS	1	3	1	6.631	6.215	6.216
47	R	SS	1	1	1	7.120	9.106	9.675
48	S	SS	2	3	1	7.985	4.714	4.189
49	R	SS	2	-	-	8.008	8.165	7.918
50	R	SS	3	3	1	8.230	10.225	10.421
51	R	RR	3	3	1	8.518	10.519	10.497
52	R	RR	2	1	1	8.580	8.028	7.719
53	R	SS	2	1	1	8.618	9.730	10.278
54	R	RR	2	2	1	9.078	9.256	8.873
55	R	SS	3	3	2	9.618	11.743	11.994
56	S	SS	1	1	1	9.794	11.380	12.131
57	S	RR	2	1	1	10.964	10.420	10.346
58	R	RR	3	3	2	11.150	13.106	13.245

5.3.2 Isotope Effects Reveal Transition State of Bifunctional Thiourea- tertiary Amine-catalyzed Michael Addition

Basic KIE reaction



To a well stirred solution containing 1.2698g (8mmol) of *trans*- β -nitrostyrene, 1.6073g (1.25equiv., 10mmol) of diethyl malonate and dry toluene (16mL) was added 0.0662g (0.16mmol) of thiourea-catalyst (**cat**) under nitrogen. The reaction was monitored via ^1H NMR analysis until it reached ~80% conversion. After reaching the desired conversion, the reaction mixture was quenched using flash chromatography (5:1 hexanes/ethyl acetate eluent). The fractions were collected and concentrated *in vacuo*. This crude mixture was purified by flash chromatography eluting 5% ethyl acetate in hexanes. By this procedure, two identical reactions were taken to $77 \pm 2\%$ and $68 \pm 2\%$ conversion based on ^1H NMR analysis, comparing the alkene proton of nitrostyrene and the alpha carbons of diethyl malonate to the doublet peak of the product.

^{13}C NMR sample preparation

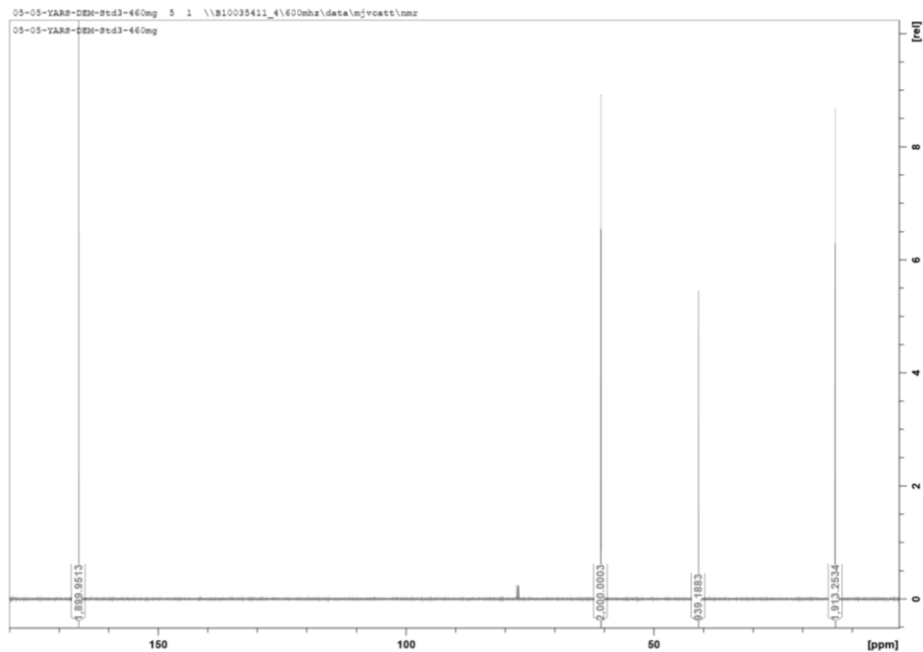
The recovered starting material (nitrostyrene or diethyl malonate) was carefully weighed and placed into a small dram vial where it was then dissolved in HPLC grade

deuterated chloroform (CDCl_3). This mixture was then pipetted into a clean NMR tube and filled with CDCl_3 to a height of five centimeters.

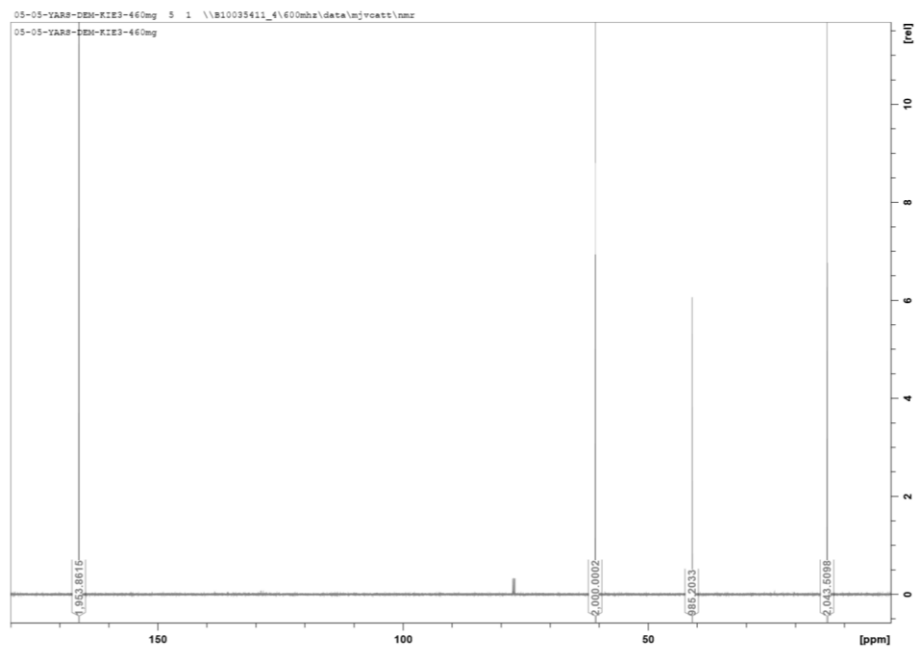
An identical mass of material was withdrawn from the bottle used for the initial experiment and also placed into a clean NMR and filled with CDCl_3 to a height of five centimeters.

Sample spectra for the determination of isotopic enrichment

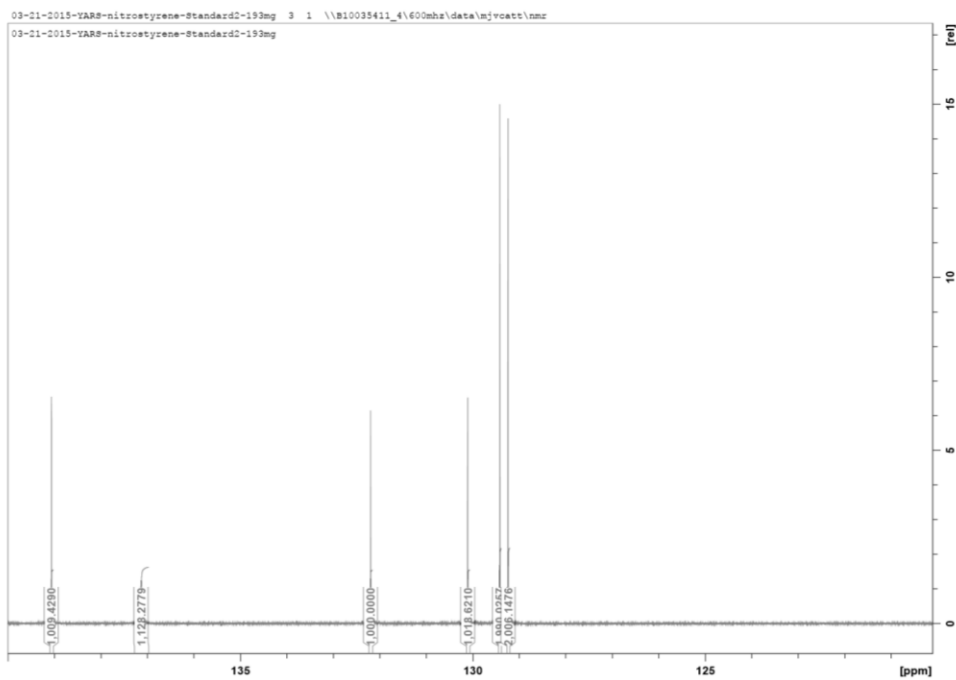
Standard (diethylmalonate):



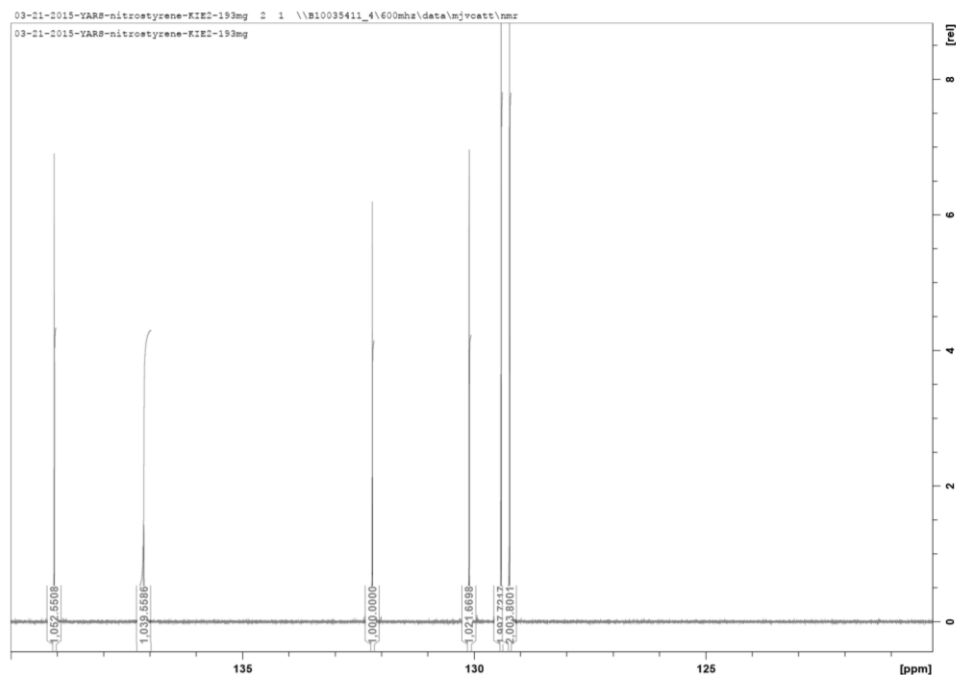
Experimental (diethylmalonate)



Standard (nitrostyrene):



Experimental (nitrostyrene):



Integrations of standard and experimental NMR spectra (diethylmalonate)

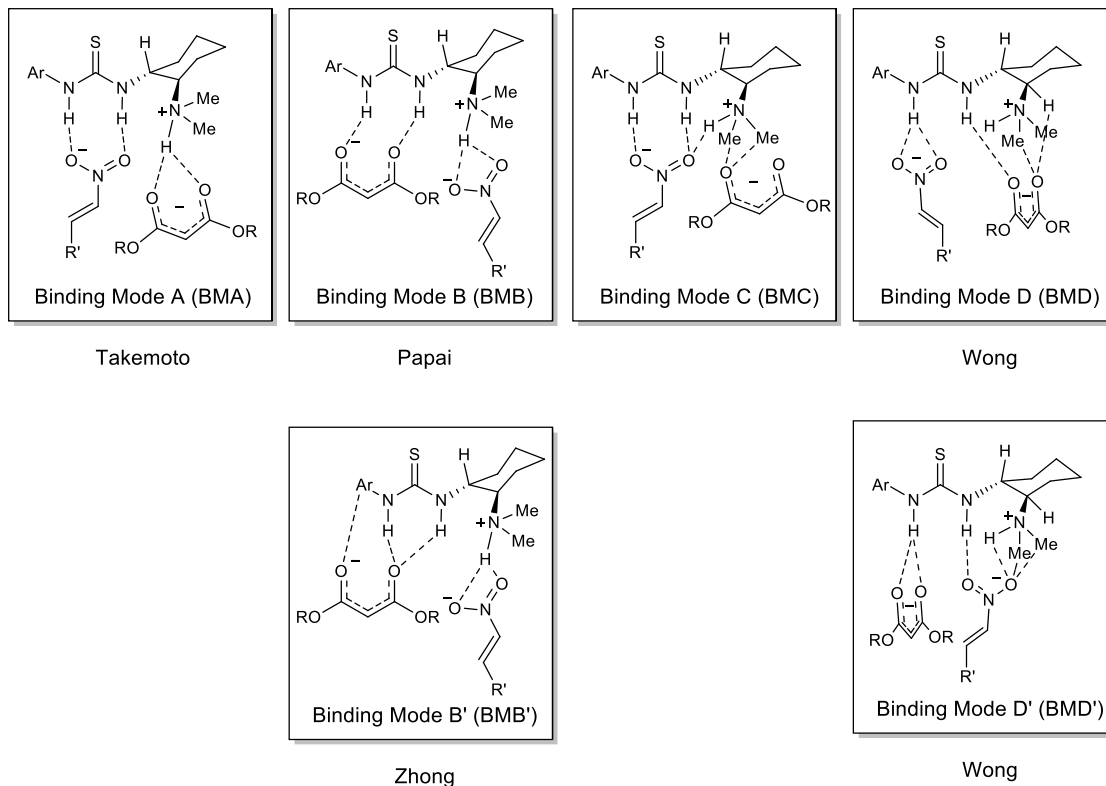
First Standard											
peak	fid1	fid2	fid3	fid4	fid5	fid6	average	stddev	cuts		
carbonyl	1955.72	1957.43	1956.35	1954.83	1955.21	1963.02	1957.09	3.05	6		
methylene	2000.00	2000.00	2000.00	2000.00	2000.00	2000.00	2000.00	0.00	5		
alpha	975.39	969.35	976.79	976.63	980.08	981.27	976.58	4.20	4		
methyl	2042.51	2039.39	2053.60	2041.85	2037.36	2044.75	2043.24	5.68	7		
First Experimental										%Conv:	65%
peak	fid1	fid2	fid3	fid4	fid5	fid6	average	stddev	KIE	stddev	
carbonyl	1977.72	1973.59	1972.33	1972.52	1978.64	1968.92	1973.96	3.64	1.008	0.002	
methylene	2000.00	2000.00	2000.00	2000.00	2000.00	2000.00	2000.00	0.00	1.000	0.000	
alpha	1009.53	1006.64	1004.95	1003.08	1011.88	1007.97	1007.34	3.17	1.030	0.005	
methyl	2026.56	2027.53	2034.53	2032.49	2024.33	2032.18	2029.60	4.02	0.994	0.003	
Second Standard											
peak	fid1	fid2	fid3	fid4	fid5	fid6	average	stddev	cuts		
carbonyl	1983.13	1977.25	1983.91	1984.04	1982.92	1981.79	1982.17	2.54	3		
methylene	2000.00	2000.00	2000.00	2000.00	2000.00	2000.00	2000.00	0.00	5		
alpha	981.78	978.38	980.62	981.38	978.01	978.67	979.81	1.65	4		
methyl	2038.38	2035.10	2044.18	2037.91	2032.89	2040.05	2038.09	3.92	7		
Second Experimental										%Conv:	65%
peak	fid1	fid2	fid3	fid4	fid5	fid6	average	stddev	KIE	stddev	
carbonyl	1984.44	1982.42	1986.35	1981.03	1985.91	1985.50	1984.28	2.12	1.001	0.002	
methylene	2000.00	2000.00	2000.00	2000.00	2000.00	2000.00	2000.00	0.00	1.000	0.000	
alpha	1012.13	1014.95	1015.49	1014.68	1016.88	1011.52	1014.28	2.05	1.034	0.003	
methyl	2044.99	2046.16	2052.75	2049.77		2046.38	2048.01	3.19	1.006	0.002	

Integrations of Standard and Experimental NMR spectra (nitrostyrene)

First Standard										
peak	fid1	fid2	fid3	fid4	fid5	fid6	average	stddev	cuts	
alpha	1023.69	1022.91	1029.27	1026.76	1028.20	1026.60	1026.24	2.49	4	
beta	1068.94	1063.96	1075.94	1062.22	1067.58		1067.73	5.32	22	
para	1000.00	1000.00	1000.00	1000.00	1000.00	1000.00	1000.00	0.00	3	
ipso	1030.87	1031.37	1027.37	1034.06	1034.10	1027.77	1030.92	2.92	4	
First Experimental										
									%Conv: 77%	
peak	fid1	fid2	fid3	fid4	fid5	fid6	average	stddev	KIE	stdev
alpha	1075.80	1073.58	1067.41	1074.15	1070.11	1077.49	1073.09	3.72	1.029	0.004
beta	1073.16	1060.05	1071.91	1066.47	1061.47	1062.26	1065.89	5.59	0.999	0.007
para	1000.00	1000.00	1000.00	1000.00	1000.00	1000.00	1000.00	0.00	1.000	0.000
ipso	1022.83	1026.48	1028.23	1029.80	1024.70	1023.71	1025.96	2.71	0.997	0.004
Second Standard										
peak	fid1	fid2	fid3	fid4	fid5	fid6	average	stddev	cuts	
alpha	1036.14	1032.84	1033.75	1035.32	1034.99	1033.84	1034.48	1.21	7	
beta	1045.37	1039.98	1041.98	1039.08	1040.97	1041.36	1041.46	2.17	4	
para	1000.00	1000.00	1000.00	1000.00	1000.00	1000.00	1000.00	0.00	5	
ipso	996.05	993.09	995.12	992.31	993.89	993.56	994.00	1.37	3	
Second Experimental										
									%Conv: 0.71	
peak	fid1	fid2	fid3	fid4	fid5	fid6	average	stddev	KIE	stdev
alpha	1072.69	1076.17	1073.38	1070.86	1070.95	1072.48	1072.75	1.95	1.029	0.002
beta	1043.04	1043.57	1037.80	1039.07	1037.73	1039.70	1040.15	2.56	0.999	0.003
para	1000.00	1000.00	1000.00	1000.00	1000.00	1000.00	1000.00	0.00	1.000	0.000
ipso	985.16	985.61	986.74	985.68	985.39	985.74	985.72	0.55	0.993	0.001

Computational investigation of alternative binding modes

As mentioned in the Chapter 3.2, several other binding modes for the C—C bond formation were suggested for similar catalysts and reaction.^{325–327} To lend increased credence for the transition state proposed in our manuscript, these binding modes were each explored for they system studied. Binding modes A, B, B', C, D, and D' are all proposed in the literature. Based on several NMR, crystallographic, and computational studies on similar systems, it has been brought to our attention that the classic orientation of the thiourea moiety (“*anti,anti*”) may not, in reality, be the lowest energy conformation.^{328–333} Rotating the N—C σ -bond of the thioamide could, in theory, give rise to five complementary binding modes. Upon actual inspection of these coordinates, only BMA and BMB could reasonably support the increased steric bulk of the aryl group in the reactive pocket. These binding modes are designated “BMAf,” and “BMBf,” respectively.



Optimizations revealed that certain binding modes were not transferrable from the systems which originally reported them to our own system. During optimizations for transition states of the type BMB', the malonate translates and BMB is found instead. The cases in literature arguing this binding mode as active have the two hydrogen-bond accepting sites on the nucleophile farther apart from each other than in the case of the malonate used herein.^{325,334} This could account for why, in those cases, BMB' is functional, but is likely not in our case. BMD' also has always led to lowest energy structures of the type BMB instead. BMD' is proposed with a squaramide catalyst which differs in orientations of its hydrogen-bond donors as compared to the thiourea used herein.³²⁶ This could account for the difference observed.

Table 5.8 records the energies of each calculation showing a cross-section of the different conformations searched. Certain geometries offered such a high barrier using a

smaller basis set that calculations at the higher level of theory were not performed in the interest of computational resources.

Table 5. 8. Relative energies for lowest energy transition states representing all major binding modes investigated

Entry	Binding Mode	Enantiomer formed	B3LYP/6-31+G**/PCM(MePh)		
			Δ Free (kcal mol ⁻¹)	Δ ZPE (kcal mol ⁻¹)	Δ PE (kcal mol ⁻¹)
<u>1</u>	C	maj	0.000	0.182	0.000
<u>2</u>	B	maj	1.347	0.000	0.028
<u>3</u>	B	maj	1.662	0.136	0.122
<u>4</u>	D	min	2.246	1.062	0.888
<u>5</u>	B	min	2.836	2.025	2.203
<u>6</u>	A	maj	3.069	2.065	1.627
<u>7</u>	D	maj	3.089	2.535	2.401
<u>8</u>	A	maj	3.505	1.998	1.542
<u>9</u>	A	min	3.512	2.735	2.413
<u>10</u>	C	min	12.465	12.231	11.871
<u>11</u>	Af	maj	13.341	12.198	11.580

Computational investigation of protonation and deprotonation steps

TS1_{O-deprot} could not be found on the B3LYP/6-31+G**/PCM(toluene) surface, therefore the B3LYP/6-31G* energy was used and compared to that of TS1_{C-deprot} using the same theoretical treatment. The relative energies of the two deprotonation steps, and the two protonation steps are shown in Table 5.9

Table 5. 9. Relative energies comparing C- and O- deprotonation/protonation

Entry	Transition State	Relative Free Energy (kcal mol ⁻¹)	Relative ZPE (kcal mol ⁻¹)
1	TS1-C-deprot	1.9	3.8
2	TS1-O-deprot	0.0	0.0
3	TS3-C-prot	27.0	25.7
4	TS3-O-prot	0.0	0.0

5.3.3 A DFT investigation of borox catalyzed aziridination

Computational comparison of transition states

The activation energies for both facial attacks of the **C—C bond forming** and both possible facial attacks for the ring-closure events are depicted in table 5.10.

Table 5. 10. Activation energy of transition states in aziridination reaction

<u>Catalyst</u>	<u>TS</u>	<u>Facial attack</u>	<u>Free (kcal mol⁻¹)</u>	<u>ZPE (kcal mol⁻¹)</u>
boroxinate	C--C bond forming	re	25.9	13.4
		si	24.1	9.6
	Ring closure	re	25.2	12.2
		si	27.4	15.6
spiro-borate	C--C bond forming	re	30.1	15.4
		si	29.8	15.7
	Ring closure	re	32.4	19.6
		si	31.2	17.5

Figure 3.22b

Figure 3.24

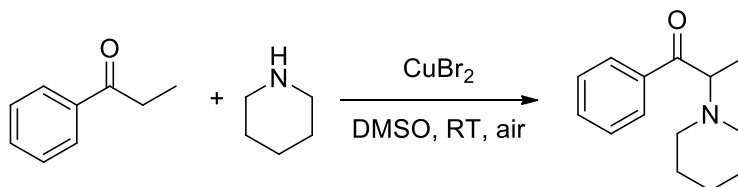
Figure 3.22a

5.4 Transition Metal Catalyzed Reactions

5.4.1 Isotope Effects Reveal Presence of Cu^{III} Intermediate In α -Amination

Reaction

Basic KIE reaction



In a 25mL round-bottom flask was placed 3.3545g (3.23mL; 25mmol) propiophenone, 0.5584g (2.5mmol; 10mol%) of copper(II) bromide, and 4.2mL of DMSO (6M with respect to propiophenone). The mixture was allowed to stir, open to air, for 10min.

Then 4.9mL (50mmol) of piperidine was added and an air balloon was placed over the flask. Periodically aliquots were withdrawn and immediately placed on a pipette column and rinsed with 3 column volumes of ethyl acetate. The eluent was evaporated off and the remaining material was dissolved in deuterated chloroform and subjected to NMR analysis. One-half the integration of the α -protons of the starting material was compared to the *para*-proton on the product to give a crude estimate ($\pm 5\%$) of the percent conversion. An example stack of NMR spectra following the reactions progression is shown in Figure 5.5.

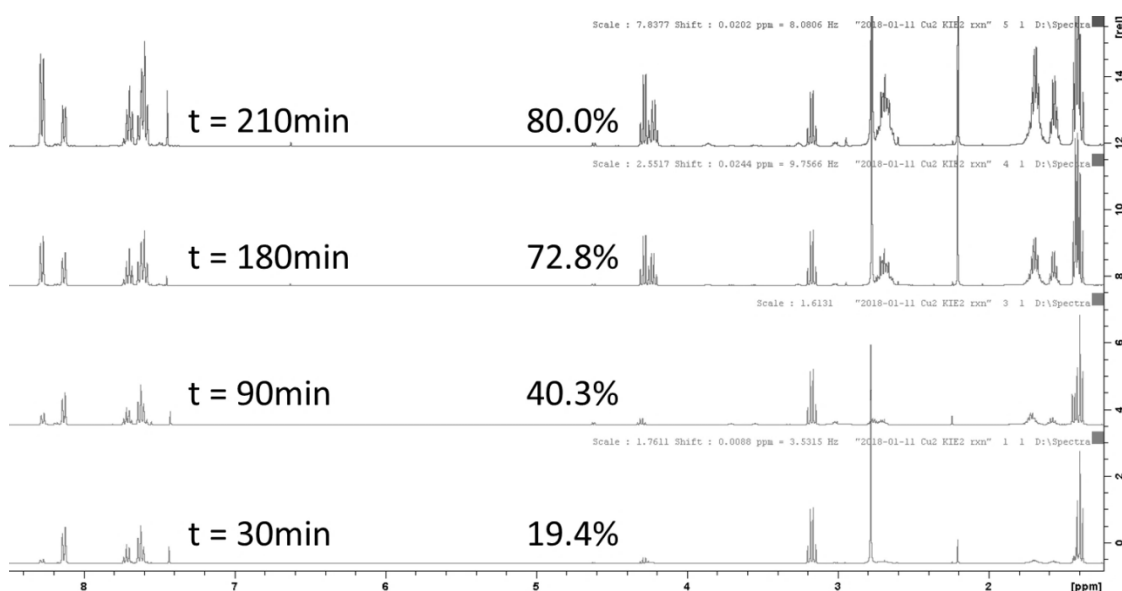
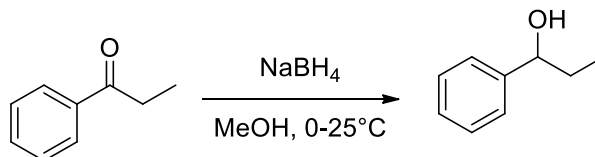


Figure 5. 5. Example stacked NMR spectra normalized to the α -protons of starting material

When the reaction was deemed to have proceeded to the desired percent conversion, the reaction was quenched by loading it onto a chromatography column and eluting 5% methanol in ethyl acetate. This “crude column” served to separate the catalyst from the rest of the reaction mixture. The eluent was evaporated, *in vacuo*, and the remaining material was purified *via* flash chromatography eluting 5% ethyl acetate in hexanes to give purified, re-isolated, isotopically enriched, propiopheone.

Sample derivatization

In an attempt to create a smaller NMR window for isotopic analysis and shorter delay times for the pulse sequences thereby saving time and resources, the propiophene that was re-isolated from the reaction mixture, and that used as a “standard” were derivative by quantitative reduction with sodium borohydride in the following manner.



In a 100mL round-bottom flask was placed propiophene (either from the same bottle as the experimental sample originated, or from the re-isolated experimental sample). 6mL of methanol was added for every 1mmol of propiophene intended to be reduced. The mixture was stirred on ice for ten minutes. 2mmol for every 1mmol of propiophene intended to be reduced of sodium borohydride was then slowly added to the stirring mixture. The flask was fitted with a septum and a nitrogen balloon and stirred overnight allowing the ice to melt and the reaction to reach room temperature. The next day, fresh ice was added and the mixture was cooled back to 0 °C. 0.1N aqueous hydrochloric acid was then added to decompose the leftover sodium borohydride. The organic layer was then extracted into methylene chloride, dried over sodium sulfate, and concentrated *in vacuo*. An NMR spectrum was obtained to confirm 100% derivatization. The obtained, reduced sample was purified *via* flash chromatography eluting 10% ethyl acetate in hexanes.

Integrations of Standard and Experimental NMR spectra

First Set								
Standard								
peak	fid1	fid2	fid3	fid4	fid5	fid6	average	stddev
ipso	995.3111	993.9172	994.2032	994.4916	995.7690	996.2943	994.9977	0.9412

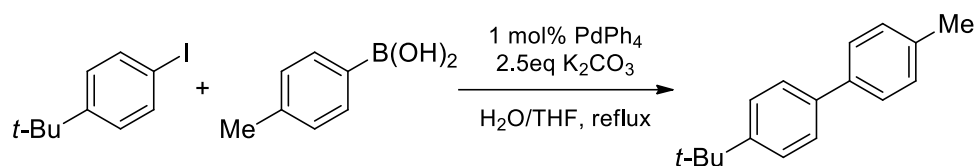
ortho	1987.3466	1986.8697	1984.1478	1986.0323	1986.3121	1986.8550	1986.2606	1.1333
para	1000.0000	1000.0000	1000.0000	1000.0000	1000.0000	1000.0000	1000.0000	0.0000
meta	1998.9820	1996.5863	1994.6106	1997.0402	1997.5708	1998.9780	1997.2947	1.6449
hydroxyl	1007.4287	1007.1239	1007.2418	1009.0424	1008.3303	1009.3532	1008.0867	0.9644
alpha	1000.2496	999.3250	998.8940	1001.0706	1001.2404	1000.8799	1000.2766	0.9738
beta	1024.6923	1023.5745	1024.1624	1024.0382	1023.8591	1025.8310	1024.3596	0.8105
Experimental								
peak	fid1	fid2	fid3	fid4	fid5	fid6	average	stddev
ipso	996.6887	997.2457	999.0685	995.5685	998.4272	997.7632	997.4603	1.2517
ortho	1987.0342	1988.5919	1988.9298	1984.7086	1988.9603	1986.9544	1987.5299	1.6535
para	1000.0000	1000.0000	1000.0000	1000.0000	1000.0000	1000.0000	1000.0000	0.0000
meta	1999.9934	1999.5600	2000.6920	1995.7276	2000.2405	1997.0388	1998.8754	2.0082
hydroxyl	1016.4805	1016.6602	1017.9098	1014.3819	1017.0076	1016.9279	1016.5613	1.1763
alpha	1027.0299	1028.8032	1026.1390	1025.7449	1028.3112	1025.5984	1026.9378	1.3586
beta	1026.9871	1027.0790	1026.6274	1024.5870	1027.1114	1026.1677	1026.4266	0.9696
	Conver:	79.9%						
peak	KIE	stdev						
ipso	1.002	0.002						
ortho	1.000	0.001						
para	1.000	0.000						
meta	1.000	0.001						
hydroxyl	1.005	0.002						
alpha	1.017	0.002						
beta	1.001	0.001						

<u>Second Set</u>								
Standard								
peak	fid1	fid2	fid3	fid4	fid5	fid6	average	stddev
ipso	990.9264	995.5459	997.1316	993.3055	994.0128	995.7338	994.4427	2.1889
ortho	1967.2197	1970.4261	1973.4339	1971.7384	1970.1606	1974.4766	1971.2426	2.5895
para	1000.0000	1000.0000	1000.0000	1000.0000	1000.0000	1000.0000	1000.0000	0.0000
meta	1993.6898	1997.5691	2000.0996	2001.3036	1999.0596	2003.6769	1999.2331	3.4150
hydroxyl	999.2632	1001.5940	1000.0801	1002.1825	1000.2920	998.9021	1000.3857	1.2847
alpha	1000.0653	999.7057	1000.5634	997.5386	998.1572	999.8132	999.3072	1.1847
beta	1022.5625	1023.8264	1027.2480	1026.0755	1026.7529	1028.6890	1025.8591	2.2708
Experimental								
peak	fid1	fid2	fid3	fid4	fid5	fid6	average	stddev
ipso	998.1371	998.9691	997.6537	996.7834	998.8719	998.8360	998.2085	0.8667
ortho	1976.6320	1974.0928	1973.1371	1970.2379	1975.8637	1975.8803	1974.3073	2.3781
para	1000.0000	1000.0000	1000.0000	1000.0000	1000.0000	1000.0000	1000.0000	0.0000
meta	2004.5322	2001.1782	2001.5174	1996.5350	2003.2286	2001.6107	2001.4337	2.7175
hydroxyl	1010.2351	1007.9536	1005.4153	1005.2863	1009.8198	1009.9465	1008.1094	2.2835
alpha	1022.0220	1020.7650	1021.0361	1014.3332	1022.7859	1021.0042	1020.3244	3.0331
beta	1025.9428	1023.1105	1027.1781	1024.1292	1027.0518	1028.9282	1026.0568	2.1402
	Conver:	77.0%						

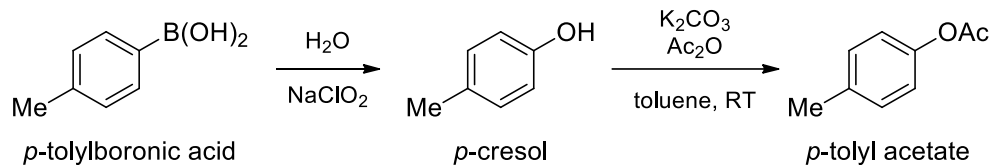
peak	KIE	stdev
ipso	1.003	0.002
ortho	1.001	0.002
para	1.000	0.000
meta	1.001	0.002
hydroxyl	1.005	0.003
alpha	1.014	0.003
beta	1.000	0.003

5.4.2 Isotope Effects Reveal Nature of Transmetalation Transition State in the Catalytic Suzuki-Miyaura Reaction

Basic KIE reaction (boronic acid)



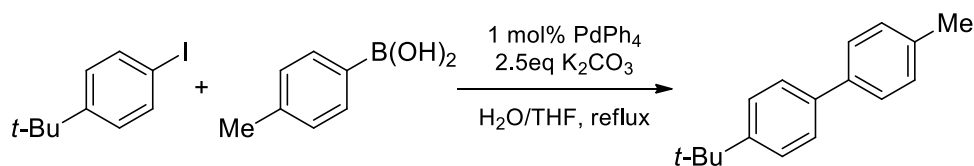
4-tertbutyliodobenzene (3.27g, 12.5mmol), *p*-tolylboronic acid (2.04g, 15mmol) and triphenylmethane (3.125mmol, 0.764g, internal standard) were weighed into a 500mL round bottomed flask. 61mL of THF was then added and the solution stirred for 5min to allow formation of a homogenous mixture. A small sample was taken out for NMR analysis to confirm the initial ratio of boronic acid to iodoenzyme. Thereafter, potassium carbonate (4.32g, 31.26mmol), tetrakis(triphenylphosphine)palladium(0) (0.144g, 0.125mmol) and 31mL of distilled water were added into the flask and mixture was stirred vigorously, at 65°C, under reflux, for 12hrs. The reaction mixture was quenched by cooling then diluting with ethyl acetate and passing through a silica plug. The unreacted boronic acid amount was determined by NMR. *p*-tolylboronic acid proved difficult to isolate and even more so to analyze via NMR, so the acid was derivatized to *p*-tolyl acetate. All reactions were observed to go to 100% completion.



A 50ml round bottomed flask was charged with isolated *p*-tolylboronic acid (1mmol). Water (5mL) was then added. Subsequently, sodium chlorite (1.2mmol) was added into the reaction mixture. The mixture was stirred, at room temperature, for about 1hr, until TLC showed that the starting material had been consumed. The reaction mixture was extracted with ethyl acetate (3x). The combined organic fraction was dried and concentrated to afford *p*-cresol.

A mixture of the *p*-cresol from above (1mmol), acetic anhydride (5mmol), potassium carbonate (2mmol), and toluene (6mL) was stirred at room temperature for 12h. The progress of the reaction was followed by TLC. After completion of the reaction, the mixture was filtered and the filtrate was concentrated. To the residue was added dichloromethane (15mL) and water (5mL) and the phases separated. The organic phase was dried and concentrated to afford *p*-tolyl acetate.

Basic KIE reaction (iodobenzene)

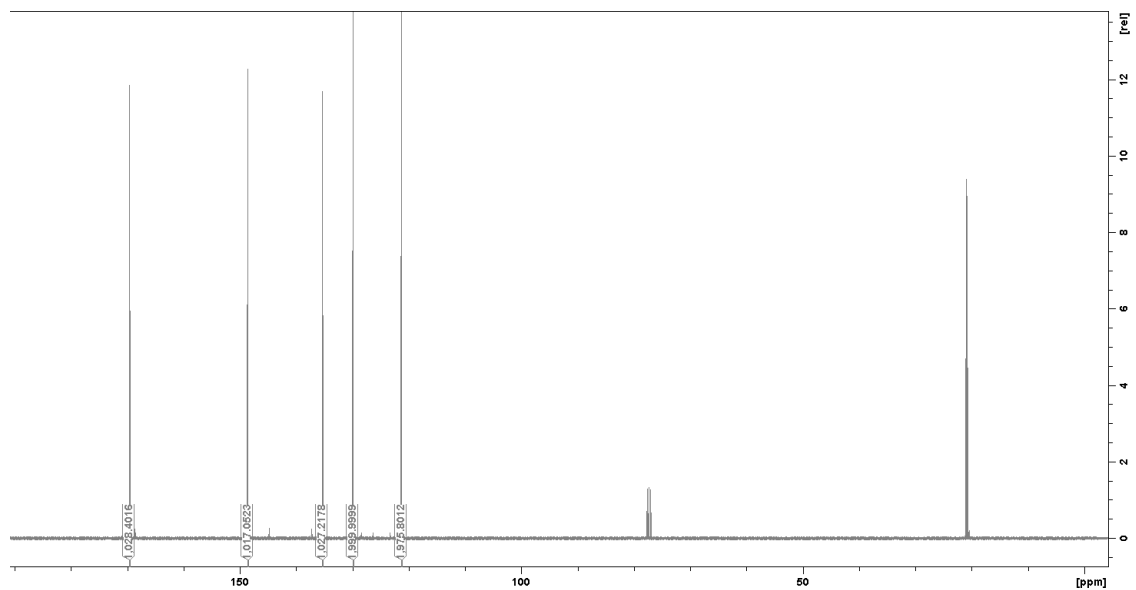


p-*tert*-butyliodobenzene (4.68g, 18mmol), *p*-tolylboronic acid (2.18g, 16mmol) and 1,4 -dimethoxybenzene (4.5mmol, 0.622g, internal standard) were weighed into a 500ml round bottomed flask. 62.5mL of THF was then added and the solution stirred for 5min to allow formation of a homogenous mixture. A small sample was taken out for NMR analysis to confirm the initial ratio of *p*-tolylboronic acid to *p*-*tert*-butyliodoenzene.

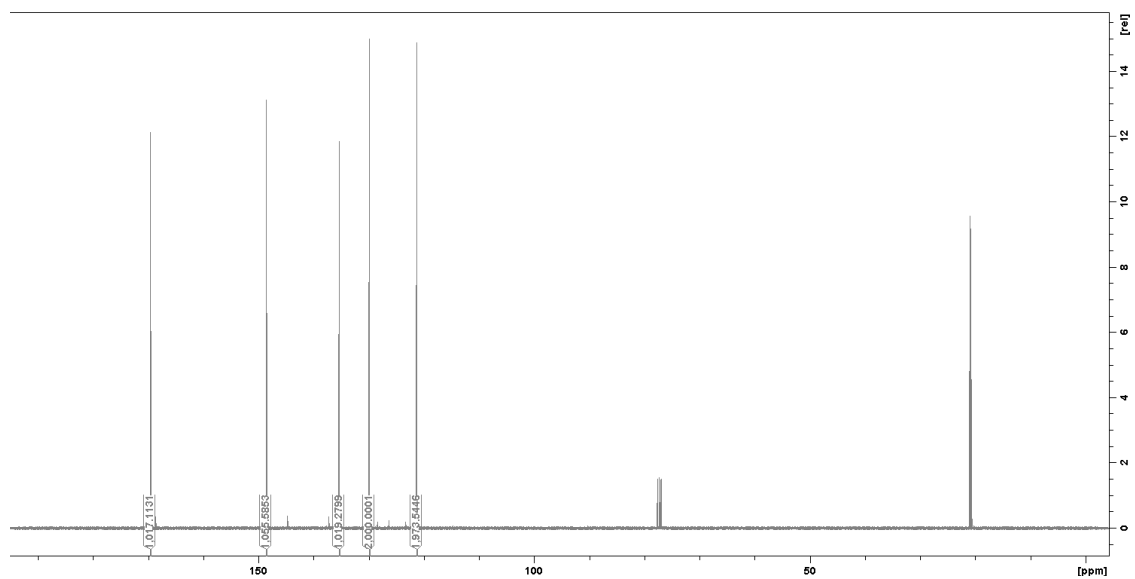
Thereafter, potassium carbonate (4.32g, 31.25mmol), tetrakis(triphenylphosphine)palladium(0) (0.145g, 0.125mmol) and 31.3mL of water were added into the flask and mixture was stirred vigorously, at 65°C, under reflux, for 12hrs. The reaction mixture was quenched by diluting in ethyl acetate and passing through a silica plug. The unreacted *p-tert*-butyliodobenzene amount was determined by NMR.

Sample spectra for the determination of isotopic enrichment

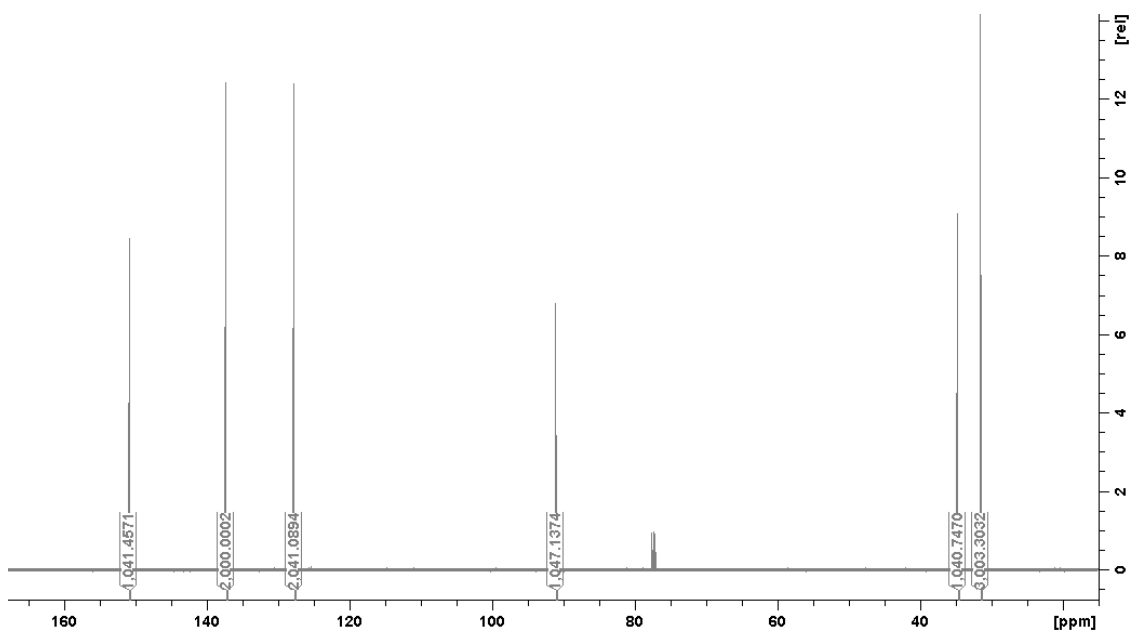
Standard (*p*-tolylboronic acid):



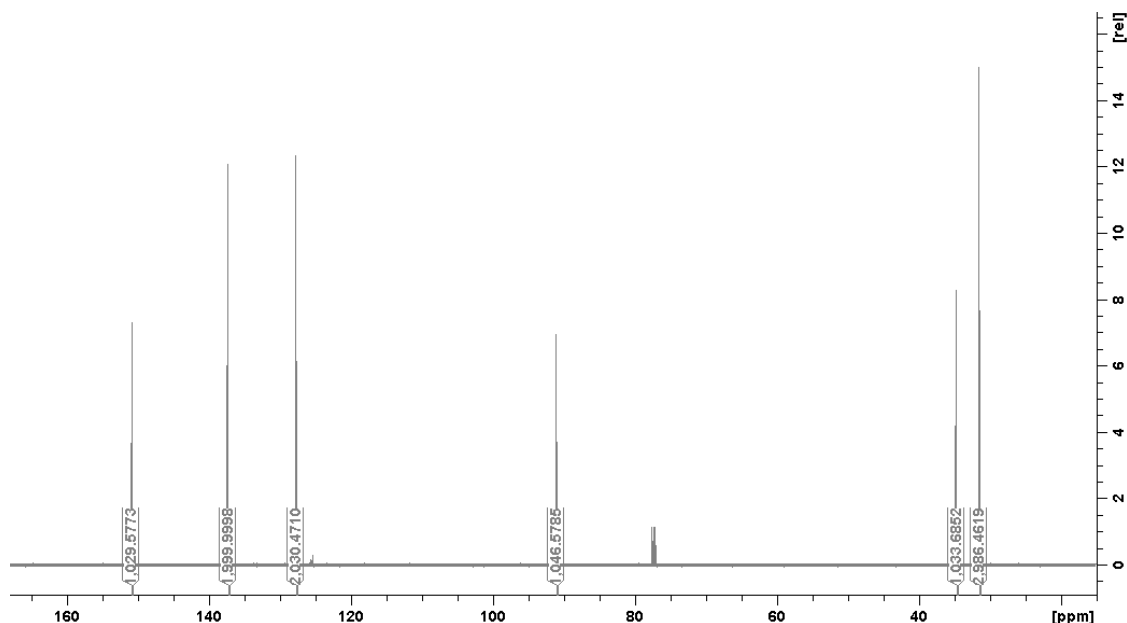
Experimental (*p*-tolylboronic acid):



Standard (*p*-*tert*-butyliodobenzene):



Experimental (*p*-*tert*-butyliodobenzene):



Integrations of standard and experimental NMR spectra (*p*-tolylboronic acid)

First set								
Standard								
peak	fid1	fid2	fid3	fid4	fid5	fid6	average	stddev
ipso	1003.8020	1001.1371	1005.9184	1000.2056	1003.7568	1001.8446	1002.7774	2.1000
para	1004.1529	1004.7639	1004.7572	1003.7881	1006.8865	1004.3493	1004.7830	1.0955
meta	2000.0000	2000.0000	2000.0000	2000.0000	2000.0000	2000.0000	2000.0000	0.0000
ortho	2011.1356	2022.5952	2010.8763	2017.0970	2011.0448	2016.3039	2014.8421	4.7163
Experimental								
peak	fid1	fid2	fid3	fid4	fid5	fid6	average	stddev
ipso	1044.7065	1042.7672	1053.7507	1046.6548	1046.1774	1046.4344	1046.7485	3.7279
para	1002.6611	1003.1017	1004.4445	1004.0704	1001.5794	1001.9177	1002.9625	1.1436
meta	2000.0000	2000.0000	2000.0000	2000.0000	2000.0000	2000.0000	2000.0000	0.0000
ortho	2018.0644	2018.8514	2022.5571	2022.6475	2020.5966	2016.6844	2019.9002	2.4455
	Conver:	71.3%						
peak	KIE	stdev						
ipso	1.036	0.004						
para	0.999	0.002						
meta	1.000	0.000						
ortho	1.002	0.003						

Second set								
Experimental								
peak	fid1	fid2	fid3	fid4	fid5	fid6	average	stddev
ipso	1001.2865	1006.8973	1007.6265	1006.3072	1001.7447	1007.8816	1005.2906	2.9796
para	1010.2128	1013.1714	1015.2696	1014.6249	1011.4569	1011.1668	1012.6504	2.0297
meta	2000.0000	2000.0000	2000.0000	2000.0000	2000.0000	2000.0000	2000.0000	0.0000
ortho	2015.4079	2016.2859	2016.0690	2018.5114	2013.1831	2014.9714	2015.7381	1.7508
Experimental								
peak	fid1	fid2	fid3	fid4	fid5	fid6	average	stddev
ipso	1054.0013	1053.7196	1049.3609	1052.3523	1050.4898	1052.2142	1052.0230	1.8097
para	1012.8024	1010.7899	1012.4851	1011.8395	1009.4577	1012.0156	1011.5650	1.2408
meta	2000.0000	2000.0000	2000.0000	2000.0000	2000.0000	2000.0000	2000.0000	0.0000

ortho	2020.8495	2026.8558	2018.2635	2020.7193	2024.7139	2019.0821	2021.7474	3.3467
	Conver:	73.7%						
peak	KIE	stdev						
ipso	1.035	0.004						
para	0.999	0.002						
meta	1.000	0.000						
ortho	1.002	0.002						

Integrations of standard and experimental NMR spectra (p-tert-butylidobenzene)

First set								
Standard								
peak	fid1	fid2	fid3	fid4	fid5	fid6	average	stddev
para	1041.4571	1041.3013	1041.0198	1046.2345	1041.3210	1037.7572	1041.5152	2.7102
ortho	2000.0000	2000.0000	2000.0000	2000.0000	2000.0000	2000.0000	2000.0000	0.0000
meta	2041.0894	2032.4410	2039.8616	2042.3753	2039.0064	2035.5007	2038.3791	3.7270
ipso	1047.1374	1049.2956	1046.0252	1052.7812	1047.5215	1047.8219	1048.4305	2.3804
quat	1040.7470	1039.0407	1040.4593	1044.8219	1039.6565	1037.7948	1040.4200	2.4026
methyl	3003.3032	2998.3894	2997.1011	3008.9544	2998.1856	2995.1666	3000.1834	5.0703
	Conver:	89.9%						
peak	KIE	stdev						
para	0.998	0.005						
ortho	1.000	0.000						
meta	0.999	0.003						
ipso	1.001	0.005						
quat	0.999	0.004						
methyl	0.998	0.002						
Second Set								
Standard								
peak	fid1	fid2	fid3	fid4	fid5	fid6	average	stddev
para	1035.5534	1036.2196	1035.6398	1035.0786	1037.2053	1035.6545	1035.8919	0.7387
ortho	2000.0000	2000.0000	2000.0000	2000.0000	2000.0000	2000.0000	2000.0000	0.0000
meta	2031.4660	2032.9406	2037.8026	2028.7483	2037.1357	2030.8633	2033.1594	3.6060
ipso	1053.6847	1053.0392	1053.2893	1050.1351	1056.7282	1053.0395	1053.3193	2.1000
quat	1047.7894	1046.0000	1050.1292	1043.4704	1048.7954	1042.1226	1046.3845	3.1181
methyl	2973.0749	2969.4672	2975.1271	2968.7377	2977.9163	2970.0230	2972.3910	3.6328
	Conver:	90.4%						
peak	KIE	stdev						
para	0.998	0.002						
ortho	1.000	0.000						
meta	0.999	0.003						
ipso	1.005	0.003						
quat	0.999	0.004						
methyl	0.999	0.002						
Experimental								
peak	fid1	fid2	fid3	fid4	fid5	fid6	average	stddev
para	1031.4120	1030.9749	1031.5258	1033.9476	1034.5514	1030.3198	1032.1219	1.7122
ortho	2000.0000	2000.0000	2000.0000	2000.0000	2000.0000	2000.0000	2000.0000	0.0000
meta	2027.3248	2030.2093	2034.1851	2028.4965	2036.9018	2023.7988	2030.1527	4.7524
ipso	1063.4200	1069.0301	1065.1402	1066.2128		1067.1050	1067.1781	3.0812
quat	1041.2683	1041.7783	1047.1991	1044.6405	1047.4311	1042.4628	1044.1300	2.7231
methyl	2957.3809	2963.8556	2962.8802	2962.3414	2966.5431	2958.9411	2961.9904	3.3367
	Conver:	90.4%						
peak	KIE	stdev						
para	0.998	0.002						
ortho	1.000	0.000						
meta	0.999	0.003						
ipso	1.005	0.003						
quat	0.999	0.004						
methyl	0.999	0.002						

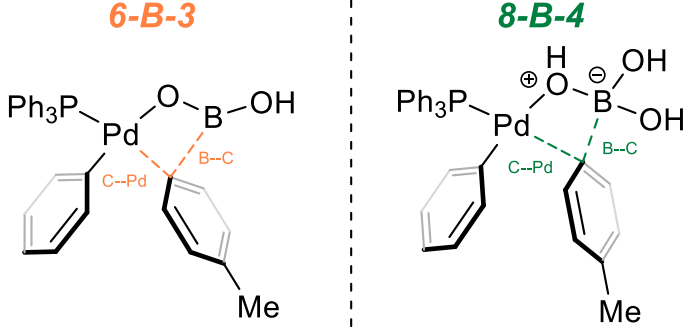
Computational investigation of 8-B-4 and 6-B-3 pathways using alternative functionals

To ensure the validity of the predicted geometries and kinetic isotope effects, the transition states for both proposed transmetalation steps (from the 8-B-4 and the 6-B-3 complexes) were optimized using ten different methods:

- {1} B3LYP/ LANL2DZ (Pd) 6-31+G** (H,B,C,O,P)^{185–188,335–337}
- {2} B3LYP-D3/LANL2DZ (Pd) 6-31+G** (H,B,C,O,P)²⁰⁶
- {3} B3LYP-D3/SDD (Pd) 6-31+G** (H,B,C,O,P)²⁸⁷
- {4} B3LYP-D3/LANL2DZ (Pd) 6-31+G** (H,B,C,O,P)/PCM(THF)²⁶²
- {5} B3LYP-D3/LANL2DZ (Pd) 6-31+G** (H,B,C,O,P)/PCM(H₂O)
- {6} B3LYP-D3/LANL2DZ (Pd) 6-31+G** (H,B,C,O,P)/SMD(THF)¹⁹²
- {7} B3LYP-D3/LANL2DZ (Pd) 6-31+G** (H,B,C,O,P)/SMD(H₂O)
- {8} M062X/LANL2DZ (Pd) 6-31+G** (H,B,C,O,P)²⁸⁶
- {9} ω B97XD/LANL2DZ (Pd) 6-31+G** (H,B,C,O,P)³¹⁹
- {10} ω B97XD/def2-SVP³²²

The B—C and C—Pd bond length for each method is detailed in Table 5.11 in Ångstroms.

Table 5. 11. Predicted bond distances

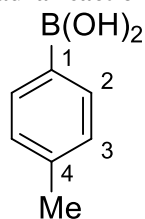


Method	6-B-3 TS		8-B-4 TS	
	B--C	C--Pd	B--C	C--Pd

B3LYP/ LANL2DZ (Pd) 6-31+G** (H,B,C,O,P)	2.39	2.09	2.05	2.20
B3LYP-D3/LANL2DZ (Pd) 6-31+G** (H,B,C,O,P)	2.32	2.09	2.05	2.20
B3LYP-D3/SDD (Pd) 6-31+G** (H,B,C,O,P)	2.42	2.07	2.04	2.19
B3LYP-D3/LANL2DZ (Pd) 6-31+G** (H,B,C,O,P)/PCM(THF)	2.51	2.07	2.08	2.22
B3LYP-D3/LANL2DZ (Pd) 6-31+G** (H,B,C,O,P)/PCM(H ₂ O)	2.53	2.07	2.09	2.22
B3LYP-D3/LANL2DZ (Pd) 6-31+G** (H,B,C,O,P)/SMD(THF)	2.59	2.07	2.07	2.23
B3LYP-D3/LANL2DZ (Pd) 6-31+G** (H,B,C,O,P)/SMD(H ₂ O)	2.79	2.06	2.11	2.21
M062X/LANL2DZ (Pd) 6-31+G** (H,B,C,O,P)	2.27	2.08	2.07	2.20
ωB97XD/LANL2DZ (Pd) 6-31+G** (H,B,C,O,P)	2.32	2.09	2.05	2.16
ωB97XD/def2-SVP	2.57	2.05	2.04	2.15
Average	2.47	2.07	2.07	2.20
Standard deviation	0.16	0.01	0.02	0.03

The predicted KIE for each method is detailed in Table 5.12.

Table 5. 12. Predicted KIEs for Suzuki-Miyaura reaction



Method	6-B-3 TS				8-B-4 TS			
	C1	C2	C3	C4	C1	C2	C3	C4
B3LYP/ LANL2DZ (Pd) 6-31+G** (H,B,C,O,P)	1.026	1.003	1.001	1.001	1.039	1.002	1.001	1.001
B3LYP-D3/LANL2DZ (Pd) 6-31+G** (H,B,C,O,P)	1.027	1.004	1.001	1.000	1.037	1.002	1.001	1.001
B3LYP-D3/SDD (Pd) 6-31+G** (H,B,C,O,P)	1.018	1.002	1.001	1.000	1.037	1.002	1.001	1.001
B3LYP-D3/LANL2DZ (Pd) 6-31+G** (H,B,C,O,P)/PCM(THF)	1.021	1.003	1.001	1.000	1.039	1.003	1.002	1.001
B3LYP-D3/LANL2DZ (Pd) 6-31+G** (H,B,C,O,P)/PCM(H ₂ O)	1.020	1.003	1.001	1.000	1.039	1.003	1.002	1.001

B3LYP-D3/LANL2DZ (Pd) 6-31+G** (H,B,C,O,P)/SMD(THF)	1.018	1.002	1.002	1.001	1.039	1.003	1.002	1.002
B3LYP-D3/LANL2DZ (Pd) 6-31+G** (H,B,C,O,P)/SMD(H ₂ O)	1.016	1.004	1.002	1.001	1.039	1.003	1.002	1.001
M062X/LANL2DZ (Pd) 6-31+G** (H,B,C,O,P)	1.028	1.004	1.001	1.001	1.039	1.003	1.001	1.001
ω B97XD/LANL2DZ (Pd) 6-31+G** (H,B,C,O,P)	1.022	1.002	1.001	1.001	1.036	1.002	1.002	1.001
ω B97XD/def2-SVP	1.016	1.002	1.001	1.001	1.033	1.002	1.001	1.001
Average	1.021	1.003	1.001	1.001	1.038	1.003	1.002	1.001
Standard deviation	0.004	0.001	0.000	0.001	0.002	0.001	0.001	0.000

From the calculations described in Tables 5.11 and 5.12, it can be seen that the transition state geometry and predicted KIE are not functional, basis set, or solvent model dependent and therefore support our interpretation of the computational data.

BIBLIOGRAPHY

- (1) Ebbing, D. D.; Gammon, S. D. *General Chemistry*, 11th ed.; Cengage Learning: Boston, 2016.
- (2) Taylor, H. S. Catalysis <https://www.britannica.com/science/catalysis> (accessed Aug 27, 2018).
- (3) Berzelius, J. J. R. *Swedish Acad. Sci.* **1835**, 245.
- (4) Kirchhoff, G. S. C. *Bull. des Neuesten und Wissenwürdigsten aus der Naturwiss.* **1811**, 9, 262–263.
- (5) Parshall, G. W.; Putscher, R. E. *J. Chem. Educ.* **1986**, 63, 189.
- (6) Picquet, M. *Platin. Met. Rev.* **2013**, 57, 272–280.
- (7) Brown, D. G.; Boström, J. J. *Med. Chem.* **2016**, 59, 4443–4458.
- (8) Schneider, N.; Lowe, D. M.; Sayle, R. A.; Tarselli, M. A.; Landrum, G. A. *J. Med. Chem.* **2016**, 59, 4385–4402.
- (9) Zhou, Q. L. *Angew. Chemie - Int. Ed.* **2016**, 55, 5352–5353.
- (10) Glaser, C. *Berichte der Dtsch. Chem. Gesellschaft* **1869**, 2, 422–424.
- (11) Glaser, C. *Ann. Chem. Pharm.* **1870**, 154, 137–171.
- (12) Ullmann, F.; Sponagel, P. *Berichte der Dtsch. Chem. Gesellschaft* **1905**, 38, 2211–2212.
- (13) Smidt, J.; Hafner, W.; Jira, R.; Sedlmeier, J.; Sieber, R.; Rüttinger, R.; Kojer, H. *Angew. Chemie* **1959**, 71, 176–182.
- (14) Hafner, W.; Jira, R.; Sedlmeier, J.; Smidt, J. *Chem. Ber.* **1962**, 95, 1575–1581.
- (15) Smidt, J.; Hafner, W.; Jira, R.; Sieber, R.; Sedlmeier, J.; Sabel, A. *Angew. Chemie Int. Ed. English* **1962**, 1, 80–88.
- (16) Tsuji, J.; Takahashi, H.; Morikawa, M. *Tetrahedron Lett.* **1965**, 6, 4387–4388.
- (17) Trost, B. M.; Fullerton, T. J. *J. Am. Chem. Soc.* **1973**, 95, 292–294.
- (18) Mizoroki, T.; Mori, K.; Ozaki, A. *Bull. Chem. Soc. Jpn.* **1971**, 44, 581–581.
- (19) Mizoroki, T.; Mori, K.; Ozaki, A. *Bull. Chem. Soc. Jpn.* **1971**, 44, 581.
- (20) Heck, R. F.; Nolley, J. P. *J. Org. Chem.* **1972**, 37, 2320–2322.
- (21) Tamao, K.; Sumitani, K.; Kumada, M. *J. Am. Chem. Soc.* **1972**, 94, 4374–4376.

- (22) Corriu, R. J. P.; Masse, J. P. *J. Chem. Soc. Chem. Commun.* **1972**, No. 3, 144a.
- (23) Sonogashira, K.; Tohda, Y.; Hagihara, N. *Tetrahedron Lett.* **1975**, 16, 4467–4470.
- (24) Baba, S.; Negishi, E. *J. Am. Chem. Soc.* **1976**, 98, 6729–6731.
- (25) King, A. O.; Okukado, N.; Negishi, E. *J. Chem. Soc. Chem. Commun.* **1977**, No. 19, 683.
- (26) Jean-Louis Hérisson, P.; Chauvin, Y. *Die Makromol. Chemie* **1971**, 141, 161–176.
- (27) Novak, B. M.; Grubbs, R. H. *J. Am. Chem. Soc.* **1988**, 110, 960–961.
- (28) Nguyen, S. B. T.; Johnson, L. K.; Grubbs, R. H.; Ziller, J. W. *J. Am. Chem. Soc.* **1992**, 114, 3974–3975.
- (29) Schrock, R.; Rocklage, S.; Wengrovius, J.; Rupprecht, G.; Fellmann, J. *J. Mol. Catal.* **1980**, 8, 73–83.
- (30) Schrock, R. R.; Murdzek, J. S.; Bazan, G. C.; Robbins, J.; Dimare, M.; O'Regan, M. *J. Am. Chem. Soc.* **1990**, 112, 3875–3886.
- (31) Milstein, D.; Stille, J. K. *J. Am. Chem. Soc.* **1978**, 100, 3636–3638.
- (32) Azarian, D.; Dua, S. S.; Eaborn, C.; Walton, D. R. M. *J. Organomet. Chem.* **1976**, 117, C55–C57.
- (33) Kosugi, M.; Sasazawa, K.; Shimizu, Y.; Migita, T. *Chem. Lett.* **1977**, 6, 301–302.
- (34) Kosugi, M.; Shimizu, Y.; Migita, T. *Chem. Lett.* **1977**, 6, 1423–1424.
- (35) Kosugi, M.; Kameyama, M.; Migita, T. *Chem. Lett.* **1983**, 12, 927–928.
- (36) Miyaura, N.; Suzuki, A. *J. Chem. Soc. Chem. Commun.* **1979**, 866–867.
- (37) Miyaura, N. A. S. *J. C. S. Chem. Comm.* **1979**, No. 866, 866–867.
- (38) Miyaura, N.; Yamada, K.; Suzuki, A. *Tetrahedron Lett.* **1979**, 36, 3437–3440.
- (39) Katsuki, T.; Sharpless, K. B. *J. Am. Chem. Soc.* **1980**, 102, 5974–5976.
- (40) Jacobsen, E. N.; Markó, I.; Mungall, W. S.; Schröder, G.; Sharpless, K. B. *J. Am. Chem. Soc.* **1988**, 110, 1968–1970.
- (41) Hatanaka, Y.; Hiyama, T. *J. Org. Chem.* **1988**, 53, 918–920.
- (42) Denmark, S. E.; Choi, J. Y. *J. Am. Chem. Soc.* **1999**, 121, 5821–5822.
- (43) Denmark, S. E.; Wehrli, D.; Choi, J. Y. *Org. Lett.* **2000**, 2, 2491–2494.
- (44) Paul, F.; Patt, J.; Hartwig, J. F. *J. Am. Chem. Soc.* **1994**, 116, 5969–5970.
- (45) Guram, A. S.; Buchwald, S. L. *J. Am. Chem. Soc.* **1994**, 116, 7901–7902.
- (46) Stille, J. K. *Angew. Chemie Int. Ed. English* **1986**, 25, 508–524.
- (47) Cabri, W.; Candiani, I. *Acc. Chem. Res.* **1995**, 28, 2–7.

- (48) Miyaura, N.; Suzuki, A. *Chem. Rev.* **1995**, *95*, 2457–2483.
- (49) Beletskaya, I. P.; Cheprakov, A. V. *Chem. Rev.* **2000**, *100*, 3009–3066.
- (50) Chemler, S. R.; Trauner, D.; Danishefsky, S. J. *Angew. Chemie - Int. Ed.* **2001**, *40*, 4544–4568.
- (51) Denmark, S. E.; Regens, C. S. *Acc. Chem. Res.* **2008**, *41*, 1486–1499.
- (52) Chinchilla, R.; Nájera, C. *Chem. Soc. Rev.* **2011**, *40*, 5084–5121.
- (53) Lennox, A. J. J.; Lloyd-Jones, G. C. *Angew. Chemie - Int. Ed.* **2013**, *52*, 7362–7370.
- (54) Lennox, A. J. J.; Lloyd-Jones, G. C. *Chem. Soc. Rev.* **2014**, *43*, 412–443.
- (55) Biswas, B.; Kulsi, G. *Asian J. Adv. Basic Sci.* **2016**, *4*, 131–140.
- (56) Anastas, P. T.; Warner, J. C. *Green Chemistry: Theory and Practice*; Oxford University Press: Oxford.
- (57) Li, C. J.; Trost, B. M. *Proc. Natl. Acad. Sci.* **2008**, *105*, 13197–13202.
- (58) Ahrendt, K. A.; Borths, C. J.; MacMillan, D. W. C. *J. Am. Chem. Soc.* **2000**, *122*, 4243–4244.
- (59) *Asymmetric Organocatalysis Vol. 1: Lewis Base and Acid Catalysts*; List, B., Ed.; Thieme: Stuttgart, 2012.
- (60) *Asymmetric Organocatalysis Vol. 2 Bronsted Base and Acid Catalysts, and Additional Topics*; Maruoka, K., Ed.; Thieme: Stuttgart, 2012.
- (61) Jordan, F. In *Enamines*; Rappoport, Z., Ed.; The Chemistry of Functional Groups; John Wiley & Sons, Ltd: Chichester, 1994; pp 1253–1302.
- (62) Knoevenagel, E. *Berichte der Dtsch. Chem. Gesellschaft* **1896**, *29*, 172.
- (63) Langenbeck, W.; Borth, G. *Berichte der Dtsch. Chem. Gesellschaft* **1942**, *75*, 951.
- (64) Wieland, P.; Miescher, K. *Helv. Chim. Acta* **1950**, *33*, 2215.
- (65) Woodward, R. B.; Sondheimer, F.; Taub, D.; Heusler, K.; McLamore, W. M. *J. Am. Chem. Soc.* **1952**, *74*, 4223–4251.
- (66) Eder, U.; Sauer, G.; Wiechert, R. *Angew. Chemie - Int. Ed.* **1971**, *10*, 496–497.
- (67) Hajos, Z. G.; Parrish, D. R. *J. Org. Chem.* **1974**, *39*, 1615–1621.
- (68) Tu, Y.; Wang, Z. X.; Shi, Y. *J. Am. Chem. Soc.* **1996**, *118*, 9806–9807.
- (69) Yang, D.; Yip, Y.-C.; Tang, M.-W.; Wong, M.-K.; Zheng, J.-H.; Cheung, K.-K. *J. Am. Chem. Soc.* **1996**, *118*, 491–492.
- (70) Denmark, S. E.; Wu, Z.; Crudden, C. M.; Matsubashi, H. *J. Org. Chem.* **1997**, *62*, 8288–8289.
- (71) List, B. *J. Am. Chem. Soc.* **2000**, *122*, 9336–9337.

- (72) List, B.; Lerner, R. a; Barbas III, C. F. *J. Am. Chem. Soc.* **2000**, *122*, 2395–2396.
- (73) Notz, W.; List, B. *J. Am. Chem. Soc.* **2000**, *122*, 7386–7387.
- (74) List, B.; Pojarliev, P.; Biller, W. T.; Martin, H. J. *J. Am. Chem. Soc.* **2002**, *124*, 827–833.
- (75) Yang, J. W.; Stadler, M.; List, B. *Angew. Chemie - Int. Ed.* **2007**, *46*, 609–611.
- (76) Hayashi, Y.; Yamaguchi, J.; Hibino, K.; Shoji, M. *Tetrahedron Lett.* **2003**, *44*, 8293–8296.
- (77) Zhong, G. *Angew. Chemie - Int. Ed.* **2003**, *42*, 4247–4250.
- (78) Brown, S. P.; Brochu, M. P.; Sinz, C. J.; MacMillan, D. W. C. *J. Am. Chem. Soc.* **2003**, *125*, 10808–10809.
- (79) Dinér, P.; Kjærsgaard, A.; Lie, M. A.; Jørgensen, K. A. *Chem. - A Eur. J.* **2008**, *14*, 122–127.
- (80) Beeson, T. D.; MacMillan, D. W. C. *J. Am. Chem. Soc.* **2005**, *127*, 8826–8828.
- (81) Steiner, D. D.; Mase, N.; Barbas, C. F. *Angew. Chemie - Int. Ed.* **2005**, *44*, 3706–3710.
- (82) List, B. *J. Am. Chem. Soc.* **2002**, *124*, 5656–5657.
- (83) Bertelsen, S.; Marigo, M.; Brandes, S.; Dinér, P.; Jørgensen, K. A. *J. Am. Chem. Soc.* **2006**, *128*, 12973–12980.
- (84) Vignola, N.; List, B. *J. Am. Chem. Soc.* **2004**, *126*, 450–451.
- (85) Cobb, A. J. A.; Shaw, D. M.; Longbottom, D. A.; Gold, J. B.; Ley, S. V. *Org. Biomol. Chem.* **2005**, *3*, 84–96.
- (86) Huang, Y.; Walji, A. M.; Larsen, C. H.; MacMillan, D. W. C. *J. Am. Chem. Soc.* **2005**, *127*, 15051–15053.
- (87) Jones, S. B.; Simmons, B.; MacMillan, D. W. C. *J. Am. Chem. Soc.* **2009**, *131*, 13606–13607.
- (88) Wang, J.; Li, H.; Xie, H.; Zu, L.; Shen, X.; Wang, W. *Angew. Chemie - Int. Ed.* **2007**, *46*, 9050–9053.
- (89) Chen, S. H.; Hong, B. C.; Su, C. F.; Sarshar, S. *Tetrahedron Lett.* **2005**, *46*, 8899–8903.
- (90) Bohórquez, A. R. R.; Romero-Daza, J.; Acelas, M. *Synth. Commun.* **2016**, Ahead of print.
- (91) Wilson, R. M.; Jen, W. S.; MacMillan, D. W. C. *J. Am. Chem. Soc.* **2005**, *127*, 11616–11617.
- (92) Sanchez-Diez, E.; Vesga, D. L.; Reyes, E.; Uria, U.; Carrillo, L.; Vicario, J. L. *Org. Lett.* **2016**, *18*, 1270–1273.
- (93) Kunz, R. K.; MacMillan, D. W. C. *J. Am. Chem. Soc.* **2005**, *127*, 3240–3241.
- (94) Yamamoto, Y.; Momiyama, N.; Yamamoto, H. *J. Am. Chem. Soc.* **2004**, *126*, 5962–5963.
- (95) Sundén, H.; Ibrahim, I.; Eriksson, L.; Córdova, A. *Angew. Chemie - Int. Ed.* **2005**, *44*,

4877–4880.

- (96) Kowalczyk, R.; Boratyński, P. J.; Wierzba, A. J.; Bąkiewicz, J. *RSC Adv.* **2015**, *5*, 66681–66686.
- (97) Austin, J. F.; MacMillan, D. W. C. *J. Am. Chem. Soc.* **2002**, *124*, 1172–1173.
- (98) Ouellet, S. G.; Tuttle, J. B.; MacMillan, D. W. C. *J. Am. Chem. Soc.* **2005**, *127*, 32–33.
- (99) Chen, Y. K.; Yoshida, M.; MacMillan, D. W. C. *J. Am. Chem. Soc.* **2006**, *128*, 9328–9329.
- (100) Izquierdo, C.; Esteban, F.; Parra, A.; Alfaro, R.; Alemán, J.; Fraile, A.; Ruano, J. L. G. *J. Org. Chem.* **2014**, *79*, 10417–10433.
- (101) Halland, N.; Aburel, P. S.; Jørgensen, K. A. *Angew. Chemie Int. Ed.* **2003**, *42*, 661–665.
- (102) Jacobsen, C. B.; Nielsen, M.; Worgull, D.; Zweifel, T.; Fisker, E.; Jørgensen, K. A. *J. Am. Chem. Soc.* **2011**, *133*, 7398–7404.
- (103) Bartoli, G.; Bosco, M.; Carlone, A.; Pesciaoli, F.; Sambri, L.; Melchiorre, P. *Org. Lett.* **2007**, *9*, 1403–1405.
- (104) Silva, F.; Sawicki, M.; Gouverneur, V. *Org. Lett.* **2006**, *8*, 5417–5419.
- (105) Basak, A. K.; Shimada, N.; Bow, W. F.; Vicic, D. A.; Tius, M. A. *J. Am. Chem. Soc.* **2010**, *132*, 8266–8267.
- (106) Marigo, M.; Franzén, J.; Poulsen, T. B.; Zhuang, W.; Jørgensen, K. A. *J. Am. Chem. Soc.* **2005**, *127*, 6964–6965.
- (107) Yang, G.; Chen, L.; Wang, J.; Jia, Q.; Wei, J.; Du, Z. *Tetrahedron Lett.* **2015**, *56*, 5889–5891.
- (108) Albertshofer, K.; Anderson, K. E.; Barbas, C. F. *Org. Lett.* **2012**, *14*, 5968–5971.
- (109) Jacobsen, C. B.; Jensen, K. L.; Udmark, J.; Jørgensen, K. A. *Org. Lett.* **2011**, *13*, 4790–4793.
- (110) Erkkilä, A.; Majander, I.; Pihko, P. M. *Chem. Rev.* **2007**, *107*, 5416–5470.
- (111) Melchiorre, P.; Jørgensen, K. A. *J. Org. Chem.* **2003**, *68*, 4151–4157.
- (112) Hayashi, Y.; Gotoh, H.; Hayashi, T.; Shoji, M. *Angew. Chemie - Int. Ed.* **2005**, *44*, 4212–4215.
- (113) Marigo, M.; Wabnitz, T. C.; Fielenbach, D.; Jørgensen, K. A. *Angew. Chemie - Int. Ed.* **2005**, *44*, 794–797.
- (114) Franze, J.; Marigo, M.; Fielenbach, D.; Wabnitz, T. C.; Kjærsgaard, A.; Jørgensen, K. A. *J. Am. Chem. Soc.* **2005**, *127*, 18296–18304.
- (115) Piel, I.; Steinmetz, M.; Hirano, K.; Fröhlich, R.; Grimme, S.; Glorius, F. *Angew. Chemie Int. Ed.* **2011**, *50*, 4983–4987.
- (116) Kerr, M. S.; Read de Alaniz, J.; Rovis, T. *J. Am. Chem. Soc.* **2002**, *124*, 10298–10299.

- (117) Enders, D.; Kallfass, U. *Angew. Chemie - Int. Ed.* **2002**, *41*, 1743–1745.
- (118) Enders, D.; Breuer, K.; Teles, J. H. *Helv. Chim. Acta* **1996**, *79*, 1217–1221.
- (119) Sohn, S. S.; Rosen, E. L.; Bode, J. W. *J. Am. Chem. Soc.* **2004**, *126*, 14370–14371.
- (120) Chow, K. Y. K.; Bode, J. W. *J. Am. Chem. Soc.* **2004**, *126*, 8126–8127.
- (121) He, M.; Struble, J. J. R.; Bode, J. W. *J. Am. Chem. Soc.* **2006**, *128*, 8418–8420.
- (122) Akiyama, T.; Itoh, J.; Yokota, K.; Fuchibe, K. *Angew. Chemie - Int. Ed.* **2004**, *43*, 1566–1568.
- (123) Müller, S.; Webber, M. J.; List, B. *J. Am. Chem. Soc.* **2011**, *133*, 18534–18537.
- (124) Hoffmann, S.; Seayad, A. M.; List, B. *Angew. Chemie - Int. Ed.* **2005**, *44*, 7424–7427.
- (125) Okino, T.; Hoashi, Y.; Takemoto, Y. *J. Am. Chem. Soc.* **2003**, *125*, 12672–12673.
- (126) Wenzel, A. G.; Jacobsen, E. N. *J. Am. Chem. Soc.* **2002**, *124*, 12964–12965.
- (127) Anslyn, E. V.; Dougherty, D. A. *Modern Physical Organic Chemistry*; Murdzek, J., Ed.; University Science Books: Sausalito, 2006.
- (128) Wiberg, K. B. *Chem. Rev.* **1955**, *55*, 713–743.
- (129) Bell, R. P. *Chem. Soc. Rev.* **1973**, *3*, 513–544.
- (130) Pascal, R. A.; Baum, M. W.; Wagner, C. K.; Rodgers, L. R.; Huang, D. S. *J. Am. Chem. Soc.* **1986**, *108*, 6477–6482.
- (131) Burger, R. M.; Tian, G.; Drlica, K. *J. Am. Chem. Soc.* **1995**, *117*, 1167–1168.
- (132) Jankowski, S.; Paneth, P.; Quin, L. D.; O'Leary, M. H. *J. Am. Chem. Soc.* **1994**, *116*, 11675–11677.
- (133) Holm, T. *J. Am. Chem. Soc.* **1994**, *116*, 8803–8803.
- (134) Kupczyk-Subotkowska, L.; Saunders, W. H.; Shine, H. J. *J. Am. Chem. Soc.* **1988**, *110*, 7153–7159.
- (135) Kupczyk-Subotkowska, L.; Subotkowski, W.; Saunders, W. H.; Shine, H. J. *J. Am. Chem. Soc.* **1992**, *114*, 3441–3445.
- (136) Kupczyk-Subotkowska, L.; Shine, H. J.; Subotkowski, W.; Saunders, W. H. *J. Am. Chem. Soc.* **1993**, *115*, 5957–5961.
- (137) Yamataka, H.; Nagareda, K.; Takatsuka, T.; Ando, K.; Hanafusa, T.; Nagase, S. *J. Am. Chem. Soc.* **1993**, *115*, 8570–8576.
- (138) Yamataka, H.; Nagareda, K.; Ando, K.; Hanafusa, T. *J. Org. Chem.* **1992**, *57*, 2865–2869.
- (139) Yamataka, H.; Nagareda, K.; Takai, Y.; Sawada, M.; Hanafusa, T. *J. Org. Chem.* **1988**, *53*, 3877–3879.
- (140) Singleton, D. A.; Thomas, A. A. *J. Am. Chem. Soc.* **1995**, *117*, 9357–9358.

- (141) Singleton, D. A.; Szymanski, M. J. *J. Am. Chem. Soc.* **1999**, *121*, 9455–9456.
- (142) Frantz, D. E.; Singleton, D. A. *J. Am. Chem. Soc.* **2000**, *122*, 3288–3295.
- (143) Melander, L.; Saunders, W. H. J. In *Reactions Rates of Isotopic Molecules*; Wiley: New York, 1980; pp 95–102.
- (144) Ashley, M. A.; Hirschi, J. S.; Izzo, J. A.; Veticatt, M. J. *J. Am. Chem. Soc.* **2016**, *138*, 1756–1759.
- (145) DelMonte, A. J.; Haller, J.; Houk, K. N.; Sharpless, K. B.; Singleton, D. A.; Strassner, T.; Thomas, A. A. *J. Am. Chem. Soc.* **1997**, *119*, 9907–9908.
- (146) Roytman, V. A.; Hong, Y.; Veticatt, M. J. **2017**, Manuscript in prep.
- (147) Gonzalez-James, O. M.; Singleton, D. A. *J. Am. Chem. Soc.* **2010**, *132*, 6896–6897.
- (148) Plata, R. E.; Singleton, D. A. *J. Am. Chem. Soc.* **2015**, *137*, 3811–3826.
- (149) Fernández, I.; Cossio, F. P. *Chem. Soc. Rev.* **2014**, *43*, 4897–5142.
- (150) Cheong, P. H. Y.; Legault, C. Y.; Um, J. M.; Çelebi-Ölçüm, N.; Houk, K. N. *Chem. Rev.* **2011**, *111*, 5042–5137.
- (151) *Applied Theoretical Organic Chemistry*; Tantillo, D. J., Ed.; World Scientific: London, 2018.
- (152) Bandar, J. S.; Sauer, G. S.; Wulff, W. D.; Lambert, T. H.; Veticatt, M. J. *J. Am. Chem. Soc.* **2014**, *136*, 10700–10707.
- (153) Hu, G.; Gupta, A. K.; Huang, L.; Zhao, W.; Yin, X.; Osminski, W. E. G.; Huang, R. H.; Wulff, W. D.; Izzo, J. A.; Veticatt, M. J. *J. Am. Chem. Soc.* **2017**, *139*, 10267–10285.
- (154) Macharia, J. M.; Wambua, V. M.; Hong, Y.; Harris, L.; Hirschi, J. S.; Evans, G. B.; Veticatt, M. J. *Angew. Chemie - Int. Ed.* **2017**, *56*, 8756–8760.
- (155) Beno, B. R.; Houk, K. N.; Singleton, D. A. *J. Am. Chem. Soc.* **1996**, *118*, 9984–9985.
- (156) Bigeleisen, J.; Mayer, M. G. *J. Chem. Phys.* **1947**, *15*, 261–267.
- (157) Bigeleisen, J. *J. Chem. Phys.* **1949**, *17*, 675–678.
- (158) Lu, D. H.; Maurice, D.; Truhlar, D. G. *J. Am. Chem. Soc.* **1990**, *112*, 6206–6214.
- (159) Bell, R. P. *The Tunnel Effect in Chemistry*; Chapman & Hall: London, 1980.
- (160) Wigner, E. P. *Phys. Chem.* **1932**, *B19*, 203.
- (161) Bahmanyar, S.; Houk, K. N.; Martin, H. J.; List, B. *J. Am. Chem. Soc.* **2003**, *125*, 2475–2479.
- (162) Seebach, D.; Beck, A. K.; Badine, D. M.; Limbach, M.; Eschenmoser, A.; Treasurywala, A. M.; Hobi, R.; Prikoszovich, W.; Linder, B. *Helv. Chim. Acta* **2007**, *90*, 425–471.
- (163) Schmid, M. B.; Zeitler, K.; Gschwind, R. M. *Angew. Chemie - Int. Ed.* **2010**, *49*, 4997–

5003.

- (164) Haindl, M. H.; Hioe, J.; Gschwind, R. M. *J. Am. Chem. Soc.* **2015**, *137*, 12835–12842.
- (165) List, B. *J. Am. Chem. Soc.* **2002**, *124*, 5656–5657.
- (166) Iwamura, H.; Wells, D. H.; Mathew, S. P.; Klussmann, M.; Armstrong, A.; Blackmond, D. G. *J. Am. Chem. Soc.* **2004**, *126*, 16312–16313.
- (167) Iwamura, H.; Mathew, S. P.; Blackmond, D. G. *J. Am. Chem. Soc.* **2004**, *126*, 11770–11771.
- (168) Mathew, S. P.; Klussmann, M.; Iwamura, H.; Wells, D. H.; Armstrong, A.; Blackmond, D. G. *Chem. Commun.* **2006**, No. 41, 4291–4293.
- (169) Sharma, A. K.; Sunoj, R. B. *Chem. Commun.* **2011**, *47*, 5759–5761.
- (170) Patora-Komisarska, K.; Benohoud, M.; Ishikawa, H.; Seebach, D.; Hayashi, Y. *Helv. Chim. Acta* **2011**, *94*, 719–745.
- (171) Moberg, C. *Angew. Chemie - Int. Ed.* **2013**, *52*, 2160–2162.
- (172) Seebach, D.; Sun, X.; Sparr, C.; Ebert, M. O.; Schweizer, W. B.; Beck, A. K. *Helv. Chim. Acta* **2012**, *95*, 1064–1078.
- (173) Seebach, D.; Sun, X.; Ebert, M. O.; Schweizer, W. B.; Purkayastha, N.; Beck, A. K.; Duschmalé, J.; Wennemers, H.; Mukaiyama, T.; Benohoud, M.; et al. *Helv. Chim. Acta* **2013**, *96*, 799–852.
- (174) Huisgen, R. *Acc. Chem. Res.* **1977**, *10*, 117–124.
- (175) Huisgen, R. *Acc. Chem. Res.* **1977**, *10*, 199–206.
- (176) Burés, J.; Armstrong, A.; Blackmond, D. G. *J. Am. Chem. Soc.* **2011**, *133*, 8822–8825.
- (177) Burés, J.; Armstrong, A.; Blackmond, D. G. *J. Am. Chem. Soc.* **2012**, *134*, 6741–6750.
- (178) Burés, J.; Armstrong, A.; Blackmond, D. G. *J. Am. Chem. Soc.* **2012**, *134*, 14264.
- (179) Burés, J.; Armstrong, A.; Blackmond, D. G. *Acc. Chem. Res.* **2016**, *49*, 214–222.
- (180) Sahoo, G.; Rahaman, H.; Madarász, Á.; Pápai, I.; Melarto, M.; Valkonen, A.; Pihko, P. M. *Angew. Chemie - Int. Ed.* **2012**, *51*, 13144–13148.
- (181) Shinisha, C. B.; Sunoj, R. B. *Org. Biomol. Chem.* **2008**, *6*, 3921–3929.
- (182) Zhao, J.-Q.; Gan, L.-H. *European J. Org. Chem.* **2009**, *2009*, 2661–2665.
- (183) Földes, T.; Madarász, Á.; Révész, Á.; Dobi, Z.; Varga, S.; Hamza, A.; Nagy, P. R.; Pihko, P. M.; Pápai, I. *J. Am. Chem. Soc.* **2017**, *139*, 17052–17063.
- (184) Villano, S. M.; Kato, S.; Bierbaum, V. M. *J. Am. Chem. Soc.* **2006**, *128*, 736–737.
- (185) Becke, A. D. *J. Chem. Phys.* **1993**, *98*, 5648–5652.
- (186) Lee, C.; Yang, W.; Parr, R. G. *Phys. Rev. B* **1998**, *37*, 785–789.

- (187) Stephens, P. J.; Devlin, F. J.; Chabalowski, C. F.; Frisch, M. J. *J. Phys. Chem.* **1994**, *98*, 11623–11627.
- (188) Hariharan, P. C.; Pople, J. A. *Theor. Chim. Acta* **1973**, *213*, 213–222.
- (189) Scott, A. P.; Radom, L. *J. Phys. Chem.* **1996**, *100*, 16502–16513.
- (190) Anisimov, V.; Paneth, P. *J. Math. Chem.* **1999**, *26*, 75–86.
- (191) Krishnan, R.; Binkley, J. S.; Seeger, R.; Pople, J. A. *J. Chem. Phys.* **1980**, *72*, 650–654.
- (192) Marenich, A. V.; Cramer, C. J.; Truhlar, D. G. *J. Phys. Chem. B.* **2009**, *113*, 6378–6396.
- (193) Grimme, S.; Ehrlich, S.; Goerigk, L. *J. Comput. Chem.* **2011**, *32*, 1456–1465.
- (194) An, F.; Paul, S.; Ammer, J.; Ofial, A. R.; Mayer, P.; Lakhdar, S.; Mayr, H. *Asian J. Org. Chem.* **2014**, *3*, 550–555.
- (195) Seebach, D.; Grošelj, U.; Badine, D. M.; Schweizer, W. B.; Beck, A. K. *Helv. Chim. Acta* **2008**, *91*, 1999–2034.
- (196) Brazier, J. B.; Evans, G.; Gibbs, T. J. K.; Coles, S. J.; Hursthouse, M. B.; Platts, J. A.; Tomkinson, N. C. O. *Org. Lett.* **2009**, *11*, 133–136.
- (197) Molnár, I. G.; Holland, M. C.; Daniliuc, C.; Houk, K. N.; Gilmour, R. *Synlett* **2016**, *27*, 1051–1055.
- (198) Holland, M. C.; Metternich, J. B.; Daniliuc, C.; Schweizer, W. B.; Gilmour, R. *Chem. - A Eur. J.* **2015**, *21*, 10031–10038.
- (199) Sparr, C.; Gilmour, R. *Angew. Chemie - Int. Ed.* **2011**, *50*, 8391–8395.
- (200) Sparr, C.; Schweizer, W. B.; Senn, H. M.; Gilmour, R. *Angew. Chemie - Int. Ed.* **2009**, *48*, 3065–3068.
- (201) Lokesh, N.; Seegerer, A.; Hioe, J.; Gschwind, R. M. *J. Am. Chem. Soc.* **2018**, *140*, 1855–1862.
- (202) Davis, R. L.; Jensen, K. L.; Gschwend, B.; Jørgensen, K. A. *Chem. Eur. J.* **2014**, *20*, 64–67.
- (203) Duarte, F. J. S.; Santos, A. G. *Org. Biomol. Chem.* **2013**, *11*, 7179–7191.
- (204) Izzo, J. A.; Poulsen, P. H.; Intrator, J. A.; Jørgensen, K. A.; Veticatt, M. J. *J. Am. Chem. Soc.* **2018**, *140*, 8396–8400.
- (205) M. J. Frisch, G. W. Trucks, H. B. Schlegel, G. E. S.; M. A. Robb, J. R. Cheeseman, G. Scalmani, V. Barone, B. M.; G. A. Petersson, H. Nakatsuji, M. Caricato, X. Li, H. P. H.; A. F. Izmaylov, J. Bloino, G. Zheng, J. L. Sonnenberg, M. H.; M. Ehara, K. Toyota, R. Fukuda, J. Hasegawa, M. Ishida, T. N.; Y. Honda, O. Kitao, H. Nakai, T. Vreven, J. A. Montgomery, J.; J. E. Peralta, F. Ogliaro, M. Bearpark, J. J. Heyd, E. B.; K. N. Kudin, V. N. Staroverov, T. Keith, R. Kobayashi, J. N.; K. Raghavachari, A. Rendell, J. C. Burant, S. S. Iyengar, J. T.; M. Cossi, N. Rega, J. M. Millam, M. Klene, J. E. Knox, J. B. C.; et al. Gaussian, Inc.: Wallingford CT 2013.

- (206) Grimme, S.; Antony, J.; Ehrlich, S.; Krieg, H. *J. Chem. Phys.* **2010**, *132*, 154104.
- (207) Stork, G.; White, W. N. *J. Am. Chem. Soc.* **1956**, *78*, 4609–4619.
- (208) Stork, G.; Kreft, A. F. I. *J. Am. Chem. Soc.* **1977**, *99*, 3851–3853.
- (209) Stork, G.; Kreft, A. F. I. *J. Am. Chem. Soc.* **1977**, *99*, 3850–3851.
- (210) Streitwieser, A.; Jayasree, E. G.; Hasanayn, F.; Leung, S. S. *J. Org. Chem.* **2008**, *73*, 9426–9434.
- (211) Guthrie, R. D. *Pure Appl. Chem.* **1988**, *61*, 23–56.
- (212) Seebach, D.; Gilmour, R.; Grošelj, U.; Deniau, G.; Sparr, C.; Ebert, M. O.; Beck, A. K.; McCusker, L. B.; Šišak, D.; Uchimaru, T. *Helv. Chim. Acta* **2010**, *93*, 603–634.
- (213) Marigo, M.; Schulte, T.; Franzén, J.; Jørgensen, K. A. *J. Am. Chem. Soc.* **2005**, *127*, 15710–15711.
- (214) Gotoh, H.; Ishikawa, H.; Hayashi, Y. *Org. Lett.* **2007**, *9*, 5307–5309.
- (215) Dinér, P.; Nielsen, M.; Marigo, M.; Jørgensen, K. A. *Angew. Chemie - Int. Ed.* **2007**, *46*, 1983–1987.
- (216) Hayashi, Y.; Gotoh, H.; Masui, R.; Ishikawa, H. *Angew. Chemie - Int. Ed.* **2008**, *47*, 4012–4015.
- (217) Gotoh, H.; Uchimaru, T.; Hayashi, Y. *Chem. - A Eur. Journal Chemistry - A Eur. J.* **2015**, *21*, 12337–12346.
- (218) Poulsen, P. H.; Feu, K. S.; Paz, B. M.; Jensen, F.; Jørgensen, K. A. *Angew. Chemie - Int. Ed.* **2015**, *54*, 8203–8207.
- (219) Orue, A.; Uria, U.; Roca-López, D.; Delso, I.; Reyes, E.; Carrillo, L.; Merino, P.; Vicario, J. L. *Chem. Sci.* **2017**, *8*, 2904–2913.
- (220) Novacek, J.; Waser, M. *European J. Org. Chem.* **2013**, No. 4, 637–648.
- (221) Provencher, B. A.; Bartelson, K. J.; Liu, Y.; Foxman, B. M.; Deng, L. *Angew. Chemie - Int. Ed.* **2011**, *50*, 10565–10569.
- (222) Poulsen, T. B.; Bernardi, L.; Alemán, J.; Overgaard, J.; Jørgensen, K. A. *J. Am. Chem. Soc.* **2007**, *129*, 441–449.
- (223) Lan, Q.; Wang, X.; Shirakawa, S.; Maruoka, K. *Org. Process Res. Dev.* **2010**, *14*, 684–686.
- (224) Bella, M.; Kobbelgaard, S.; Jørgensen, K. A. *J. Am. Chem. Soc.* **2005**, *127*, 3670–3671.
- (225) Poulsen, T. B.; Bernardi, L.; Bell, M.; Jørgensen, K. A. *Angew. Chemie - Int. Ed.* **2006**, *45*, 6551–6554.
- (226) Berkessel, A.; Guixà, M.; Schmidt, F.; Neudörfl, J. M.; Lex, J. *Chem. - A Eur. J.* **2007**, *13*, 4483–4498.
- (227) Ooi, T.; Ohara, D.; Tamura, M.; Maruoka, K. *J. Am. Chem. Soc.* **2004**, *126*, 6844–6845.

- (228) Fiandra, C. Del; Piras, L.; Fini, F.; Disetti, P.; Moccia, M.; Adamo, M. F. A. *Chem. Commun.* **2012**, 48, 3863–3865.
- (229) MacIver, E. E.; Knipe, P. C.; Cridland, A. P.; Thompson, A. L.; Smith, M. D. *Chem. Sci.* **2012**, 3, 537–540.
- (230) Herrera, R. P.; Sgarzani, V.; Bernardi, L.; Fini, F.; Pettersen, D.; Ricci, A. *J. Org. Chem.* **2006**, 71, 9869–9872.
- (231) Uraguchi, D.; Koshimoto, K.; Ooi, T. *J. Am. Chem. Soc.* **2012**, 134, 6972–6975.
- (232) Uraguchi, D.; Koshimoto, K.; Ooi, T. *Chem. Commun.* **2010**, 46, 300–302.
- (233) González, P. B.; Lopez, R.; Palomo, C. *J. Org. Chem.* **2010**, 75, 3920–3922.
- (234) Liu, Y.; Provencher, B. A.; Bartelson, K. J.; Deng, L. *Chem. Sci.* **2011**, 2, 1301–1304.
- (235) He, R.; Shirakawa, S.; Maruoka, K. *J. Am. Chem. Soc.* **2009**, 131, 16620–16621.
- (236) Wang, L.; Shirakawa, S.; Maruoka, K. *Angew. Chemie - Int. Ed.* **2011**, 50, 5327–5330.
- (237) Uraguchi, D.; Koshimoto, K.; Miyake, S.; Ooi, T. *Angew. Chemie - Int. Ed.* **2010**, 49, 5567–5569.
- (238) Bernal, P.; Fernández, R.; Lassaletta, J. M. *Chem. - A Eur. J.* **2010**, 16, 7714–7718.
- (239) Mase, N.; Ohno, T.; Hoshikawa, N.; Ohishi, K.; Morimoto, H.; Yoda, H.; Takabe, K. *Tetrahedron Lett.* **2003**, 44, 4073–4075.
- (240) Kull, T.; Peters, R. *Angew. Chemie - Int. Ed.* **2008**, 47, 5461–5464.
- (241) Uraguchi, D.; Oyaizu, K.; Ooi, T. *Chem. - A Eur. J.* **2012**, 18, 8306–8309.
- (242) Okada, A.; Shibuguchi, T.; Ohshima, T.; Masu, H.; Yamaguchi, K.; Shibasaki, M. *Angew. Chemie Int. Ed.* **2005**, 44, 4564–4567.
- (243) Ohshima, T.; Gnanadesikan, V.; Shibuguchi, T.; Fukuta, Y.; Nemoto, T.; Shibasaki, M. *J. Am. Chem. Soc.* **2003**, 125, 11206–11207.
- (244) Fukuta, Y.; Ohshima, T.; Gnanadesikan, V.; Shibuguchi, T.; Nemoto, T.; Kisugi, T.; Okino, T.; Shibasaki, M. *Proc. Natl. Acad. Sci. U. S. A.* **2004**, 101, 5433–5438.
- (245) Novacek, J.; Monkowius, U.; Himmelsbach, M.; Waser, M. *Monatshefte für Chemie* **2016**, 147, 533–538.
- (246) Novacek, J.; Waser, M. *European J. Org. Chem.* **2014**, No. 4, 802–809.
- (247) Novacek, J.; Izzo, J. A.; Veticatt, M. J.; Waser, M. *Chem. - A Eur. J.* **2016**, 22, 17339–17344.
- (248) Di Mola, A.; Tiffner, M.; Scorzelli, F.; Palombi, L.; Filosa, R.; De Caprariis, P.; Waser, M.; Massa, A. *Beilstein J. Org. Chem.* **2015**, 11, 2591–2599.
- (249) Tiffner, M.; Novacek, J.; Busillo, A.; Gratzer, K.; Massa, A.; Waser, M. *RSC Adv.* **2015**, 5, 78941–78949.

- (250) Reed, A. E.; Weinstock, R. B.; Weinhold, F. *J. Chem. Phys.* **1985**, *83*, 735–746.
- (251) Lin, X.; Ruan, S.; Yao, Q.; Yin, C.; Lin, L.; Feng, X.; Liu, X. *Org. Lett.* **2016**, *18*, 3602–3605.
- (252) Okino, T.; Nakamura, S.; Furukawa, T.; Takemoto, Y. *Org. Lett.* **2004**, *6*, 625–627.
- (253) Berkessel, A.; Cleemann, F.; Mukherjee, S.; Müller, T. N.; Lex, J. *Angew. Chemie Int. Ed.* **2005**, *44*, 807–811.
- (254) Hoashi, Y.; Okino, T.; Takemoto, Y. *Angew. Chemie - Int. Ed.* **2005**, *44*, 4032–4035.
- (255) Sakamoto, S.; Kazumi, N.; Kobayashi, Y.; Tsukano, C.; Takemoto, Y. *Org. Lett.* **2014**, *16*, 4758–4761.
- (256) Manna, M. S.; Mukherjee, S. *J. Am. Chem. Soc.* **2015**, *137*, 130–133.
- (257) Yoneda, N.; Fukata, Y.; Asano, K.; Matsubara, S. *Angew. Chemie - Int. Ed.* **2015**, *54*, 15497–15500.
- (258) Okino, T.; Hoashi, Y.; Furukawa, T.; Xu, X.; Takemoto, Y. *J. Am. Chem. Soc.* **2005**, *127*, 119–125.
- (259) Hamza, A.; Schubert, G.; Soós, T.; Pápai, I. *J. Am. Chem. Soc.* **2006**, *128*, 13151–13160.
- (260) Azuma, T.; Kobayashi, Y.; Sakata, K.; Sasamori, T.; Tokitoh, N.; Takemoto, Y. *J. Org. Chem.* **2014**, *79*, 1805–1817.
- (261) Zhu, R.; Zhang, D.; Wu, J.; Liu, C. *Tetrahedron Asymmetry* **2006**, *17*, 1611–1616.
- (262) Amovilli, C.; Barone, V.; Cammi, R.; Cancès, E.; Cossi, M.; Mennucci, B.; Pomelli, C. S.; Tomasi, J. *Adv. Quantum Chem.* **1998**, *32*, 227–261.
- (263) Elstner, M.; Porezag, D.; Jungnickel, G.; Elsner, J.; Haugk, M.; Frauenheim, T.; Suhai, S.; Seifert, G. *Phys. Rev. B* **1998**, *58*, 7260–7268.
- (264) Slater, J. C.; Koster, G. F. *Phys. Rev.* **1954**, *94*, 1498–1524.
- (265) Papaconstantopoulos, D. A. *Handbook of the Band Structure of Elemental Solids*; Plenum Press: New York, 1986.
- (266) Hu, G.; Gupta, A. K.; Huang, L.; Zhao, W.; Yin, X.; Osminski, W. E. G.; Huang, R. H.; Wulff, W. D.; Izzo, J. A.; Veticatt, M. J. *J. Am. Chem. Soc.* **2017**, *139*, 10267–10285.
- (267) Pandey, S. K. *Synlett* **2006**, No. 19, 3366–3367.
- (268) Akiyama, T. *Chem. Rev.* **2007**, *107*, 5744–5758.
- (269) Chen, Y.; Yekta, S.; Yudin, A. K. *Chem. Rev.* **2003**, *103*, 3155–3211.
- (270) Bao, J.; Wulff, W. D.; Rheingold, A. L. *J. Am. Chem. Soc.* **1993**, *115*, 3814–3815.
- (271) Zhang, Y.; Desai, A.; Lu, Z.; Hu, G.; Ding, Z.; Wulff, W. D. *Chem. - A Eur. J.* **2008**, *14*, 3785–3803.

- (272) Hu, G.; Gupta, A. K.; Huang, R. H.; Mukherjee, M.; Wulff, W. D. *J. Am. Chem. Soc.* **2010**, *132*, 14669–14675.
- (273) Vetticatt, M. J.; Desai, A. A.; Wulff, W. D. *J. Org. Chem.* **2013**, *78*, 5142–5152.
- (274) Myers, M. C.; Wang, J. L.; Iera, J. A.; Bang, J. K.; Saito, S.; Hara, T.; Zambetti, G. P.; Appella, D. H. *J. Am. Chem. Soc.* **2005**, *127*, 6152–6153.
- (275) Meltzer, P. C.; Butler, D.; Deschamps, J. R.; Madras, B. K. *J. Med. Chem.* **2006**, *49*, 1420–1432.
- (276) Bouteiller, C.; Becerril-Ortega, J.; Marchand, P.; Nicole, O.; Barré, L.; Buisson, A.; Perrio, C. *Org. Biomol. Chem.* **2010**, *8*, 1111–1120.
- (277) Juhl, K.; Jørgensen, K. A. *J. Am. Chem. Soc.* **2002**, *124*, 2420–2421.
- (278) Marigo, M.; Juhl, K.; Jørgensen, K. A. *Angew. Chemie, Int. Ed.* **2003**, *42*, 1367–1369.
- (279) Evans, D. A.; Johnson, D. S. *Org. Lett.* **1999**, *1*, 595–598.
- (280) Anders, B.; Juhl, K.; Kumaragurubaran, N.; Zhuang, W.; Jørgensen, K. A. *Angew. Chemie Int. Ed.* **2002**, *41*, 1790–1793.
- (281) Vogt, H.; Vanderheiden, S.; Bräse, S. *Chem. Commun.* **2003**, *3*, 2448–2449.
- (282) De La Torre, A.; Tona, V.; Maulide, N. *Angew. Chemie Int. Ed.* **2017**, *56*, 12416–12423.
- (283) Evans, R. W.; Zbieg, J. R.; Zhu, S.; Li, W.; MacMillan, D. W. C. *J. Am. Chem. Soc.* **2013**, *135*, 16074–16077.
- (284) Guha, S.; Rajeshkumar, V.; Kotha, S. S.; Sekar, G. *Org. Lett.* **2015**, *17*, 406–409.
- (285) Sharley, J. S.; Collado Pérez, A. M.; Ferri, E. E.; Miranda, A. F.; Baxendale, I. R. *Tetrahedron* **2016**, *72*, 2947–2954.
- (286) Zhao, Y.; Truhlar, D. G. *Theor. Chem. Acc.* **2008**, *120*, 215–241.
- (287) Andrae, D.; Häußermann, U.; Dolg, M.; Stoll, H.; Preuß, H. *Theor. Chim. Acta* **1990**, *77*, 123–141.
- (288) Jie, X.; Shang, Y.; Zhang, X.; Su, W. *J. Am. Chem. Soc.* **2016**, *138*, 5623–5633.
- (289) Beckwith, A. L. J.; Zavitsas, A. A. *J. Am. Chem. Soc.* **1986**, *108*, 8230–8234.
- (290) King, A. E.; Ryland, B. L.; Brunold, T. C.; Stahl, S. S. *Organometallics* **2012**, *31*, 7948–7957.
- (291) King, A. E.; Brunold, T. C.; Stahl, S. S. *J. Am. Chem. Soc.* **2009**, *131*, 5044–5045.
- (292) Yamanaka, M.; Nakamura, E. *Organometallics* **2001**, *20*, 5675–5681.
- (293) Mayoral, J. A.; Rodríguez-Rodríguez, S.; Salvatella, L. *Chem. - A Eur. J.* **2008**, *14*, 9274–9285.
- (294) Frantz, D. E.; Singleton, D. A.; Snyder, J. P. *J. Am. Chem. Soc.* **1997**, *119*, 3383–3384.

- (295) Hickman, A. J.; Sanford, M. S. *Nature* **2012**, *484*, 177–185.
- (296) Larsen, R. In *Organometallics in Process Chemistry*; 2004; Vol. 6, pp 205–245.
- (297) Roughley, S. D.; Jordan, A. M. *J. Med. Chem.* **2011**, *54*, 3451–3479.
- (298) Miyaura, N.; Yamada, K.; Suginome, H.; Suzuki, A. *J. Am. Chem. Soc.* **1985**, *107*, 972–980.
- (299) Smith, G. B.; Dezeny, G. C.; Hughes, D. L.; King, A. O.; Verhoeven, T. R. *J. Org. Chem.* **1994**, *59*, 8151–8156.
- (300) Butters, M.; Harvey, J. N.; Jover, J.; Lennox, A. J. J.; Lloyd-Jones, G. C.; Murray, P. M. *Angew. Chemie - Int. Ed.* **2010**, *49*, 5156–5160.
- (301) Carrow, B. P.; Hartwig, J. F. *J. Am. Chem. Soc.* **2011**, *133*, 2116–2119.
- (302) Braga, A. A. C.; Morgon, N. H.; Ujaque, G.; Maseras, F. *J. Am. Chem. Soc.* **2005**, *127*, 9298–9307.
- (303) Braga, A. A. C.; Ujaque, G.; Maseras, F. *Organometallics* **2006**, *25*, 3647.
- (304) Braga, A. A. C.; Morgon, N. H.; Ujaque, G.; Lledós, A.; Maseras, F. *J. Organomet. Chem.* **2006**, *691*, 4459–4466.
- (305) Sicre, C.; Braga, A. A. C.; Maseras, F.; Cid, M. M. *Tetrahedron* **2008**, *64*, 7437–7443.
- (306) Kozuch, S.; Martin, J. M. L. *ACS Catal.* **2011**, *1*, 246–253.
- (307) Barrios-Landeros, F.; Hartwig, J. F. *J. Am. Chem. Soc.* **2005**, *127*, 6944–6945.
- (308) Barrios-Landeros, F.; Carrow, B. P.; Hartwig, J. F. *J. Am. Chem. Soc.* **2009**, *131*, 8141–8154.
- (309) Matos, K.; Soderquist, J. A. *J. Org. Chem.* **1998**, *63*, 461–470.
- (310) Amatore, C.; Le Duc, G.; Jutand, A. *Chem. - A Eur. J.* **2013**, *19*, 10082–10093.
- (311) Thomas, A. A.; Denmark, S. E. *Science (80-.)*. **2016**, *352*, 329–332.
- (312) Thomas, A. A.; Wang, H.; Zahrt, A. F.; Denmark, S. E. *J. Am. Chem. Soc.* **2017**, *139*, 3805–3821.
- (313) Lima, C. F. R. A. C.; Rodrigues, A. S. M. C.; Silva, V. L. M.; Silva, A. M. S.; Santos, L. M. N. B. F. *ChemCatChem* **2014**, *6*, 1291–1302.
- (314) Zhang, H.; Kwong, F. Y.; Tian, Y.; Chan, K. S. *J. Org. Chem.* **1998**, *63*, 6886–6890.
- (315) Wasicak, J. T.; Garvey, D. S.; Holladay; Mark, W.; Nan-Horng, L.; Ryther, K. B. US5733912, 1998.
- (316) Mardirossian, N.; Head-Gordon, M. *Mol. Phys.* **2017**, *115*, 2315–2372.
- (317) Zhao, Y.; Schultz, N. E.; Truhlar, D. G. *J. Chem. Theory Comput.* **2006**, *2*, 364–382.
- (318) Zhao, Y.; Truhlar, D. G. *J. Chem. Phys.* **2006**, *125*, 194101.

- (319) Chai, J. Da; Head-Gordon, M. *Phys. Chem. Chem. Phys.* **2008**, *10*, 6615–6620.
- (320) Adamo, C.; Barone, V. *J. Chem. Phys.* **1999**, *110*, 6158–6170.
- (321) Lynch, B. J.; Fast, P. L.; Harris, M.; Truhlar, D. G. *J. Phys. Chem. A* **2000**, *104*, 4811–4815.
- (322) Weigend, F.; Ahlrichs, R. *Phys. Chem. Chem. Phys.* **2005**, *7*, 3297–3305.
- (323) Yu, H. S.; He, X.; Truhlar, D. G. *J. Chem. Theory Comput.* **2016**, *12*, 1280–1293.
- (324) Frisch, M. J.; Trucks, G. W.; Schlegel, H. B.; Scuseria, G. E.; Robb, M. A.; Cheeseman, J. R.; Scalmani, G.; Barone, V.; Petersson, G. A.; Nakatsuji, H.; et al. Gaussian, Inc.: Wallingford CT 2016.
- (325) Tan, B.; Lu, Y.; Zeng, X.; Chua, P. J.; Zhong, G. *Org. Lett.* **2010**, *12*, 2682–2685.
- (326) Guo, J.; Wong, M. W. *J. Org. Chem.* **2017**, *82*, 4362–4368.
- (327) Zhu, J.; Zhang, Y.; Liu, C.; Zheng, A.; Wang, W. *J. Org. Chem.* **2012**, *77*, 9813–9825.
- (328) Zhang, Z.; Lippert, K. M.; Hausmann, H.; Kotke, M.; Schreiner, P. R. *J. Org. Chem.* **2011**, *76*, 9764–9776.
- (329) Supady, A.; Hecht, S.; Baldauf, C. *Org. Lett.* **2017**, *19*, 4199–4202.
- (330) Hayama, N.; Kuramoto, R.; Földes, T.; Nishibayashi, K.; Kobayashi, Y.; Pápai, I.; Takemoto, Y. *J. Am. Chem. Soc.* **2018**, jacs.8b07511.
- (331) Heshmat, M. *J. Phys. Chem. A* **2018**, ASAP.
- (332) Madarász, Á.; Dósa, Z.; Varga, S.; Soós, T.; Csámpai, A.; Pápai, I. *ACS Catal.* **2016**, *6*, 4379–4387.
- (333) Tárkányi, G.; Király, P.; Soós, T.; Varga, S. *Chem. - A Eur. J.* **2012**, *18*, 1918–1922.
- (334) Esteban, F.; Ciešlik, W.; Arpa, E. M.; Guerrero-Corella, A.; Díaz-Tendero, S.; Perles, J.; Fernández-Salas, J. A.; Fraile, A.; Alemán, J. *ACS Catal.* **2018**, *8*, 1884–1890.
- (335) Hay, P. J.; Wadt, W. R. *J. Chem. Phys.* **1985**, *82*, 270.
- (336) Ehlers, A. W.; Böhme, M.; Dapprich, S.; Gobbi, A.; Höllwarth, A.; Jonas, V.; Köhler, K. F.; Stegmann, R.; Veldkamp, A.; Frenking, G. *Chem. Phys. Lett.* **1993**, *208*, 111–114.
- (337) Roy, L. E.; Hay, P. J.; Martin, R. L. *J. Chem. Theory Comput.* **2008**, *4*, 1029–1031.